



UNIVERSITY OF IOANNINA  
School of Sciences  
Department of Physics

# Study of neutron induced reactions in rare earth isotopes

PhD thesis

Efstathia Georgali



**Operational Programme**  
**Human Resources Development,**  
**Education and Lifelong Learning**  
Co-financed by Greece and the European Union



This research is co-financed by Greece and the European Union (European Social Fund-ESF) through the Operational Programme «Human Resources Development, Education and Lifelong Learning» in the context of the project “Strengthening Human Resources Research Potential via Doctorate Research-2<sup>nd</sup> Cycle” (MIS-5000432), implemented by the State Scholarships Foundation (IKY).



ΠΑΝΕΠΙΣΤΗΜΙΟ ΙΩΑΝΝΙΝΩΝ  
Σχολή Θετικών Επιστημών  
Τμήμα Φυσικής

# Μελέτη αντιδράσεων νετρονίων σε ισότοπα σπάνιων γαιών

Διδακτορική Διατριβή  
Ευσταθία Γεωργαλή



Επιχειρησιακό Πρόγραμμα  
Ανάπτυξη Ανθρώπινου Δυναμικού,  
Εκπαίδευση και Διά Βίου Μάθηση

Με τη συγχρηματοδότηση της Ελλάδας και της Ευρωπαϊκής Ένωσης



Το έργο συγχρηματοδοτείται από την Ελλάδα και την Ευρωπαϊκή Ένωση (Ευρωπαϊκό Κοινωνικό Ταμείο) μέσω του Επιχειρησιακού Προγράμματος «Ανάπτυξη Ανθρώπινου Δυναμικού, Εκπαίδευση και Διά Βίου Μάθηση», στο πλαίσιο της Πράξης «Ενίσχυση του ανθρώπινου ερευνητικού δυναμικού μέσω της υλοποίησης διδακτορικής έρευνας-2<sup>ος</sup> Κύκλος» (ΜΙΣ-5000432), που υλοποιεί το Ίδρυμα Κρατικών Υποτροφιών (ΙΚΥ).



Three-member Advisor Committee:

Nikolaos Patronis, Associate Professor, Physics Department, University of Ioannina, Ioannina, Greece (Supervisor)

Michael Kokkoris, Professor, School of Applied Mathematical and Physical Sciences, National Technical University of Athens, Athens, Greece

Anastasios Lagoyannis, Research Director, National Centre for Scientific Research “Demokritos”, Athens, Greece

Seven-member Examination Committee:

Nikolaos Patronis, Associate Professor, Physics Department, University of Ioannina, Ioannina, Greece

Michael Kokkoris, Professor, School of Applied Mathematical and Physical Sciences, National Technical University of Athens, Athens, Greece

Anastasios Lagoyannis, Research Director, National Centre for Scientific Research “Demokritos”, Athens, Greece

Nicola Colonna, First Researcher, Istituto Nazionale di Fisica Nucleare (INFN), Sez. di Bari, Bari, Italy

Michail Axiotis, Researcher, National Centre for Scientific Research “Demokritos”, Athens, Greece

Nikolaos Nicolis, Associate Professor, Physics Department, University of Ioannina, Ioannina, Greece

Stylianos Stoulos, Associate Professor, Physics Department, Aristotle University of Thessaloniki, Thessaloniki, Greece



Τριμελής Συμβουλευτική Επιτροπή:

Νικόλαος Πατρώνης, Αναπληρωτής Καθηγητής, Τμήμα Φυσικής, Πανεπιστήμιο Ιωαννίνων, Ιωάννινα, Ελλάδα (Επιβλέπων Καθηγητής)

Μιχαήλ Κόκκορης, Καθηγητής, Σχολή Εφαρμοσμένων Μαθηματικών και Φυσικών Επιστημών, Εθνικό Μετσόβιο Πολυτεχνείο, Αθήνα, Ελλάδα

Αναστάσιος Λαγογιάννης, Διευθυντής Ερευνών, Εθνικό Κέντρο Έρευνας Φυσικών Επιστημών «Δημόκριτος», Αθήνα, Ελλάδα

Επταμελής Εξεταστική Επιτροπή:

Νικόλαος Πατρώνης, Αναπληρωτής Καθηγητής, Τμήμα Φυσικής, Πανεπιστήμιο Ιωαννίνων, Ιωάννινα, Ελλάδα

Μιχαήλ Κόκκορης, Καθηγητής, Σχολή Εφαρμοσμένων Μαθηματικών και Φυσικών Επιστημών, Εθνικό Μετσόβιο Πολυτεχνείο, Αθήνα, Ελλάδα

Αναστάσιος Λαγογιάννης, Διευθυντής Ερευνών, Εθνικό Κέντρο Έρευνας Φυσικών Επιστημών «Δημόκριτος», Αθήνα, Ελλάδα

Nicola Colonna, Διευθυντής Ερευνών, Istituto Nazionale di Fisica Nucleare (INFN), Sez. di Bari, Bari, Italy

Μιχαήλ Αξιώτης, Ερευνητής Γ', Εθνικό Κέντρο Έρευνας Φυσικών Επιστημών «Δημόκριτος», Αθήνα, Ελλάδα

Νικόλαος Νικολής, Αναπληρωτής Καθηγητής, Τμήμα Φυσικής, Πανεπιστήμιο Ιωαννίνων, Ιωάννινα, Ελλάδα

Στυλιανός Στούλος, Αναπληρωτής Καθηγητής, Τμήμα Φυσικής, Αριστοτέλειο Πανεπιστήμιο Θεσσαλονίκης, Θεσσαλονίκη, Ελλάδα



To my parents,  
Gerasimos and Persefoni







# Ευχαριστίες

Στον τομέα της έρευνας κάποιος πρέπει να έχει ξεχωριστούς συναδέλφους και φίλους να τον συνοδεύουν στις προσπάθειες να φτάσει στην «αλήθεια». Προσωπικά, θα ήθελα να ευχαριστήσω όλους τους ανθρώπους που στάθηκαν δίπλα μου και συνέβαλαν σε αυτό το έργο με τις γνώσεις και την εμπειρία τους, καθώς και με το χαμόγελο και τη στήριξή τους.

Θα ήθελα να πω ένα ξεχωριστό ευχαριστώ στον επιβλέποντα καθηγητή μου, Δρ. Νικόλα Πατρώνη. Η συνεργασία με ένα τόσο λαμπρό μυαλό, ήταν πολύ δημιουργική για μένα, καθώς μπόρεσα να βελτιώσω τις δεξιότητες και τις γνώσεις μου και να γίνω καλύτερος φυσικός μαθαίνοντας από αυτόν. Θα ήθελα, επίσης, να τον ευχαριστήσω που ήταν πάντα εκεί για να με στηρίξει και να με βοηθήσει να ξεπεράσω όλες τις προκλήσεις που αντιμετώπισα κατά τη διάρκεια της παρούσας έρευνας.

Θα ήθελα, επίσης, να ευχαριστήσω τον Δρ. Ξενοφών Ασλάνογλου και τον Δρ. Μιχαήλ Κόκκορη που ήταν πάντα πρόθυμοι να μου δώσουν πολύτιμες συμβουλές. Η βοήθεια και η στήριξη που προσέφεραν κατά την πραγματοποίηση των πειραμάτων ήταν, επίσης, ανεκτίμητη.

Φυσικά, η συμβολή της ομάδας του Ινστιτούτου Πυρηνικής και Σωματιδιακής Φυσικής του Ε.Κ.Ε.Φ.Ε. «Δημόκριτος» ήταν, επίσης, πολύ σημαντική για την πραγματοποίηση των παρουσών μετρήσεων. Πρώτον, θα ήθελα να ευχαριστήσω τον Δρ. Σωτήριο Χαρισσόπουλο για την υποστήριξή του. Η συμβολή του Δρ. Αναστάσιου Λαγογιάννη και του Δρ. Μιχαήλ Αξιώτη ήταν, επίσης, πρωταρχικής σημασίας για τη διευθέτηση σημαντικών ζητημάτων κατά την πραγματοποίηση των ακτινοβολήσεων και για την παροχή επιστημονικής και τεχνικής βοήθειας. Επιπλέον, θα ήθελα να ευχαριστήσω τη Δρ. Ελένη Βαγενά που ήταν εκεί και συνέβαλε σε οτιδήποτε χρειαζόταν.

Υψίστης σημασίας ήταν, επίσης, η συμβολή του Ινστιτούτου Πυρηνικών και Ραδιολογικών Επιστημών, Τεχνολογίας Ενέργειας και Ασφάλειας του Ε.Κ.Ε.Φ.Ε. «Δημόκριτος», όπου πραγματοποιήθηκε ένα μεγάλο μέρος των μετρήσεων της επαγόμενης ενεργότητας των δειγμάτων. Ως εκ τούτου, θα ήθελα να ευχαριστήσω τον Δρ. Ίων Σταματελάτο μαζί με τη Δρ. Θεοδώρα Βασιλοπούλου και τη Δρ. Μαρία Σάββα που με βοήθησαν να εξοικειωθώ με το εργαστήριο, συνέβαλαν στις μετρήσεις με την εμπειρία τους και δημιούργησαν ένα πολύ φιλικό περιβάλλον εργασίας.

Ένα σημαντικό μέρος των μετρήσεων πραγματοποιήθηκε, επίσης, στο Τμήμα Παρακολούθησης Ραδιενέργειας Περιβάλλοντος της Ελληνικής Επιτροπής Ατομικής Ενέργειας. Για αυτό τον λόγο, θέλω να ευχαριστήσω τον Δρ. Κωνσταντίνο Ποτηριάδη και τον Δρ. Κωνσταντίνο Καρφοπούλο για τη φιλοξενία τους και για όλες τις εποικοδομητικές συζητήσεις που είχαμε σε θέματα που προέκυπταν κατά τη διάρκεια των μετρήσεων.

Επιπλέον, θα ήθελα να ευχαριστήσω όλα τα μέλη της ομάδας μου που συνεργαστήκαμε όλα αυτά τα χρόνια στα Ιωάννινα και ήταν συνταξιδιώτες στο ταξίδι μου μέχρι σήμερα. Ιδιαίτερες ευχαριστίες στις Ζηνοβία Ελεμέ, Ελισσώ Σταμάτη και Μαρία Πεοβίτη για τη συνεργασία, τη συμβολή τους στα πειράματα και τις τόσες ώρες που περάσαμε μαζί δουλεύοντας και συζητώντας για την επιστήμη και τη ζωή.

Επιπλέον, θα ήθελα να ευχαριστήσω τη Δρ. Ρόζα Βλαστού για την στήριξη σε αυτό το έργο αλλά και για τις συμβουλές της. Ιδιαίτερες ευχαριστίες στους Δρ. Αντιγόνη Καλαμάρα, Δρ. Αθανάσιο Σταματόπουλο, Αναστάσιο Αναστασιάδη, Ελένη Μήτση και Σωτήρη Χασάπογλου για τη συμμετοχή τους στα πειράματα και τη συμβολή τους ώστε αυτά να πραγματοποιηθούν το ομαλότερο και καλύτερο δυνατόν.

Ακόμη, ευχαριστώ το Ίδρυμα Κρατικών Υποτροφιών (ΙΚΥ) για την υποστήριξη αυτής της διατριβής καθώς και το έργο “CALIBRA / EYIE” (MIS 5002799) που υλοποιείται στο πλαίσιο της Δράσης «Ενίσχυση της υποδομής έρευνας και καινοτομίας», χρηματοδοτείται από το Επιχειρησιακό Πρόγραμμα «Ανταγωνιστικότητα, Επιχειρηματικότητα και Καινοτομία» (ΕΣΠΑ 2014-2020) και συγχρηματοδοτείται από την Ελλάδα και την Ευρωπαϊκή Ένωση (Ευρωπαϊκό Ταμείο Περιφερειακής Ανάπτυξης).

Τέλος, σας ευχαριστώ Γεράσιμε, Περσεφόνη, Αναστάση, Ανδρέα και Δήμητρα για όλη τη δύναμη και την αισιοδοξία που μου δίνετε με την αγάπη και την αγκαλιά σας.

# Acknowledgements

In the field of research someone needs to have special colleagues and friends to accompany him to the attempts of reaching the “truth”. Personally, I would like to thank all the people who stood next to me and contributed to this work with their knowledge and experience, as well as with their smile and support.

I would like to give special thanks to my Supervisor, Dr Nikolas Patronis. Cooperating with such a brilliant mind as his was very creative for me, as I was able to improve my skills and knowledge and become a better physicist by learning from him. I would also like to thank him for being always there to support and help me to overcome all the challenges that I encountered during the present work.

I would also like to thank Dr Xenofon Aslanoglou and Dr Michael Kokkoris for being always willing to give me valuable advice. The help and support they offered during the performance of the experiments was also priceless.

Of course, the contribution of the team of the accelerator facility at the Institute of Nuclear and Particle Physics at N.C.S.R. “Demokritos” was also very crucial for the realization of the present measurements. Firstly, I would like to thank Dr Sotirios Harissopoulos for his support. The contribution of Dr Anastasios Lagoyannis and Dr Michael Axiotis was also of prime importance for taking care of significant issues for the realization of the irradiations and offering scientific and technical support. In addition, I would like to thank Dr Eleni Vagena for being there and contributing to anything needed.

Fundamental was also the support of the Institute of Nuclear and Radiological Sciences, Energy, Technology and Safety at N.C.S.R. “Demokritos”, where a large part of the activity measurements was performed. Therefore, I would like to thank Dr Ion Stamatelatos along with Dr Theodora Vasilopoulou and Dr Maria Savva for helping me get familiarized with the laboratory, supporting the measurements with their experience and making a very friendly environment for me to work.

A significant part of the measurements was also performed at the Environmental Radioactivity Monitoring Department at Greek Atomic Energy Commission. For this reason, I want to thank Dr Constantinos Potiriadis and Dr Konstantinos Karfopoulos for their hospitality and for all the fruitful discussions we had on issues emerged during the measurements.

Furthermore, I would like to thank all the members of my group with whom we have worked together all these years at Ioannina and were co-travelers in my journey up to now. Special thanks to Zinovia Eleme, Elisso Stamati and Maria Peoviti for the cooperation, the experiments support and the so many hours we spent together working and discussing about science and life.

In addition, I would like to thank Dr Roza Vlastou for supporting this work and for her advice. Special thanks to Dr Antigoni Kalamara, Dr Athanasios Stamatopoulos, Anastasios Anastasiadis, Eleni Mitsi and Sotirios Chasapoglou for their participation to the experiments and their contribution so that they were done the smoother it was possible.

I acknowledge support of this work by the State Scholarships Foundation (IKY) and by the project “CALIBRA/EYIE” (MIS 5002799) which is implemented under the Action “Reinforcement of the Research and Innovation Infrastructure”, funded by the Operational Programme “Competitiveness, Entrepreneurship and Innovation” (NSRF 2014-2020) and cofinanced by Greece and the European Union (European Regional Development Fund).

Finally, thank you Gerasimos, Persefoni, Anastasis, Andreas and Dimitra for all the strength and optimism you give me with your love and hug.

# Περίληψη

Παρόλο που η μελέτη των πυρηνικών αντιδράσεων ξεκίνησε ήδη από το 1919, όταν έγινε η πρώτη παρατήρηση του πυρήνα από τον Ernest Rutherford, η μελέτη των πυρηνικών αντιδράσεων εξακολουθεί να είναι ένα ανοιχτό πεδίο γεμάτο προκλήσεις, καθώς το πρόβλημα των πυρηνικών αντιδράσεων δεν μπορεί να λυθεί μέσω των αναλυτικών εξισώσεων της κβαντικής μηχανικής. Αυτή η πολυπλοκότητα προέρχεται τόσο από το γεγονός ότι η ισχυρή αλληλεπίδραση μέσω της οποίας τα νουκλεόνια αλληλεπιδρούν μεταξύ τους παραμένει ένα ανοιχτό ερευνητικό πεδίο αλλά και λόγω του μεγάλου αριθμού νουκλεονίων που συμμετέχουν σε μια αντίδραση. Η έρευνα στο πεδίο της πυρηνικής φυσικής αντιμετωπίζει αυτά τα ζητήματα μέσω της ανάπτυξης θεωρητικών μοντέλων που στοχεύουν στην περιγραφή των πυρηνικών αντιδράσεων και στην αναπαραγωγή των αντίστοιχων παρατηρήσιμων μεγεθών.

Τα θεωρητικά μοντέλα είναι ένα είδος «προσομοίωσης της πραγματικότητας» και έχουν αναπτυχθεί είτε ώστε να αναπαραγάγουν τα παρατηρήσιμα μεγέθη είτε στη βάση της ήδη υπάρχουσας εμπειρίας από συστήματα που μοιάζουν προσεγγιστικά με τον πυρήνα είτε στη βάση της υπάρχουσας γνώσης των ιδιοτήτων του πυρήνα. Αυτά είναι τα λεγόμενα φαινομενολογικά μοντέλα. Επιπλέον, τις τελευταίες δεκαετίες η έρευνα στον τομέα της θεωρητικής φυσικής οδήγησε σε πρόοδο στο πεδίο των μικροσκοπικών προσεγγίσεων των πυρηνικών αντιδράσεων, και ως εκ τούτου μικροσκοπικά μοντέλα έχουν επίσης αναπτυχθεί.

Φυσικά, δεν υπάρχει ένα γενικό και ευρέως χρησιμοποιούμενο μοντέλο που μπορεί να περιγράψει συνολικά μία πυρηνική αντίδραση. Αντί αυτού, έχουν αναπτυχθεί διαφορετικοί κώδικες, όπως οι TALYS και EMPIRE, όπου τα διάφορα θεωρητικά μοντέλα συνδυάζονται και καθένα από αυτά πληροί διαφορετικούς σκοπούς. Μεταξύ αυτών των σκοπών είναι η συνεισφορά διαφορετικών μηχανισμών σε μια πυρηνική αντίδραση, ο υπολογισμός των συντελεστών εκπομπής σωματιδίων και ο υπολογισμός της πυκνότητας των ενεργειακών επιπέδων του πυρήνα. Η βελτίωση των θεωρητικών μοντέλων βρίσκεται σε εξέλιξη προκειμένου να κατανοηθεί σε βάθος η φύση των πυρηνικών αντιδράσεων. Αυτό επιτυγχάνεται είτε με τροποποιήσεις στη βάση των μοντέλων είτε με τη βελτίωση της αντίστοιχης παραμετροποίησης έτσι ώστε να επιτευχθεί καλύτερη συμφωνία με τα πειραματικά δεδομένα.

Οι πυρηνικές αντιδράσεις των σταθερών ισωτόπων εξακολουθούν να είναι μία ερευνητική περιοχή όπου η σύγκριση των πειραματικών δεδομένων με τους αντίστοιχους θεωρητικούς υπολογισμούς συχνά αποκαλύπτει μεγάλες αποκλίσεις μεταξύ τους. Επιπλέον, παρατηρείται ασυνέπεια ακόμη και μεταξύ των υπάρχοντων πειραματικών δεδομένων. Συνεπώς, η πειραματική μελέτη των πυρηνικών αντιδράσεων σε ανεξερεύνητες περιοχές (μάζας και ενέργειας), αλλά ακόμη και σε ήδη μελετημένες περιοχές, είναι απαραίτητη για την ανανέωση των βιβλιοθηκών δεδομένων. Με αυτόν τον τρόπο, ενισχύεται η εγκυρότητα της σύγκρισης των θεωρητικών μοντέλων με τα πειραματικά δεδομένα.

Επιπλέον, χάρη στη συνεχή βελτίωση της τεχνολογίας των ανιχνευτών και των επιταχυντών, αλλά και χάρη στους κώδικες προσομοίωσης (π.χ. GEANT4,

MCNP5, FLUKA), έχουν ανοίξει νέοι ορίζοντες στις πειραματικές τεχνικές, καθώς και στην ανάλυση των πειραματικών δεδομένων. Χρησιμοποιώντας αυτές τις νέες δυνατότητες καθίσταται δυνατή η πραγματοποίηση προηγούμενων ανέφικτων ή απαιτητικών πειραμάτων.

Είναι γνωστό ότι τα θεωρητικά μοντέλα έχουν διαφορετικό επίπεδο επιτυχίας στην αναπαραγωγή των πειραματικών δεδομένων για διαφορετικές ενεργειακές και μαζικές περιοχές. Επομένως, μια συστηματική μελέτη των πυρηνικών αντιδράσεων για μια συγκεκριμένη μαζική περιοχή που χρησιμοποιεί παράλληλα τα πλεονεκτήματα των τεχνολογικών εξελίξεων αποτελεί ένα πολύτιμο εργαλείο για την αξιολόγηση των θεωρητικών μοντέλων. Η παρούσα εργασία αναφέρεται στη μελέτη πυρηνικών αντιδράσεων για ισότοπα σπάνιων γαιών για ενέργειες μεταξύ 10-20 MeV. Εκτός από το ισότοπο Sc που ανήκει στην περιοχή χαμηλής έως μεσαίας μάζας ( $A=45$ ), τα ισότοπα των υπόλοιπων στοιχείων σπάνιων γαιών ανήκουν στην περιοχή μεσαίας έως βαριάς μάζας.

Συγκεκριμένα, στην παρούσα εργασία μελετήθηκε η αντίδραση  $(n,2n)$  για το σταθερό ισότοπο Ho ( $^{165}\text{Ho}$ ), καθώς και για τα δύο ελαφρύτερα σταθερά ισότοπα Er και Dy ( $^{162}\text{Er}$  και  $^{156}\text{Dy}$ ). Πιο συγκεκριμένα, οι αντίστοιχες ενεργές διατομές αυτών των αντιδράσεων μετρήθηκαν πειραματικά σε διαφορετικές ενέργειες. Οι μετρούμενες ενεργές διατομές συγκρίθηκαν με προηγούμενες μετρήσεις, καθώς και με τους θεωρητικούς υπολογισμούς με βάση τον ευρέως χρησιμοποιούμενο στατιστικό κώδικα TALYS σε μια προσπάθεια διερεύνησης της απόδοσης του κώδικα για τα διάφορα θεωρητικά μοντέλα και πρότυπα που είναι ενσωματωμένα σε αυτόν.

Το κανάλι  $(n,2n)$  του  $^{165}\text{Ho}$  τροφοδοτεί δύο καταστάσεις του πυρήνα  $^{164}\text{Ho}$ : την ισομερή κατάσταση ( $J^\pi = 6^-$ ) σε ενέργεια διέγερσης  $E_{ex}=139.8$  keV, καθώς και την βασική κατάσταση ( $J^\pi = 1^+$ ). Λόγω αυτού, η μέτρηση των ενεργών διατομών των δύο αυτών καναλιών αποτελεί μία ενδιαφέρουσα παρατήρηση σε σχέση με το spin των δύο αυτών καταστάσεων. Από την άλλη πλευρά, τα ισότοπα  $^{162}\text{Er}$  και  $^{156}\text{Dy}$  είναι τα ελαφρύτερα σταθερά ισότοπα των αντίστοιχων στοιχείων, χαρακτηριστικό που προσθέτει ένα επιπλέον κίνητρο και ενδιαφέρον για τη μελέτη των συγκεκριμένων αντιδράσεων.

Τα πειραματικά δεδομένα είναι επίσης απαραίτητα για την κατασκευή των βιβλιοθηκών πυρηνικών δεδομένων, όπως οι ENDF (Evaluated Nuclear Data File), JEFF (Joint Evaluated Fission and Fusion File) και JENDL (Japanese Evaluated Nuclear Data Library). Ο βιβλιοθήκες πυρηνικών δεδομένων βασίζονται στην αξιολόγηση των πειραματικών δεδομένων και έχουν μεγάλη σημασία για τους σκοπούς της πυρηνικής επιστήμης. Πρώτον, μπορούν να χρησιμοποιηθούν είτε ως αρχεία εισαγωγής για τους κώδικες θεωρητικών υπολογισμών είτε για την εξαγωγή της παραμετροποίησης αυτών. Επίσης, οι βιβλιοθήκες πυρηνικών δεδομένων συμβάλλουν σημαντικά σε σκοπούς πυρηνικής τεχνολογίας που σχετίζονται π.χ. με την πυρηνική ιατρική, την ασφάλεια και την ακτινοπροστασία και τον χαρακτηρισμό υλικών.

Οι βιβλιοθήκες νετρονίων, ειδικότερα, σε συνδυασμό με τη θεωρητική μοντελοποίηση διαδραματίζουν καθοριστικό ρόλο στις εφαρμογές πυρηνικής ενέργειας και, ειδικότερα, στην τεχνολογία των αντιδραστήρων. Πιο συγκεκριμένα, η ακριβής γνώση και κατανόηση των αντιδράσεων που επάγονται από νετρόνια είναι σημαντική, έτσι ώστε να προσδιοριστούν τα στοιχεία και τα ισότοπα που μπορούν να χρησιμοποιηθούν π.χ. ως δομικά υλικά και απορροφητές σε αυτά τα συστήματα. Τα ισότοπα σπάνιων

γαίων, ειδικότερα, χρησιμοποιούνται ή έχουν προταθεί για χρήση σε διάφορους τύπους αντιδραστήρων, π.χ. το Dy και Er μπορούν να χρησιμοποιηθούν ως απορροφητές νετρονίων.

Οι βιβλιοθήκες πυρηνικών δεδομένων είναι επίσης υψίστης σημασίας για αστροφυσικούς σκοπούς, όπως η εξαγωγή της φυσικής περιεκτικότητας στοιχείων και ισotόπων, καθώς και η μείωση των αντίστοιχων αβεβαιοτήτων μέσω της σύγκρισης των πειραματικών δεδομένων με τους αντίστοιχους υπολογισμούς που βασίζονται στις βιβλιοθήκες δεδομένων. Συγκεκριμένα, οι αντιδράσεις νετρονίων διαδραματίζουν βασικό ρόλο στον υπολογισμό των περιεκτικότητων ισotόπων που παράγονται μέσω των διαδικασιών s και r, οι οποίες περιγράφουν την παραγωγή ισotόπων μέσω αντιδράσεων σύλληψης νετρονίων.

Τα πειραματικά δεδομένα από προηγούμενες μετρήσεις για τις αντιδράσεις  $^{162}\text{Er}(n, 2n)^{161}\text{Er}$  και  $^{156}\text{Dy}(n, 2n)^{155}\text{Dy}$  περιορίζονται σε μια στενή ενεργειακή περιοχή μεταξύ 13.5-14.8 MeV και, επιπλέον, παρουσιάζουν σημαντικές αποκλίσεις μεταξύ τους. Τα δεδομένα των αντιδράσεων  $^{165}\text{Ho}(n,2n)^{164}\text{Ho}^m$  και  $^{165}\text{Ho}(n,2n)^{164}\text{Ho}^g$  αναφέρονται σε μια ευρύτερη ενεργειακή περιοχή μεταξύ 12-20 MeV, παρουσιάζουν, όμως, επίσης σημαντικές αποκλίσεις μεταξύ τους.

Στην παρούσα έρευνα, η ενεργός διατομή των αντιδράσεων  $^{162}\text{Er}(n,2n)^{161}\text{Er}$ ,  $^{156}\text{Dy}(n,2n)^{155}\text{Dy}$ ,  $^{165}\text{Ho}(n,2n)^{164}\text{Ho}^m$  and  $^{165}\text{Ho}(n,2n)^{164}\text{Ho}^g$  μετρήθηκε μέσω της τεχνικής της ενεργοποίησης σε σχέση με τις αντιδράσεις αναφοράς  $^{197}\text{Au}(n, 2n)^{196}\text{Au}$ ,  $^{27}\text{Al}(n, \alpha)^{24}\text{Na}$  και  $^{93}\text{Nb}(n,2n)^{92}\text{Nb}^m$ . Οι ημι-μονοενεργειακές δέσμες νετρονίων παρήχθησαν μέσω των αντιδράσεων  $^2\text{H}(d,n)^3\text{He}$  (DD) και  $^3\text{H}(d,n)^4\text{He}$  (DT). Οι δέσμες δευτερίων επιταχύνθηκαν από τον 5.5 MV Tandem Van de Graaff επιταχυντή του Ινστιτούτου Πυρηνικής και Σωματιδιακής Φυσικής του Ε.Κ.Ε.Φ.Ε. «Δημόκριτος», Αθήνα, Ελλάδα. Μετά το τέλος των ακτινοβολήσεων η επαγόμενη ενεργότητα στα δείγματα μετρήθηκε μέσω φασματοσκοπίας-γ χρησιμοποιώντας ανιχνευτές γερμανίου υπερ-υψηλής καθαρότητας (HPGe).

Για την ακριβή ερμηνεία των πειραματικών δεδομένων το λογισμικό GEANT4 χρησιμοποιήθηκε εκτενώς. Αρχικά, χρησιμοποιήθηκε για την προσομοίωση της δέσμης νετρονίων που παράγεται στο εργαστήριο Πυρηνικής και Σωματιδιακής Φυσικής του Ε.Κ.Ε.Φ.Ε. «Δημόκριτος» μέσω της προσομοίωσης των αντιδράσεων DD και DT. Για το σκοπό αυτό, η πλήρης γεωμετρία των στόχων (δευτερίου και τριτίου), καθώς και η γραμμή της δέσμης δευτερίων ελήφθη υπόψη στις προσομοιώσεις. Τα αποτελέσματα χρησιμοποιήθηκαν για τον υπολογισμό της κατανομής ενέργειας της δέσμης νετρονίων, η οποία βρέθηκε σε συμφωνία με τα αντίστοιχα αποτελέσματα του κώδικα NEUSDESC.

Το λογισμικό GEANT4 χρησιμοποιήθηκε, επίσης, για την προσομοίωση της γεωμετρίας των HPGe ανιχνευτών. Συγκεκριμένα, μέσω του GEANT4 προσδιορίστηκε η βέλτιστη γεωμετρία των ανιχνευτών για την οποία αναπαραγάγονται τα πειραματικά δεδομένα της απόδοσης του ανιχνευτή που λήφθησαν μέσω πηγών βαθμονόμησης γνωστής ενεργότητας. Οι κώδικες που αναπτύχθηκαν χρησιμοποιήθηκαν, κατόπιν, για τον υπολογισμό της απόδοσης του ανιχνευτή στις ενέργειες των ακτίνων-γ που εκπέμπονται από τους ασταθείς πυρήνες, που παρήχθησαν μετά το πέρας των ακτινοβολήσεων.

Στο πλαίσιο της ανάλυσης δεδομένων, ιδιαίτερο ενδιαφέρον παρουσιάζει η περίπτωση της αντίδρασης  $^{165}\text{Ho}(n,2n)^{164}\text{Ho}^m$ , η ενεργός διατομή της οποίας μετρήθηκε μέσω



της φωτοκορυφής στα 37.3 keV, όπου 37.3 keV είναι η ενέργεια ακτίνων-γ που εκπέμπονται κατά την αποδιέγερση του  $^{164}\text{Ho}^m$ . Ειδικότερα, η συγκεκριμένη φωτοκορυφή ήταν μολυσμένη από ακτίνες διαφυγής ακτίνων-X, με αποτελέσματα να δυσχεραίνεται η ανάλυσή της. Ο ορθός προσδιορισμός της στατιστικής των γεγονότων προερχόμενων από τις ακτίνες-γ στα 37.3 keV, έγινε μέσω της πλήρους αναπαραγωγής του φάσματος ύψους παλμών μέσω εκτεταμένων προσομοιώσεων με το λογισμικό GEANT4. Στη συνέχεια, μέσω της σύγκρισης με το πειραματικό φάσμα του  $^{164}\text{Ho}$  μπορέσαμε να αναλύσουμε την συνεισφορά του κάθε μηχανισμού αποδιέγερσης στη σύνθετη φωτοκορυφή ανεξάρτητα από την πειραματική διακριτική ικανότητα.

Ένα δεύτερο, αλλά εξίσου σημαντικό στοιχείο, της παρούσας ανάλυσης αφορά στην περίπτωση της αντίδρασης  $^{165}\text{Ho}(n,2n)^{164}\text{Ho}^g$  και σχετίζεται με το γεγονός ότι η ισομερής κατάσταση και η βασική κατάσταση του  $^{164}\text{Ho}$  έχουν παραπλήσιους χρόνους ημι-ζωής (36.6 και 28.8 min αντίστοιχα). Ως εκ τούτου και δεδομένου ότι η ισομερής αποδιεγείρεται 100% στη βασική κατάσταση, η τροφοδοσία της βασικής από την ισομερή κατάσταση ελήφθη υπόψιν καθ' όλο το χρονικό διάστημα από την αρχή της ακτινοβολήσης μέχρι το τέλος της μέτρησης της επαγόμενης ενεργότητας. Στα πλαίσια της παρούσας εργασίας παρουσιάζεται ο αντίστοιχος μαθηματικός φορμαλισμός για την ακριβή περιγραφή της τροφοδοσίας και αποδιέγερσης των ενεργειακών καταστάσεων του  $^{164}\text{Ho}$ . Με τον τρόπο αυτό, μπορέσαμε με ακρίβεια να προσδιορίσουμε την ενεργό διατομή της αντίδρασης  $^{165}\text{Ho}(n,2n)^{164}\text{Ho}^g$  λαμβάνοντας υπόψιν την τροφοδοσία της ισομερούς.

Όπως έχει ήδη αναφερθεί, οι πειραματικές μετρήσεις της ενεργού διατομής των υπό μελέτη αντιδράσεων συγκρίθηκαν με τους θεωρητικούς υπολογισμούς του κώδικα TALYS. Οι θεωρητικοί υπολογισμοί πραγματοποιήθηκαν για τα διαφορετικά μοντέλα που είναι ενσωματωμένα στον κώδικα με σκοπό να ελεγχθεί η ευαισθησία των υπολογισμών, αλλά και να ταυτοποιηθούν οι συνδιασμοί των μοντέλων που αναπαραγάγουν καλύτερα τα πειραματικά δεδομένα. Για το σκοπό αυτό, οι θεωρητικοί υπολογισμοί πραγματοποιήθηκαν σε τέσσερα στάδια:

1. Επιλογή διαφορετικών μοντέλων για την πυκνότητα καταστάσεων του πυρήνα.
2. Επιλογή διαφορετικών μοντέλων για τον μηχανισμό αποδιέγερσης του σύνθετου πυρήνα πριν την επίτευξη θερμοδυναμικής ισορροπίας (pre-equilibrium mechanism) για κάθε μοντέλο πυκνότητας καταστάσεων του πυρήνα.
3. Επιλογή διαφορετικών μοντέλων για τις συναρτήσεις ισχύος του πολυπόλου E1 της ακτινοβολίας-γ για κάθε μοντέλο πυκνότητας καταστάσεων του πυρήνα.
4. Επιλογή διαφορετικών μοντέλων για το οπτικό δυναμικό των νουλεονίων για κάθε μοντέλο πυκνότητας καταστάσεων του πυρήνα.

Στη βάση αυτών των υπολογισμών, τα ακόλουθα συμπεράσματα προέκυψαν:

- Οι σημαντικότερες μεταβολές στη συνάρτηση διέγερσης των αντιδράσεων παρατηρούνται για διαφορετικά μοντέλα της πυκνότητας καταστάσεων του πυρήνα.
- Η συμπεριφορά των μοντέλων της πυκνότητας καταστάσεων μπορεί να βελτιωθεί αν αυτά τα μοντέλα συνδιαστούν με διαφορετικά μοντέλα για το μηχανισμό της

αποδιέγερσης του σύνθετου πυρήνα πριν την επίτευξη θερμοδυναμικής ισορροπίας ή με διαφορετικά μοντέλα για τις συναρτήσεις ισχύος του πολυπόλου E1 της ακτινοβολίας-γ.

- Η επιλογή διαφορετικών μοντέλων οπτικού δυναμικού νουκλεονίων (οπτικό δυναμικό του Koning-Delaroche και ημι-μικροσκοπικό δυναμικό του Baugé ) δεν ανέδειξε (τουλάχιστον για τις παραπάνω περιπτώσεις) αξιοσημείωτες αλλαγές στη συνάρτηση διέγερσης των υπό μελέτη αντιδράσεων.
- Μία σημαντική παρατήρηση αφορά το μοντέλο GSM (Generalized Superfluid model) για την πυκνότητα καταστάσεων του πυρήνα. Συγκεκριμένα, στην παρούσα μελέτη διαπιστώθηκε ότι αυτό το μοντέλο αποτυγχάνει για τα ελαφρύτερα σταθερά ισότοπα Er και Dy,  $^{162}\text{Er}$  και  $^{156}\text{Dy}$ , που βρίσκονται στα όρια της κοιλάδας σταθερότητας. Αναλυτικότερα, παρατηρήθηκε πλήρης ασυμφωνία των θεωρητικών υπολογισμών με τα πειραματικά δεδομένα. Αντιθέτως, το μοντέλο GSM μπορεί να περιγράψει πολύ αποτελεσματικά την ενεργό διατομή των ισοτόπων που δεν ανήκουν στην κατηγορία των ισοτόπων με έλλειψη νετρονίων. Για παράδειγμα, οι υπολογισμοί με βάση αυτό το μοντέλο περιγράφουν επιτυχώς το (n,2n) κανάλι του  $^{165}\text{Ho}$  και για τις δύο περιπτώσεις τροφοδοσίας της ισομερούς και της βασικής κατάστασης του  $^{164}\text{Ho}$ .

Στο μέλλον, θα είναι ιδιαίτερα ενδιαφέρον να επεκτείνουμε τις μετρήσεις της ενεργού διατομής της αντίδρασης (n,2n) στην περιοχή μεσαίας έως βαριάς μάζας. Συγκεκριμένα, μεγάλο ενδιαφέρον παρουσιάζει η μελέτη των ισοτόπων  $^{127}\text{I}$ ,  $^{133}\text{Cs}$  και  $^{136}\text{Ce}$  για τα οποία έχουν γίνει εκτεταμένοι υπολογισμοί και προσομοιώσεις για την εφικτότητα των πειραμάτων στο εργαστήριο του επιταχυντού του Ε.Κ.Ε.Φ.Ε. «Δημόκριτος». Οι μετρήσεις που θα προκύψουν μπορούν να χρησιμοποιηθούν για να διερευνηθεί εάν ο βέλτιστος συνδυασμός μοντέλων του κώδικα TALYS που προέκυψε στην παρούσα διατριβή, καθώς και οι παρατηρήσεις που έγιναν σε σχέση με τη συμπεριφορά των μοντέλων ισχύουν επίσης και για αυτά τα ισότοπα. Με αυτόν τον τρόπο, θα εξαχθούν ακόμη πιο ισχυρά συμπεράσματα. Ακόμη, είναι ενδιαφέρον να διερευνηθεί η απόδοση του GSM για το ισότοπο  $^{136}\text{Ce}$ , δεδομένου ότι αυτό είναι το ελαφρύτερο σταθερό ισότοπο του Ce.

# List of publications

- In peer-reviewed journals:

- “The (n,2n) reaction for the lightest stable erbium isotope  $^{162}\text{Er}$  from reaction threshold up to 19 MeV”. E. Georgali, Z. Eleme, N. Patronis, X. Aslanoglou, M. Axiotis, M. Diakaki, V. Foteinou, S. Harissopulos, A. Kalamara, M. Kokkoris, A. Lagoyannis, N. G. Nicolis, G. Provatas, A. Stamatopoulos, S. Stoulos, A. Tsinganis, E. Vagena, R. Vlastou, and S. M. Vogiatzi, Phys. Rev. C 98, 014622 (2018). (DOI: <https://doi.org/10.1103/PhysRevC.98.014622>)
- “Experimental study of the  $^{165}\text{Ho}(n,2n)$  reaction: Cross section measurements for the population of the  $^{164}\text{Ho}$  ground state and isomeric state from the threshold up to 20 MeV”. E. Georgali, N. Patronis, A. Anastasiadis, X. Aslanoglou, M. Axiotis, Z. Eleme, S. Harissopulos, A. Kalamara, K. Karfopoulos, M. Kokkoris, A. Lagoyannis, M. Peoviti, C. Potiriadis, M. I. Savva, I. E. Stamatelatos, M. E. Stamati, A. Stamatopoulos, E. Vagena, T. Vasilopoulou, and R. Vlastou, Phys. Rev. C 102, 034610 (2020). (DOI: <https://doi.org/10.1103/PhysRevC.102.034610>)
- “Using GEANT4 Monte Carlo simulations to resolve low energy  $\gamma$ -ray spectra: The study of  $^{164}\text{Ho}^{g+m}$  decay using a broad energy HPGe detector”. E. Georgali, N. Patronis, A. Anastasiadis, M. Axiotis, S. Harissopulos, K. Karfopoulos, M. Kokkoris, A. Lagoyannis, C. Potiriadis, R. Vlastou, Nuclear Inst. and Methods in Physics Research, A 985, 164711 (2021). (DOI: <https://doi.org/10.1016/j.nima.2020.164711>)
- “Differential cross-section measurements for proton elastic scattering on  $^{nat}\text{Si}$  in the energy range  $E_{p,lab}=3-5$  MeV, suitable for EBS”. F. Maragos, N. Dimitrakopoulos, E. Georgali, M. Kokkoris, A. Lagogiannis, E. Ntemou, N. Patronis, Th. Tsakiris, A. Ziagkova (submitted).
- “Cross Section measurements for the (n,2n) reaction channel of the lightest stable dysprosium isotope  $^{156}\text{Dy}$  for energies higher than 17 MeV”. E. Georgali, N. Patronis, A. Anastasiadis, X. Aslanoglou, M. Axiotis, S. Chasapoglou, Z. Eleme, S. Harissopulos, A. Kalamara, M. Kokkoris, A. Lagoyannis, E. Mitsi, M.I. Savva, I. E. Stamatelatos, T. Vasilopoulou, and R. Vlastou (to be submitted).

- In conference proceedings:

- “Study of the  $^{162}\text{Er}(n,2n)^{161}\text{Er}$  reaction from the reaction threshold up to 19 MeV neutron energy”. E. Georgali, Z. Eleme, N. Patronis, X. Aslanoglou, M. Axiotis, M. Diakaki, V. Foteinou, A. Georgiadou, S.

- Harissopoulos, A. Kalamara, M. Kokkoris, A. Lagoyannis, N. Nicolis, G. Provatas, S. Stoulos, A. Tsinganis, E. Vagena, R. Vlastou, and S. M. Vogiatzi, HNPS Advances in Nuclear Physics 25, 102-108 (2017). (DOI: <http://dx.doi.org/10.12681/hnps.1959>)
- “Neutron beam spatial profile at nTOF using CR-39 nuclear track detectors”. Z. Eleme, S. Gerovasili, N. Patronis, E. Georgali, K.G. Ioannides, A. Kalamara, M. Kokkoris, C. Papachristodoulou, T. Stamatopoulos, A. Tsinganis, R. Zanni-Vlastou and the nTOF Collaboration, HNPS Advances in Nuclear Physics, 25, 109-114. (DOI: <http://dx.doi.org/10.12681/hnps.1960>)
  - “Study of the  $^{165}\text{Ho}(n,2n)^{164}\text{Ho}^{g-m}$  reaction at near threshold energies”. E. Georgali, N. Patronis, A. Anastasiadis, M. Axiotis, Z. Eleme, S. Harissopoulos, A. Kalamara, K. Karfopoulos, M. Kokkoris, A. Lagoyannis, M. Peoviti, C. Potiriadis, M. I. Savva, I. Stamatelatos, M. E. Stamati, A. Stamatopoulos, T. Vasilopoulou, R. Vlastou, HNPS Advances in Nuclear Physics, 27, 160-167. (DOI: <http://dx.doi.org/10.12681/hnps.3001>)
  - “Characterization of the Canberra BE5030 Broad Energy High Purity Germanium Detector by means of the GEANT4 Monte Carlo simulation package”. E. Georgali, M. E. Stamati, M. Peoviti, N. Patronis, C. Potiriadis, K. Karfopoulos, A. Anastasiadis, M. Axiotis, Z. Eleme, S. Harissopoulos, A. Kalamara, M. Kokkoris, A. Lagoyannis, M. I. Savva, I. Stamatelatos, A. Stamatopoulos, T. Vasilopoulou, R. Vlastou, HNPS Advances in Nuclear Physics, 27, 152-154. (DOI: <http://dx.doi.org/10.12681/hnps.3002>)

# Contents

## Abstract

<b>1</b>	<b>Introduction</b>	<b>1</b>
<b>2</b>	<b>The physics cases and the activation technique</b>	<b>4</b>
2.1	The nuclear reactions and the previous experimental data . . . . .	4
2.2	Energy diagrams . . . . .	6
2.3	Activation technique . . . . .	7
2.4	Decay schemes of the product-nuclei . . . . .	11
2.5	Neutron flux . . . . .	15
2.5.1	Reference reactions . . . . .	15
<b>3</b>	<b>Experimental set-up</b>	<b>18</b>
3.1	Irradiations at the N.C.S.R. “Demokritos” facility . . . . .	18
3.1.1	The D <sub>2</sub> gas cell . . . . .	18
3.1.2	The Ti-tritiated target . . . . .	20
3.2	The samples . . . . .	21
3.3	Irradiations set-up . . . . .	22
3.4	Neutron beam energy distribution . . . . .	22
3.4.1	The NEUSDESC code . . . . .	24
3.5	GEANT4 simulation of the neutron beam . . . . .	27
3.6	Neutron beam intensity fluctuations . . . . .	31
3.7	Activity measurements . . . . .	32
3.7.1	GEANT4 characterization of the HPGe detectors . . . . .	33
3.7.2	The 50% rel. efficiency BE HPGe detector . . . . .	34
3.7.3	The 80% and 40% rel. efficiency HPGe detectors . . . . .	35
<b>4</b>	<b>Data analysis</b>	<b>38</b>
4.1	Efficiency calculations . . . . .	38
4.1.1	Efficiency calculations for the <sup>165</sup> Ho(n,2n) <sup>164</sup> Ho reaction study	38
4.1.1.1	Efficiency calculations for the Ho samples . . . . .	38
4.1.1.2	Efficiency calculations for the reference foils . . . . .	39
4.1.2	Efficiency calculations for the <sup>156</sup> Dy(n,2n) <sup>155</sup> Dy reaction study	40
4.1.2.1	Efficiency calculations for the Dy samples . . . . .	40
4.1.2.2	Efficiency calculations for the reference foils . . . . .	41

4.2	The experimental spectra . . . . .	43
4.3	The Ge X-ray escape peaks and the Ho samples spectra . . . . .	46
4.4	The GEANT4 simulation of the Ho samples spectra . . . . .	46
4.5	The study of the 37.3 keV $\gamma$ -ray photopeak . . . . .	50
<b>5</b>	<b>Experimental Results</b>	<b>52</b>
<b>6</b>	<b>Theoretical Calculations</b>	<b>56</b>
6.1	Types of nuclear reactions . . . . .	56
6.2	The TALYS code . . . . .	57
6.2.1	Hauser-Feschbach theory . . . . .	58
6.2.2	Pre-equilibrium reactions . . . . .	61
6.2.3	Optical model . . . . .	63
6.2.4	$\gamma$ -ray Strength functions . . . . .	64
6.2.5	Level density models . . . . .	65
6.2.5.1	The Fermi Gas model . . . . .	65
6.2.5.2	The Constant Temperature model . . . . .	66
6.2.5.3	The Back-Shifted Fermi Gas model . . . . .	67
6.2.5.4	The Generalized Superfluid model . . . . .	67
6.2.5.5	Microscopic Level Density models . . . . .	68
6.3	The TALYS calculations . . . . .	68
6.3.1	Adoption of different level density models . . . . .	69
6.3.2	Adoption of different pre-equilibrium models for each level density model . . . . .	70
6.3.3	Adoption of different $\gamma$ -ray strength function models of the E1 transition for each level density model . . . . .	74
6.3.4	The final TALYS results . . . . .	79
6.4	The Generalized Superfluid model for the Er and Dy stable isotopes . . . . .	79
6.5	$^{165}\text{Ho}(n,2n)^{164}\text{Ho}$ reaction: The angular momentum distribution and the ground to isomeric cross section ratio . . . . .	82
<b>7</b>	<b>Summary and Discussion</b>	<b>85</b>
<b>A</b>	<b>Energy diagram</b>	<b>88</b>
<b>B</b>	<b>Standard equation of activation technique</b>	<b>90</b>
<b>C</b>	<b>The <math>f_B</math> correction factor</b>	<b>93</b>
<b>D</b>	<b>Equation of activation technique when the population from an isomeric state is considered</b>	<b>95</b>
<b>E</b>	<b>The <math>f_C</math> correction factor</b>	<b>99</b>
<b>F</b>	<b>GEANT4 geometry file of the irradiation set-up in DD reaction</b>	<b>101</b>

G	GEANT4 geometry file of the irradiation set-up in DT reaction	112
H	Efficiency and counting rate calculations	122
I	Coincidence-Summing effect	124
J	Photons Attenuation	125
K	GEANT4 tracking cuts	127
	References	129

# Abstract

Within the present work the (n,2n) reaction channel was studied for the rare earth isotopes:  $^{162}\text{Er}$ ,  $^{156}\text{Dy}$  and  $^{165}\text{Ho}$ . In particular, for  $^{165}\text{Ho}$  the cross sections of populating the ground and the isomeric state of  $^{164}\text{Ho}$  were measured independently.

The reactions cross sections were measured via the activation technique relative to the  $^{197}\text{Au}(n,2n)^{196}\text{Au}$ ,  $^{27}\text{Al}(n,\alpha)^{24}\text{Na}$  and  $^{93}\text{Nb}(n,2n)^{92}\text{Nb}^m$  reference reactions. The quasi-monoenergetic neutron beams were produced via the  $^2\text{H}(d,n)^3\text{He}$  (DD) and  $^3\text{H}(d,n)^4\text{He}$  (DT) reactions, while the primary deuteron beams were delivered by the 5.5 MV Tandem Van de Graaff accelerator of the institute of Nuclear and Particle Physics at N.C.S.R. “Demokritos”, Athens, Greece. After the end of the irradiations the induced activity in the samples was measured through  $\gamma$ -ray spectroscopy using HPGe detectors.

For the accurate physics interpretation of the experimental data the GEANT4 toolkit was extensively used for the simulation of the HPGe detectors. The developed codes were utilized in the data analysis for the determination of the detectors efficiency including corrections for the self-attenuation and the coincidence-summing effect. In addition, the GEANT4 toolkit was utilized for the calculation of the neutron beam energy distribution. The results were validated in the basis of the NEUSDESC code.

The measured cross section data were compared to previous measurements of the literature, as well as to theoretical calculations based on the latest version of TALYS (v. 1.95). The TALYS performance was tested for different models that are used in the Hauser-Feshbach calculations. The impact of the models variation on the cross section of the reactions under study was investigated and the best combinations of models relevant to the reproduction of the present data were determined. In general, the default parametrization of the TALYS models was utilized. Only in the case of the  $^{165}\text{Ho}(n,2n)^{164}\text{Ho}^m$  and  $^{165}\text{Ho}(n,2n)^{164}\text{Ho}^g$  reactions a different parametrization for the width of the angular momentum distribution (spin cut-off parameter,  $\sigma^2$ ) was adopted so as to test the impact of this parametrization on the calculated cross sections.



# Chapter 1

## Introduction

Even though the study of nuclear reactions has its origins back in 1919, when the first observation of the nucleus was made by Ernest Rutherford, the nuclear reactions study is still an open field full of challenges since the nuclear reactions problem cannot be solved through the analytical expressions of quantum mechanics. This complexity emanates both from the fact that the strong interaction through which the nucleons interact with each other remains an open research topic and due to the large number of nucleons that participate in a reaction. The nuclear research copes with these issues through the development of theoretical models that aim at describing the nuclear reactions and reproducing the corresponding observables.

The theoretical models are a kind of “simulation of the reality” and they have been developed into the basis either of reproducing the observables or of the so-far knowledge for the nuclear interactions and nuclear properties. In addition, in the last decades the research in the domain of theoretical physics led to progress towards the field of the microscopic approaches of the nuclear reactions [1], and therefore microscopic models have also been developed.

Of course, a general and broadly used model which can in total describe a nuclear reaction does not exist. Instead, different codes have been developed, e.g. TALYS [2] and EMPIRE [3], where the various theoretical models are combined and each of them serves different purposes. Among these purposes there are the determination of the contribution of different mechanisms in a nuclear reaction, the calculation of the particle emission coefficients and the calculation of the level density. The improvement of theoretical models is in progress in order to reach a deep understanding of the nature of nuclear reactions. This is achieved either by modifications in the basis of the models or by the improvement of their corresponding parametrization so as to obtain a better agreement with the experimental observables.

Nuclear reactions on stable isotopes is still an area where the comparison of the experimental data with theoretical calculations often reveals large discrepancies between them. Apart from this, inconsistency is noticed even between the existing experimental data. Based on this, the experimental study of nuclear reactions for stable isotopes on unexplored regions (mass and energy regions), but also on already

studied regions, is essential for the update of the data libraries. In this way, the validity of the comparison of the theoretical models with the experimental data is enhanced.

Thanks to the continuous improvement in the detector and accelerator technology, but also thanks to the simulation codes (e.g. GEANT4 [4], MCNP5 [5], FLUKA [6]), new horizons have been opened in the experimental techniques, as well as in the data analysis. Taking advantage of these capabilities, the study of previously unattainable or challenging physics cases becomes possible.

It is known that the theoretical models have a different success level on the reproduction of the experimental data for different energy and mass regions. Therefore, a systematic study of nuclear reactions for a particular mass region utilizing in parallel the technological and simulation advances constitutes a valuable tool for testing the theoretical models. The present work refers to the study of nuclear reactions on rare earth isotopes for energies in the region 10-20 MeV. Apart from the Sc isotope which belongs to the low-to-medium mass region ( $A=45$ ), the isotopes of the rest rare earth elements belong to the medium-to-heavy mass region.

In particular, in the present work the (n,2n) reaction channel for the Ho stable isotope ( $^{165}\text{Ho}$ ), as well as for the two lightest stable isotopes of Er and Dy ( $^{162}\text{Er}$  and  $^{156}\text{Dy}$ ) were studied. More specifically, the corresponding cross sections of these reactions were determined experimentally after the neutron irradiations in the accelerator laboratory of N.C.S.R. "Demokritos". The measured cross sections were compared to the theoretical predictions based on the broadly used statistical code TALYS in an attempt to investigate the performance of the code for the different theoretical models implemented within it.

The (n,2n) channel on  $^{165}\text{Ho}$  presents the specific feature of populating two isomers of the  $^{164}\text{Ho}$  product-nucleus: the isomeric state ( $J^\pi = 6^-$ ) at  $E_{ex} = 139.8$  keV excitation energy, as well as the ground state ( $J^\pi = 1^+$ ). The cross section measurement of both reaction channels constitutes an interesting observable relative to the spin distribution of the populated states. On the other hand,  $^{162}\text{Er}$  and  $^{156}\text{Dy}$  are the lightest stable isotopes of the corresponding elements. The experimental study of the (n,2n) reaction channel for these neutron deficient isotopes and the comparison with the corresponding theoretical calculations is an extra motivation for the present work. It is interesting to test the performance of the reaction mechanism modeling and parametrization at the limits of the valley of stability of the chart of nuclides.

The experimental data are also necessary for the construction of nuclear data libraries such as ENDF (Evaluated Nuclear Data File) [7], JEFF (Joint Evaluated Fission and Fusion File) [8] and JENDL (Japanese Evaluated Nuclear Data Library) [9]. These libraries are based on the validation and the evaluation of the experimental data and are of considerable importance for the nuclear science. Firstly, they can be used either as input files for the theoretical calculations codes or for the extraction of the parametrization of them. In addition to this, the nuclear data libraries contribute significantly to nuclear technology purposes related to e.g. nuclear medicine, radiation safety and protection, material characterization and nuclear energy.

The neutron evaluated libraries in combination with the theoretical modeling play a crucial role in nuclear energy applications and, in particular, in the reactors

technology. More specifically, the accurate knowledge and understanding of the neutron induced reactions are important so that the elements and the isotopes that can be used as structural materials, absorbers or poisons in these systems are identified. The rare earth isotopes, especially, are used or have been proposed to be used in several reactor assemblies, e.g. Dy and Er can be used as absorbing materials and burnable poisons [10, 14].

The nuclear data libraries are also of paramount importance for astrophysical purposes, such as for the extraction of elemental and isotopic abundances, as well as for our general understanding on the nucleosynthesis processes and stellar evolution. Specifically, the neutron capture reactions define the path of the s- and r-nucleosynthesis processes and eventually the elemental production for  $A > 56$  [15, 16].

# Chapter 2

## The physics cases and the activation technique

In this Chapter the nuclear reactions under study will be presented along with the adopted method.

### 2.1 The nuclear reactions and the previous experimental data

During the present work four different threshold nuclear reactions were studied. They refer to the (n,2n) channel of the rare earth isotopes  $^{162}\text{Er}$ ,  $^{156}\text{Dy}$  and  $^{165}\text{Ho}$ :

- $^{162}\text{Er}(n,2n)^{161}\text{Er}$
- $^{156}\text{Dy}(n,2n)^{155}\text{Dy}$
- $^{165}\text{Ho}(n,2n)^{164}\text{Ho}^g$
- $^{165}\text{Ho}(n,2n)^{164}\text{Ho}^m$

The cross section of the above listed reactions were determined experimentally for several neutron beam energies, as can be seen in Table 2.1. The irradiations were performed at the 5.5 MV Tandem Van de Graaff accelerator of the Institute of Nuclear and Particle Physics at N.C.S.R. “Demokritos”.

Table 2.1: The neutron induced reactions studied in the present work and the corresponding neutron beam energies.

Nuclear reaction	$E_{th}$ (MeV)	Neutron beam energies (MeV)						
$^{162}\text{Er}(n,2n)^{161}\text{Er}$	9.26	10.7	11.0	11.3	17.1	18.1	19.0	
$^{156}\text{Dy}(n,2n)^{155}\text{Dy}$	9.51				17.1	18.1	19.0	
$^{165}\text{Ho}(n,2n)^{164}\text{Ho}^m$	8.04	10.1	10.4	10.7	17.1	18.1	19.0	19.6
$^{165}\text{Ho}(n,2n)^{164}\text{Ho}^g$	8.04	10.1	10.4	10.7	17.1	18.1	19.0	19.6

In Figure 2.1 the previous data of the reactions are presented, as extracted from the EXFOR database [17].

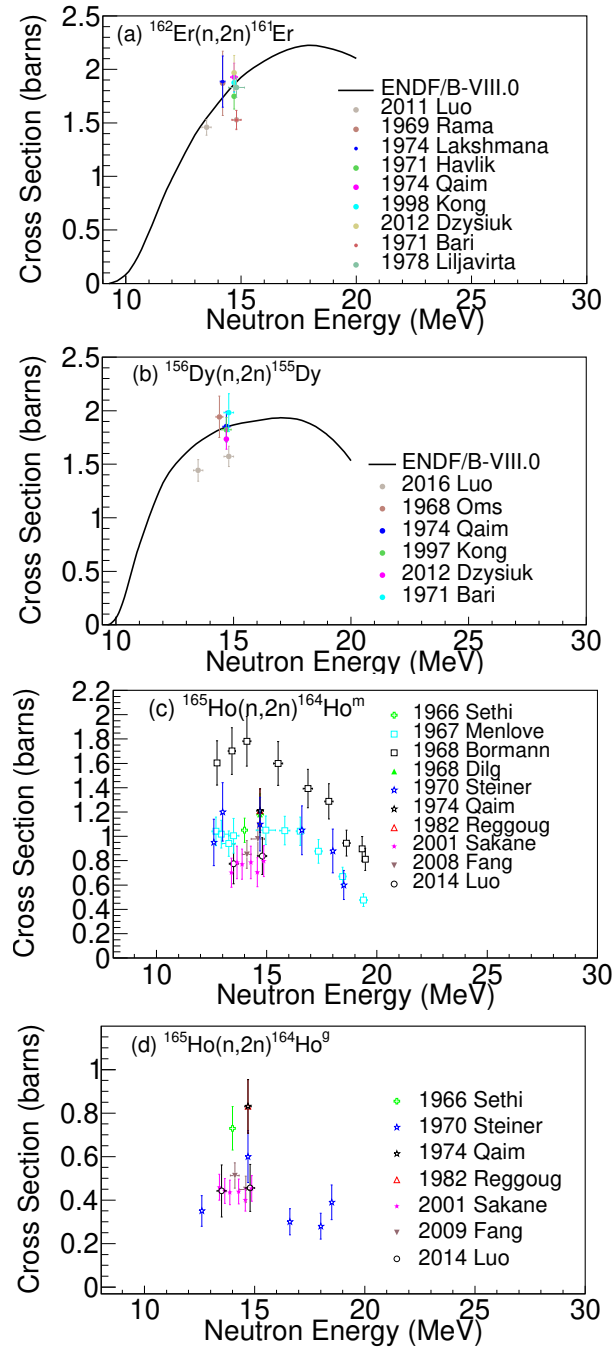


Figure 2.1: The previous data of the  $^{162}\text{Er}(n,2n)^{161}\text{Er}$  [18–26],  $^{156}\text{Dy}(n,2n)^{155}\text{Dy}$  [18, 20, 22, 24, 27, 28],  $^{165}\text{Ho}(n,2n)^{164}\text{Ho}^m$  [22, 29–37] and  $^{165}\text{Ho}(n,2n)^{164}\text{Ho}^g$  [22, 29, 31–33, 37, 38] reactions, along with ENDF/B-VIII.0 library [39] when this is available.

As can be seen from Figures 2.1(a) and (b), the previous experimental data for the  $^{162}\text{Er}(n,2n)^{161}\text{Er}$  and  $^{156}\text{Dy}(n,2n)^{155}\text{Dy}$  reactions are limited in a narrow energy region

between 13.5-14.8 MeV. Furthermore, the experimental data are very discrepant. In the case of the  $^{165}\text{Ho}(n,2n)$  reaction channel, more experimental data exist as it is depicted in Figures 2.1(c) and (d). The experimental data for the population of both the isomeric and ground state refer to the energy region between 12-20 MeV. However, the data are also discrepant.

## 2.2 Energy diagrams

The interaction of neutrons with each one of the  $^{162}\text{Er}$ ,  $^{156}\text{Dy}$  and  $^{165}\text{Ho}$  isotopes for neutron beam energies between 10-20 MeV is dominated by the compound-nucleus mechanism, which is discussed in Section 6.1.

Based on the Bohr hypothesis about the independence between the input and output channels in the compound-nucleus reactions (see also Section 6.1), different reaction channels with different probabilities can be induced by each nuclear interaction. These channels can be represented in an energy diagram taking into account the excitation energy of the compound-nucleus. In Figures 2.2-2.4 the energy diagrams of each interaction are presented along with the most probable nuclear channels. More details for the energy diagrams are given in Appendix A.

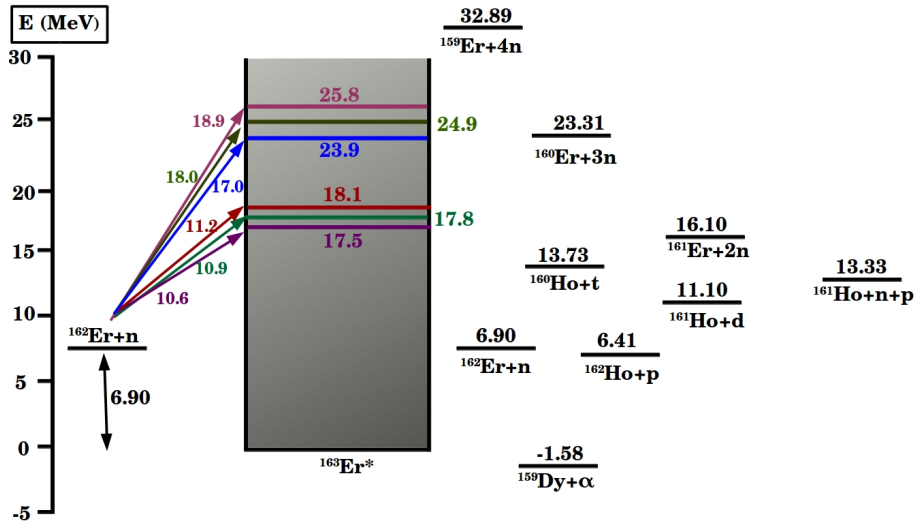


Figure 2.2: The energy diagram of the  $^{162}\text{Er}+n$  interaction.

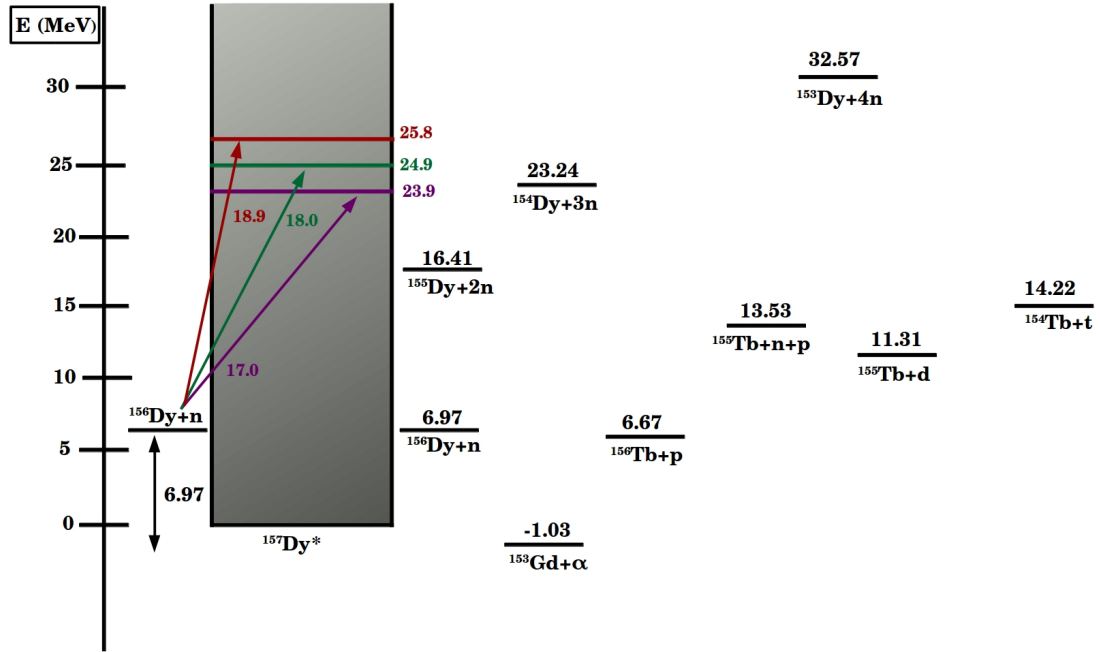


Figure 2.3: The energy diagram of the  $^{156}\text{Dy}+n$  interaction.

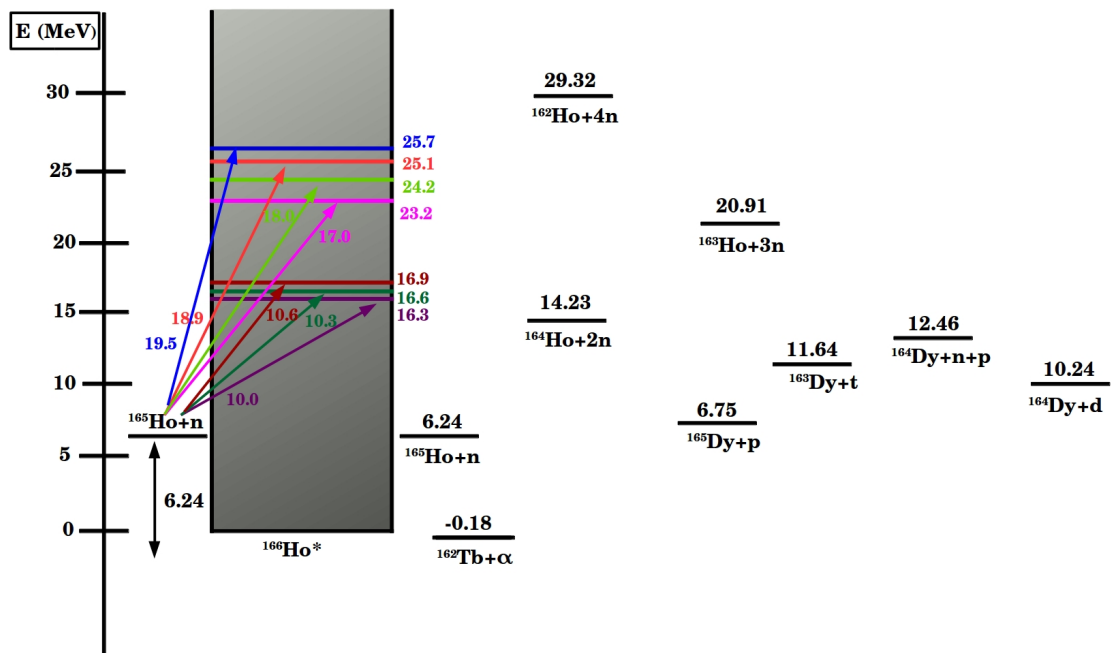


Figure 2.4: The energy diagram of the  $^{165}\text{Ho}+n$  interaction.

## 2.3 Activation technique

The method used for the experimental determination of the cross sections of the reactions under study is the activation technique. This method was first applied

by Hevesy and Leni in 1936, who performed a quantitative analysis of samples [40]. Nowadays the method widely applies, apart from the qualitative and quantitative analysis of samples in many other aspects of nuclear physics research, such as for cross sections measurements in fundamental research, as well as for the determination of beams intensity and safety studies in accelerator technology [41–43]. The method consists of two stages:

1. the irradiation of the samples with a particle beam in order to induce the nuclear reaction of interest.
2. the measurement of the activity induced by this particular reaction in the irradiated samples.

The induced activity  $A$  is given by Eq. 2.1:

$$A = \sigma * \Phi * N_T * f_B \quad (2.1)$$

where,

$\sigma$  is the reaction cross section

$\Phi$  is the total beam flux

$N_T$  is the number of target-nuclei in the sample

$f_B$  is the correction factor for the activated nuclei decay during the irradiation

By measuring the activity of the sample and considering that two of the these three quantities,  $N_T$ ,  $\Phi$  and  $\sigma$ , are known, the remaining one can be determined.

Although the initial idea of the method seems straightforward, in fact there are several factors that have to be taken into account in actual applications of this method. These are mainly related to the induced counting statistics, the purity of the recorded spectrum, the interfering reactions and the possible overlapping of the decay energies. Some of these factors are discussed below.

First of all, it has to be mentioned that the applicability of the activation technique depends on the decay parameters of the product-nuclei. For example, the method cannot be implemented when the half-life of the isotope is too long ( $\gg$  year) or too short ( $\ll$  min). In particular, the long half-lives result in slow emission rates. This means that extremely long irradiation times are needed along with long activity measurements in order to measure an adequate counting statistics. On the other hand, isotopes with too short half-lives decay rapidly and the core activity is often too low to be measured. In addition, the intensity of the emitted radiation plays a major role, since the higher this is, the higher statistics in the measured activity will be obtained. In cases that the intensity is too low ( $< 1\%$ ), the radiation emission rate is very often below the detection limit.

Special care is needed in these cases that multiple isotopes of the same element or contaminants, that are present in the sample, lead to the production of the same product-nucleus through different reactions. These are the so-called interfering reactions. In some cases, interfering reactions hinder the application of the activation technique. In other cases, activation technique can still be applied if the contribution of the interfering reactions to the total measured activity can be estimated. A



similar constrain exists when there are nuclear reactions that result in the emission of radiation with energy close enough to the decay energy of interest. In these cases, the available experimental resolution may not be good enough to resolve the two different decay mechanisms. As previously, the activation technique can be applied when the correction factor for the interfering activity can be safely estimated. In general, the possibility that these kind of interferences are present increases with the number of isotopes that are present in the sample. In addition, the samples must be well prepared, stored and handled so as to avoid any external contamination [44].

However, the impact of the above mentioned constraints varies depending on the experimental conditions, such as the accelerator facility and the detection system. For instance, a high beam intensity may compensate for the low intensity of the emitted particles or the too long half-life.

The general equation for the deduction of the reaction cross section by means of this method is the following:

$$\sigma = \frac{\text{counts} * C}{\Phi * N_T * \varepsilon * I * e^{-\lambda t_w} * (1 - e^{-\lambda t_m}) * f_B} \quad (2.2)$$

where,

*counts* are the recorded counts in the experimental spectrum

*C* is the correction factor of the recorded activity including e.g. self-attenuation corrections, coincidence-summing effect corrections, dead-time corrections

$\Phi$  is the total beam flux

$N_T$  is the number of target-nuclei in the sample

*I* is the intensity of the emitted radiation

$\varepsilon$  is the efficiency of the detector at the energy of the emitted radiation for the geometry of measurement

$t_m$  is the activity measurement time

$t_w$  is the “waiting time” between the end of the irradiation and the start of the measurement

$f_B$  is the correction factor for the decay of the product-nuclei during the irradiation time.

Eq. 2.2 is the standard formula of activation technique, which is based on the assumption that the nuclear reaction under study populates only the ground state of the product-nucleus or the population of isomeric states is negligible or it can be ignored due to their short half-lives in comparison with the ground state half-life. In Appendix B its mathematical proof is given.

The  $f_B$  factor is given by Eq. 2.3:

$$f_B = \frac{\int_0^{t_{irr}} f(t) * e^{\lambda t} dt}{\int_0^{t_{irr}} f(t) dt} * e^{-\lambda t_{irr}} \quad (2.3)$$

where,

$f(t)$  is the beam flux at a moment  $t$

$\lambda$  is the decay constant of the product-nucleus

$t_{irr}$  is the total irradiation time

In the present experiments, during the irradiations the neutron flux  $f(t)$  and/or the deuteron beam intensity were recorded and integrated for regular time periods,  $\Delta t$ , through a multichannel scaler (MCS), as it is discussed in Section 3.6. For each irradiation the MCS output was processed through a computer code developed in C++ language for the determination of the  $f_B$  factor. The code, as well as the equations through which the  $f_B$  factor is obtained for constant flux are given in Appendix C.

However, there are cases that an isomeric state is also populated and decays to the ground state. When the ground and the isomeric states have similar half-lives, the possible population of the ground state from the isomeric state has to be taken into account in the calculations. The formula through which the cross section of the ground state is determined when the population from the isomeric state is considered in all the involved time intervals: irradiation time, “waiting time” and measurement time, is given in Eq. 2.4. The mathematical proof of Eq. 2.4 and its full explanation are given in Appendix D.

$$\sigma_g = \frac{counts_g C_g}{\Phi N_T \varepsilon_g I_g e^{-\lambda_g t_w} (1 - e^{-\lambda_g t_m}) f'_B} - \quad (2.4)$$

$$\sigma_m \left( \frac{f_B}{f'_B} \frac{\frac{1}{\lambda_g - \lambda_m} (\lambda_g e^{-\lambda_m t_w} (1 - e^{-\lambda_m t_m}) - \lambda_m e^{-\lambda_g t_w} (1 - e^{-\lambda_g t_m}))}{e^{-\lambda_g t_w} (1 - e^{-\lambda_g t_m})}} + \frac{f_C}{f'_B} \right)$$

In Eq. 2.4 the terms *counts*,  $C$ ,  $I$ ,  $\varepsilon$ ,  $\lambda$  and  $\sigma$  have the same meaning as previously: the index  $g$  refers to the ground state, whereas the index  $m$  refers to the isomeric state.

The minuend in Eq. 2.4 is the formula through which the cross section is determined in the absence the isomeric state or when its contribution is negligible. Through the subtrahend the needed correction for the ground state population from the isomeric state is taken into account.

The factor  $f'_B$  is identical to the  $f_B$  factor, but  $f'_B$  refers to the ground state, whereas  $f_B$  refers to the isomeric state.

Through the  $f_B$  factor the needed correction is taken into account for the decay of the isomeric state during irradiation:

$$f_B = \frac{\int_0^{t_{irr}} f(t) * e^{\lambda_m t} dt}{\int_0^{t_{irr}} f(t) dt} * e^{-\lambda_m t_{irr}} \quad (2.5)$$

The  $f'_B$  factor corrects for the decay of the ground state during irradiation:

$$f'_B = \frac{\int_0^{t_{irr}} f(t) * e^{\lambda_g t} dt}{\int_0^{t_{irr}} f(t) dt} * e^{-\lambda_g t_{irr}} \quad (2.6)$$

Eq. 2.6 corrects only for the nuclei that were produced directly from the induced reaction. For the nuclei that were populated from the isomeric state, the correction for the decay during irradiation is taken into account via Eq. 2.7:

$$f_C = \frac{\int_0^{t_{irr}} f(t)e^{\lambda_g t} dt}{\int_0^{t_{irr}} f(t) dt} e^{-\lambda_g t_{irr}} - \frac{\int_0^{t_{irr}} f(t)e^{(\lambda_g - \lambda_m)t} dt}{\int_0^{t_{irr}} f(t) dt} e^{-\lambda_g t_{irr}} \quad (2.7)$$

As previously, a C++ code has been developed for the calculation of the  $f_C$  factor so as to take into account the fluctuations in the neutron flux. The code, as well as the equation through which the  $f_C$  factor is calculated for constant flux are presented in Appendix E

## 2.4 Decay schemes of the product-nuclei

- the  $^{162}\text{Er}(n,2n)^{161}\text{Er}$  reaction

The  $^{161}\text{Er}$  isotope, produced through the  $^{162}\text{Er}(n,2n)^{161}\text{Er}$  reaction, has an isomeric state ( $J^\pi = \frac{11}{2}^-$ ) at 397 keV excitation energy which decays to the ground state of  $^{161}\text{Er}$  via 100% Isomeric Transition (IT) with a half-life which is equal to 7.5  $\mu\text{s}$ . The ground state ( $J^\pi = \frac{3}{2}^-$ ) decays to  $^{161}\text{Ho}$  via 100%  $\varepsilon$  (EC+ $\beta^+$ ) with a half-life which is equal to 3.21 h. Due to the short half-life of the isomeric state the population of the ground state from this state is negligible, and consequently, the total cross section of the  $^{162}\text{Er}(n,2n)^{161}\text{Er}$  reaction is calculated by measuring the total induced activity of the  $^{161}\text{Er}$  ground state (Eq. 2.2). The decay scheme of  $^{161}\text{Er}$  is quite complicated. A simplified decay scheme is presented in Figure 2.5. As can be seen in this Figure, among the emitted  $\gamma$ -rays the one of 826.6 keV has the highest intensity, I=64 % [45].

- the  $^{156}\text{Dy}(n,2n)^{155}\text{Dy}$  reaction

The  $^{155}\text{Dy}$  product-nucleus, produced by the  $^{156}\text{Dy}(n,2n)$  reaction channel, has an isomeric state ( $J^\pi = \frac{11}{2}^-$ ) excited at 234.3 keV with a very short half-life (6  $\mu\text{s}$ ). The isomeric state decays to the ground state of  $^{155}\text{Dy}$  via 100% IT. The  $^{155}\text{Dy}$  ground state ( $J^\pi = \frac{3}{2}^-$ ) decays to  $^{155}\text{Tb}$  via 100%  $\varepsilon$  (EC+ $\beta^+$ ) with a half-life of 9.9 h. As in the case of the  $^{162}\text{Er}(n,2n)^{161}\text{Er}$  reaction the population of the isomeric state is negligible, and consequently, the total cross section of the  $^{156}\text{Dy}(n,2n)^{155}\text{Dy}$  reaction is determined by measuring the total induced activity of the  $^{155}\text{Dy}$  ground state (Eq. 2.2). The decay scheme of  $^{155}\text{Dy}$  is also quite complicated. A simplified decay scheme is presented in Figure 2.6. As can be seen in this Figure, the stronger transition is the one of 226.9 keV with intensity I=68.7 %. The remaining ones have much lower intensities [46].

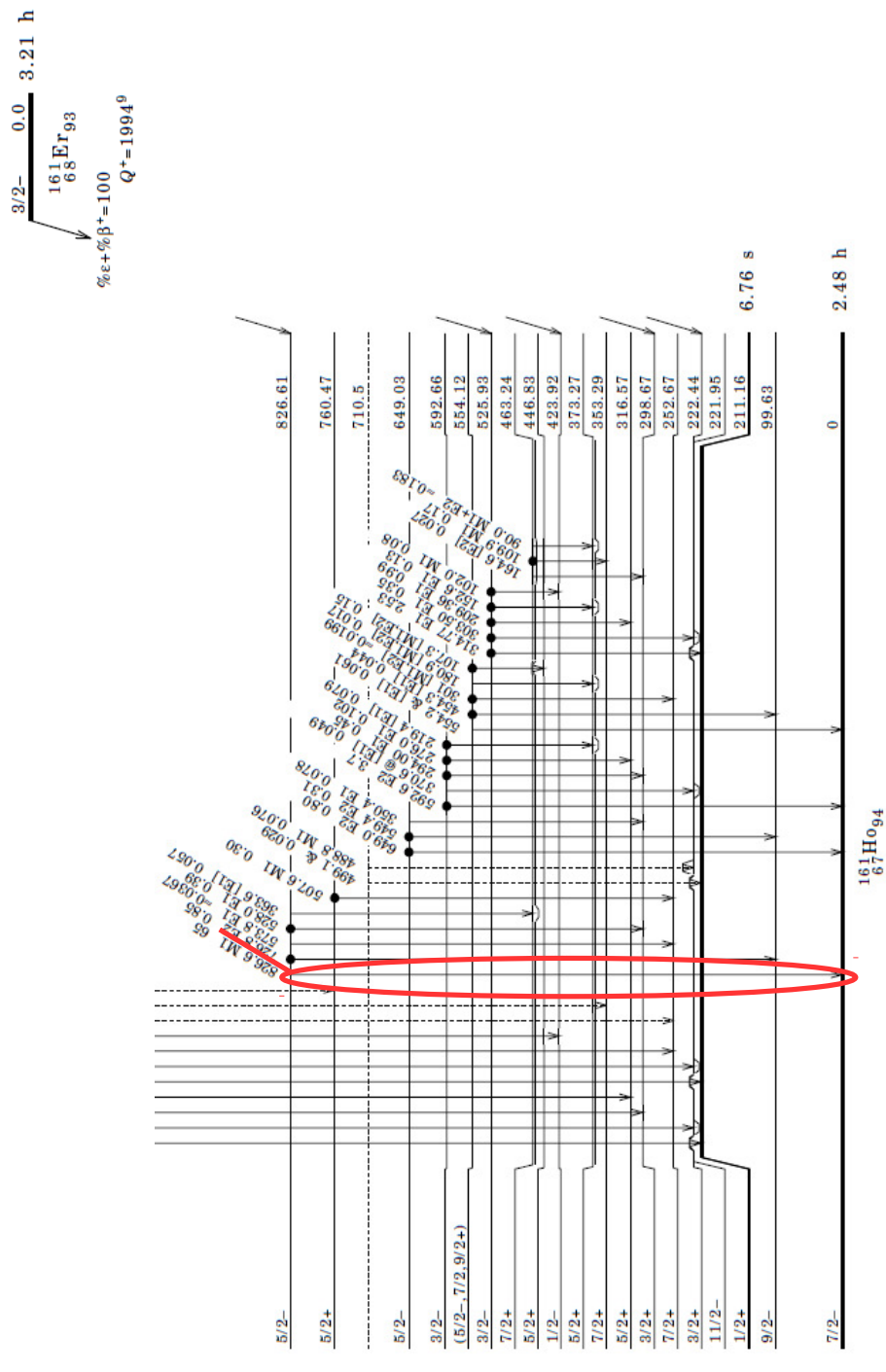


Figure 2.5: A simplified representation of the decay scheme of  $^{161}\text{Er}$ . Taken from Ref. [45].

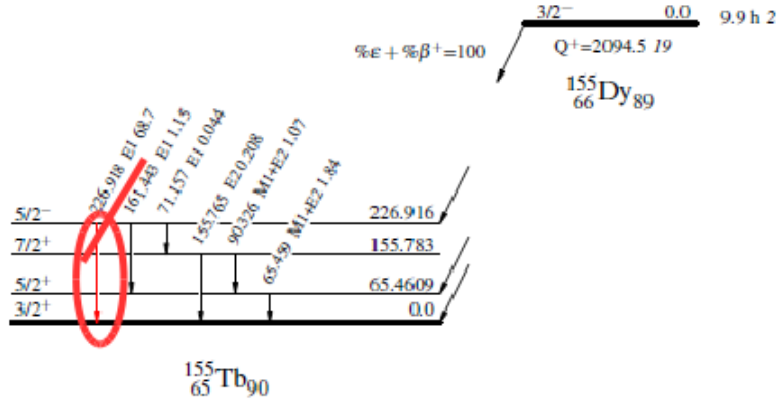


Figure 2.6: A simplified representation of the decay scheme of  $^{155}\text{Dy}$ . Taken from Ref. [46].

- the  $^{165}\text{Ho}(n,2n)^{164}\text{Ho}$  reaction

As has been mentioned, the  $(n,2n)$  channel of the  $^{165}\text{Ho}$  isotope populates two states of the product-nucleus  $^{164}\text{Ho}$ : the ground state with spin  $J^\pi = 1^+$  and an isomeric state, excited at 139.8 keV, with spin  $J^\pi = 6^-$ . In Figure 2.7 a simplified outline of the population and decay of the  $^{164}\text{Ho}$  isotope is presented. The Figure indicates that the isomeric state decays via 100% IT to the ground state. The ground state decays either to  $^{164}\text{Dy}$  via 60%  $\varepsilon$  ( $\text{EC}+\beta^+$ ) or to  $^{164}\text{Er}$  via 40%  $\beta^-$  [47].

The ground and the isomeric states have similar half-lives:  $T_{1/2}^g = 28.8$  min and  $T_{1/2}^m = 36.6$  min, respectively. Due to this, the population of the ground state from the decay of the isomeric state has to be taken into account. Accordingly, for the determination of the cross section of the  $^{165}\text{Ho}(n,2n)^{164}\text{Ho}^g$  reaction a different mathematical approach is adopted (see Eq. 2.4). The  $^{165}\text{Ho}(n,2n)^{164}\text{Ho}^m$  reaction cross section was calculated via the standard formula of activation technique (Eq. 2.2).

In the Isomeric Transition decay mode, which was mentioned above, the nucleus de-excites without changing its atomic and mass number. In this mode the de-excitation is performed via  $\gamma$ -emission which competes with the internal conversion process. In internal conversion the nucleus interacts electromagnetically with the electrons of the inner atomic shells which are ejected by the atom. Prerequisite for this is that the nucleus excitation energy is higher than the ejected electrons binding energy. The “holes” formed are filled by electrons of the higher states with the simultaneous emission of characteristic X-rays [48].

In Table 2.2 the product-nuclei decay parameters, which were used for the cross section calculations, are summarized.

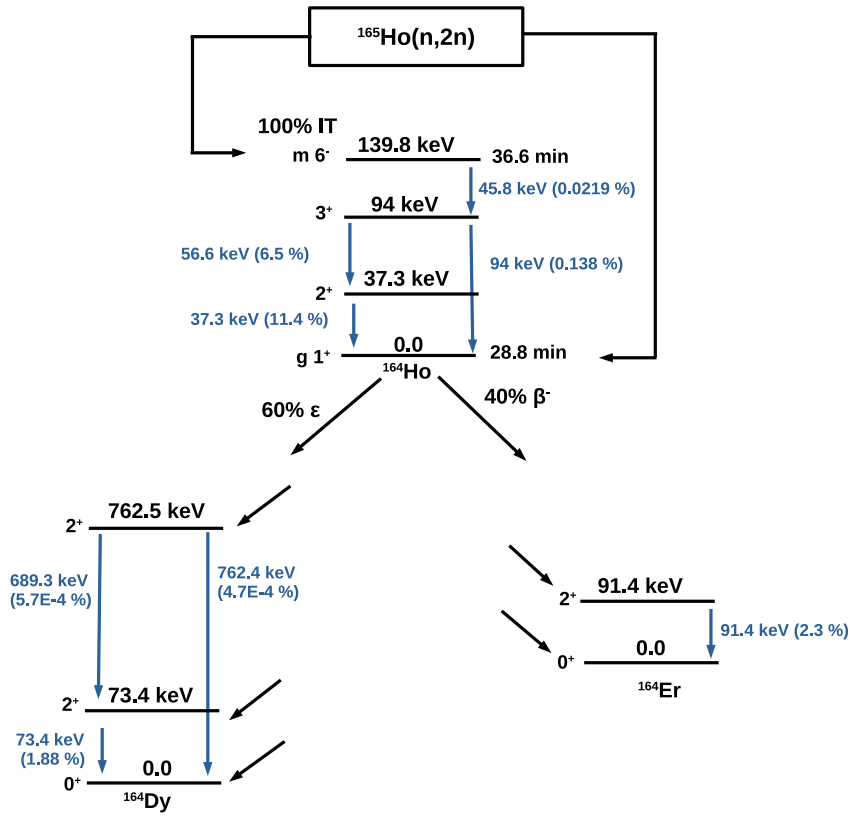


Figure 2.7: A simplified representation of the population and decay of  $^{164}\text{Ho}$ . Taken from Ref. [49]

Table 2.2: Decay properties of the product-nuclei.

Nuclear reaction	Product-nucleus	Decay mode	Half-life	$\gamma$ -ray energy (keV)	Intensity per decay (%)
$^{162}\text{Er}(n,2n)^{161}\text{Er}$	$^{161}\text{Er}$ [45]	100% $\epsilon$	$(3.21 \pm 0.03)$ h	826.6	$64 \pm 4$
$^{156}\text{Dy}(n,2n)^{155}\text{Dy}$	$^{155}\text{Dy}$ [46]	100% $\epsilon$	$(9.9 \pm 0.2)$ h	226.9	$68.7 \pm 1.6$
$^{165}\text{Ho}(n,2n)^{164}\text{Ho}^m$	$^{164}\text{Ho}^m$ [47]	100% IT	$(36.6 \pm 0.3)$ min	37.3	$11.4 \pm 0.7$
$^{165}\text{Ho}(n,2n)^{164}\text{Ho}^g$	$^{164}\text{Ho}^g$ [47]	60% $\epsilon$	$(28.8 \pm 0.5)$ min	73.4	$1.88 \pm 0.21$
		40% $\beta^-$	$(28.8 \pm 0.5)$ min	91.4	$2.3 \pm 0.3$

## 2.5 Neutron flux

The neutron flux was determined by means of the activation technique. For this reason, in each irradiation the sample (Er, Dy or Ho) was placed between monitor foils (Au, Al, Nb) of equal diameter. For these foils a reference reaction was used as standard for the determination of the neutron flux.

### 2.5.1 Reference reactions

In general, any reaction whose the excitation function is accurately known through multiple experimental and theoretical investigations can serve as reference reaction. Given that the reaction cross section is known for the energy region of interest, the neutron flux  $\Phi$  can be determined by applying Eq. 2.2.

Through the neutron beam irradiation of the Al, Au and Nb foils, the  $^{27}\text{Al}(n, \alpha)^{24}\text{Na}$ ,  $^{197}\text{Au}(n, 2n)^{196}\text{Au}$  and  $^{93}\text{Nb}(n, 2n)^{92}\text{Nb}^m$  reactions are induced. In Figure 2.8 the reference reactions cross sections, obtained from the IRDFF-1.05 standardized evaluated cross section library [50], are presented.

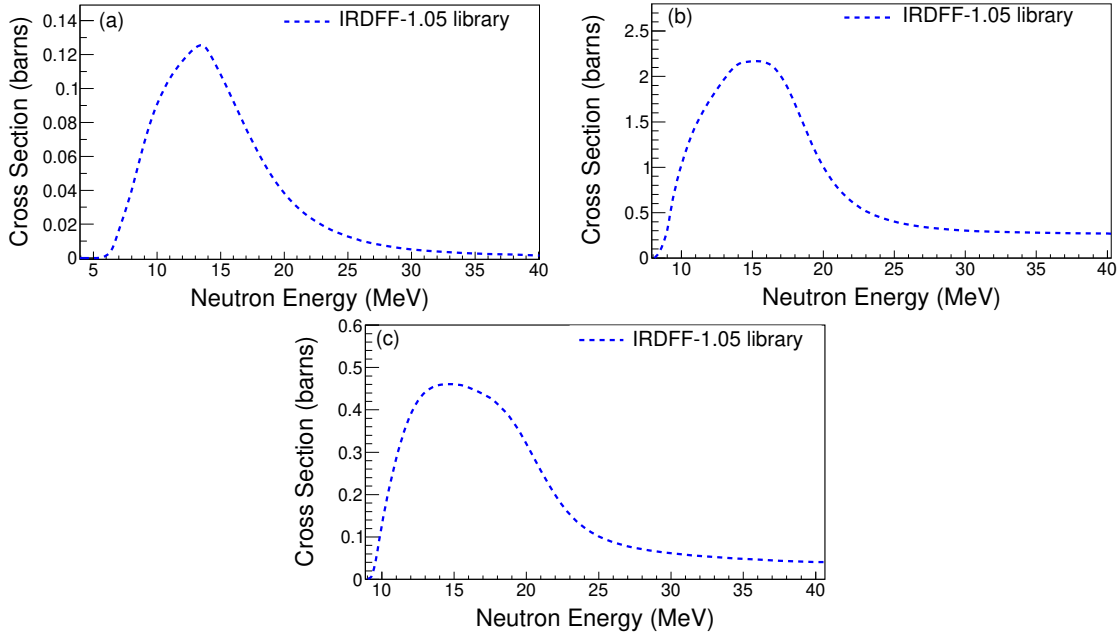


Figure 2.8: The IRDFF-1.05 library [50] for the reference reactions: (a)  $^{27}\text{Al}(n, \alpha)^{24}\text{Na}$ , (b)  $^{197}\text{Au}(n, 2n)^{196}\text{Au}$  and (c)  $^{93}\text{Nb}(n, 2n)^{92}\text{Nb}^m$ .

The decay schemes of the reference foils product-nuclei are illustrated in Figures 2.9-2.11 and the decay properties are summarized in Table 2.3. In the Table only the  $\gamma$ -rays of interest are mentioned.

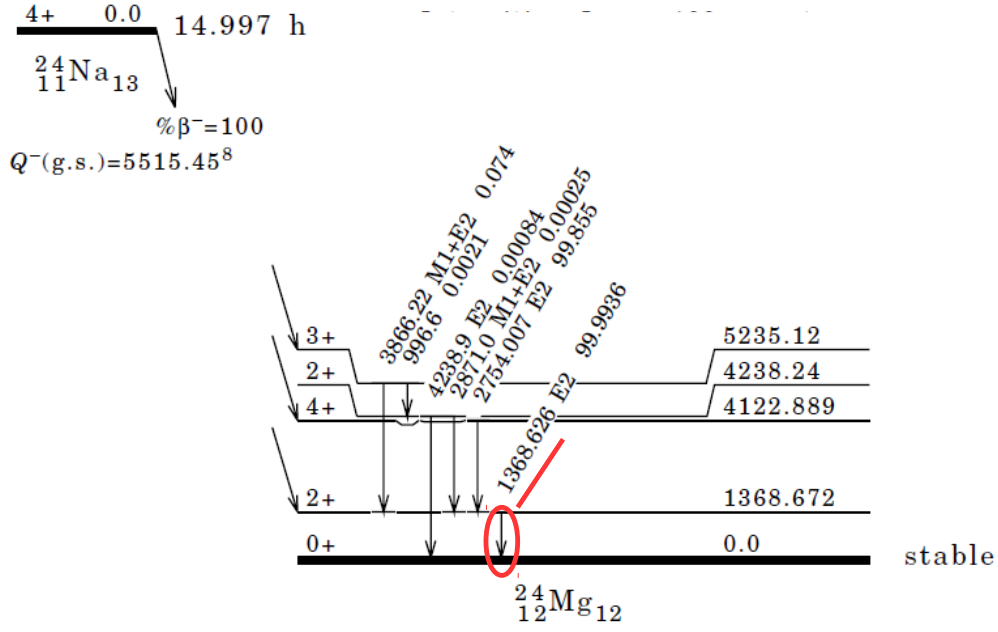


Figure 2.9: A representation of the decay scheme of  $^{24}\text{Na}$  (taken from Ref. [51]).

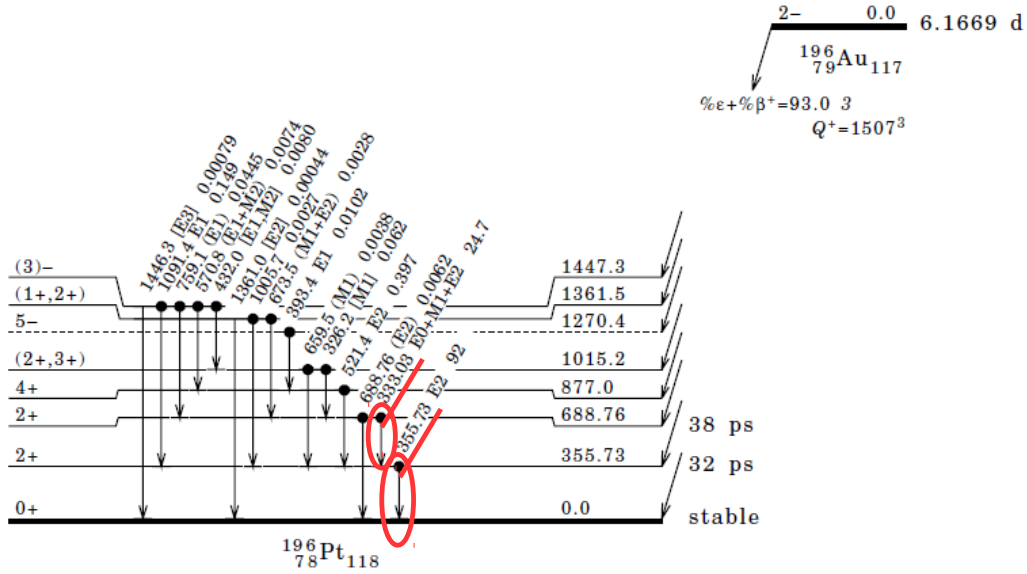


Figure 2.10: A representation of the decay scheme of  $^{196}\text{Au}$  (taken from Ref. [52]).



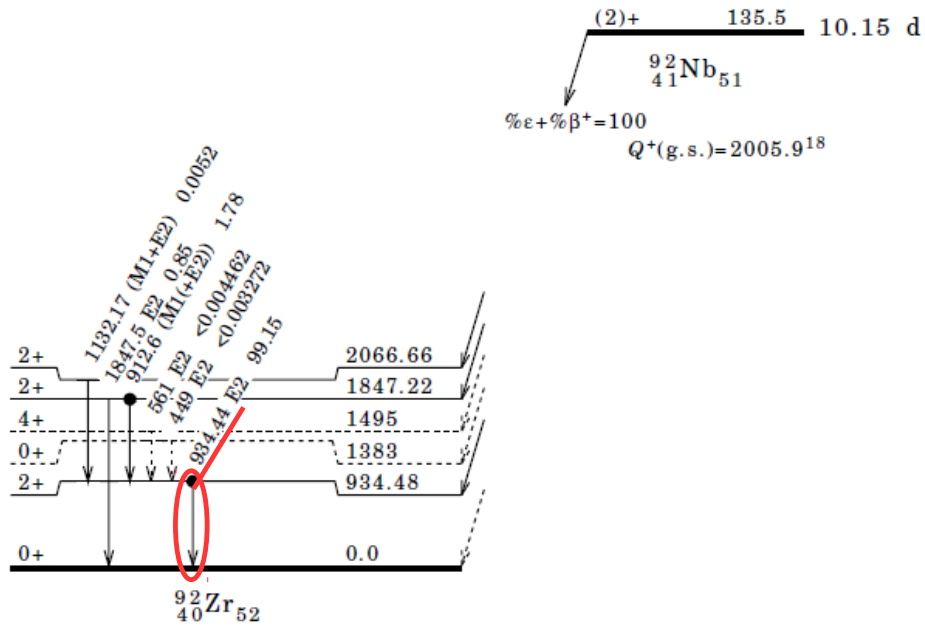


Figure 2.11: A representation of the decay scheme of  $^{92}\text{Nb}^m$  (taken from Ref. [53]).

Table 2.3: Decay properties of the reference reactions product-nuclei. In the Table only the  $\gamma$ -rays used in the analysis are mentioned.

Reference Nuclear Reaction	Product-nucleus	Decay mode	Half-life	$\gamma$ -ray energy (keV)	Intensity per decay (%)
$^{27}\text{Al}(n, \alpha)^{24}\text{Na}$	$^{24}\text{Na}$ [51]	100% $\beta^-$	(14.997 $\pm$ 0.012) h	1368.6	99.9936 $\pm$ 0.0015
$^{197}\text{Au}(n, 2n)^{196}\text{Au}$	$^{196}\text{Au}$ [52]	93% $\varepsilon$	(6.1669 $\pm$ 0.0006) d	355.7	87
$^{93}\text{Nb}(n, 2n)^{92}\text{Nb}^m$	$^{92}\text{Nb}^m$ [53]	100% $\varepsilon$	(10.15 $\pm$ 0.02) d	333.0	22.9 $\pm$ 0.9
				934.4	99.15

# Chapter 3

## Experimental set-up

This chapter deals with the concept of the experimental set-up: the irradiations and the activity measurements.

### 3.1 Irradiations at the N.C.S.R. “Demokritos” facility

The irradiations were performed at the 5.5 MV Tandem Van de Graaff accelerator of the Institute of Nuclear and Particle Physics at the National Center for Scientific Research (N.C.S.R.) “Demokritos”, Athens, Greece [54]. The neutron beams were produced via the  ${}^2\text{H}(d,n){}^3\text{He}$  (DD) reaction (Q-value=3.27 MeV) and the  ${}^3\text{H}(d,n){}^4\text{He}$  (DT) reaction (Q-value=17.59 MeV). The neutron beams between 10-11.3 MeV were produced through the DD reaction, whereas for the higher energies between 17-20 MeV, the DT reaction was used on account of its higher Q-value.

In the following two Sections the set-up of the irradiations is described.

#### 3.1.1 The $\text{D}_2$ gas cell

The primary target in the DD reaction consists of a  $\text{D}_2$  gas cell of 3.7 cm length. A Mo foil of 5  $\mu\text{m}$  thickness is used as entrance foil and a 0.02 cm thick Pt foil as the beam stop. In Figure 3.1 a simplified representation of the gas cell is depicted, whereas in Figures 3.2 and 3.3 a lateral and a front picture of the  $\text{D}_2$  gas cell are presented. In Figure 3.3 the ring-shaped holder of the samples is also depicted. In order to avoid the temperature increase the  $\text{D}_2$  gas target was cooled during the irradiations via an air jet [55].

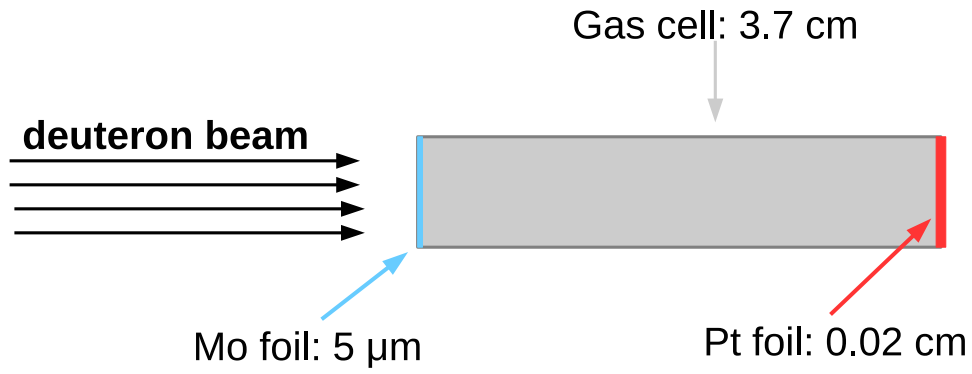


Figure 3.1: A simplified representation of the  $D_2$  gas cell configuration at the accelerator laboratory of “Demokritos” (not in scale).



Figure 3.2: The lateral view of the  $D_2$  gas cell at the accelerator facility of “Demokritos”.

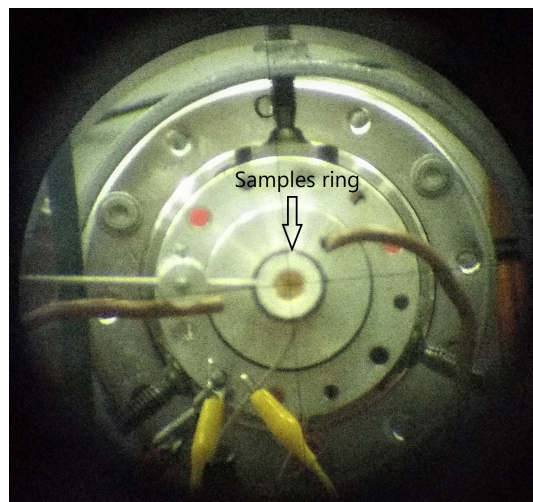


Figure 3.3: The front view of the  $D_2$  gas cell at the accelerator facility of “Demokritos” along with the ring-shaped holder.

### 3.1.2 The Ti-tritiated target

For the DT reaction, a  $2.1 \text{ mg/cm}^2$  Ti-tritiated target (TiT) was used lying on an 1 mm thick Cu foil. Tritium activity had a nominal value of 373 GBq at the 14<sup>th</sup> of June 2007, whereas the ratio of Tritium to Titanium nuclei was 1.543. Two Mo foils of  $5 \mu\text{m}$  thickness each are utilized so as decrease the energy of the deuteron beam to the desired energy which will induce the DT reaction. In any case, the energy of the deuteron beam before impinging on the Mo foils have to be higher than 2.5 MeV for which the transmission efficiency of the accelerator is in tolerable levels. A simplified outline of the configuration is depicted in Figure 3.4, whereas in Figure 3.5 a picture of the target is presented. The target was air-cooled during the irradiations to minimize the effect of heating.

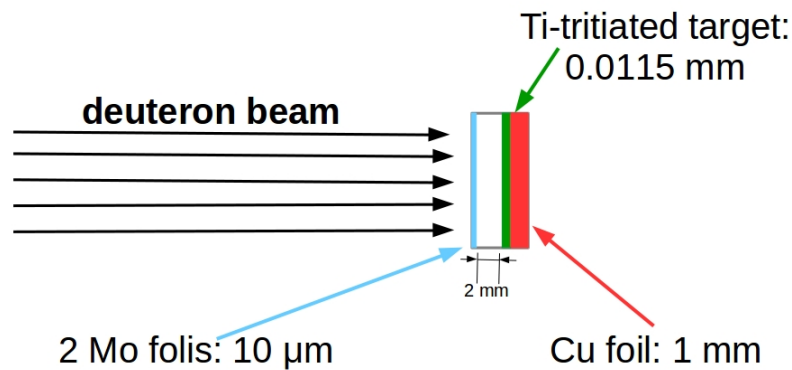


Figure 3.4: A simplified representation of the Ti-tritiated target at the accelerator laboratory of “Demokritos” (not in scale).

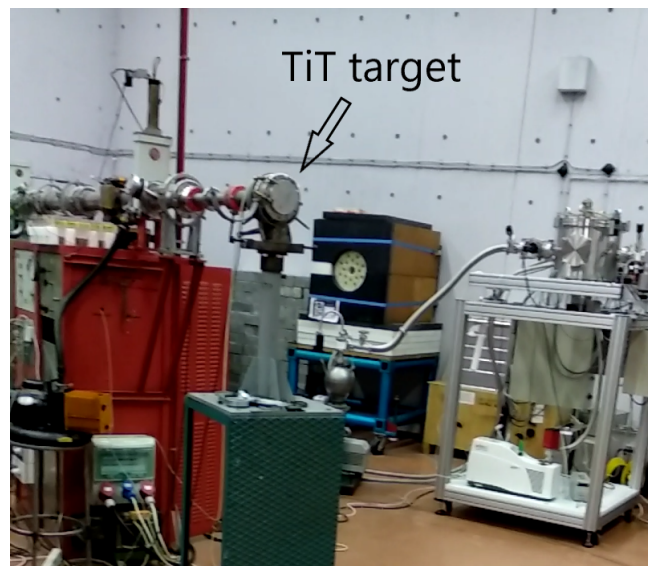


Figure 3.5: The Ti-tritiated target at the accelerator facility of “Demokritos”.

## 3.2 The samples

In the present study pellets of 13 mm diameter were used. The Er pellets were 2 mm thick, the Dy pellets were 0.9 and 0.8 mm thick and the Ho pellets were 1 mm thick.

The Er and Ho pellets were formed from the  $\text{Er}_2\text{O}_3$  and  $\text{Ho}_2\text{O}_3$  oxides, respectively. In both cases the oxides were mixed with cellulose powder in order to enhance the mechanical stability of the pellets. The cellulose consisted the 10% of the total mass of the pellets. The Dy pellets consisted of the Dy element.

The Ho element has only one stable isotope ( $^{165}\text{Ho}$ ) with 100% abundance. The Er and Dy elements consist of many stable isotopes given in Table 3.1 along with the abundances in the natural composition (Ref. [56]). As can be seen in these Tables,  $^{162}\text{Er}$  and  $^{156}\text{Dy}$  are the lightest stable isotopes with minor abundance, 0.139% and 0.056% respectively.

The number of nuclei of a particular isotope in the samples, when the samples are formed either from an element or a chemical compound, is calculated as following:

$$N_T = \text{abundance} * N * \frac{m}{W} * N_A \quad (3.1)$$

where abundance is the natural abundance of the isotope and N is the number of nuclei in the chemical compound (in case of an element N=1). The term m stands for the mass of the chemical compound or the element in the sample and W stands for the molecular weight (or the atomic weight in case of an element). The  $N_A$  term is the Avogadro number (6.022E+023).

Table 3.1: The stable isotopes of the (a) Er element and (b) Dy element along with the respective natural abundances [56].

(a) Er Isotopes	Natural abundance (%)
$^{162}\text{Er}$	$0.139 \pm 0.005$
$^{164}\text{Er}$	$1.601 \pm 0.003$
$^{166}\text{Er}$	$33.503 \pm 0.036$
$^{167}\text{Er}$	$22.869 \pm 0.009$
$^{168}\text{Er}$	$26.978 \pm 0.018$
$^{170}\text{Er}$	$14.910 \pm 0.036$
(b) Dy Isotopes	Natural abundance (%)
$^{156}\text{Dy}$	$0.056 \pm 0.003$
$^{158}\text{Dy}$	$0.095 \pm 0.003$
$^{160}\text{Dy}$	$2.329 \pm 0.018$
$^{161}\text{Dy}$	$18.889 \pm 0.042$
$^{162}\text{Dy}$	$25.475 \pm 0.036$
$^{163}\text{Dy}$	$24.896 \pm 0.042$
$^{164}\text{Dy}$	$28.260 \pm 0.054$

### 3.3 Irradiations set-up

The samples and the reference foils were placed in front of the primary target (the optimum samples-primary target distance is discussed in Section 3.4). The reference foils were placed on the two sides of the samples (“sandwich structure”). A simplified outline of the irradiations configuration is depicted in Figure 3.6.

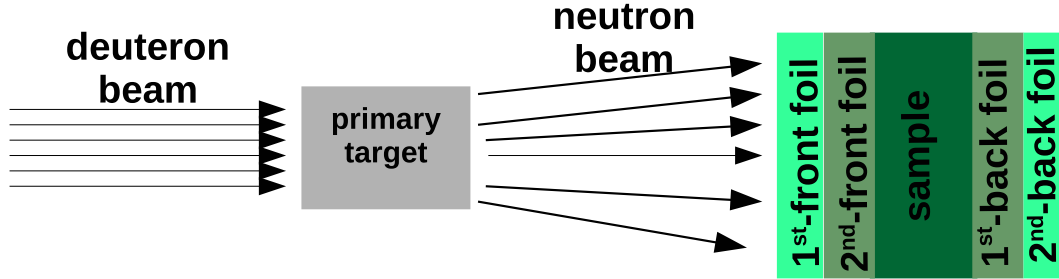


Figure 3.6: A simplified representation of the irradiation configuration of the samples and the primary targets (not in scale).

The masses of the samples and the reference foils that were used in each irradiation are summarized in Table 3.2.

### 3.4 Neutron beam energy distribution

In Figure 3.7 the differential cross sections of the DD and DT reactions are presented along with the kinematic curves of the emitted neutrons, at indicated deuteron beam energies close to the adopted ones. These data were obtained from Ref. [57] and they correspond to deuteron beam energies at 7.5 MeV for the DD reaction (Figure 3.7(a)) and 3 MeV for the DT reaction (Figure 3.7(b)). Calculations of the angular distribution of the emitted neutrons were also performed for different beam deuteron energies via the relativistic kinematics program CATKIN [58]. The results are illustrated in Figure 3.8.

Table 3.2: The masses of the samples and the reference foils used in each irradiation along with the deuteron beam energy ( $E_d$ ) and the distance of the samples with respect to the primary target ( $\ell$ ) for (a) the  $^{162}\text{Er}(n,2n)^{161}\text{Er}$  reaction, (b) the  $^{156}\text{Dy}(n,2n)^{155}\text{Dy}$  reaction and (c) the  $^{165}\text{Ho}(n,2n)^{164}\text{Ho}$  reaction.

$E_d$ (MeV)	$\ell$ (mm)	1 <sup>st</sup> front-foil (g)	2 <sup>nd</sup> front-foil (g)	sample (g)	1 <sup>st</sup> back-foil (g)	2 <sup>nd</sup> back-foil (g)
(a) $^{162}\text{Er}(n,2n)^{161}\text{Er}$						
7.86	70	0.6787 (Au)	0.1853 (Al)	0.9944	0.1879 (Al)	0.3375 (Nb)
8.17	70	1.5113 (Au)	0.1913 (Al)	0.9944	0.2215 (Al)	1.4369 (Au)
8.47	70	0.3002 (Nb)	0.2203 (Al)	1.0597	0.2213 (Al)	0.3022 (Nb)
2.50	20	0.6791 (Au)	0.2207 (Al)	1.0597	0.2210 (Al)	1.4374 (Au)
3.00	20	0.6466 (Au)	0.1808 (Al)	0.9944	0.1817 (Al)	0.6548 (Au)
3.55	20	0.3026 (Nb)	0.1662 (Al)	1.0597	0.1918 (Al)	0.3375 (Nb)
(b) $^{156}\text{Dy}(n,2n)^{155}\text{Dy}$						
2.49	23	0.6669 (Au)	0.1808 (Al)	1.0596	0.1929 (Al)	0.6779 (Au)
2.97	23	0.6805 (Au)	0.1821 (Al)	1.0849	0.2074 (Al)	0.6535 (Au)
3.51	24	0.6456 (Au)	0.1920 (Al)	0.8376	0.2015 (Al)	1.5109 (Au)
(c) $^{165}\text{Ho}(n,2n)^{164}\text{Ho}$						
7.23	70	0.6677 (Au)		0.5612		0.6462 (Au)
7.54	71	1.4392 (Au)	0.2077 (Al)	0.5456	0.1930 (Al)	1.5118 (Au)
7.84	72	0.6549 (Au)	0.1670 (Al)	0.5120	0.1930 (Al)	0.6809 (Au)
2.49	25	0.6460 (Au)	0.1925 (Al)	0.5612	0.1921 (Al)	0.6536 (Au)
2.97	25	0.6672 (Au)	0.2013 (Al)	0.5456	0.2204 (Al)	0.6788 (Au)
3.51	25	0.6807 (Au)	0.1915 (Al)	0.5120	0.2209 (Al)	1.4372 (Au)
3.95	25		0.1669 (Al)	0.5338	0.181 (Al)	

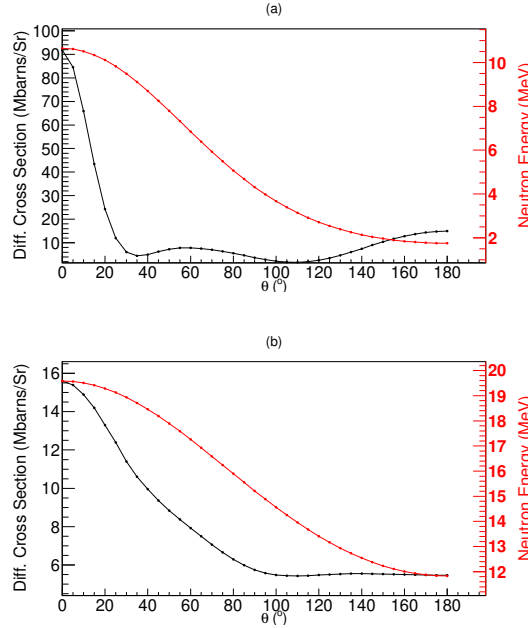


Figure 3.7: The differential cross section (black color) and the emitted neutrons energy (red colour) in the laboratory system for (a) the DD reaction (7.5 MeV deuteron beam energy) and (b) the DT reaction (3 MeV deuteron beam energy).

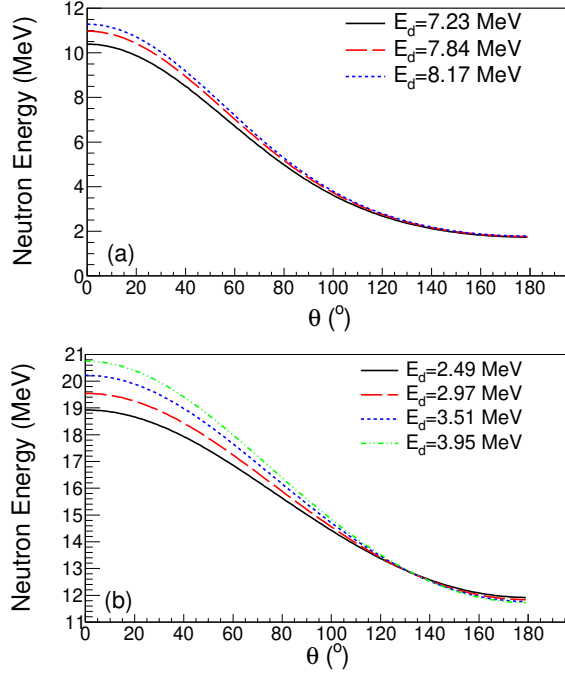


Figure 3.8: The kinematics of emitted neutrons, as resulting from CATKIN program for (a) the DD reaction (7.23, 7.84 and 8.17 MeV deuteron beam energies) and (b) the DT reaction (2.49, 2.97, 3.51 and 3.95 MeV deuteron beam energies).

The energy distribution of the neutron beams produced at “Demokritos” depends on the geometrical characteristics of the irradiation setup. Specifically, it depends on the angle with respect to the primary deuteron beam, as well as on the solid angle covered. Taking into account the primary-targets configuration in NEUSDESC [59], it resulted that for  $\approx 7$  cm distance from the center of the  $D_2$  gas cell and  $\approx 2$  cm from the Ti-tritiated target the angular acceptance of the beams corresponds to quasi-monoenergetic neutron beams.

### 3.4.1 The NEUSDESC code

The NEUSDESC code was developed at JRC, Belgium. Through this the neutron energy spectra of the following reactions can be calculated using relativistic kinematics [60, 61]:

- ${}^7\text{Li}(p,n){}^7\text{Be}$
- ${}^3\text{H}(p,n){}^3\text{He}$
- ${}^2\text{H}(d,n){}^3\text{He}$
- ${}^7\text{Li}(\alpha, n){}^{10}\text{B}$
- ${}^3\text{H}(d,n){}^4\text{He}$
- ${}^{45}\text{Sc}(p,n){}^{45}\text{Ti}$



- ${}^2\text{H}(d,pn){}^2\text{H}$

Due to the fact that the primary beam consists of charged particles the energy loss inside the primary target must be included in the calculations. This is achieved by dividing the primary target into 100 slices and adopting the stopping powers from Refs. [62] and [63].

NEUSDESC disposes the option of including calculations with the SRIM-2008 software package [64]. By activating this option Monte Carlo simulations are performed through SRIM-2008 for the energy loss calculations and the angular and energy straggling of the primary beam is taken into account.

In Figure 3.9 an outline of the needed input information of NEUSDESC is presented. To this outline the values related to the targets characteristics have been included. The deuterons energy and the distance of the samples with respect to primary targets vary in different irradiations.

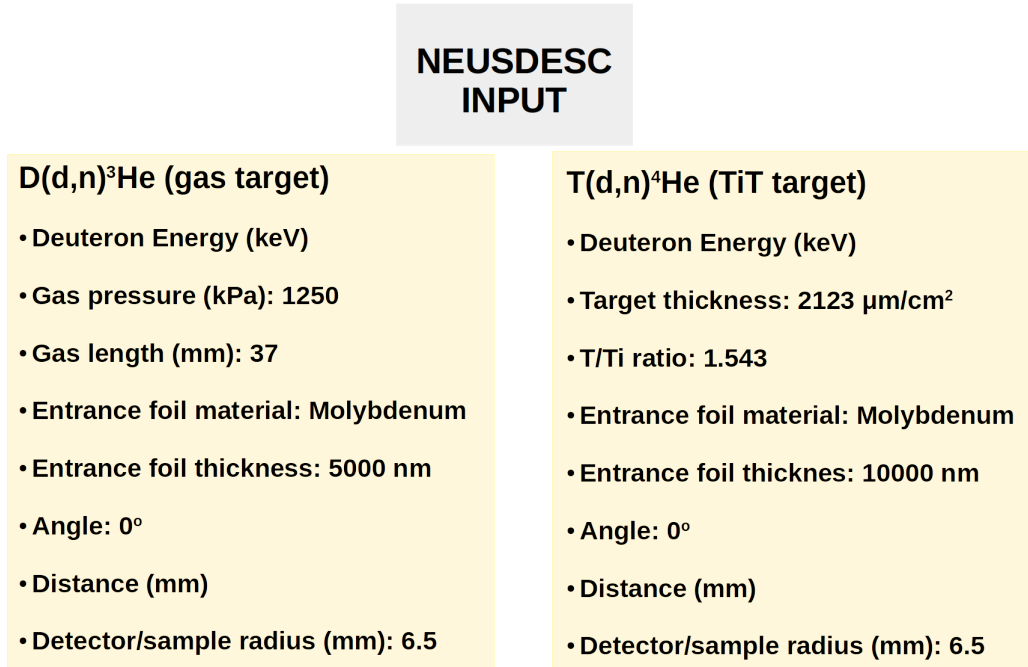


Figure 3.9: An outline of the inputs that must be defined in NEUSDESC.

In Figure 3.10 the neutron beam energy distributions are presented, as resulting from NEUSDESC by enabling the SRIM-2008 stopping power calculations. The first five Figures (a), (b), (c), (d) and (e) correspond to the neutron beams produced by the DD reaction for  $E_d=7.23, 7.54, 7.84$  MeV, 8.17 MeV and 8.47 MeV deuteron beam energies, respectively, and for primary target to samples distance  $\approx 70$  mm. The last four Figures (f), (g), (h) and (i) correspond to the neutron beams produced by the DT reaction for  $E_d=2.49, 2.97, 3.51$  and 3.95 MeV, respectively, and for primary target to samples distance 25 mm.

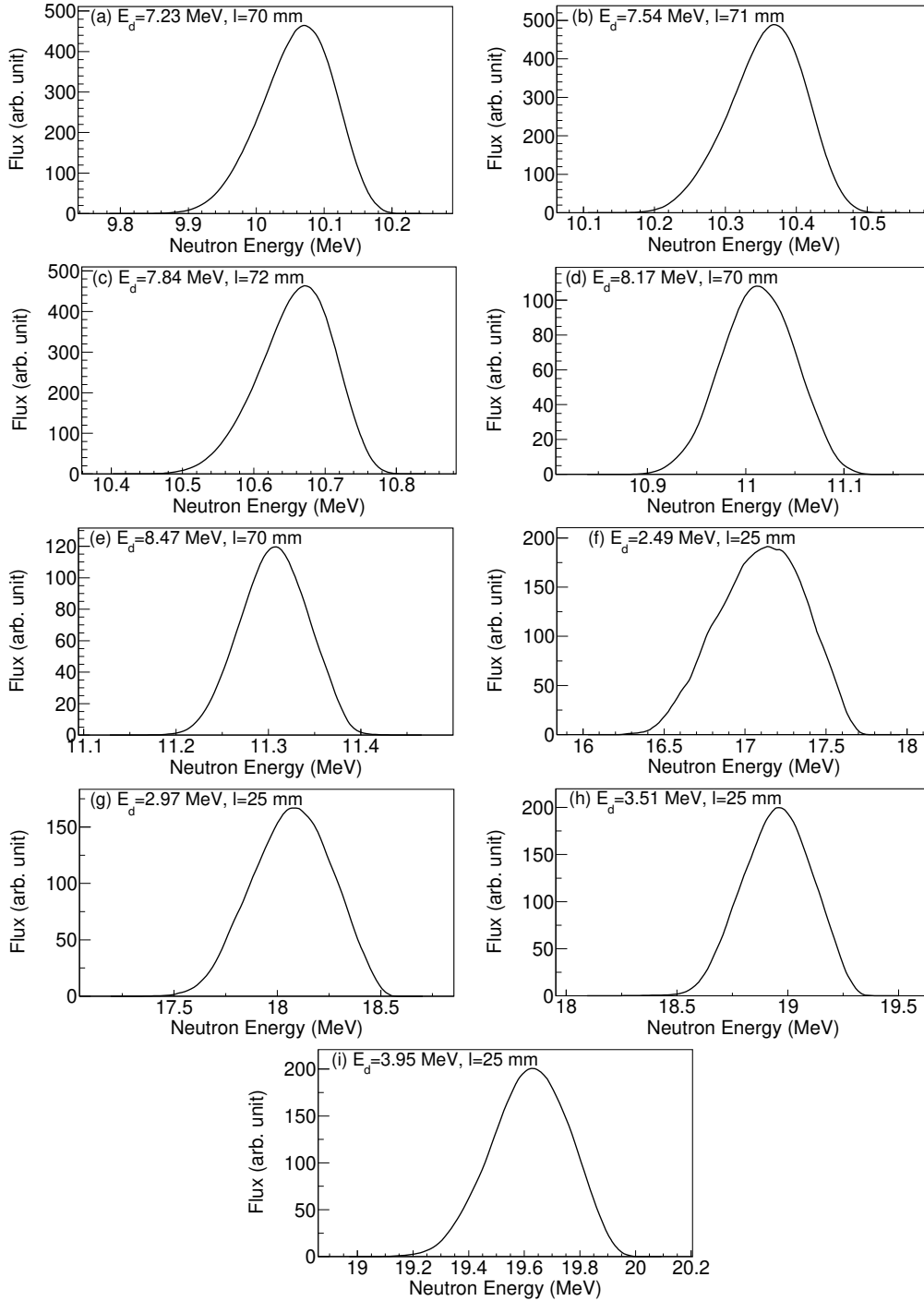


Figure 3.10: The neutron beam energy distribution spectra resulting from NEUSDESC code taking into account the irradiation set-up for each deuteron beam energy.

Taking into account Figure 3.10, the respective neutron beam energies and their uncertainties were calculated as the average energy and the FWHM of the neutron beam energy distributions. The results are summarized in Table 3.3.

Table 3.3: The neutron beam energies and their uncertainties as resulting for NEUSDESC code.

	Deuteron beam energy (MeV)	Neutron beam energy (MeV)	Neutron beam energy uncertainty (MeV)
DD reaction	7.23	10.1	0.1
	7.54	10.4	0.1
	7.84	10.7	0.1
	8.17	11.0	0.1
	8.47	11.3	0.1
DT reaction	2.49	17.1	0.3
	2.97	18.1	0.2
	3.51	19.0	0.2
	3.95	19.6	0.2

### 3.5 GEANT4 simulation of the neutron beam

The neutron beam energy distributions have also been calculated through Monte Carlo simulations with the GEANT4 toolkit [4]. In these simulations the production of neutrons was performed through the simulation of the DD and DT reactions. The structure of the targets was also taken into account by simulating the D<sub>2</sub> gas and the Ti-tritiated materials along with the full geometry of each target assembly as described in Sections 3.1.1 and 3.1.2. In addition, the deuteron beam line was simulated in detail by including the last two collimators at 43.2 cm and 45 cm distance from the targets.

In Appendices F and G the GEANT4 geometry files are given. The visualization of the GEANT4 geometries (DAWN [65]) are presented in Figures 3.11 and 3.12.

For the simulation of the physics interactions the QGSP\_BIC\_A11HP Physics List of GEANT4 was used [66]. This is suitable for hadronic interactions below 200 MeV and, in addition, it is a high precision model for the neutron transport below 20 MeV up to thermal energies.

In Figure 3.13 the comparison of the neutron beam energy distributions as resulting from the NEUSDESC and GEANT4 codes can be seen for the deuteron beam energies of 7.23, 7.84, 2.49, 2.97, 3.51 and 3.95 MeV. The results of the two calculations are consistent.

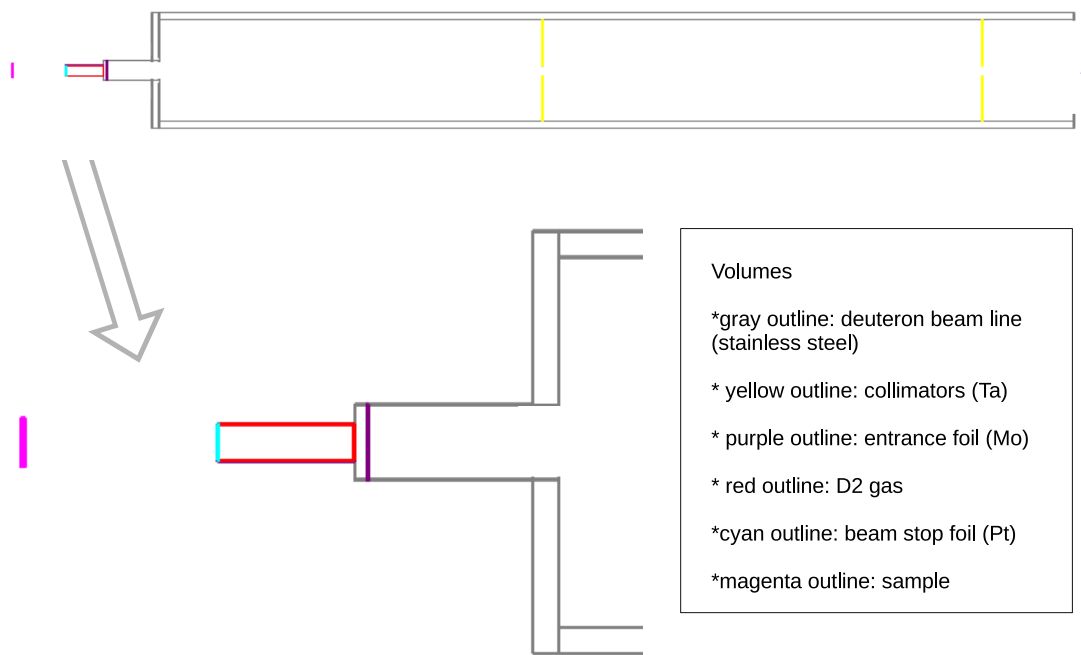


Figure 3.11: The GEANT4 visualization of the deuteron beam line and the  $D_2$  gas target in the accelerator facility at “Demokritos”, using the DAWN visualization driver.



Figure 3.12: The GEANT4 visualization of the deuteron beam line and the TiT target in the accelerator facility at “Demokritos”, using the DAWN visualization driver.

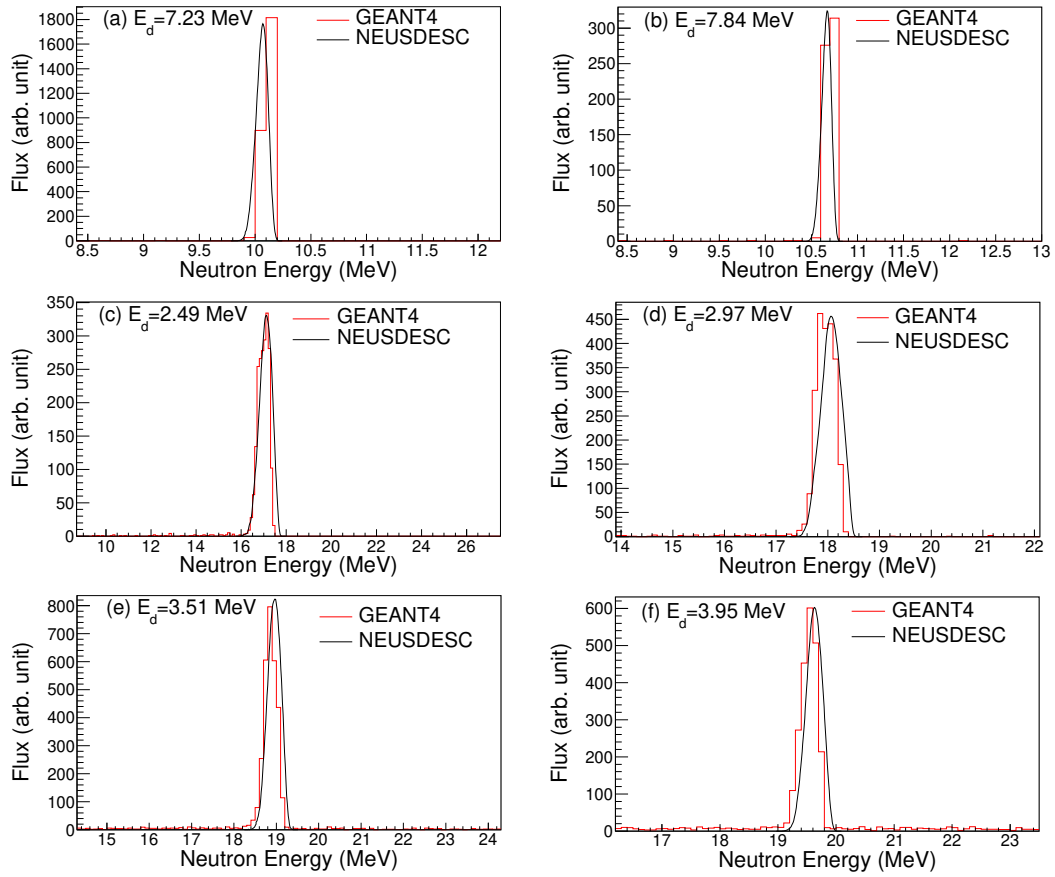


Figure 3.13: The comparison of the neutron beam energy distributions as resulting from the NEUSDESC and GEANT4 codes for the deuteron beams of (a) 7.23 MeV, (b) 7.84 MeV, (c) 2.49 MeV, (d) 2.97 MeV, (e) 3.51 MeV and (f) 3.95 MeV.

### 3.6 Neutron beam intensity fluctuations

In spite of the fact that the total beam flux impinging on the samples is calculated using reference reactions, the neutron monitoring is very important as it provides the information about the beam intensity fluctuations during the irradiation time. In the framework of the present experiments a BF<sub>3</sub> neutron detector was used so as to record the beam fluctuations of each irradiation in the form of a multichannel scaler file.

BF<sub>3</sub> detector is a gas-proportional counter. Its principle of operation is based on the detection of the  $\alpha$ -particles and the <sup>7</sup>Li isotopes which are produced, when neutrons interact with <sup>10</sup>B of the BF<sub>3</sub> gas (Boron-Trifluoride). In reality, the <sup>7</sup>Li product-nucleus can be left either at the ground (6 % of the reactions) or at an isomeric state at 0.48 MeV excitation energy (94 % of the reactions):

- i.  $^{10}\text{B} + n \rightarrow \alpha + ^7\text{Li}$ ,  $Q=2.79$  MeV
- ii.  $^{10}\text{B} + n \rightarrow \alpha + ^7\text{Li}^*$ ,  $Q=2.31$  MeV

<sup>10</sup>B constitutes approximately the 20% of the natural B. The remaining 80% is <sup>11</sup>B. Therefore, the counter is enriched with <sup>10</sup>B and its intrinsic efficiency is increased.

In Figure 3.14 the experimental data [17] and the results of the ENDF/B-VIII.0 evaluated library [39] for the <sup>10</sup>B(n, $\alpha$ )<sup>7</sup>Li reaction cross section are illustrated. As can be seen, the lower the neutron energy is, the higher the cross section is. The latter decreases very rapidly as the neutrons energy increases, approximately with the reciprocal of the neutron velocity ( $\frac{1}{u}$ ). On account of this, during the irradiations the BF<sub>3</sub> detector was placed inside a paraffin cylindrical configuration, which was used as neutron moderator.

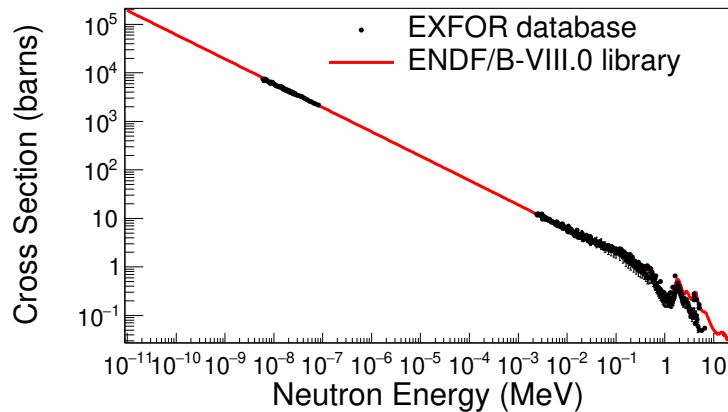


Figure 3.14: The experimental cross section data of the <sup>10</sup>B(n, $\alpha$ )<sup>7</sup>Li reaction, as presented at the EXFOR database [17], along with the ENDF/B-VIII.0 library [39].

In general, BF<sub>3</sub> detectors are used as counters. By looking at the excitation function of the <sup>10</sup>B(n, $\alpha$ ) reaction, we can conclude that most of the detected neutrons

are low energy neutrons. As a result, their energy is much lower than the released energy of  ${}^7\text{Li}$  and  $\alpha$  particles. This is one of the reasons that  $\text{BF}_3$  detectors cannot be used for the determination of the neutrons energy. Additionally, the  $\text{BF}_3$  detector could be used only as counter during irradiations at “Demokritos”, since the neutrons were moderated through the paraffin and therefore, the initial information on the neutrons energy was lost.

The  $\text{BF}_3$  detector was placed at a distance of 2 cm and at an angle of  $20^\circ$  with respect to the  $\text{D}_2$  gas and TiT targets. Apparently, apart from the neutron beam, the detector also detects parasitic neutrons. The latter mainly originate from the break-up reactions and the scattering of neutrons with the surrounding area. Any fluctuations of the detected neutrons is mainly attributed to corresponding fluctuations of the deuteron beam. For this reason, the deuteron beam intensity was also recorded during the irradiations.

The information of the neutron beam fluctuations is essential in order to determine the correction factors for the activated nuclei decay during irradiations (Eq. 2.3 and 2.7), as discussed in Section 2.3.

### 3.7 Activity measurements

The activity measurements of the samples and the reference foils were performed using HPGe detectors due to the superior energy resolution they provide in comparison with other types of  $\gamma$ -ray detectors. In particular, for the present study seven HPGe detectors were used:

- two 100% rel. efficiency HPGe detectors of the Institute of Nuclear and Particle Physics at N.C.S.R. “Demokritos”.
- two 16% rel. efficiency HPGe detectors of the Institute of Nuclear and Particle Physics at N.C.S.R. “Demokritos”.
- one 50% rel. efficiency Broad Energy HPGe detector of the Environmental Radioactivity Monitoring Department of Greek Atomic Energy Commission.
- one 80% rel. efficiency HPGe detector of the Institute of Nuclear and Radiological Sciences, Technology, Energy and Safety at N.C.S.R. “Demokritos”.
- one 40% rel. efficiency HPGe detector of the Institute of Nuclear and Radiological Sciences, Technology, Energy and Safety at N.C.S.R. “Demokritos”.

In Table 3.4 can be seen the correspondence between the samples and the detectors which were used for their activity measurements. In the Table the distance of the samples to the detector window,  $\ell$ , is also referred.

In case of the  ${}^{162}\text{Er}(n,2n){}^{161}\text{Er}$  reaction study, the Er samples were placed between the two 100% rel. efficiency HPGe detectors at 1.1 cm distance from the window of



Table 3.4: The HPGe detectors that were used for the activity measurements of the samples along with the distance of the samples to the detector window,  $\ell$ .

	detector	$\ell$ (cm)
Er samples	2x100% rel. efficiency BE HPGe	1.1
reference foils	two 16% rel. efficiency HPGe	7.0
Dy samples	80% rel. efficiency HPGe	1.0
reference foils	40% rel. efficiency HPGe	7.3-11.1
Ho samples	50% rel. efficiency BE HPGe	0.15
reference foils	80% rel. efficiency HPGe	1.0

each one of them. Through the close detection geometry the maximum solid angle ( $\approx 4\pi$ ) for the detection of  $\gamma$ -rays was covered. For the determination of the efficiency of the detection system at this geometry for the  $\gamma$ -rays at 826.6 keV (emitted by  $^{161}\text{Er}$ ) a  $^{54}\text{Mn}$  [67] point source was used. The advantage of this source is that  $^{54}\text{Mn}$  emits only one  $\gamma$ -ray at 834.8 keV, which is very close to the 826.6 keV.

The reference foils were placed at 7 cm distance from the detector window: the first 16% rel. efficiency HPGe detector was used at the low neutron energy irradiations (10.7-11.3 MeV) and the second at the high neutron energy irradiations (17.1-19.6 MeV). The detection efficiency at this distance was determined using a  $^{152}\text{Eu}$  [68] point source.

The efficiency calibration of the detectors used in the study of the  $^{162}\text{Er}(n,2n)^{161}\text{Er}$  reaction has been discussed extensively in Refs. [69]- [71]. For this reason, within the present thesis the discussion will be limited on the efficiency calibration of the detection systems used in  $^{156}\text{Dy}(n,2n)^{155}\text{Dy}$  and  $^{165}\text{Ho}(n,2n)^{164}\text{Ho}$  reaction studies.

### 3.7.1 GEANT4 characterization of the HPGe detectors

The response of each one of the detectors was simulated through the GEANT4 code. Initially, the geometrical characteristics (crystal dimensions, dead layer thickness, gap: distance from the crystal to the detector window, borehole) as provided by the manufacturer were utilized in the simulations to construct the detectors model. Afterwards, the detector geometrical characteristics were slightly modified so as to reproduce the experimentally deduced efficiency and counting rate data.

The tuning of the detector geometry is a common practice in the detector simulations and there are two main reasons for this. Firstly, there is an uncertainty regarding the actual dimensions coming from e.g. the mounting of the crystal in the detector housing or the change of the Ge active volume over the years (dead-layer increase). The other reason is the incomplete charge collection phenomenon during the real measurements, which has as a result the decrease of the experimental efficiency [72, 73].

As mentioned above, the GEANT4 characterization of the detectors was performed so that the experimental efficiencies and counting rates are reproduced. The counting rates were preferred against the efficiency data as a criterion for the detectors simulation at close detection geometries. The reason is that at close

geometries the decay scheme of the isotopes affects the  $\gamma$ -rays detection, on account of the coincidence-summing effect which becomes important when close detection geometries are considered along with multi-photon decays ( $\gamma$ -ray multiplicity  $> 1$ ). The difference between the terms efficiency and counting rate, as well as the formula through which they are calculated are described in Appendix H.

During the calibration procedures various calibration sources were used in different source to detector distances for the experimental determination of the full energy peak efficiency for different  $\gamma$ -ray energies. In this way, the performance of the GEANT4 simulations could be benchmarked for different photon energies and for different source to detector distances.

### 3.7.2 The 50% rel. efficiency BE HPGe detector

The 50% rel. efficiency BE HPGe detector was selected for the measurements of the low energy photons ( $< 100$  keV) coming from  $^{164}\text{Ho}$  due its ability to detect photons from the MeV region down to 3 keV. This type of detectors combines carbon fiber detector window along with minimum Ge crystal dead layer (a few  $\mu\text{m}$ ).

For the efficiency calibration of the 50% rel. efficiency BE HPGe detector the following calibration point sources were used:  $^{60}\text{Co}$  [74],  $^{137}\text{Cs}$  [75],  $^{133}\text{Ba}$  [76] and  $^{241}\text{Am}$  [77] at distances of 20, 11.4 and 0.4 cm. Moreover, a filter with evaporated metallic salts of  $^{60}\text{Co}$  [74],  $^{137}\text{Cs}$  [75],  $^{241}\text{Am}$  [77] and  $^{210}\text{Pb}$  [78] was utilized. The filter had an extended geometry of 4.5 cm in diameter, whereas its thickness was 1  $\mu\text{m}$ . It was placed at a distance of 0.8 cm from the detector window. In short source to detector distances (0.4 cm and 0.8 cm) the simulation results were compared to the experimental data in terms of the counting rate and not in terms of the efficiency due to the fact that at short distances the coincidence-summing effect becomes important.

In Figure 3.15 the experimental efficiency and counting rate data are illustrated in comparison with the respective results of the simulations for the 50% rel. efficiency BE HPGe detector. In Figures 3.15(a) and (b) the simulation results are presented with a solid line as the graphs present the detector efficiency at the corresponding geometries. On the other hand, Figures 3.15(c) and (d) correspond to the counting rates of the full-energy peaks including coincidence-summing effects. Therefore, the simulation results are depicted with points.

In the GEANT4 simulations either the emission of one specific  $\gamma$ -ray with isotropic distribution (“mono-energetic” emission) or the full decay scheme of the isotopes of interest were defined. For the long source to detector distances (20 and 11.4 cm) the “mono-energetic” emission was sufficient but for the short ones (0.4 and 0.8 cm) the decay schemes of the isotopes should be included in the simulations so as to calculate the counting rate data including coincidence-summing effect.

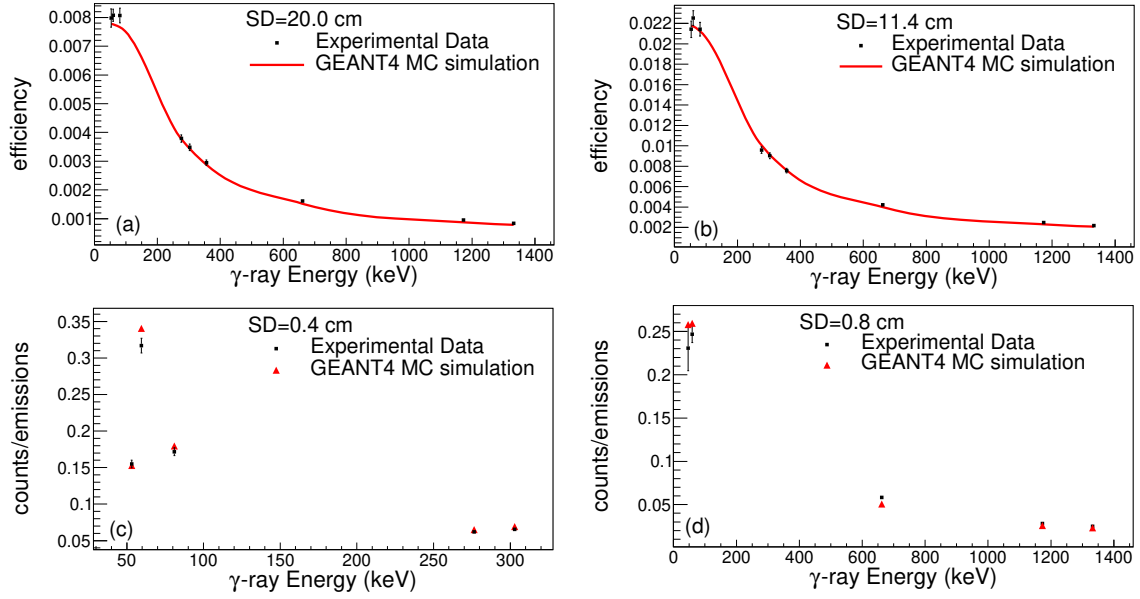


Figure 3.15: Comparison of the experimental efficiencies and counting rates obtained for the 50% rel. efficiency BE HPGe detector with the GEANT4 MC simulations. In Figures 3.15(a) and (b) the efficiencies at 20 and 11.4 cm distance from the detector window are, respectively, presented. Figure 3.15(c) corresponds to the counting rates of the  $\gamma$ -rays of the simulated isotopes at 0.4 cm distance from the detector window. Figure 3.15(d) depicts the counting rates of the  $\gamma$ -rays of the simulated isotopes as resulting using a filter with extended geometry at 0.8 cm distance from the detector window.

### 3.7.3 The 80% and 40% rel. efficiency HPGe detectors

For the characterization of the 80% and 40% rel. efficiency HPGe detectors an  $^{152}\text{Eu}$  [68] calibration point source was used for different source to detector distances: 24.1, 23.9, 12.3, 11.8, 3.1, 2.9, 1.3 and 0.9 cm for the 80% rel. efficiency HPGe detector and at 21.1, 11.1, 7.3 and 4.3 cm for the 40% rel. efficiency HPGe detector. In the simulations, as previously, the “mono-energetic” emission of the  $\gamma$ -rays was adequate for the long distances (24.1, 23.9, 12.3, 11.8 cm for the 80% rel. efficiency HPGe detector and 21.1, 11.1 and 7.3 cm for the 40% rel. efficiency HPGe detector). On the other hand, the full decay scheme of the  $^{152}\text{Eu}$  isotope was adopted for the short distances (3.1, 2.9, 1.3 and 0.9 cm for the 80% rel. efficiency HPGe detector and 4.3 cm for the 40% relative efficiency HPGe detector), so as to take into account the coincidence-summing effect and calculate the corresponding counting rates.

In Figures 3.16 and 3.17 the experimental efficiency and counting rate data are illustrated in comparison with the respective results of the simulations for the 80% and 40% rel. efficiency HPGe detectors. As previously, Figures 3.16(a), (b), (c) and (d), as well as Figures 3.17(a), (b) and (c) present the efficiency of the detectors in the corresponding geometries. On the other hand, Figures 3.16(e), (f), (g) and (h) and Figure 3.17(d) present the counting rates of  $^{152}\text{Eu}$  due to the coincidence summing.

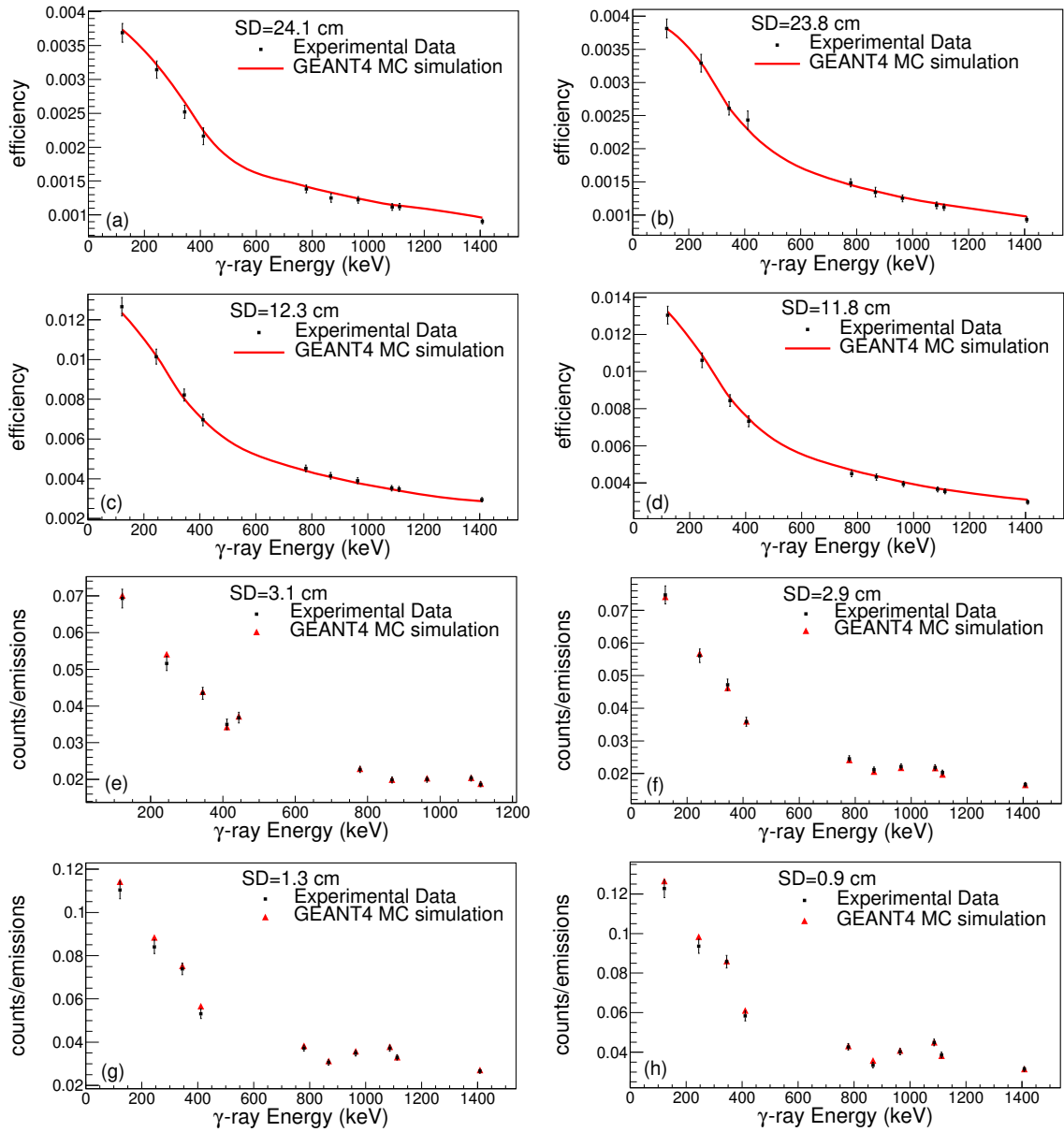


Figure 3.16: Comparison of the experimental efficiencies and counting rates obtained for the 80% rel. efficiency HPGe detector with the GEANT4 MC simulations. In Figures 3.16(a), (b), (c) and (d) the efficiencies at 24.1, 23.8, 12.3 and 11.8 cm distance from the detector window are, respectively, presented. Figure 3.16 (e), (f), (g) and (h) correspond to the counting rates of the  $\gamma$ -rays of  $^{152}\text{Eu}$  at 3.1, 2.9, 1.3 and 0.9 cm distance from the detector window.

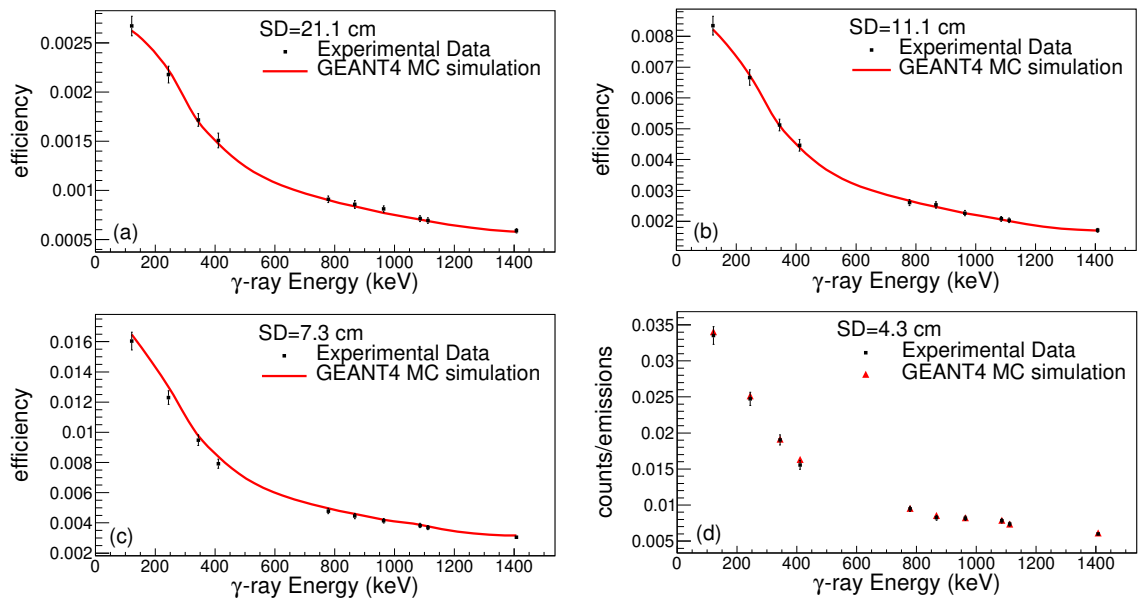


Figure 3.17: Comparison of the experimental efficiencies and counting rates obtained for the 40% rel. efficiency HPGe detector with the GEANT4 MC simulations. In Figures 3.17(a), (b) and (c) the efficiencies at 21.1, 11.1 and 7.3 cm distance from the detector window are, respectively, presented. Figure 3.17 (d) corresponds to the counting rates of the  $\gamma$ -rays of  $^{152}\text{Eu}$  at 4.3 cm distance from the detector window.

# Chapter 4

## Data analysis

### 4.1 Efficiency calculations

The data analysis of the present work is based on the analysis of numerous spectra obtained by different HPGe detectors. Each HPGe detector was fully characterized by means of detailed GEANT4 Monte-Carlo simulations. The simulations were validated through the comparison with experimentally deduced efficiency and counting rate data. In this way, the GEANT4 codes could be utilized for the efficiency calculations of the  $\gamma$ -rays emitted by the samples and the reference foils after the irradiations.

#### 4.1.1 Efficiency calculations for the $^{165}\text{Ho}(n,2n)^{164}\text{Ho}$ reaction study

##### 4.1.1.1 Efficiency calculations for the Ho samples

The activity of the Ho samples was measured by means of the 50% rel. efficiency BE HPGe detector. The samples were placed at 1.5 mm distance with respect to the detector window. This short source to detector distance was adopted in order to maximize the counting statistics against the low intensity of the recorded  $\gamma$ -rays (see Table 2.2) and the self-attenuation phenomenon.

The close detection geometry causes limitations in the efficiency calculations due to the coincidence-summing phenomenon which possibly affects the recorded counting rate not only of the efficiency calibration, but also of the actual measurement. Nevertheless, these issues were finally resolved through extensive GEANT4 simulations as described in Section 3.7.1. For the efficiency calculations at the decay energies of the samples, the actual dimensions and material of the Ho samples (homogeneous mixture of  $\text{Ho}_2\text{O}_3$  and cellulose) were specified in the simulations. In this way, the correction of the self-attenuation phenomenon was included in the efficiency calculations. The full-decay scheme of  $^{164}\text{Ho}$  was also defined for the emission of the  $\gamma$ -rays. Therefore, the coincidence-summing photons were also considered in the efficiency simulations. In other words, the precise GEANT4 simulation of the detector response allowed the direct calculation of the

detector efficiency at energy of the  $\gamma$ -rays considering the self-attenuation and coincidence-summing effects.

In Table 4.1 the efficiency of the detector at 1.5 mm distance for the decay energies of  $^{164}\text{Ho}$  is presented, as resulting from GEANT4 simulations, when:

- i) neither the Ho samples material (void samples considered) nor the  $^{164}\text{Ho}$  decay scheme are defined in the simulations
- ii) the Ho samples material is defined in the simulations, but not the  $^{164}\text{Ho}$  decay scheme
- iii) both the Ho samples material and the  $^{164}\text{Ho}$  decay scheme are defined in the simulations.

Table 4.1: The full energy peak efficiency of the 50% rel. efficiency BE HPGe detector at 1.5 mm distance for the decay energies of  $^{164}\text{Ho}$ , as resulting from the GEANT4 simulations, for the cases where: i) neither the Ho samples material nor the  $^{164}\text{Ho}$  decay scheme is defined in the simulations, ii) the Ho samples material is defined in the simulations, but not the  $^{164}\text{Ho}$  decay scheme and iii) both the Ho samples material and the  $^{164}\text{Ho}$  decay scheme are defined in the simulations.

isotope	$\gamma$ -ray (keV)	efficiency without including self-attenuation and coincidence-summing effects	efficiency including only the self-attenuation effect	efficiency including both self-attenuation and coincidence-summing effects
$^{164}\text{Ho}^m$	37.3	0.365	0.082	0.064
$^{164}\text{Ho}^g$	73.4	0.371	0.095	0.078
$^{164}\text{Ho}^g$	91.4	0.363	0.146	0.150

The total uncertainty of the efficiency was 5%. This value was deduced by the deviation of the simulation efficiencies and the counting rates of the low energy  $\gamma$ -rays (below 100 keV) of the calibration sources from the corresponding experimental values.

As can be seen from Table 4.1 all three  $\gamma$ -rays are highly attenuated. The attenuation is higher for the lowest  $\gamma$ -ray at 37.3 keV and lower for the highest  $\gamma$ -ray at 91.4 keV.

As far as the coincidence-summing effect is considered, this is dominant for the two  $\gamma$ -rays at 37.3 and 73.4 keV, for which the detector efficiency is lower when the decay schemes are included in the simulations.

#### 4.1.1.2 Efficiency calculations for the reference foils

The reference foils activity was measured by means of the 80% rel. efficiency HPGe detector at a distance of 1.0 cm with respect to the detector window. For the efficiency calculations for the characteristic  $\gamma$ -ray energies from the decay of the reference foils (see Table 2.3), the GEANT4 code was utilized following the same procedure described in the previous Section: the efficiency was calculated including the self-attenuation and coincidence-summing effects by defining in the simulations the foils material, as well as the product-nuclei decay schemes. The results are summarized in Table 4.2.

Table 4.2: The full energy peak efficiency of the 80% rel. efficiency HPGe detector at 1.0 cm distance for the  $\gamma$ -ray energies emitted by the activated reference foils as resulting from the GEANT4 simulations, for the cases where: i) neither the foils material nor the decay schemes is defined in the simulations, ii) the foils material is defined in the simulations, but not the decay schemes and iii) both the foils material and the decay schemes are defined in the simulations.

product-nuclei	samples thickness (mm)	$\gamma$ -ray (keV)	efficiency without including self-attenuation and coincidence-summing effects	efficiency including only the self-attenuation effect	efficiency including both self-attenuation and coincidence-summing effects
$^{196}\text{Au}$	0.3	333.0	0.096	0.087	0.070
		355.7	0.091	0.083	0.078
	0.5	333.0	0.096	0.082	0.067
		355.7	0.091	0.079	0.074
$^{24}\text{Na}$	0.55	1368.6	0.033	0.033	0.029

The total uncertainty of the efficiency was 3%. As previously, this value was obtained from the deviation between the simulation efficiencies and counting rates of the calibration sources from the corresponding experimental values.

The results of Table 4.2 show that the lowest  $\gamma$ -rays are the most highly attenuated, as well as that the attenuation increases with the samples thickness. Indeed, for the two  $\gamma$ -rays at 333.0 and 355.7 keV the self-attenuation phenomenon is intense in contrast to the 1368.6 keV  $\gamma$ -ray for which the the inclusion of the Al material does not make any effect. Between the low energy  $\gamma$ -rays the attenuation is higher for the 333.0 keV. Additionally, the attenuation is lower for the thinner Au foils compared to the thicker Au foils.

When the decay schemes are taken into account in the simulations, the efficiency of all three  $\gamma$ -rays is reduced because of the presence of the coincidence-summing effect.

## 4.1.2 Efficiency calculations for the $^{156}\text{Dy}(n,2n)^{155}\text{Dy}$ reaction study

### 4.1.2.1 Efficiency calculations for the Dy samples

The 80% rel. efficiency HPGe detector was also used for the activity measurements of the Dy samples. The samples were placed at 1 cm distance with respect to the detector window. This close detection geometry was adopted so as to compensate for the small natural abundance of  $^{156}\text{Dy}$  (0.056%).

The full energy peak efficiency at the 226.9 keV  $\gamma$ -ray coming from the decay of  $^{155}\text{Dy}$  was obtained through GEANT4. The full decay scheme of the isotope was taken into account so as to include the coincidence-summing effect in the simulations. The actual material (Dy foil of natural abundance) of the samples was also defined so as to include the self-attenuation phenomenon. The results are summarized in Table 4.3.

As previously mentioned (Section 4.1.1) the total uncertainty of the efficiency for the 80% rel. efficiency HPGe detector was 3%.



Table 4.3: The full energy peak efficiency of the 80% rel. efficiency HPGe detector at 1.0 cm distance for the 226.9 keV  $\gamma$ -ray of  $^{155}\text{Dy}$ , as resulting from the GEANT4 simulations, for the cases where: i) neither the samples material nor the decay scheme is defined in the simulations, ii) the samples material is defined in the simulations, but not the isotope decay scheme and iii) both the samples material and the isotope decay scheme are defined in the simulations.

isotope	samples thickness (mm)	$\gamma$ -ray (keV)	efficiency without including self-attenuation and coincidence-summing effects	efficiency including only the self-attenuation effect	efficiency including both self-attenuation and coincidence-summing effects
$^{155}\text{Dy}$	0.8	226.9	0.129	0.108	0.095
$^{155}\text{Dy}$	0.9	226.9	0.130	0.106	0.094

As can be seen in Table 4.3, the results reveal a reduction of the efficiency when the self-attenuation phenomenon is included in the simulations.

The inclusion of the decay scheme in the simulations seems to affect the 226.9 keV  $\gamma$ -ray. In particular, the efficiency for this  $\gamma$ -ray decreases which reveals that this transition is subjected to “summing-out” effects.

#### 4.1.2.2 Efficiency calculations for the reference foils

The reference foils were placed at 7.3 and 11.1 cm distance with respect to the window of the 40% rel. efficiency HPGe detector. In particular, the Au foils were placed at the distance of the 7.3 cm distance, while the Al foils were placed at both distances.

In the previous cases discussed above, a very short sample to detector distance was adopted for the activity measurements. This hindered the calculations of the efficiency directly through the efficiency calibration process, because of the coincidence-summing effect arising in the calibration spectra. At the distances of 7.3 and 11.1 cm the coincidence-summing effect does not have a strong impact on the recorded spectra of  $^{152}\text{Eu}$ .

Therefore, for this case the efficiency at the decay energies of the reference foils was calculated with two ways. Firstly, the efficiency was calculated through the linear fitting of the neperian logarithm of the experimental efficiency obtained for the decay energies of  $^{152}\text{Eu}$ , as it is presented in Figure 4.1. In the same graph the 95% confidence level bands are also depicted. The efficiency values were extracted from the fitting line, whereas its uncertainty was calculated as the semi-difference of the upper and lower efficiency limits obtained from the confidence bands.

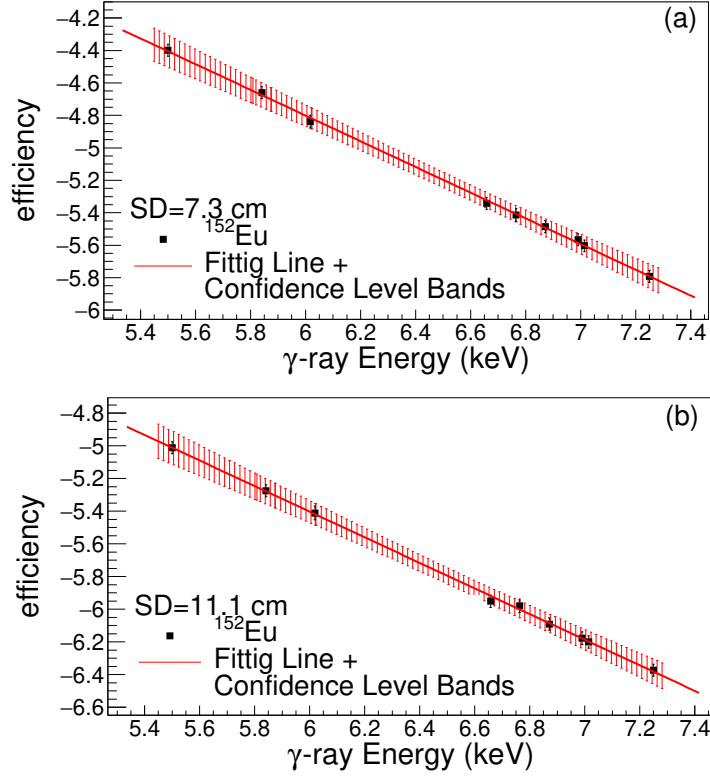


Figure 4.1: The neperian logarithm of the efficiency as a function of the neperian logarithm of the energies. In the same graph the fitting line is also presented, along with the 95% confidence level bands for (a) 7.3 cm and (b) 11.1 cm distance from the detector window.

The efficiency that was obtained from these graphs was corrected for self-attenuation and coincidence-summing effects. The corresponding correction factors were obtained from the GEANT4 as following:

1) The self-attenuation correction factor,  $CF_{SA}$ , was calculated as the ratio of the efficiency when the foils material was defined in the simulations to the efficiency when massless foils were considered.

2) The coincidence-summing effect correction factor,  $CF_{CS}$ , was determined as ratio of the efficiency when the decay scheme of the isotopes was taken into account to the efficiency when the  $\gamma$ -rays were emitted “mono-energetically”.

The results are summarized in Table 4.4.

The GEANT4 code of the 40% rel. efficiency HPGe detector was also used for the direct efficiency calculations including the self-attenuation and the coincidence-summing effects. The results are given in Table 4.5.

The uncertainty of the efficiencies calculated through the GEANT4 code is 3%. This value was obtained from the deviation between the experimental and the simulation efficiency and counting rate data corresponding to the decay energies of  $^{152}\text{Eu}$ .

Similar to Table 4.2, Tables 4.4 and 4.5 show that the self-attenuation becomes

higher for the thickest foils and for the lowest energies. The impact of the inclusion of the decay scheme in the simulations was less important in comparison with the results of Table 4.2, due to the smaller Ge crystal dimensions and the larger sample to detector distance.

The results of the efficiency for the decay energies of the reference foils, as presented in both Tables 4.4 and 4.5, agree with each other within the uncertainties.

Table 4.4: The efficiency of the 40% rel. efficiency HPGe detector for the decay energies of reference foils product nuclei, as resulting from linear fitting of the neperian logarithm of the efficiency. The corrected efficiency taking into account the self-attenuation and the coincidence-summing effect is also presented.

isotope	foil thickness (mm)	$\gamma$ -ray (keV)	efficiency	efficiency uncertainty	$CF_{SA}$	$CF_{CS}$	corrected efficiency
SD= 7.3 cm							
$^{196}\text{Au}$	0.3	333.0	0.0096	0.0004	0.92224	0.98034	0.0087
		355.7	0.0091	0.0003	0.92763	0.97773	0.0082
	0.5	333.0	0.0096	0.0004	0.85753	0.96646	0.0079
		355.7	0.0091	0.0003	0.86943	0.98644	0.0078
$^{24}\text{Na}$	0.55	1368.6	0.0031	0.0001	0.99190	0.98690	0.0031
SD= 11.1 cm							
$^{24}\text{Na}$	0.55	1368.6	0.0017	0.00007	0.9900	1.0042	0.0017

Table 4.5: The efficiency of the 40% rel. efficiency HPGe detector for the decay energies of the reference foils product-nuclei, as resulting from GEANT4, for the cases where: i) neither the foils material nor the decay schemes is defined in the simulations, ii) the foils material is defined in the simulations, but not the decay schemes and iii) both the foils material and the decay schemes are defined in the simulations.

product-nuclei	samples thickness (mm)	$\gamma$ -ray (keV)	efficiency without including self-attenuation and coincidence-summing effects	efficiency including only the self-attenuation effect	efficiency including both self-attenuation and coincidence-summing effects
SD= 7.3 cm					
$^{196}\text{Au}$	0.3	333.0	0.0100	0.0092	0.0089
		355.7	0.0095	0.0088	0.0087
	0.5	333.0	0.0100	0.0085	0.0085
		355.7	0.0094	0.0082	0.0081
$^{24}\text{Na}$	0.55	1368.6	0.0032	0.0032	0.0031
SD= 11.1 cm					
$^{24}\text{Na}$	0.55	1368.6	0.0017	0.0017	0.0017

## 4.2 The experimental spectra

The induced activity from the reactions under study was measured through the photopeaks of the  $\gamma$ -rays presented in Table 2.2. In Figures 4.2, 4.3 and 4.4 representative experimental spectra for each sample are presented along with the background spectra for the same data acquisition time.

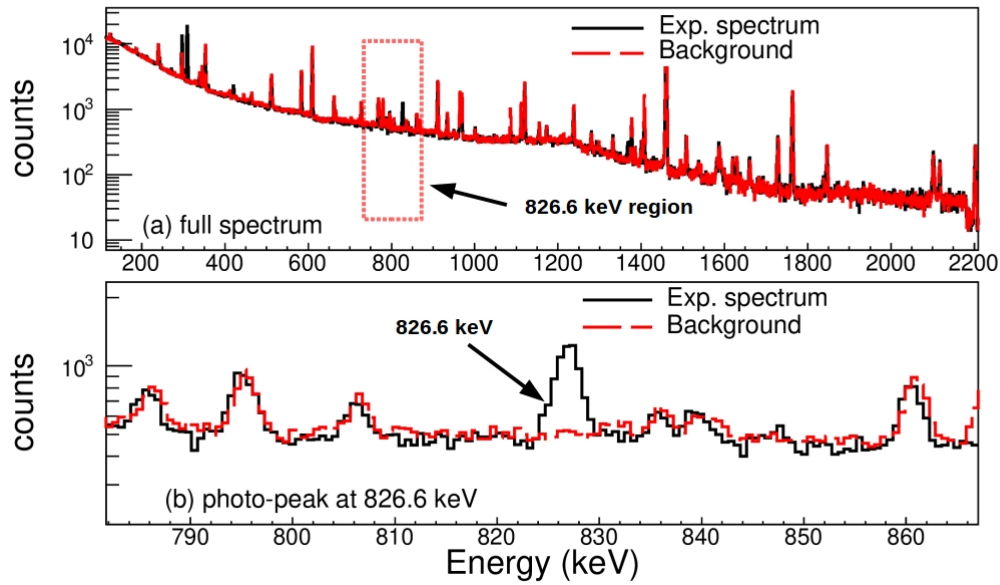


Figure 4.2: The Er sample spectrum for 11.0 MeV neutron beam energy and 10 h of measurement along with the corresponding background spectrum. In (a) the full spectrum is presented, while in (b) the region around 826.6 keV is illustrated.

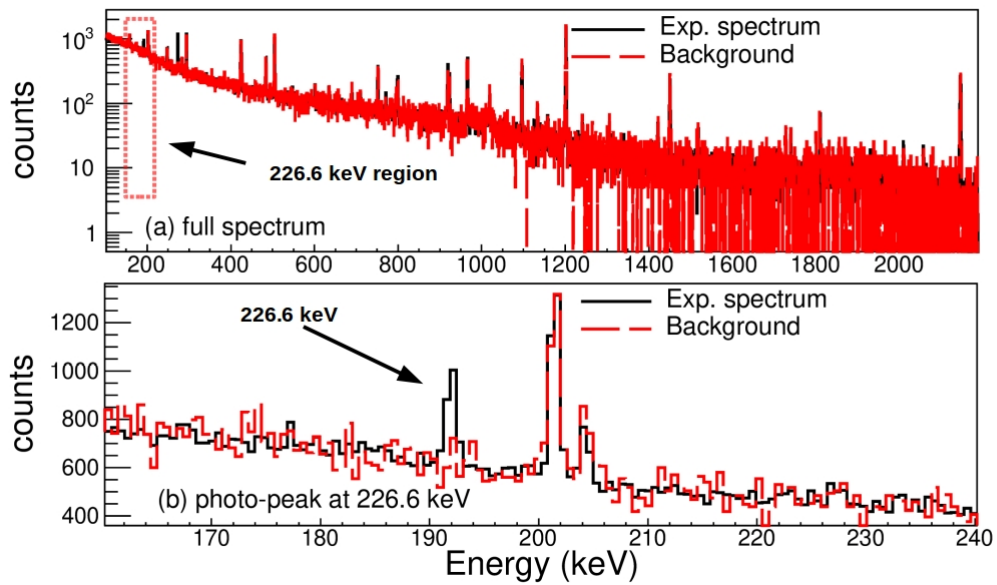


Figure 4.3: The Dy sample spectrum for 17.1 MeV neutron beam energy and 16 h of measurement along with the corresponding background spectrum. In (a) the full spectrum is presented, while in (b) the region around 226.6 keV is illustrated.

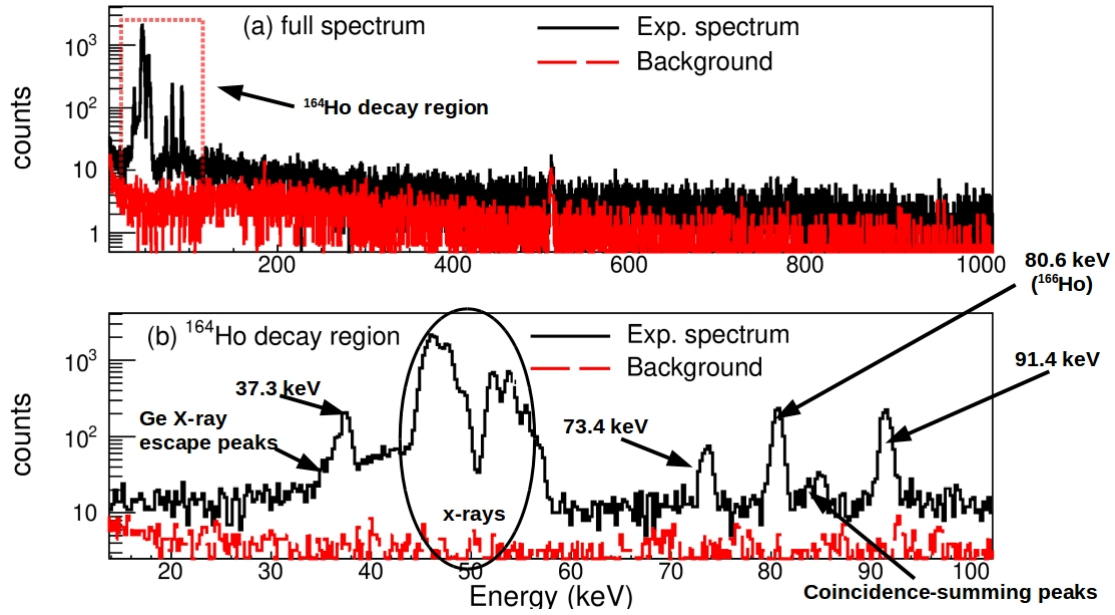


Figure 4.4: The Ho sample spectrum for 10.1 MeV neutron beam energy and 92 min of measurement. In (a) the full spectrum is presented, while in (b) the low energy part is illustrated.

As can be seen in Figure 4.4 the Ho spectra are complicated due to the fact that the energy of the emitted  $\gamma$ - rays is very close to the energy region of the X-rays. In addition, for the photopeak at 37.3 keV there is a strong overlapping with Ge X-ray escape peaks. An analytical description of the Ho spectra, the Ge X-ray escape peaks phenomenon, as well as the method developed for the determination of the counts integral of 37.3 keV photopeak is discussed in the next Sections. The developed method is also described in Ref. [79].

During the measurements the spectra were saved regularly: every 0.5-1 h for the Er samples, every 10 min for the Ho samples and every 0.5 h for the Dy samples. This was essential for the data analysis so as to follow the counting rate of the photopeaks of interest, as well as to optimize the analysis with respect to the statistical uncertainty variation over the data acquisition time. In particular, based on the decay law the “Net Area” of the photopeaks increases with decreasing rate in contrast to the background radiation that is recorded with constant rate. Therefore, after a certain time interval the increase of the background radiation leads to increase in the uncertainty of the photopeaks counting statistics. Accordingly, the adopted data acquisition time was always optimized so as to minimize the overall statistical uncertainty on the photopeaks counts.

### 4.3 The Ge X-ray escape peaks and the Ho samples spectra

The X-rays can transfer a part of their energy to the atomic electrons of the detector active volume and as a result, photoelectrons are produced. The fluorescence photons which are emitted during the de-excitation of the atoms can be reabsorbed by the detector. In this case, the full X-ray energy will be recorded. However, there is a possibility that the fluorescence photons will escape the detector active volume. The probability of this escape increases when the fluorescence photons are produced close to the detector active volume surface. When the fluorescence photons escape the detector, the X-rays are recorded at lower energy:

$$E_{ep} = E_{in} - E_b \quad (4.1)$$

The term  $E_{in}$  stands for the initial energy of the X-rays, whereas  $E_b$  stands for the energy of the fluorescence photons. The peaks which are recorded at energy  $E_{ep}$  are called X-ray escape peaks [80].

The X-ray photons mainly transfer their energy to the electrons of the K shells. Therefore, for a HPGe detector the corresponding escape peaks will be recorded at lower energies by 9.8 and 11.0 keV than the initial X-ray energy. These values are the Ge  $K_\alpha$  and  $K_\beta$  X-ray emission lines.

In Table 4.6 the X-rays that are emitted during the decay of  $^{164}\text{Ho}$  and  $^{166}\text{Ho}$  are summarized along with Ge X-ray escape peaks that are expected.

Table 4.6 indicates that Ge X-ray escape peaks are produced in the region between 35-47 keV. The Ge X-ray escape peaks at 35-39 keV coming from the incomplete absorption of the Ge  $K_\alpha$  X-rays contaminate the photopeak at 37.3 keV. The counts integral of this photopeak was determined via GEANT4 (v. 10.4) simulations which reproduced the experimental spectra.

### 4.4 The GEANT4 simulation of the Ho samples spectra

For the reproduction of the experimental spectra, three GEANT4 independent simulations were combined: one for the decay of  $^{166}\text{Ho}$  and one for each one of the decays of the two states of  $^{164}\text{Ho}$  (isomeric and ground). The three simulation spectra were superimposed so as to obtain the final simulation spectra.

The number of decays for the isomeric state was adjusted so that the 84.0 keV and 84.9 keV photopeaks are reproduced. These photopeaks originate from the coincidence summing of the 37.3 keV  $\gamma$ -ray with the X-rays at 46.7 and 47.5 keV (emitted by  $^{164}\text{Ho}^m$ ). The number of decays for the ground state was adjusted so that the photopeaks at 73.4 and 91.4 keV are reproduced after adding the simulation spectra of the isomeric and ground state decay. The reason is that the isomeric state

Table 4.6: The  $K_\alpha$  and  $K_\beta$  X-rays coming from the decay of the  $^{164}\text{Ho}^g$ ,  $^{164}\text{Ho}^m$  and  $^{166}\text{Ho}$  isotopes along with their absolute intensity per decay and the corresponding Ge X-ray escape peaks.

Isotope	Reaction channel	Decay mode	$T_{1/2}$	X-rays	Energy (keV)	Intensity (%)	Escape peaks energy (keV)
$^{164}\text{Ho}^m$	$^{165}\text{Ho}(n, 2n)$	100% IT	36.6 min	$K_{\alpha 2}$	46.7	$21.2 \pm 1.6$	36.9, 35.7
				$K_{\alpha 1}$	47.6	$37 \pm 3$	37.8, 36.6
				$K_{\beta 1}$	53.9	$7.6 \pm 0.6$	44.1, 42.9
				$K_{\beta 2}$	55.3	$2.55 \pm 0.20$	45.5, 44.3
				$K_{\beta 3}$	53.7	$3.9 \pm 0.3$	43.9, 42.7
$^{164}\text{Ho}^g$	$^{165}\text{Ho}(n, 2n)$	60% $\varepsilon$	28.8 min	$K_{\alpha 2}$	45.21	$14.4 \pm 1.4$	35.34, 34.23
				$K_{\alpha 1}$	46.0	$25 \pm 3$	36.2, 35.0
				$K_{\beta 1}$	52.1	$5.1 \pm 0.5$	42.3, 41.1
				$K_{\beta 2}$	53.5	$1.72 \pm 0.17$	43.7, 42.5
				$K_{\beta 3}$	51.9	$2.7 \pm 0.3$	42.1, 40.9
$^{164}\text{Ho}^g$	$^{165}\text{Ho}(n, 2n)$	40% $\beta^-$	28.8 min	$K_{\alpha 2}$	48.22	$0.823 \pm 0.018$	38.35, 37.24
				$K_{\alpha 1}$	49.1	$1.45 \pm 0.03$	39.3, 38.1
				$K_{\alpha 1}$	46.0	$25 \pm 3$	36.2, 35.0
				$K_{\beta 1}$	55.7	$0.298 \pm 0.006$	45.9, 44.7
				$K_{\beta 2}$	57.1	$0.1000 \pm 0.0021$	47.3, 46.1
				$K_{\beta 3}$	55.5	$0.154 \pm 0.003$	45.7, 44.5
$^{166}\text{Ho}^g$	$^{165}\text{Ho}(n, \gamma)$	100% $\beta^-$	26.824 h	$K_{\alpha 2}$	48.22	$2.96 \pm 0.10$	38.35, 37.24
				$K_{\alpha 1}$	49.13	$5.21 \pm 0.17$	39.26, 38.15
				$K_{\alpha 1}$	45.99	$25 \pm 3$	36.12, 35.01
				$K_{\beta 1}$	55.7	$1.07 \pm 0.03$	45.9, 44.7
				$K_{\beta 2}$	57.1	$0.360 \pm 0.012$	47.3, 46.1
				$K_{\beta 3}$	55.5	$0.555 \pm 0.017$	45.7, 44.5

decays entirely to the ground state and therefore, the  $\gamma$ -rays at 73.4 and 91.4 keV are also emitted when only the decay of the isomeric state is considered. Finally, the number of decays for the  $^{166}\text{Ho}$  isotope was fixed so as to reproduce the  $\gamma$ -ray photopeak at 80.6 keV.

In the case where a Broad Energy detector is used, the coincidence-summing effect between  $\gamma$ - and the X-rays coming from the electron capture (EC) or internal conversion (IT), as well as the coincidence summing-effect between only X-rays, can generally be recorded in the spectrum [81] depending on the decay scheme of the isotopes and the source to detector distance. This phenomenon was, indeed, observed in the Ho spectra, where the coincidence-summing photopeaks at 84.0 and 84.9 keV were recorded. As aforementioned, these photopeaks originate from the coincidence summing of the 37.3 keV  $\gamma$ -ray with the X-rays at 46.7 and 47.5 keV, respectively, which are emitted due to the internal conversion process in  $^{164}\text{Ho}^m$ .

A significant element of the GEANT4 simulations was the inclusion of the Ge X-ray escape peaks phenomenon, which has been discussed in detail in Section 4.3. To simulate Ge X-ray escape peaks the photons “tracking cut”, that is the limit below which secondary photons and particles are not produced, should be reduced to 1 nm. More information on the GEANT4 “tracking cut” can be found in Appendix K

Furthermore, the self attenuation was considered in the GEANT4 simulations through the definition of the actual Ho samples material. The inclusion of the self-attenuation phenomenon was significant for the reproduction of the spectra, because the Ho X-rays are also produced due to the absorption of  $\gamma$  photons from the samples. For instance, in Figure 4.5 a GEANT4 qualitative simulation of the energy deposition of the 91.4 keV  $\gamma$ -ray coming from the  $^{164}\text{Ho}^g$  decay is presented for the cases of (a) a “void” sample and (b) an Ho extended sample with 1 mm thickness. As it is shown in this Figure, the absorption of the  $\gamma$ -rays from the Ho sample leads to the production of the characteristic Ho X-rays, which are accompanied with corresponding Ge escape peaks at  $\approx 10$  keV lower energies.

For the representation of the energy deposition resulting from the simulations, a response function based on a Gaussian distribution was implemented. The FWHM of the distribution was given by the Eq. 4.2:

$$FWHM = 2.355\sqrt{F \cdot E_{dep} \cdot e} \quad (4.2)$$

where  $F \cdot E_{dep} \cdot e$  is the standard deviation of the distribution and expresses the number of electron-hole pairs which are created for a particular value of deposited energy  $E_{dep}$ . The term  $e$  is the energy needed for the creation of one electron-hole pair and  $F$  is the Fano factor as it is defined in Ref. [82]. The values suggested in the literature for these factors were adjusted in order to reproduce the experimental spectra.



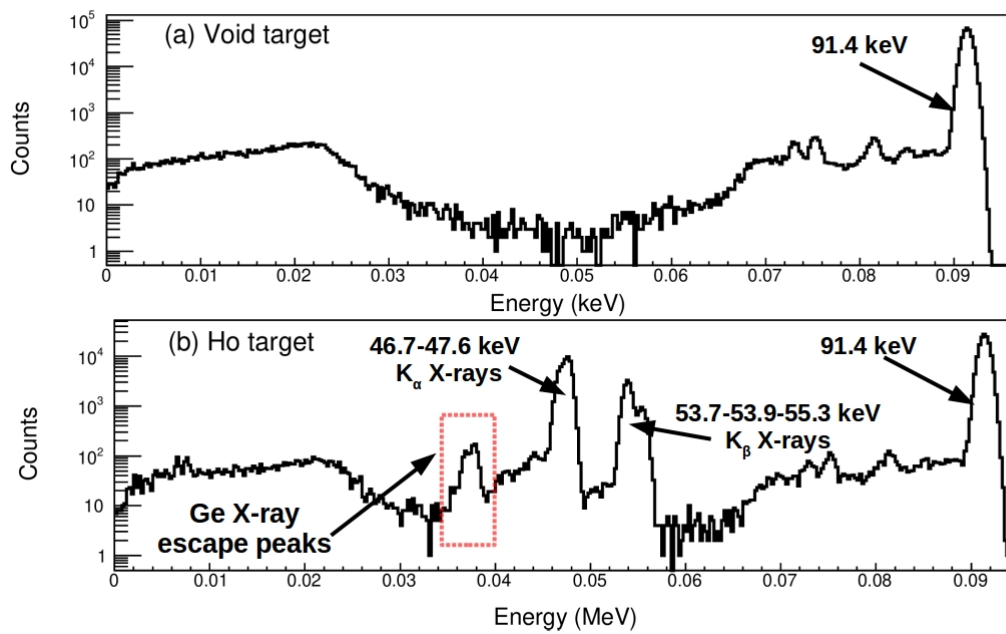


Figure 4.5: A GEANT4 qualitative simulation of the energy deposition for the  $\gamma$ -ray at 91.4 keV when considering (a) a “void” sample and (b) an Ho sample with 1 mm thickness.

In Figure 4.6 the experimental spectrum recorded after the irradiation with 10.1 MeV neutrons and after 92 min of measurement is presented in comparison with the GEANT4 simulation. The background spectrum of equal data acquisition time has been subtracted from the experimental spectrum. As can be seen, the simulation and the experimental spectrum are in agreement.

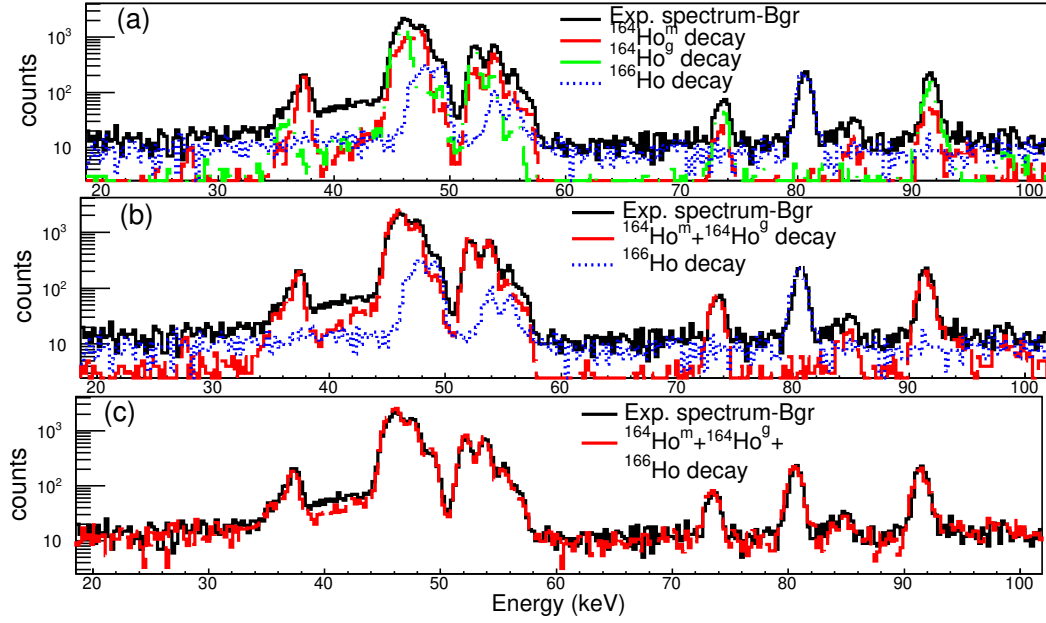


Figure 4.6: The reproduction of the experimental spectrum recorded after the irradiation of the Ho sample with 10.1 MeV neutron beam energy and after 92 min of measurement time considering (a) the  $^{164}\text{Ho}^m$  decay, (b) the  $^{164}\text{Ho}^m$  along with the  $^{164}\text{Ho}^g$  decay and (c) the  $^{164}\text{Ho}^m$  along with the  $^{164}\text{Ho}^g$  and  $^{166}\text{Ho}$  decays. A background spectrum of equal measurement time has been subtracted from the experimental one.

## 4.5 The study of the 37.3 keV $\gamma$ -ray photopeak

The cross section of the  $^{165}\text{Ho}(n,2n)^{164}\text{Ho}^m$  reaction was obtained through the determination of the “Net Area” of the photopeak originating from the 37.3 keV transition. However, the counts of this transition could not be deduced directly due to its contamination from the Ge X-ray escape peaks between 34.5-39 keV as described in Section 4.3.

For this reason, the GEANT4 simulation spectra was utilized so as to calculate the ratio of the peak counts originating from the 37.3 keV  $\gamma$ -ray (below denoted at A) to the counts of the peak areal integral in the region 34.5-39 keV (below denoted as B). Based on this, the accurate number of counts of the 37.3 keV  $\gamma$ -ray transition in the experimental spectra was determined by multiplying the experimentally deduced counts integral (after background subtraction) of the peak area of the region between 34.5-39 keV (below denoted as  $counts'$ ) with the ratio  $\frac{A}{B}$  (Eq. 4.3).

$$counts = counts' * \frac{A}{B} \quad (4.3)$$

The ratio  $\frac{A}{B}$  was calculated for each one of the spectra corresponding to each one of the seven irradiations at neutron beam energies: 10.1, 10.4, 10.7, 17.1, 18.1, 19.0

and 19.6 MeV. The results are summarized in Table 4.7.

Table 4.7: The ratio of the counts originating from the 37.3 keV decay line to the peak integral between 34.5-39 keV ( $\frac{A}{B}$ ) as resulted from the simulations with the GEANT4 toolkit.

Neutron energy (MeV)	$\frac{A}{B}$ (%)
10.1	58
10.4	58
10.7	58
17.1	62
18.1	62
19.0	65
19.6	66

In order to investigate the fluctuations of the ratio  $\frac{A}{B}$ , a sensitivity test was performed where the number of decays for the ground and the isomeric state was slightly changed. All tests resulted in the same value for the ratio  $\frac{A}{B}$  for each spectrum. Therefore, the uncertainty of the recorded counting rates was finally defined from the statistical uncertainty of the experimentally deduced peak area counts.

As mentioned in Section 4.4 in order to compare the experimental spectra with the simulations, the room background spectrum of equal measurement time with the corresponding experimental spectrum was subtracted. This could affect the uncertainty of the counting statistics of the experimental spectra. However, due to the short measurement time of the spectra (1.5-2 h), the detector shielding as well as the geometry of the Ge crystal the contribution from the background to the counting statistics was negligible. According to Ref. [83] the Ge crystal is transparent to high energy cosmogenic background radiation and to high energy  $\gamma$ -rays from naturally occurring radioisotopes such as  $^{40}\text{K}$  and  $^{208}\text{Tl}$ . The negligible contribution from natural background to the spectra is also depicted in Figure 4.4.

# Chapter 5

## Experimental Results

In Table 5.1 the experimental results of the  $^{162}\text{Er}(n,2n)^{161}\text{Er}$ ,  $^{156}\text{Dy}(n,2n)^{155}\text{Dy}$ ,  $^{165}\text{Ho}(n,2n)^{164}\text{Ho}^m$  and  $^{165}\text{Ho}(n,2n)^{164}\text{Ho}^g$  reactions cross section are presented.

Table 5.1: The experimental cross section results for the (a)  $^{162}\text{Er}(n,2n)^{161}\text{Er}$ , (b)  $^{156}\text{Dy}(n,2n)^{155}\text{Dy}$ , (c)  $^{165}\text{Ho}(n,2n)^{164}\text{Ho}^m$  and (d)  $^{165}\text{Ho}(n,2n)^{164}\text{Ho}^g$  reactions.

(a) $^{162}\text{Er}(n,2n)^{161}\text{Er}$ [69–71]		(b) $^{156}\text{Dy}(n,2n)^{155}\text{Dy}$	
$E_n$ (MeV)	$\sigma$ (barns)	$E_n$ (MeV)	$\sigma$ (barns)
$10.7 \pm 0.1$	$0.44 \pm 0.08$		
$11.0 \pm 0.1$	$0.57 \pm 0.06$		
$11.3 \pm 0.1$	$0.72 \pm 0.11$		
$17.1 \pm 0.3$	$1.97 \pm 0.22$	$17.1 \pm 0.3$	$1.67 \pm 0.21$
$18.1 \pm 0.2$	$1.84 \pm 0.23$	$18.1 \pm 0.2$	$1.82 \pm 0.31$
$19.0 \pm 0.2$	$1.92 \pm 0.23$	$19.0 \pm 0.2$	$1.60 \pm 0.30$
(c) $^{165}\text{Ho}(n,2n)^{164}\text{Ho}^m$ [49]		(d) $^{165}\text{Ho}(n,2n)^{164}\text{Ho}^g$ [49]	
$E_n$ (MeV)	$\sigma$ (barns)	$E_n$ (MeV)	$\sigma$ (barns)
$10.1 \pm 0.1$	$0.32 \pm 0.04$	$10.1 \pm 0.1$	$0.43 \pm 0.10$
$10.4 \pm 0.1$	$0.33 \pm 0.04$	$10.4 \pm 0.1$	$0.53 \pm 0.11$
$10.7 \pm 0.1$	$0.39 \pm 0.05$	$10.7 \pm 0.1$	$0.66 \pm 0.11$
$17.1 \pm 0.3$	$0.64 \pm 0.07$	$17.1 \pm 0.3$	$0.64 \pm 0.15$
$18.1 \pm 0.2$	$0.59 \pm 0.07$	$18.1 \pm 0.2$	$0.58 \pm 0.14$
$19.0 \pm 0.2$	$0.49 \pm 0.06$	$19.0 \pm 0.2$	$0.49 \pm 0.13$
$19.6 \pm 0.2$	$0.39 \pm 0.05$	$19.6 \pm 0.2$	$0.32 \pm 0.09$

At this point it has to be reminded that the cross section of the  $^{162}\text{Er}(n,2n)^{161}\text{Er}$ ,  $^{156}\text{Dy}(n,2n)^{155}\text{Dy}$  and  $^{165}\text{Ho}(n,2n)^{164}\text{Ho}^m$  reactions was determined through Eq. 2.2, which is the standard equation of Activation Technique. For the  $^{165}\text{Ho}(n,2n)^{164}\text{Ho}^g$  reaction Eq. 2.4 was adopted in order to take into account the population of the ground state from the isomeric state during the irradiation time, the “waiting time” and the activity measurement time.

Moreover, it has to be clarified that for the  $^{165}\text{Ho}(n,2n)^{164}\text{Ho}^g$  reaction the cross section refers to the weighted average  $\langle \sigma \rangle$  of each of the cross sections determined

through the 73.4 and 91.4 keV  $\gamma$ -rays, according to Eq. 5.1.

$$\langle \sigma \rangle = \frac{(V_2 - V_{12})\sigma_1 + (V_1 - V_{12})\sigma_2}{V_1 + V_2 - 2V_{12}} \quad (5.1)$$

where  $\sigma_1$  and  $\sigma_2$  are the cross sections determined from each  $\gamma$ -ray. The  $V_1$  and  $V_2$  terms stand for the variances of the cross sections and they are equal to the square of the uncertainties. Finally, the  $V_{12}$  term is the covariance element between  $\sigma_1$  and  $\sigma_2$ , which takes into account the existing correlations. The correlations originate from the fact that the same neutron flux, the same Ho sample and the same photopeak at 37.3 keV (for the population from the isomeric state) were used for the cross section calculations. Based on this the covariance element was calculated as following:

$$\begin{aligned} V_{12} = & \frac{\partial\sigma_1}{\partial\Phi_1} Cov(\Phi_1, \Phi_2) \frac{\partial\sigma_2}{\partial\Phi_2} + \frac{\partial\sigma_1}{\partial N_{T1}} Cov(N_{T1}, N_{T2}) \frac{\partial\sigma_2}{\partial N_{T2}} + \\ & \frac{\partial\sigma_1}{\partial Counts_1} Cov(Counts_1, Counts_2) \frac{\partial\sigma_2}{\partial Counts_2} + \\ & \frac{\partial\sigma_1}{\partial \varepsilon_{m1}} Cov(\varepsilon_{m1}, \varepsilon_{m2}) \frac{\partial\sigma_2}{\partial \varepsilon_{m2}} + \frac{\partial\sigma_1}{\partial I_{m1}} Cov(I_{m1}, I_{m2}) \frac{\partial\sigma_2}{\partial I_{m2}} \quad (5.2) \end{aligned}$$

The cross sections uncertainty was calculated by summing-up quadratically all the individual uncertainties. However, there is again an exception for the  $^{165}\text{Ho}(n,2n)^{164}\text{Ho}^g$  reaction. For this reaction the final cross sections uncertainty was obtained through Eq. 5.3:

$$var(\sigma) = \frac{V_1 V_2 - (V_{12})^2}{V_1 + V_2 - 2V_{12}} \quad (5.3)$$

In Tables 5.2, 5.3 and 5.4 the compilation of the uncertainties for the measured reactions and the reference reactions are presented.

Table 5.2: Compilation of uncertainties (in %) for the  $^{162}\text{Er}(n,2n)^{161}\text{Er}$  reaction [69–71].

$E_n$ (MeV) reference reaction	10.7 $^{27}\text{Al}(n,\alpha)^{24}\text{Na}$ (1368.6 keV $\gamma$ -ray)	11.0 $^{197}\text{Au}(n,2n)^{196}\text{Au}$ (333.0 keV $\gamma$ -ray)	11.3 $^{93}\text{Nb}(n,2n)^{92m}\text{Nb}$ (934.4 keV $\gamma$ -ray)
reference reaction cross section	1.0	2.7	1.2
neutron flux	7.0	7.0	7.0
$^{161}\text{Er}$ peak counting statistics	16.0	2.9	10.5
2x100% HPGe detectors efficiency	3.8	3.8	3.8
$^{161}\text{Er}$ $\gamma$ -ray intensity per decay	5.8	5.8	5.8
erbium target self-attenuation correction factor	0.5	0.5	0.5
$^{162}\text{Er}$ natural abundance	3.6	3.6	3.6
reference foils peak counting statistics	2.6, 3.4	2.1, 1.1	14.0, 11.8
16% HPGe detectors efficiency	2.0	1.6	1.3
reference foils $\gamma$ -ray intensity per decay	0.0015	4.1	—
reference foils self-attenuation correction factor	0.50	0.18	0.4
statistical uncertainty of cross section	16.0	2.9	7.5
systematic uncertainty of cross section	10.5	10.5	10.5
total uncertainty of cross section	18.2	10.7	14.1
$E_n$ (MeV) reference reaction	17.1 $^{197}\text{Au}(n,2n)^{196}\text{Au}$ (333.0 keV $\gamma$ -ray)	18.1 $^{197}\text{Au}(n,2n)^{196}\text{Au}$ (333.0 keV $\gamma$ -ray)	19.0 $^{93}\text{Nb}(n,2n)^{92m}\text{Nb}$ (1368.6 keV $\gamma$ -ray)
reference reaction cross section	2.1	1.9	1.2
neutron flux	7.0	7.0	7.0
$^{161}\text{Er}$ peak counting statistics (front-back)	5.5	7.5	7.0
2x100% HPGe detectors efficiency	3.8	3.8	3.8
$^{161}\text{Er}$ $\gamma$ -ray intensity per decay	5.8	5.8	5.8
erbium target self-attenuation correction factor	0.5	0.5	0.5
$^{162}\text{Er}$ natural abundance	3.6	3.6	3.6
reference foils peak counting statistics (front-back)	4.6, 3.0	5.4, 6.4	7.1, 7.6
16% HPGe detectors efficiency	1.9	1.9	1.6
reference foils $\gamma$ -ray intensity per decay	4.1	4.1	—
reference foils self-attenuation correction factor	0.18, 0.13	0.13	0.4
statistical uncertainty of cross section	5.5	7.5	7.0
systematic uncertainty of cross section	9.9	9.9	9.9
total uncertainty of cross section	11.2	12.5	12.0

Table 5.3: Compilation of uncertainties (in %) for the  $^{156}\text{Dy}(n,2n)^{155}\text{Dy}$  reaction.

$E_n$ (MeV) reference reaction	17.1 $^{24}\text{Al}(n,\alpha)^{24}\text{Na}$	18.1 $^{1368.6}$ keV $\gamma$ -ray)	19.0
reference reaction cross section	0.83	0.98	1.19
neutron flux	7.0	7.0	7.0
$^{155}\text{Dy}$ peak counting statistics	8.2	13.7	16.4
80% HPGe detector efficiency	3.0	3.0	3.0
$^{155}\text{Dy}$ $\gamma$ -ray intensity per decay	2.3	2.3	2.3
$^{156}\text{Dy}$ natural abundance	5.4	5.4	5.4
reference foils peak counting statistics (front-back)	3.1, 3.1	4.6, 5.1	4.1, 5.1
40% HPGe detectors efficiency	3.0	3.0	3.0
reference foils $\gamma$ -ray (1368.6 keV) intensity per decay	0.0015	0.0015	0.0015
statistical uncertainty of cross section	8.2	13.7	16.4
systematic uncertainty of cross section	9.5	9.6	9.1
total uncertainty of cross section	12.6	16.7	18.8

Table 5.4: Compilation of uncertainties (in %) for the  $^{165}\text{Ho}(n,2n)^{164}\text{Ho}^m$  and  $^{165}\text{Ho}(n,2n)^{164}\text{Ho}^g$  reactions [49].

$E_n$ (MeV) reference reaction	10.1	10.4	10.7	
	$^{197}\text{Au}(n,2n)^{196}\text{Au}$ (355.7 keV $\gamma$ -ray)			
reference reaction cross section	3.0	3.0	2.8	
neutron flux	7.0	7.0	7.0	
37.3 keV peak counting statistics	7.1	7.6	6.3	
73.4 keV peak counting statistics	6.8	7.0	5.3	
91.4 keV peak counting statistics	3.7	3.7	3.0	
BE5030 HPGe detector efficiency	5.0	5.0	5.0	
37.3 keV $\gamma$ -ray intensity per decay	6.3	6.3	6.3	
reference foils peak counting statistics (front-back)	2.5-2.7	1.2-1.6	1.6-2.2	
80% HPGe detector efficiency	3.0	3.0	3.0	
reference foils $\gamma$ -ray intensity per decay	-	-	-	
statistical uncertainty of cross section for isomeric state	7.1	7.6	6.3	
systematic uncertainty of cross section for isomeric state	10.7	10.7	10.7	
total uncertainty of cross section for isomeric state	13	13	12	
statistical uncertainty of cross section for ground state	15.2	12.7	9.5	
systematic uncertainty of cross section for ground state	17.7	14.7	13.9	
total uncertainty of cross section for ground state	24	20	17	
$E_n$ (MeV) reference reaction	17.1	18.1	19.0	19.6
	$^{24}\text{Al}(n,\alpha)^{24}\text{Na}$ (1368.6 keV $\gamma$ -ray)			
reference reaction cross section	0.83	0.98	1.19	1.31
neutron flux	7.0	7.0	7.0	7.0
37.3 keV peak counting statistics	2.9	4.2	5.2	5.4
73.4 keV peak counting statistics	2.9	4.5	5.8	6.2
91.4 keV peak counting statistics	1.8	2.9	3.7	3.7
BE5030 HPGe detector efficiency	5.0	5.0	5.0	5.0
37.3 keV $\gamma$ -ray intensity per decay	6.3	6.3	6.3	6.3
reference foils peak counting statistics (front-back)	0.5-1.5	2.5-2.8	3.0-4.0	3.4-3.9
80% HPGe detector efficiency	3.0	3.0	3.0	3.0
reference foils $\gamma$ -ray intensity per decay	0.0015	0.0015	0.0015	0.0015
statistical uncertainty of cross section for isomeric state	2.9	4.0	5.2	5.4
systematic uncertainty of cross section for isomeric state	10.7	10.7	10.7	10.7
total uncertainty of cross section for isomeric state	11	11	12	12
statistical uncertainty of cross section for ground state	7.9	11.3	15.1	16.3
systematic uncertainty of cross section for ground state	21.5	21.2	22	22.3
total uncertainty of cross section for ground state	23	24	27	28

# Chapter 6

## Theoretical Calculations

### 6.1 Types of nuclear reactions

The nuclear reactions on a specific mass region can be classified into different types depending on the dominant reaction mechanism. The three main categories are the compound-nucleus reactions, the direct reactions and the pre-equilibrium reactions:

- Compound-nucleus reactions

In compound-nucleus reactions the projectile transfers its energy through successive collisions to target nucleons, which subsequently cause new successive collisions. This process is continued until the projectile shares its energy with the target-nucleus and thermodynamic equilibrium is reached. Under this scope, the projectile energy has been distributed statistically to the target-nucleus and therefore, the information for the reaction input channel has been lost. The incident particle and the target-nucleus create a complex system, the compound-nucleus, which is excited at an energy that equals to the sum of the projectile energy and its binding energy in the compound-nucleus. The complex system “lives” for a time scale of  $10^{-18} - 10^{-16}$  s before it decays. Due to the thermodynamic equilibrium, the compound-nucleus can decay to any channel, which is permissible with respect to the energy, spin and parity conservation laws. In other words, the decay of the compound-nucleus does not depend on its formation. This statement is known as Bohr’s independence hypothesis, which for the  $A + \alpha \rightarrow C^* \rightarrow A' + \alpha'$  reaction is summarized to the following mathematical formula:

$$\sigma_{\alpha\alpha'} = \sigma_C * \frac{\Gamma_{\alpha'}}{\Gamma_{\alpha''}} \quad (6.1)$$

where  $\sigma_C$  expresses the cross section for the formation of the compound-nucleus,  $\Gamma_{\alpha'}$  corresponds to the decay width for the emission of the  $\alpha'$  particle and  $\Gamma_{\alpha''}$  is the decay width for all possible decay channels. The  $\frac{\Gamma_{\alpha'}}{\Gamma_{\alpha''}}$  ratio expresses the probability that the compound-nucleus will decay through the emission of the  $\alpha'$  particle against all the other possible output channels.



- Direct reactions

The duration of direct reactions is much smaller ( $10^{-22}$  s) than the one of compound-nucleus reactions. The projectile interacts mainly with the peripheral nucleons or with a few internal nucleons of the target-nucleus to which it transfers a part of its energy. Therefore, the interaction proceeds without the formation of an intermediate system. Examples of direct reactions are the scattering, the transfer reactions, the break-up reactions, the knock-out reactions etc [48].

The direct reactions are favored against the compound-nucleus ones as the projectile energy increases: for higher energies the de Broglie wavelength decreases and it is more possible for the projectile to interact with only a few nucleons of the target-nucleus rather than the nucleus in its entirety.

- Pre-equilibrium reactions

The borders between the direct and the compound-nucleus reactions are not very specific. At intermediate energies, the pre-equilibrium mechanism arises. In this type of reactions the projectile enters the target-nucleus and gradually loses its energy through successive collisions. However, the complex system of the projectile and the target-nucleus that is formed decays before thermodynamic equilibrium is reached and therefore, only some “memory” of the input channel is conserved.

The three mechanisms (compound-nucleus mechanism, direct reactions mechanism, pre-equilibrium mechanism) can contribute all to a particular nuclear reaction to a different extent depending on the projectile energy.

In this point it has to be clarified that the residual nucleus which is produced after the compound-nucleus reaction (where the pre-equilibrium mechanism may also contribute) can further decay through particle emission. This process is called multiple emission and proceeds either through the multiple compound emission or through the multiple pre-equilibrium emission.

## 6.2 The TALYS code

TALYS is a nuclear reactions simulation code optimized for the energy range 1 keV-200 MeV [2]. As projectile it can be defined neutrons, protons, deuterons, tritons, helions, alpha-particles or  $\gamma$ -rays, whereas it calculates the cross section of reactions which involve any of them or any combination of them as ejectiles. Fission cross section can also be calculated.

The function of the code can be explained on the basis of the FIG. 6.1 taken from Ref. [2].

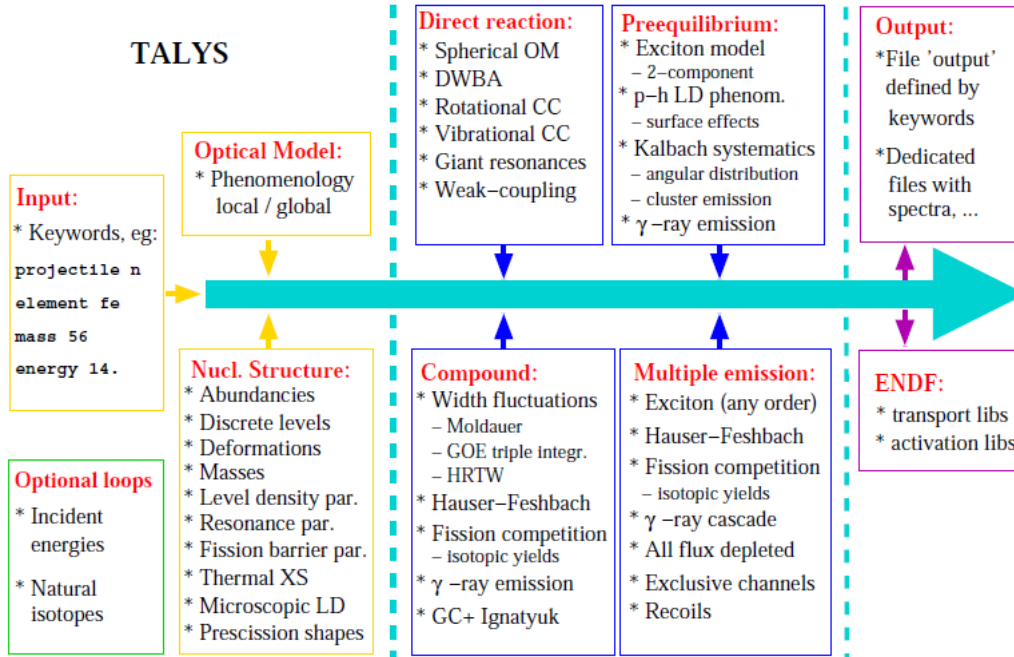


Figure 6.1: A simplified representation of the function and the incorporated models of the TALYS code taken from Ref. [2].

The necessary parameters that must be specified in the code are the projectile, the target-nucleus and the projectile energy, but TALYS also disposes and other keywords that can be defined in the input file. These keywords are mainly related to the replacement of the default models and changes in their parametrization. Through the input file the user can also define additional information with respect to the input channel, as well as the kind of the provided information in the output files. TALYS calculates the cross section of a nuclear reaction taking into account all the possible mechanisms (compound-nucleus reactions, pre-equilibrium reactions, direct reactions, multiple emission) and the competition among the different reaction channels.

In case of (n,2n) reactions for medium-to-heavy mass nuclei and for the energies considered in the present work the dominant reaction mechanism is the compound-nucleus mechanism. In TALYS the compound-nucleus calculations are performed via the Hauser-Feshbach theory [84].

In the next Sections the Hauser-Feshbach theory and the TALYS models upon which the theoretical calculations are based will be discussed along with the theoretical framework.

### 6.2.1 Hauser-Feshbach theory

The Hauser-Feshbach theory is a quantum-mechanical formalism of the cross section calculations of compound-nucleus reactions, which obeys in the conservation laws of energy, angular momentum and parity. Under this scope, the cross section of the reaction  $A + a \rightarrow C^* \rightarrow a' + A'$  is given by Eq. 6.2:

$$\begin{aligned}
\sigma_{\alpha\alpha'} = & D^{comp} \frac{\pi}{k^2} \sum_{J=\text{mod}(I+s,1)}^{\ell_{max}+I+s} \sum_{\Pi=-1}^1 \frac{2J+1}{(2I+1)(2s+1)} \\
& \times \sum_{j=|J-I|}^{J+I} \sum_{\ell=|j-s|}^{j+s} \sum_{j'=|J-I|}^{J+I'} \sum_{\ell'=|j'-s'|}^{j'+s'} \\
& \times \delta_{\pi}(a) \delta_{\pi}(a') \frac{T_{a\ell j}^J(E_a) \langle T_{a'\ell' j'}^J(E_{a'}) \rangle}{\sum_{a'', \ell'', j''} \delta_{\pi}(a'') \langle T_{a''\ell'' j''}^J(E_{a''}) \rangle} W_{a\ell j a' \ell' j'}^J
\end{aligned} \tag{6.2}$$

The symbols used in the above equation have the following meanings:

$E_a$  is the energy of the projectile

$s$  is the spin of the projectile

$\pi_0$  is the parity of the projectile

$\ell$  is the orbital angular momentum of the projectile

$j$  is the total angular momentum of the projectile

$\delta_{\pi}(a)=1$ , when  $(-1)^{\ell} \pi_0 \Pi_0 = \Pi$ . In any other case  $\delta_{\pi}(a)=0$

$a$  is used to denote the initial system of the projectile and target-nucleus:  $a=(a,s,E_a,E_x^0,I,\Pi_0)$ , where  $a$  is the projectile type and  $E_x^0$  is the target-nucleus excitation energy (usually zero)

$\ell_{max}$  is the maximum  $l$ -value for the projectile

$S_{\alpha}$  is the separation energy of the projectile

$E'_a$  is the energy of the ejectile

$s'$  is the spin of the ejectile

$\pi_f$  is the parity of the ejectile

$\ell'$  is the orbital angular momentum of the ejectile

$j'$  is the total angular momentum of the ejectile

$\delta_{\pi}(a')=1$ , when  $(-1)^{\ell'} \pi_f \Pi_f = \Pi$ . In any other case  $\delta_{\pi}(a')=0$

$a'$  is used to denote the final system of the ejectile and residual-nucleus:  $a=(a',s',E'_a,E_x,I',\Pi_f)$ , where  $a'$  is the ejectile type and  $E_x$  is the residual-nucleus excitation energy

$I$  is the spin of the target-nucleus

$\Pi_0$  is the parity of the target-nucleus

$I'$  is the spin of the residual-nucleus

$\Pi_f$  is the parity of the residual-nucleus

$\Pi$  is the parity of the compound-nucleus

$J$  is the total angular momentum of the compound-nucleus

$k$  is wave number of the relative motion of the input channel

$T$  is the transmission coefficient

$D^{comp}$  is the depletion factor to account for direct and pre-equilibrium effects.

$W$  is the width fluctuation correction (WFC) factor, which takes into account the correlations between the input and output channel: this factor causes the enhancement of the elastic channel at low incident energies, whereas it is negligible for energies above some MeV. By default  $W=1$  in TALYS for incident energies above the projectile separation energy. In such cases that  $W=1$  the cross section equation follows the Bohr hypothesis:

$$\sigma_{aa'} = \sum_{J=\text{mod}(I+s,1)}^{\ell_{max}+I+s} \sum_{\Pi=-1}^1 \sigma_C \frac{\Gamma_{a'}(E_{tot}, J, \Pi \rightarrow E_x, I', \Pi_f)}{\Gamma^{tot}(E_{tot}, J, \Pi)} \quad (6.3)$$

where  $\sigma_C$  is the cross section for the formation of the compound-nucleus:

$$\sigma_C = D^{comp} \frac{\pi}{k^2} \frac{2J+1}{(2I+1)(2s+1)} \sum_{j=|J-I|}^{J+I} \sum_{\ell=|j-s|}^{j+s} T_{a\ell j}^J(E_a) \delta_\pi(a) \quad (6.4)$$

and  $\frac{\Gamma_{a'}(E_{tot}, J, \Pi \rightarrow E_x, I', \Pi_f)}{\Gamma^{tot}(E_{tot}, J, \Pi)}$  is the propability that the compound nucleus will decay through the emission of the  $\alpha'$  particle. The ratio is expressed in terms of the transmission coefficients:

$$\frac{\Gamma_{a'}(E_{tot}, J, \Pi \rightarrow E_x, I', \Pi_f)}{\Gamma^{tot}(E_{tot}, J, \Pi)} = \sum_{j'=|J-I'|}^{J+I'} \sum_{l'=|j'-s'|}^{j'+s'} \delta_{\pi}(a') \quad (6.5)$$

$$\frac{\langle T_{a' l' j'}^J(E_{a'}) \rangle}{\sum_{a'', l'', j''} \delta_{\pi}(a'') \langle T_{a'' l'' j''}^J(E_{a'') \rangle}$$

After the compound-nucleus decay the residual-nucleus may further decay, e.g. (n,2n) channel, through the multiple emission mechanism. TALYS takes into account the multiple compound emission for energies above the projectile separation energy. The multiple compound calculations are performed in the framework of the Hauser-Feschbach theory. For the isotopes studied in the present work the contribution of the multiple pre-equilibrium emission becomes important above 20 MeV. The default option of TALYS for the multiple pre-equilibrium emission is based on exciton model calculations.

## 6.2.2 Pre-equilibrium reactions

As the projectile energy increases the contribution of the pre-equilibrium mechanism into the compound-nucleus reactions increases.

A powerful and successful model of the pre-equilibrium reactions is the exciton model which is based on the semi-classical approach proposed by Griffin [85, 86] and is developed into the basis of the compound-nucleus reactions concept. The main idea behind this is that the excited nuclear state can be characterized in terms of the particles (p) that exist above the Fermi surface and the holes (h) that exist below the Fermi surface. More specifically, the term particles denotes the protons,  $p_{\pi}$ , (or the neutrons,  $p_{\nu}$ ) that have been excited above the Fermi surface. Accordingly, for each particle excitation a hole is created. The sum of particles and holes is denoted with the term exciton ( $n_{\pi} = p_{\pi} + h_{\pi}$  for protons and  $n_{\nu} = p_{\nu} + h_{\nu}$  for neutrons). Over time as the nucleons interact with each other, the number of excitons changes. In Figure 6.2 a simplified representation of the creation of the excitons after the projectile interaction with the target-nucleus and the time-variation of them is presented.

Within the exciton model the nuclear reactions are described through the time-dependent population of exciton states. When an excited particle has enough energy, it can escape the composite-nucleus. This energy must be higher than the separation energy for the neutron and higher than the separation energy plus the Coulomb barrier for the proton. The differential cross section for the pre-equilibrium emission of a particle k with emission energy  $E_k$  is given by Eq. 6.6:

$$\frac{d\sigma_k^{PE}}{dE_k} = \sigma^{CF} \sum_{p_{\pi}=p_{\pi}^0}^{p_{\pi}^{max}} \sum_{p_{\nu}=p_{\nu}^0}^{p_{\nu}^{max}} W_k(p_{\pi}, h_{\pi}, p_{\nu}, h_{\nu}, E_k) \tau(p_{\pi}, h_{\pi}, p_{\nu}, h_{\nu}) P(p_{\pi}, h_{\pi}, p_{\nu}, h_{\nu}) \quad (6.6)$$

where,

$\sigma^{CF}$  is the cross section for the formation of the composite nucleus

$W_k$  is the emission rate of particle k

$\tau$  is the mean half-life of the exciton state

$P$  represents the part of the pre-equilibrium population that has survived emission from the previous states and now passes through the  $(p_\pi, h_\pi, p_\nu, h_\nu)$  configurations, averaged over time.

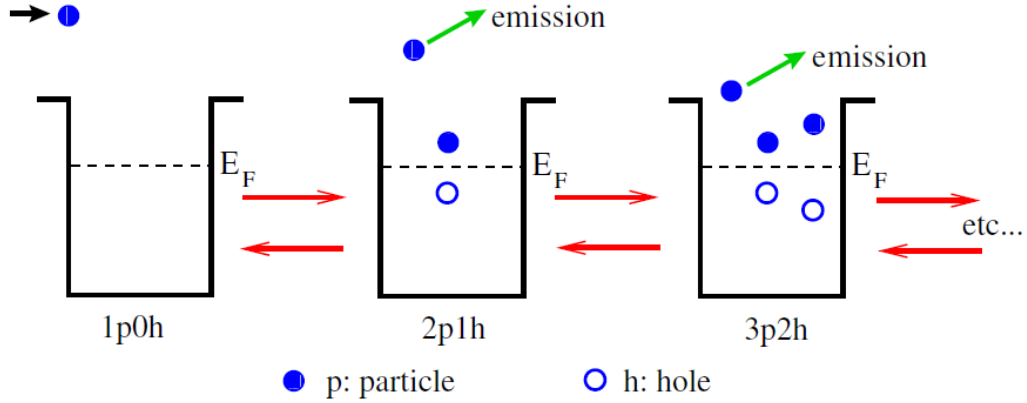


Figure 6.2: A simplified representation of the creation and time-evolution of the excitons after the projectile interaction with the target-nucleus. The Figure is taken from Ref. [2]

An important quantity that enters the calculations of factors  $P$  and  $\tau$  is the transition rate of a state with exciton number  $n$  to a state with exciton number  $n'$ .

This is calculated through:

i) the Fermi's golden rule of the time-dependent perturbation theory:

$$\lambda_{nn'} = \frac{2\pi}{\hbar} |M|^2 \omega_{n'}(E) \quad (6.7)$$

where  $\omega_{n'}(E)$  is the particle-hole state density and  $M$  is the average squared matrix elements of the interaction

ii) its relation with the average over the whole volume of the nucleus imaginary part of the optical model.

In this point it has to be clarified that in case that the emitted particles are other than protons and neutrons (deuterons, tritons, helium-3, and  $\alpha$ -particles), the contribution of stripping, pick-up, break-up and knock-out mechanisms has to be considered in the cross section calculations. TALYS achieves this via the adoption of the Kalbach approach presented in Ref. [87], where pre-equilibrium cross section is given as the sum of an exciton model, nucleon transfer and knock-out contributions. Moreover, photon pre-equilibrium emission is also considered in the framework of the exciton model by including in the calculations the photon emission rates.

In the TALYS code four models are available for the pre-equilibrium mechanism. The first three of them are based on the exciton model. The last is a phenomenological model suggested by Kalbach [88]. This model has been developed so as to describe the isotropic part (multi-step compound) and the forward peaked part (multi-step direct) of the angular distributions, respectively.

The pre-equilibrium reaction models of TALYS are the following:

- Exciton model: Analytical transition rates with energy-dependent matrix element (TALYS keyword “preeqmode 1”).
- Exciton model: Numerical transition rates with energy-dependent matrix element (TALYS keyword “preeqmode 2”, **default option**).
- Exciton model: Numerical transition rates with optical model for collision probability (TALYS keyword “preeqmode 3”).
- Multi-step direct/compound model (TALYS keyword “preeqmode 4”).

### 6.2.3 Optical model

The transmission coefficients play a crucial role in the Hauser-Feshbach theory, as they are used for the calculations both of the formation and the decay of the compound-nucleus. They are calculated via the optical model, which was introduced in order to describe the nuclear interactions using a mean nucleus potential. The potential has the form of Eq. 6.8. The real part  $V(r)$  is responsible for the shape elastic scattering, whereas the imaginary part  $W(r)$  is responsible for the absorbing effects, including all the interactions except for the shape elastic. The optical model is a valuable tool that can also be used for calculations of pre-equilibrium and direct reactions, whereas it can provide observables such as the elastic reaction cross section, elastic angular distribution and polarization, as well as the total cross section.

$$U(r) = V(r) + iW(r) \quad (6.8)$$

The real part of the phenomenological optical potential for neutron-nucleus (and proton-nucleus) interactions is equal to:

$$V(r) = -V_V(r, E) + V_{SO}(r, E).l.\sigma + V_C(r), \quad (6.9)$$

where,

$V_V(r, E) = V_V(E)f(r, R_V, \alpha_V)$  is the real volume potential

$V_{SO}(r, E) = V_{SO}(E)(\frac{\hbar}{m_\pi c})^2 \frac{1}{r} \frac{df(r, R_{SO}, \alpha_{SO})}{dr}$  is the real spin-orbit potential

$V_C(r)$  is the Coulomb potential and it is equal to:

$$V_C(r) = \frac{Zze^2}{2R_C} \left(3 - \frac{r^2}{R_C^2}\right), \text{ for } r \leq R_C$$

$$V_C(r) = \frac{Zze^2}{r}, \text{ for } r \geq R_C$$

Its imaginary part is equal to:

$$W(r) = -W_V(r, E) - W_D(r, E) + W_{SO}(r, E).l.\sigma \quad (6.10)$$

where,

$W_V(r, E) = W_V(E)f(r, R_V, \alpha_V)$  is the imaginary volume potential

$W_D(r, E) = -4\alpha_D W_D(E) \frac{df(r, R_D, \alpha_D)}{dr}$  is the imaginary surface potential

$W_{SO}(r, E) = W_{SO}(E) \left(\frac{\hbar}{m\pi c}\right)^2 \frac{1}{r} \frac{df(r, R_{SO}, \alpha_{SO})}{dr}$  is the imaginary spin-orbit potential

In the above equations the functions  $f(r, R_V, \alpha_V)$ ,  $f(r, R_{SO}, \alpha_{SO})$  and  $f(r, R_D, \alpha_D)$  are the Woods-Saxon shapes:

$$f(r, R_i, a_i) = (1 + e^{[(r-R_i)/a_i]})^{-1} \quad (6.11)$$

where the  $R_i$  terms stand for the nucleus radius and the  $\alpha_i$  terms are the diffusion parameters.

In TALYS the parametrization of Koning-Delaroche [89] is implemented for neutrons and protons. This is applicable for the mass region  $A=24-209$  and over the energy range  $E=1$  keV-200 MeV. TALYS also provides the ability of replacing the Koning-Delaroche optical potential with the semi-microscopic optical potential of Bauge [90, 91] (TALYS keyword “jlmomp y”). This is a spherical potential for nuclei in the mass region  $A=30-240$  and for the energies 10-200 MeV.

For the deuteron, triton and helion particles the default option of TALYS for the optical potential is based on a folding approach of the neutron and proton optical potential as proposed by Watanabe [92, 93]. For the  $\alpha$ -particles the default option of TALYS is the optical potential of V. Avrigeanu [94].

In TALYS all the optical model calculations, such as the transmission coefficients calculations and the calculations of direct reactions, are performed by the ECIS-06 code [95], which is incorporated as a subroutine.

## 6.2.4 $\gamma$ -ray Strength functions

The  $\gamma$ -ray emission is a universal channel that can accompany the emission of any other particle. Therefore, the  $\gamma$ -ray transmission coefficients enter the Hauser-Feschbach calculations so as to take into account the competition of the  $\gamma$  emission with other particles.

The transmission coefficient of a  $\gamma$ -ray with multipolarity  $\ell$  and energy  $E_\gamma$  is given by the Eq. 6.12:

$$T_{X\ell}(E_\gamma) = 2\pi f_{X\ell}(E_\gamma) E_\gamma^{2\ell+1} \quad (6.12)$$

In Eq. 6.12 X stands for the type of the electromagnetic radiation (X=E for electric radiation or X=M for magnetic radiation), whereas  $f_{X\ell}(E_\gamma)$  is the so-called  $\gamma$ -ray strength functions.



In TALYS the  $\gamma$ -ray strength functions are calculated according to the Brink-Axel Lorentzian model [96, 97]. For the  $E_1$  multipolarity which is the dominant radiation TALYS disposes eight options:

- Kopecku-Uhl Generalized Lorentzian model [98] (TALYS keyword “strength 1”, **default option for incident neutrons**)
- Brink Axel Lorentzian model [96, 97] (TALYS keyword “strength 2”)
- Hartree-Fock BCS tables (TALYS keyword “strength 3”)
- Hartree-Fock-Bogolyubov tables [99] (TALYS keyword “strength 4”)
- Goriely’s hybrid model [100] (TALYS keyword “strength 5”)
- Goriely T-dependent HFB (TALYS keyword “strength 6”)
- T-dependent RMF (TALYS keyword “strength 7”)
- Gogny D1M HFB+QRPA (TALYS keyword “strength 8”)

## 6.2.5 Level density models

The residual-nucleus that is produced after the compound-nucleus decay is left at excitation energy  $E_x$ . However, there are several nuclear states with excitation energy  $E_x$ , which differ in the total spin  $J$  and in parity  $\Pi$ . The existence of different states with the same excitation energy can be expressed in terms of the level density.

In reality, the compound-nucleus has a possibility to decay in each of these states. Therefore, in the Hauser-Feschbach calculations the transmission coefficients are calculated in terms of the level density:

$$\langle T_{a'l'j'}^J(E_{a'}) \rangle = \int_{E_x - \frac{1}{2}\Delta E_x}^{E_x + \frac{1}{2}\Delta E_x} \rho(E_{x'}, J, \Pi) dE_{x'} T_{a'l'j'}^J(E_{a'}) \quad (6.13)$$

For the majority of nuclei, experimental information about the level density is available for low excitation energies, where the discrete states are known. For higher energies where discrete states are unavailable or the knowledge about them is incomplete, several theoretical level density models have been developed. The TALYS code provides the ability of selection among six models, three phenomenological and three microscopic. Each of them will be discussed below.

### 6.2.5.1 The Fermi Gas model

Before presenting each phenomenological level density model of TALYS, it is useful to talk about the Fermi Gas level density model, since this is related to all of them. This model is based on the two principles that the levels are equally spaced and the collective effects are absent. Based on this model, the level density is obtained by Eq. 6.14:

$$\rho_F(E_x, J, \Pi) = \frac{1}{2} R_F(E_x, J) \rho_F^{tot}(E_x) \quad (6.14)$$

where

the factor  $\frac{1}{2}$  corrects for the equiparity distribution

$R_F(E_x, J) = \frac{2J+1}{2\sigma^2} e^{-\frac{(J+\frac{1}{2})^2}{2\sigma^2}}$  is the Fermi gas spin distribution

$\rho_F^{tot}(E_x) = \frac{1}{\sqrt{2\pi\sigma}} \frac{\sqrt{\pi}}{12} \frac{e^{2\sqrt{\alpha U}}}{\alpha^{\frac{1}{4}} U^{\frac{5}{4}}}$  is the total Fermi Gas level density over all spins and parities

The term  $U$  that appears in the above equations is called effective excitation energy and it is related to the true excitation energy  $E_x$  via the formula:  $U = E_x - \Delta$ , where  $\Delta$  is the pairing energy, which simulates odd-even effects.

The parameter  $\alpha$  is called level density parameter. For this parameter TALYS uses the theory of Ignatyuk [101], which introduced for the first time the energy dependent level density parameter  $\alpha$  in order to take into account the existence of shell effects at low excitation energies and their damping as the excitation energy increases:

$$\alpha = \alpha(E) = \hat{\alpha} \left( 1 + \delta W \frac{1 - e^{-\gamma U}}{U} \right) \quad (6.15)$$

where

$\delta W$  is the shell effects correction energy

$\gamma$  is the shell effects damping parameter as the excitation energy increases

$\hat{\alpha}$  is the asymptotic level density value of the parameter ( $\hat{\alpha} = \alpha(E_x \rightarrow \infty)$ )

The  $\sigma^2$  parameter is called spin cut-off parameter and it refers to the width of the angular momentum distribution of the level density.

### 6.2.5.2 The Constant Temperature model

The first phenomenological level density model of TALYS is the Constant Temperature model (CTM) (TALYS keyword “ldmodel 1”, **default option**), which is also known as the Gilbert-Cameron formula [102]. This model is based on the fact that the exponential function of Eq. 6.16 has been proven to reproduce the experimental discrete levels at low excitation energies.

$$\rho_{CTM}^{tot}(E_x) = \frac{1}{T} e^{\frac{E_x - E_0}{T}} \quad (6.16)$$

Therefore, in this model the level density is divided into two parts: at low energies a Constant Temperature law is applied, whereas for higher energies the level density is described through the Fermi Gas theory:

$$\rho(E_x, J, \Pi) = \frac{1}{2} R_F(E_x, J) \rho_{CTM}^{tot}(E_x), E_x \leq E_M \quad (6.17)$$

$$\rho(E_x, J, \Pi) = \rho_F(E_x, J, \Pi), E_x \geq E_M \quad (6.18)$$

$E_M$  is the matching energy between the two theories. The three constant terms  $T$ ,  $E_0$  and  $E_M$  are calculated by the continuity equations of the level densities and their derivatives at  $E_M$  and by the condition that the constant temperature law reproduces the experimental discrete levels at low excitation energies.

### 6.2.5.3 The Back-Shifted Fermi Gas model

The second phenomenological model of TALYS is called Back-Shifted Fermi Gas model (BSFG) (TALYS keyword “ldmodel 2”). In this approach the Fermi Gas theory is applied over all energies. The issue on this assumption is that the level density becomes infinity at zero excitation energy (see Eq. 6.14). This problem is solved through the theory of Grossjean and Feldmeier [103], which was applied by Demetriou and Goriely [104]. This work, which has been adopted by TALYS, proposes the calculation of the level density as following:

$$\rho_{BSFM}^{tot}(Ex) = \left[ \frac{1}{\rho_F^{tot}(Ex)} + \frac{1}{\rho_0(t)} \right]^{-1} \quad (6.19)$$

where

$$\rho_0(t) = \frac{e}{24\sigma} \frac{(\alpha_n + \alpha_p)^2}{\sqrt{\alpha_n \alpha_p}} e^{4\alpha_n \alpha_p t^2} \quad (6.20)$$

In the above equation  $\alpha_n = \alpha_p = \frac{\alpha}{2}$  and  $t$  is so called thermodynamic temperature and it is equal to  $t = \sqrt{\frac{U}{\alpha}}$ .

### 6.2.5.4 The Generalized Superfluid model

In the Generalized Superfluid model (GSM) (TALYS keyword “ldmodel 3”), the level density is distinguished into two energy parts. In the high energy region the Fermi Gas model is applied with a different parametrization than in the Constant Temperature and the Back-Shifted Fermi Gas models. For low excitation energies, it is considered that the level density is affected by pairing correlations which cause a superfluid behavior [105, 106]:

$$\rho(E_x, J, \Pi) = \frac{1}{2} R_F(E_x, J) \rho_{GSM}^{tot}(E_x), U' \leq U_C \quad (6.21)$$

$$\rho(E_x, J, \Pi) = \frac{1}{2} R_F(E_x, J) \rho_F^{tot}(E_x), U' \geq U_C \quad (6.22)$$

where,

$$\rho_{GSM}^{tot}(E_x) = \frac{1}{\sqrt{2\pi\sigma}} \frac{e^S}{\sqrt{(D)}} \quad (6.23)$$

The superfluid behavior is applied below a critical energy  $U_C$  which is defined based on thermodynamical functions. The entropy of the nucleus  $S$  and the determinant  $D$  are defined in terms of  $U_C$  and  $U'$ , where  $U'$  is the effective excitation energy:

$$S = S_C \frac{T_C}{T} \frac{U'}{U_C} \quad (6.24)$$

$$D = D_C \frac{U'}{U_C} \left(2 - \frac{U'}{U_C}\right)^2 \quad (6.25)$$

In the equations above  $S_C$  and  $D_C$  are the critical entropy and the critical determinant, whereas  $T_C$  and  $T$  are the critical temperature and the temperature below  $U_C$ , respectively. These quantities are deduced from the theory of thermodynamics. The spin cut-off parameter,  $\sigma^2$ , of Eq. 6.23, is obtained by Eq. 6.26, where  $\sigma_C^2$  is the spin cut-off parameter at the critical energy.

$$\sigma^2 = \sigma_C^2 \frac{U'}{U_C} \quad (6.26)$$

This model resembles the Constant Temperature model due to the distinguishing between two energy regions. However, in Generalized Superfluid model this distinguishing follows the theory and it is not based on the experimental evidence about the discrete levels.

#### 6.2.5.5 Microscopic Level Density models

In TALYS three microscopic level density models are incorporated based on Hartree-Fock calculations:

- microscopic model 1: S. Goriely et al. [107] (TALYS keyword “ldmodel 4”)
- microscopic model 2: S. Goriely et al. [108] (TALYS keyword “ldmodel 5”)
- microscopic model 3: S. Hilaire et al. [109] (TALYS keyword “ldmodel 6”)

## 6.3 The TALYS calculations

The TALYS calculations were validated through the comparison with the experimental data of the present work. In particular, it was investigated the performance of the code by modifying the default options for the theoretical models as described in Section 6.2. The validation procedure was based on three steps. At each step only one component was modified so as to track the impact of the different models on the calculated excitation functions:

- **Fist step:** adoption of different level density models.

- **Second step:** adoption of different pre-equilibrium models for each level density model.
- **Third step:** adoption of different  $\gamma$ -ray strength function models of the E1 transition for each level density model.

In addition to the above, the behavior of the calculations was investigated by changing the nucleon optical potential of Koning-Delaroche to the semi-microscopic potential of Bauge by keeping fixed the rest of the models. However, this change did not affect remarkably the theoretical trends.

It has to be mentioned that in the TALYS calculations performed in the present work the the full  $j, \ell$  coupling was considered in the Hauser-Feshbach theory (TALYS keyword: “fullhf y”).

### 6.3.1 Adoption of different level density models

Firstly, calculations were performed for the six level density models of the code by adopting the default options for the rest of the models. The results are illustrated in Figure 6.3.

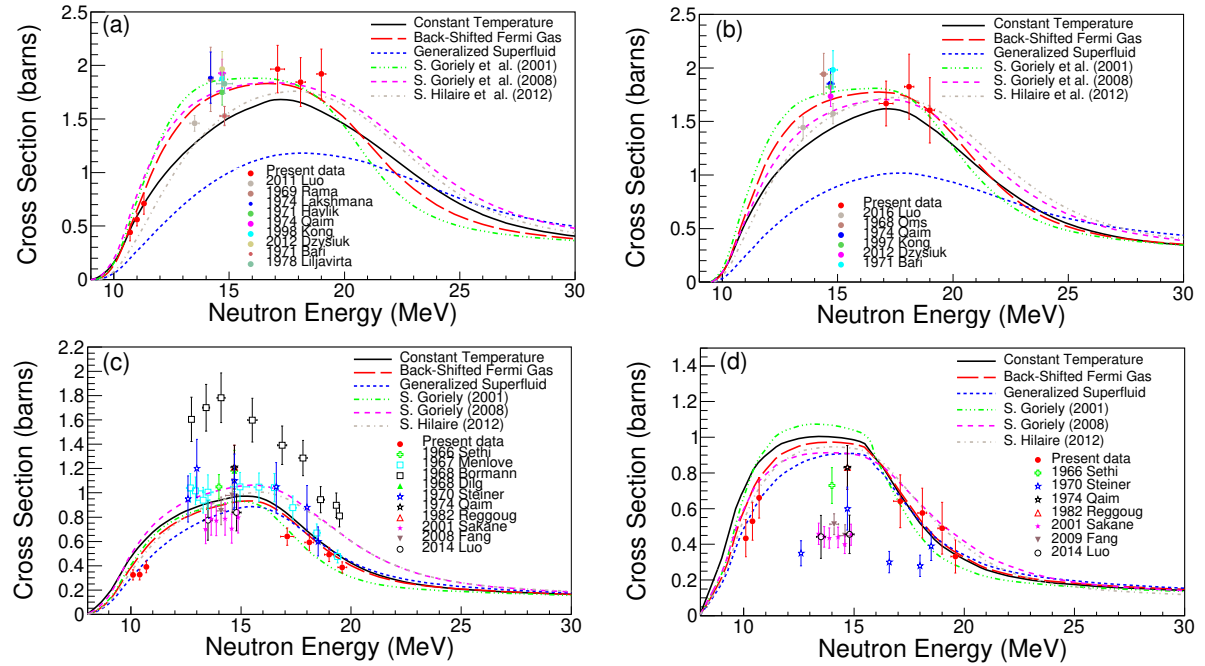


Figure 6.3: The TALYS calculations corresponding to the different level density models for (a) the  $^{162}\text{Er}(n,2n)^{161}\text{Er}$  reaction, (b) the  $^{156}\text{Dy}(n,2n)^{155}\text{Dy}$  reaction, (c) the  $^{165}\text{Ho}(n,2n)^{164}\text{Ho}^m$  reaction and (d) the  $^{165}\text{Ho}(n,2n)^{164}\text{Ho}^g$  reaction.

For the (n,2n) reaction channel on the  $^{162}\text{Er}$  isotope the best reproduction of the present data is achieved adopting the Back-Shifted Fermi Gas model. The Constant Temperature model fails to reproduce the high energy measurements. An important

outcome of the Figure 6.3 is that the Generalized Superfluid model underestimates significantly the cross section for the whole energy range. As far as the microscopic level density models are concerned all of them reproduce the present data in the high energy region above 17 MeV, but none of these yields good results with respect to the experimental data of the present work at near threshold energies.

The Generalized Superfluid model is also characterized by a very poor performance when the  $^{156}\text{Dy}(n,2n)^{155}\text{Dy}$  reaction is concerned. The rest of the models are compatible with the present measurements.

On the other hand, for the  $^{165}\text{Ho}(n,2n)^{164}\text{Ho}^m$  and  $^{165}\text{Ho}(n,2n)^{164}\text{Ho}^g$  reactions the theoretical line of the Generalized Superfluid model is the most satisfactory with respect to the data of the present work for both reaction channels. Among the rest of the models, only the microscopic model of S. Hilaire et al. (2012) has a good agreement with the present measurements of the  $^{165}\text{Ho}(n,2n)^{164}\text{Ho}^g$  reaction.

### 6.3.2 Adoption of different pre-equilibrium models for each level density model

#### 1. $^{162}\text{Er}(n,2n)^{161}\text{Er}$ reaction

Based on Figure 6.4 the following remarks can be made:

- The “preeqmode 1” and “preeqmode 2” (**default option**) models for the pre-equilibrium mechanism produce compatible results over the whole energy range and for all level density models. This feature is also common for the calculations presented in Figures 6.5, 6.6, and 6.7.
- The behavior of the Constant Temperature model is improved when it is combined with the “preeqmode 3” or the “preeqmode 4” models. The results of this combination are in agreement with the present measurements.
- The Back-Shifted Fermi Gas model presents a good behavior with the present data when it is combined with the “preeqmode 1”, “preeqmode 2” (**default option**) and “preeqmode 4” models.
- On the other hand, when the Generalized Superfluid model is adopted any kind of pre-equilibrium model cannot provide a satisfactory reproduction of the experimental data.

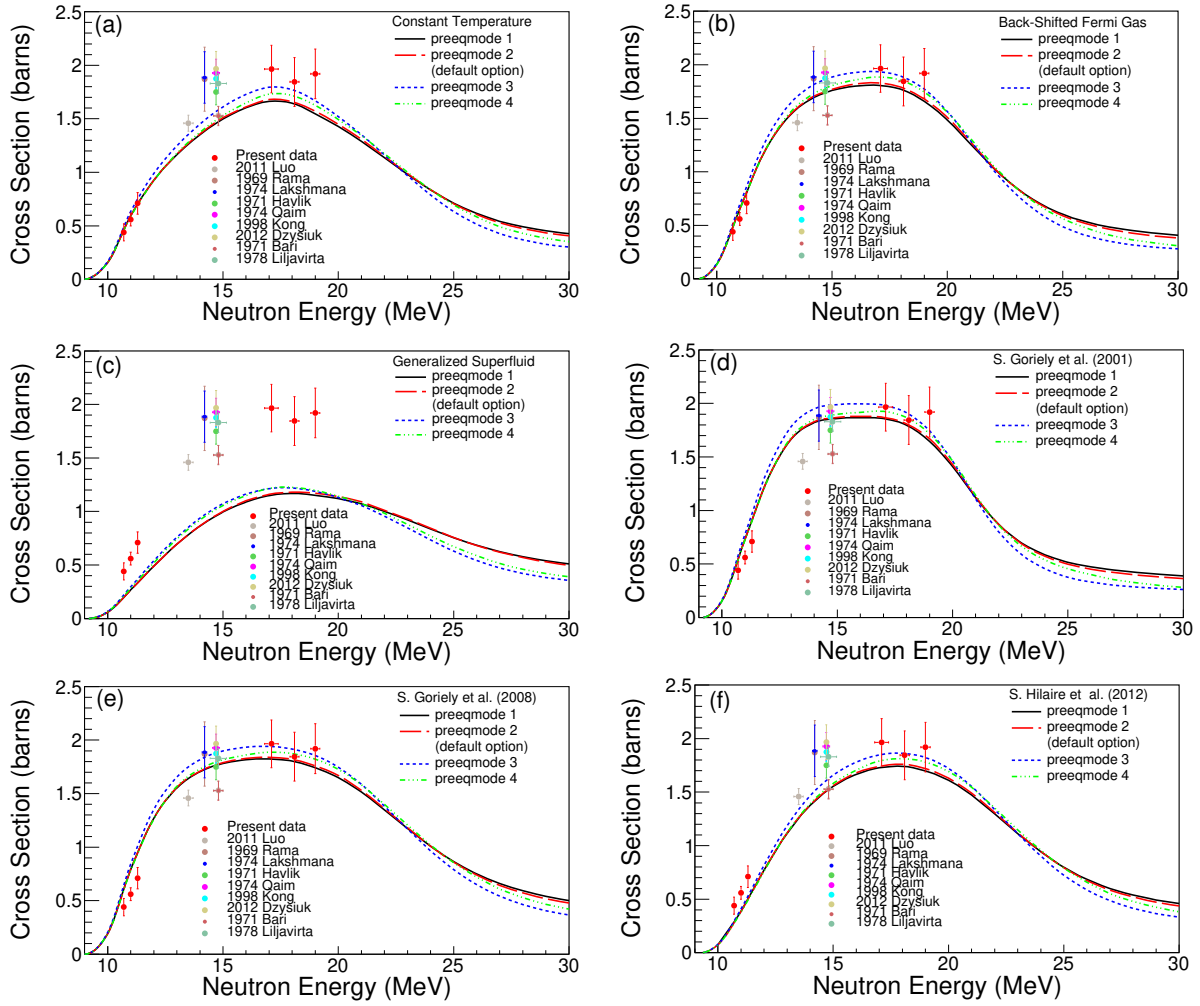


Figure 6.4: The TALYS calculations for the  $^{162}\text{Er}(n,2n)^{161}\text{Er}$  reaction corresponding to each level density model combined with different models for the pre-equilibrium mechanism.

## 2. $^{156}\text{Dy}(n,2n)^{155}\text{Dy}$ reaction

From Figure 6.5 it is concluded that:

- The present data are still reproduced via all the theoretical trends excluding the ones that are based on the Generalized Superfluid model.

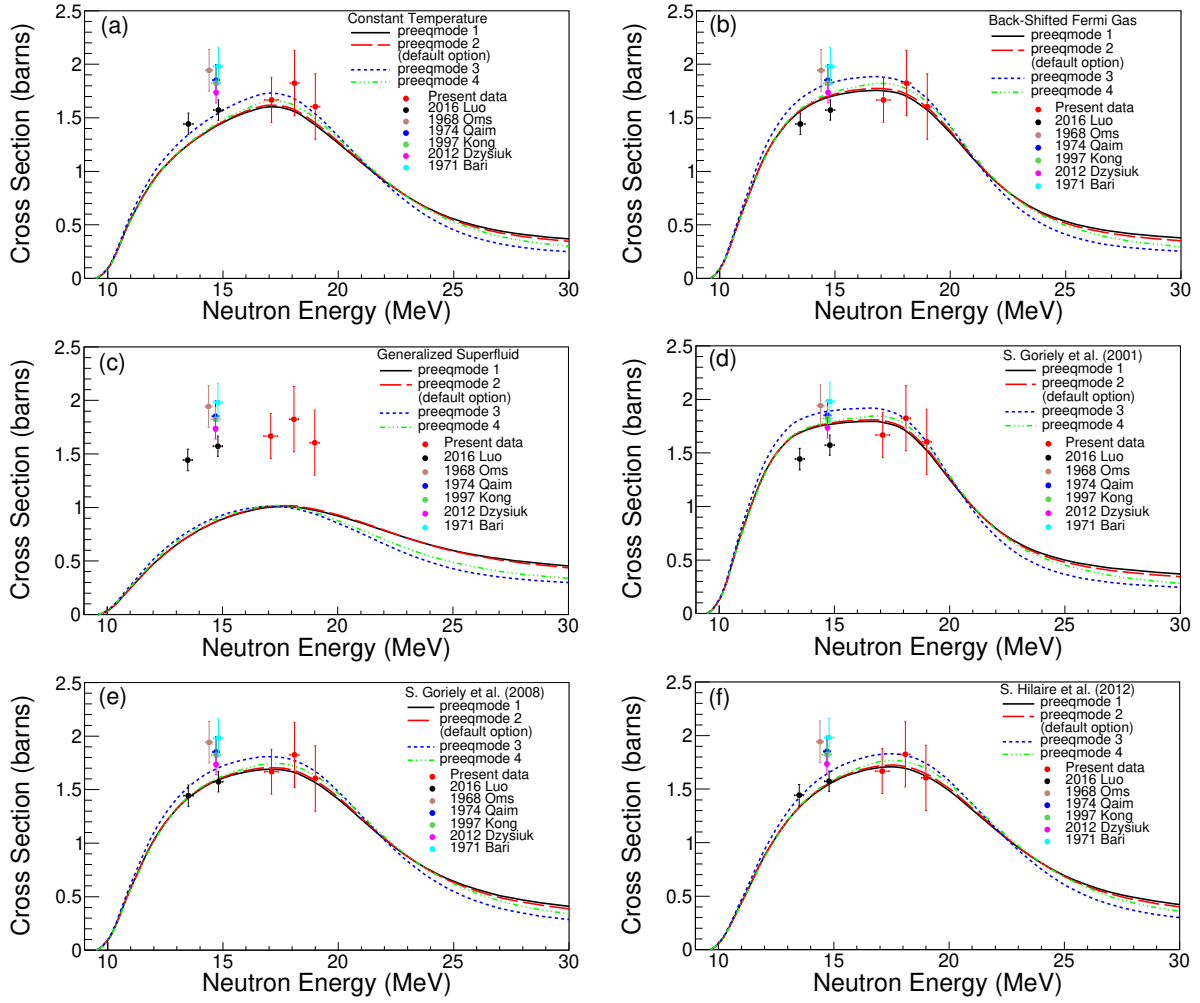


Figure 6.5: The TALYS calculations for the  $^{156}\text{Dy}(n,2n)^{155}\text{Dy}$  reaction corresponding to each level density model combined with different models for the pre-equilibrium mechanism .

### 3. $^{165}\text{Ho}(n,2n)^{164}\text{Ho}^m$ reaction

From Figure 6.6 it results that:

- Only the Generalized Superfluid model, when it is combined with the “preeqmode 1” and “preeqmode 2” (**default option**) models, has a good agreement with the present data both at the low and the high energies.



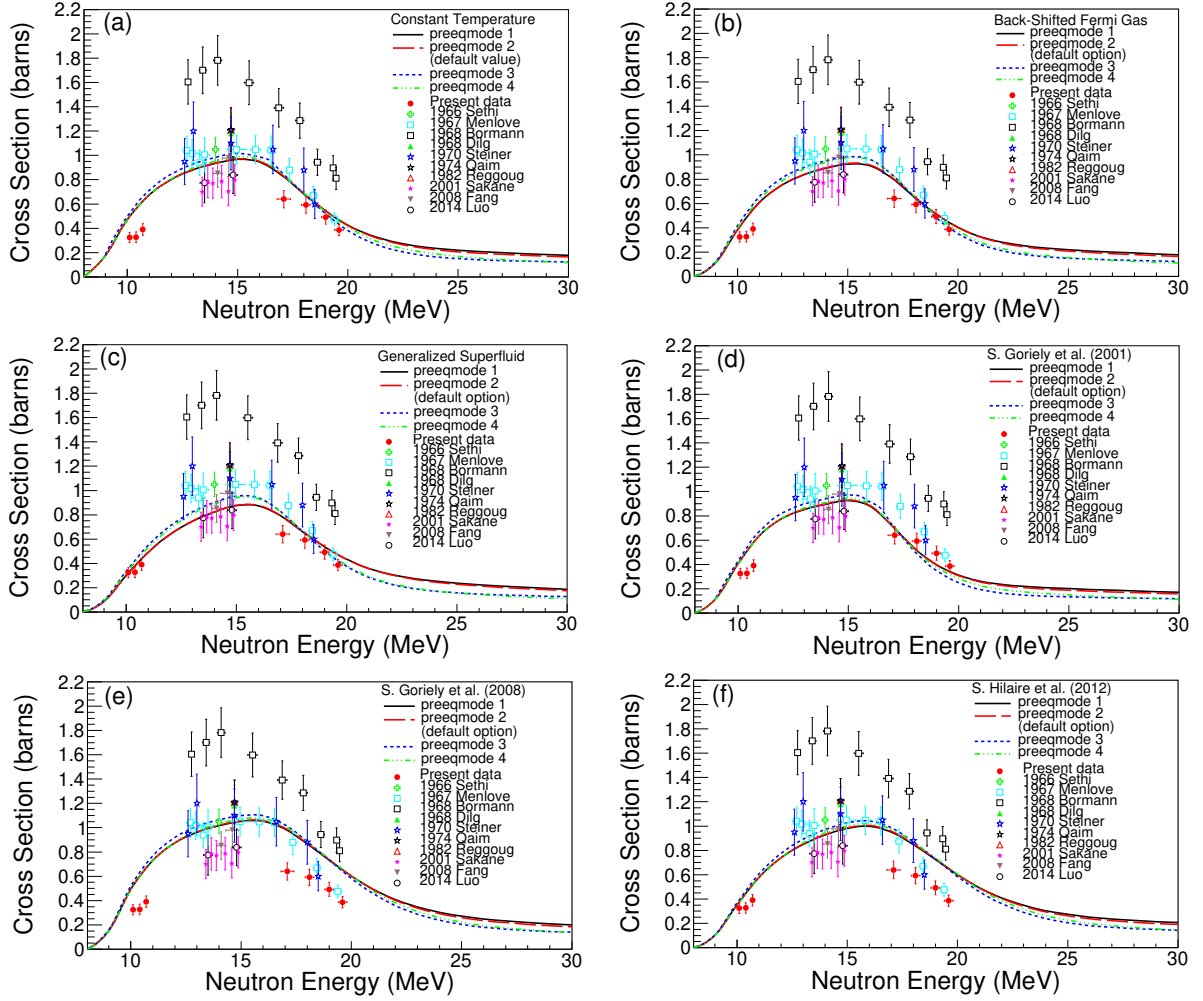


Figure 6.6: The TALYS calculations for the  $^{165}\text{Ho}(n,2n)^{164}\text{Ho}^m$  reaction corresponding to each level density model combined with different models for the pre-equilibrium mechanism.

#### 4. $^{165}\text{Ho}(n,2n)^{164}\text{Ho}^g$ reaction

According to Figure 6.7 it results that:

- The Generalized Superfluid model has a good agreement with the present data both at the low and the high energies, when it is combined with the “preeqmode 1”, “preeqmode 2” (**default option**) and “preeqmode 4” models for the pre-equilibrium mechanism.
- The behavior of the microscopic level density model proposed by S. Hilaire et al. (2012) is satisfactory relevant to the present measurements only when it is combined with the “preeqmode 1”, “preeqmode 2” (**default option**) and “preeqmode 4” models.

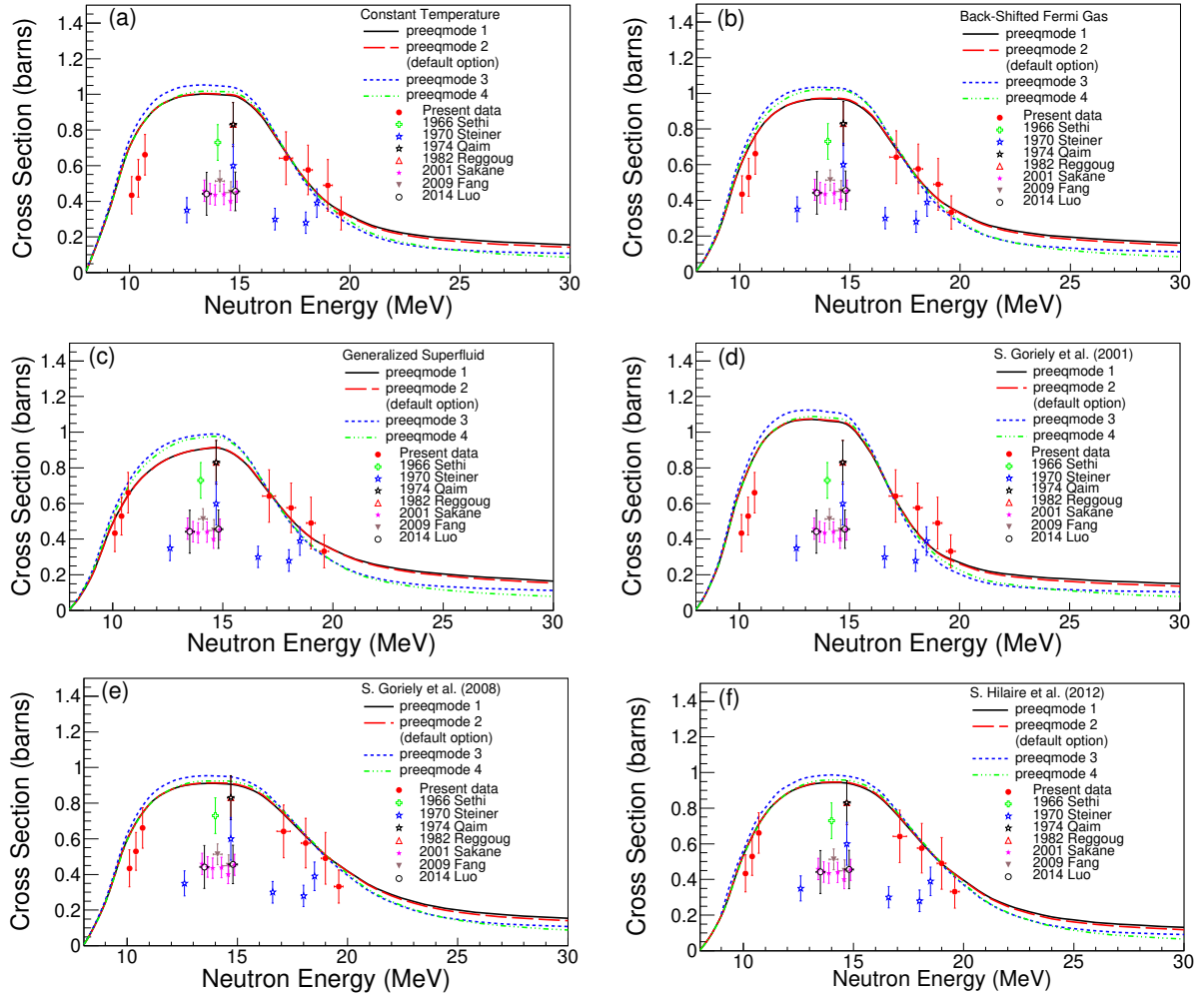


Figure 6.7: The TALYS calculations for the  $^{165}\text{Ho}(n,2n)^{164}\text{Ho}^g$  reaction corresponding to each level density model combined with different models for the pre-equilibrium contribution to the compound-nucleus mechanism .

### 6.3.3 Adoption of different $\gamma$ -ray strength function models of the E1 transition for each level density model

#### 1. $^{162}\text{Er}(n,2n)^{161}\text{Er}$ reaction

Based on Figure 6.8 the following features result:

- The calculations based on the Back-Shifted Fermi Gas model are in agreement with the present data when they are combined with the “strength 1” (Kopecky-Ulh model, **default option**), “strength 5” and “strength 8” models.
- The calculations using the Generalized Superfluid model are in disagreement with the data of the present work.

- By adopting the microscopic level density model of S. Goriely et al. (2001) (microscopic model 1) combined with the “strength 8” model the present data are reproduced both at the low and the high energy region.
- By using the microscopic level density model of S. Hilaire et al. (2012) (microscopic model 3) the present data are reproduced for the following  $\gamma$ -ray strength functions: “strength 3”, “strength 4” and “strength 7” models.

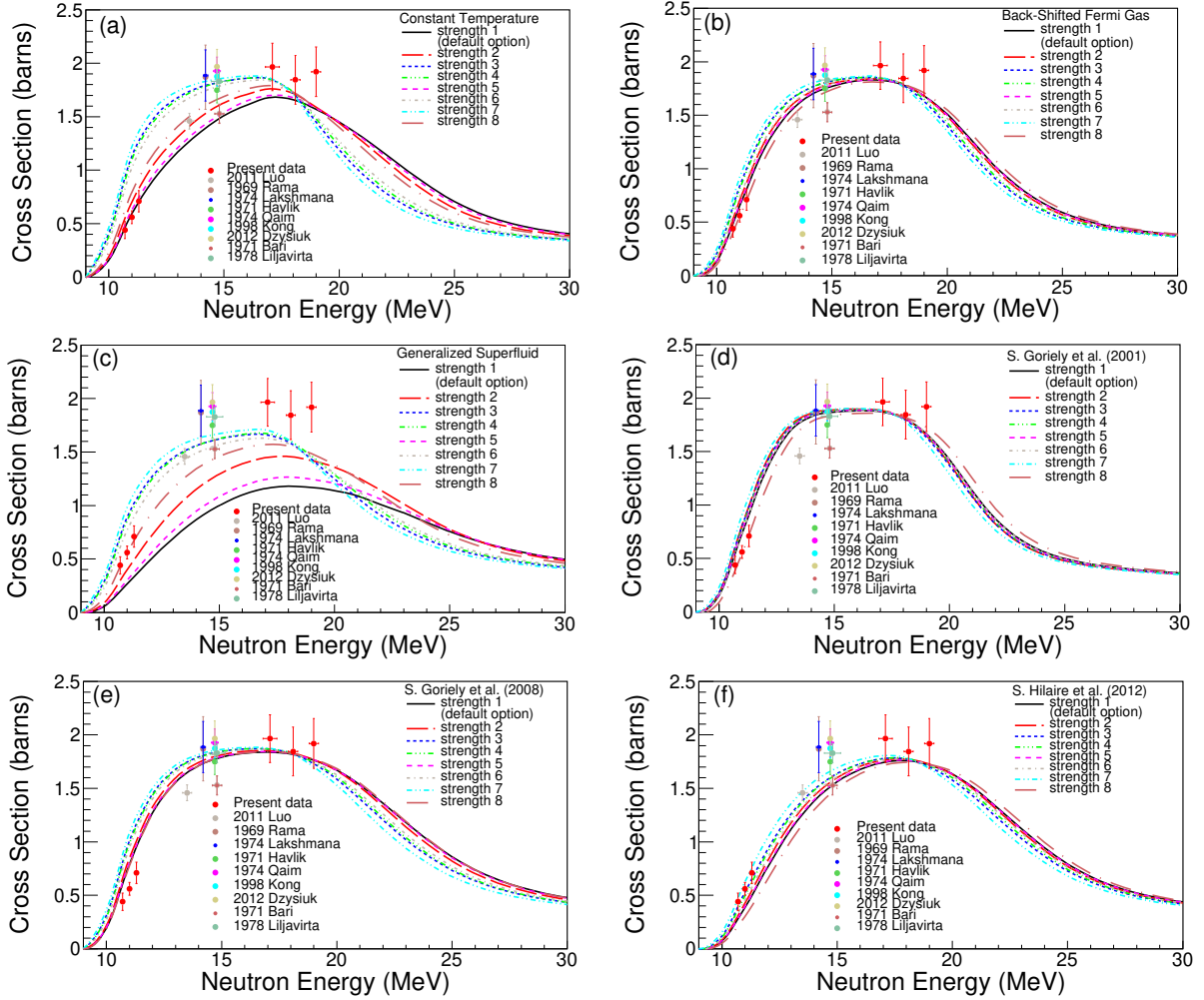


Figure 6.8: The TALYS calculations for the  $^{162}\text{Er}(n,2n)^{161}\text{Er}$  reaction corresponding to each level density model combined with different models for the  $\gamma$ -ray strength functions of the E1 transition.

## 2. $^{156}\text{Dy}(n,2n)^{155}\text{Dy}$ reaction

Based on Figures 6.11 the following feature results:

- The experimental data of the present work are reproduced via all the theoretical trends excluding the ones based on the Generalized Superfluid model. This models still seems to underestimate significantly the experimental measurements.

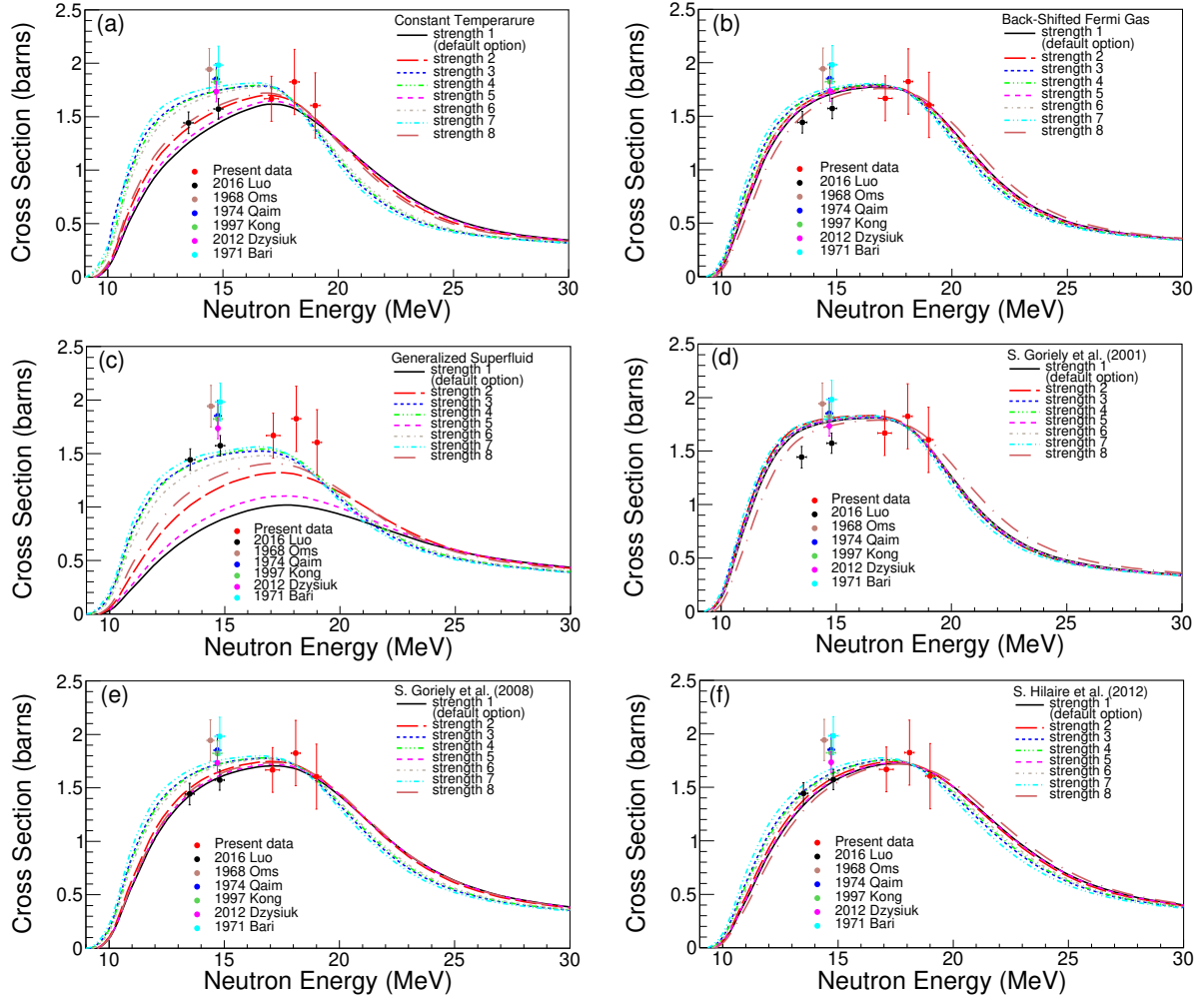


Figure 6.9: The TALYS calculations for the  $^{156}\text{Dy}(n,2n)^{155}\text{Dy}$  reaction corresponding to each level density model combined with different models for the  $\gamma$ -ray strength function of the E1 transition.

### 3. $^{165}\text{Ho}(n,2n)^{164}\text{Ho}^m$ reaction

As far as the  $^{165}\text{Ho}(n,2n)^{164}\text{Ho}^m$  reaction is concerned it is concluded that:

- The level density calculations using the Generalized Superfluid model combined with the  $\gamma$ -ray strength function model “strength 1” (Kopecky-Uhl, **default option**) are in better agreement with the data of the present work.

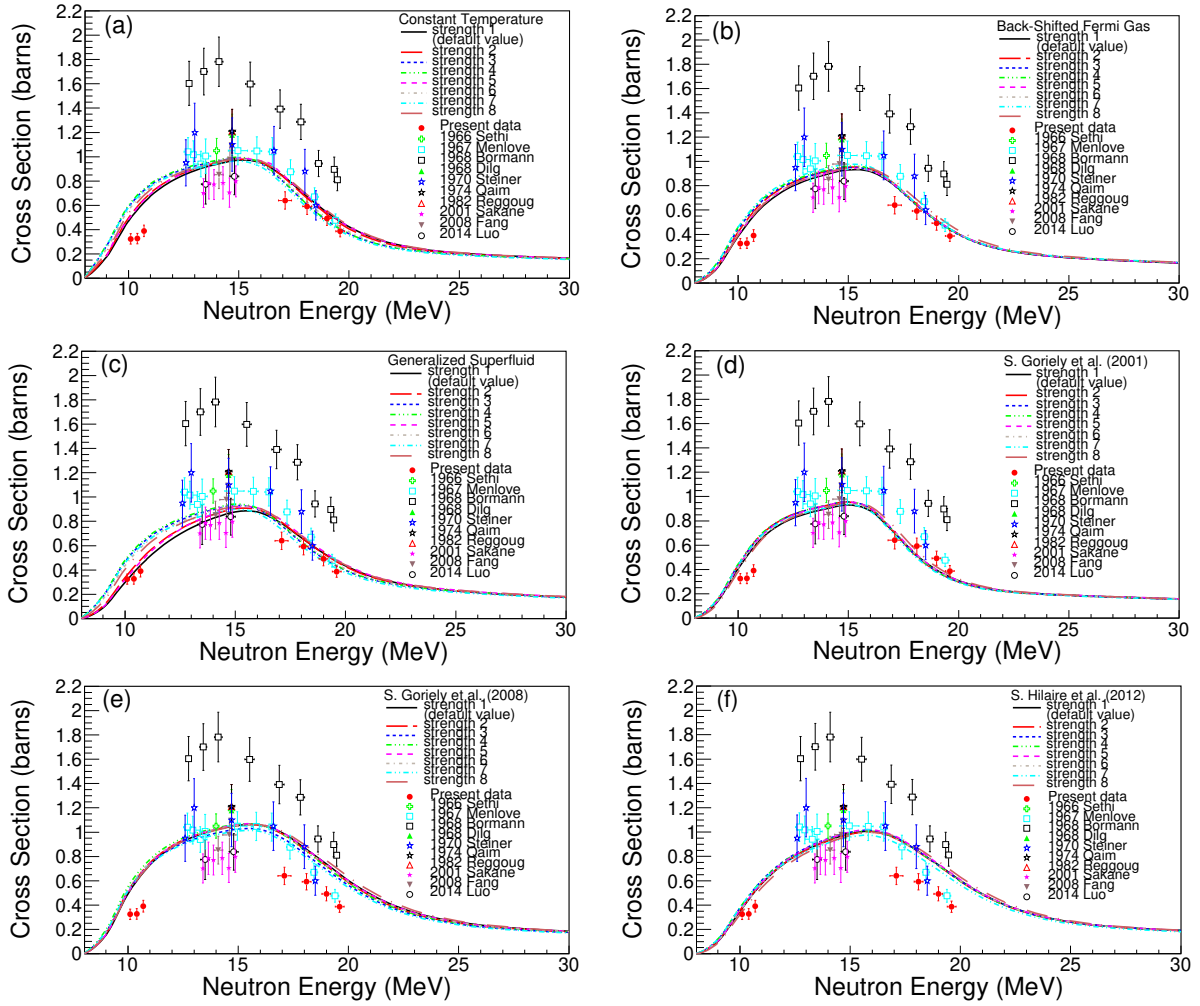


Figure 6.10: The TALYS calculations for the  $^{165}\text{Ho}(n,2n)^{164}\text{Ho}^m$  reaction corresponding to each level density model combined with different models for the  $\gamma$ -ray strength function of the E1 transition.

#### 4. $^{165}\text{Ho}(n,2n)^{164}\text{Ho}^g$ reaction

As far as the  $^{165}\text{Ho}(n,2n)^{164}\text{Ho}^g$  reaction is concerned:

- The calculations using the Generalized Superfluid model are closer to the experimental data of the present work when combined with the “strength 1” (Kopecky-Uhl, **default option**), “strength 2” and “strength 5” models.
- Concerning the microscopic level density models better agreement with the experimental data of the present work is achieved using model of S. Hilaire et al. (2012) combined with the “strength 1”, (Kopecky-Uhl model, **default option**), “strength 5” and “strength 8” models.

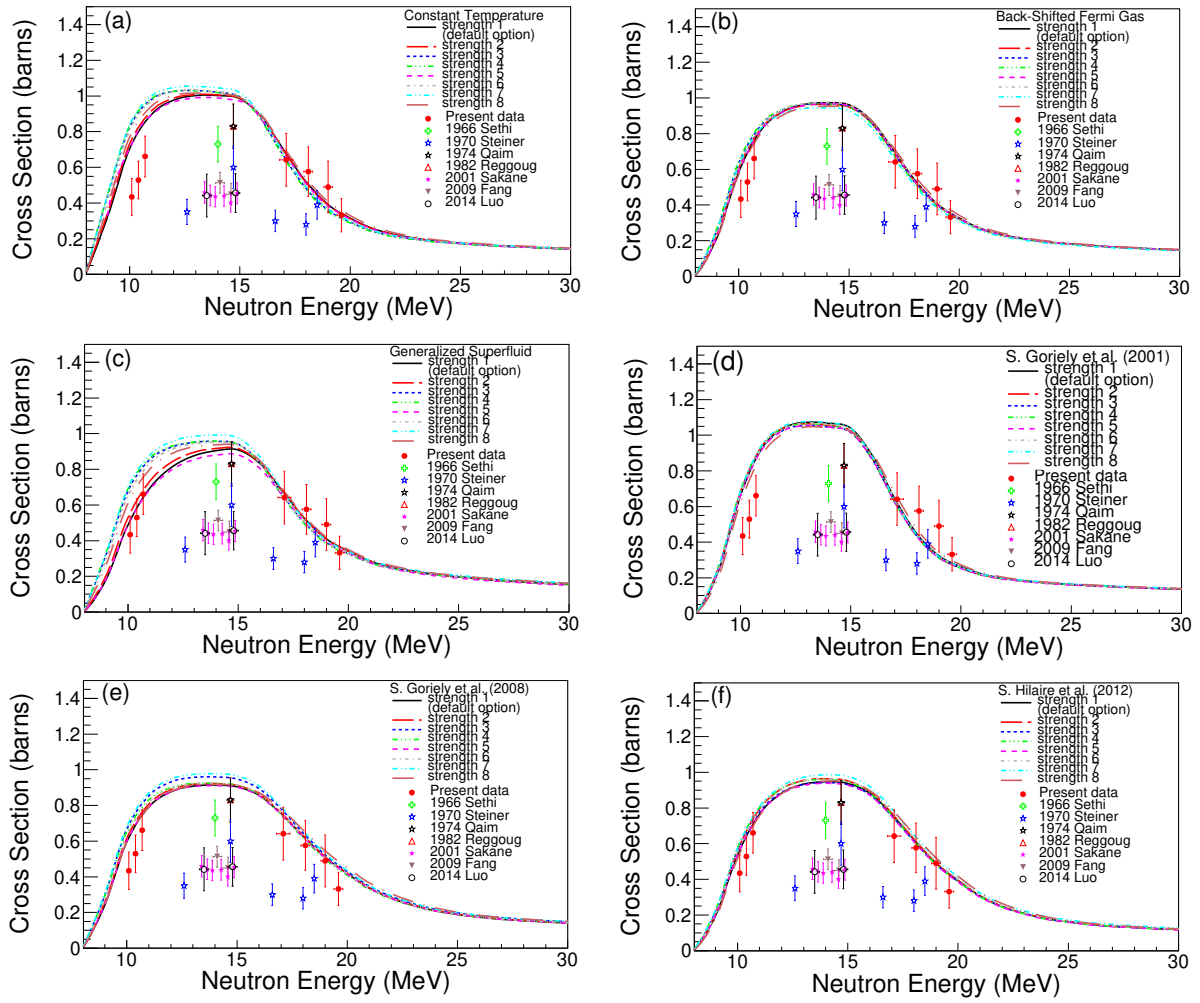


Figure 6.11: The TALYS calculations for the  $^{165}\text{Ho}(n,2n)^{164}\text{Ho}^g$  reaction corresponding to each level density model combined with different models for the  $\gamma$ -ray strength function of the E1 transition.

### 6.3.4 The final TALYS results

The combinations of models that result in the best reproduction of the present measurements are summarized in Table 6.1:

Table 6.1: The combination of TALYS models that better reproduce the present measurements of the (a)  $^{162}\text{Er}(n,2n)^{161}\text{Er}$ , (b)  $^{156}\text{Dy}(n,2n)^{155}\text{Dy}$ , (c)  $^{165}\text{Ho}(n,2n)^{164}\text{Ho}^m$  and (d)  $^{165}\text{Ho}(n,2n)^{164}\text{Ho}^g$  reactions.

	level density	pre-equilibrium mechanism	level density	$\gamma$ -ray strength function for the E1 transition
(a) $^{162}\text{Er}(n,2n)^{161}\text{Er}$	Constant Temperature	preeqmode 3 preeqmode 4	Back-Shifted Fermi Gas	strength 1 strength 5 strength 8
	Back-Shifted Fermi Gas	preeqmode 1 preeqmode 2 preeqmode 4		
	S. Goriely et al. (2001)			
	s. Hilaire et al. (2012)			
(b) $^{156}\text{Dy}(n,2n)^{155}\text{Dy}$	any combination of models that excludes the Generalized Superfluid model		any combination of model that excludes the Generalized Superfluid model	
(c) $^{165}\text{Ho}(n,2n)^{164}\text{Ho}^m$	Generalized Superfluid model	preeqmode 1 preeqmode 2	Generalized Superfluid model	strength 1
(d) $^{165}\text{Ho}(n,2n)^{164}\text{Ho}^g$	Generalized Superfluid model	preeqmode 1 preeqmode 2 preeqmode 4	Generalized Superfluid model	strength 1 strength 2 strength 5
	S. Hilaire et al. (2012)	preeqmode 1 preeqmode 2 preeqmode 4	S. Hilaire et al. (2012)	strength 1 strength 5 strength 8

## 6.4 The Generalized Superfluid model for the Er and Dy stable isotopes

A general conclusion that can be drawn is that when the neutron deficient isotopes,  $^{162}\text{Er}$  and  $^{156}\text{Dy}$ , are considered, the Generalized Superfluid level density model seems to fail to reproduce the experimental data of the (n,2n) reaction channel. In general, the calculations based on this model underestimate significantly the present measurements, as well as the measurements reported in previous works [17]. In an attempt to investigate if this behavior is also noticed for all the stable isotopes of Er and Dy, the TALYS calculations of the (n,2n) reaction for the Generalized Superfluid level density model combined with the default options for the rest of the models are presented in Figures 6.12 and 6.13 for all the stable isotopes of Er and Dy. In these

Figures the TALYS results are illustrated along with the ENDF/B-VIII.0 library [39] and the experimental data [17], when these are available.

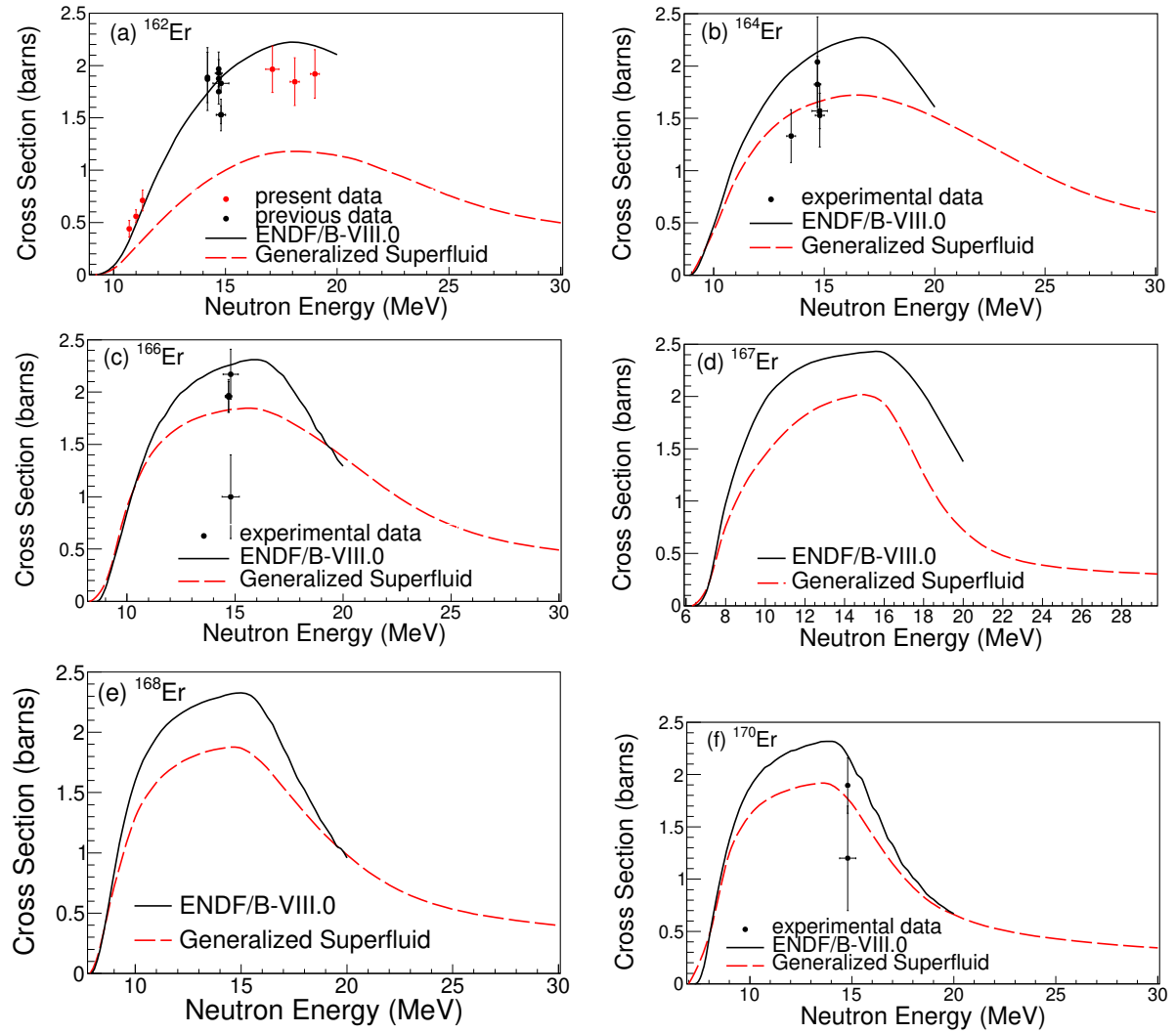


Figure 6.12: The TALYS calculations of the (n,2n) reaction based on the Generalized Superfluid level density model along with the ENDF/B-VIII.0 library [39] and the experimental data [17], when these are available, for each one of the stable isotopes of Er: (a)  $^{162}\text{Er}$ , (b)  $^{164}\text{Er}$ , (c)  $^{166}\text{Er}$ , (d)  $^{167}\text{Er}$ , (e)  $^{168}\text{Er}$  and (f)  $^{170}\text{Er}$ .



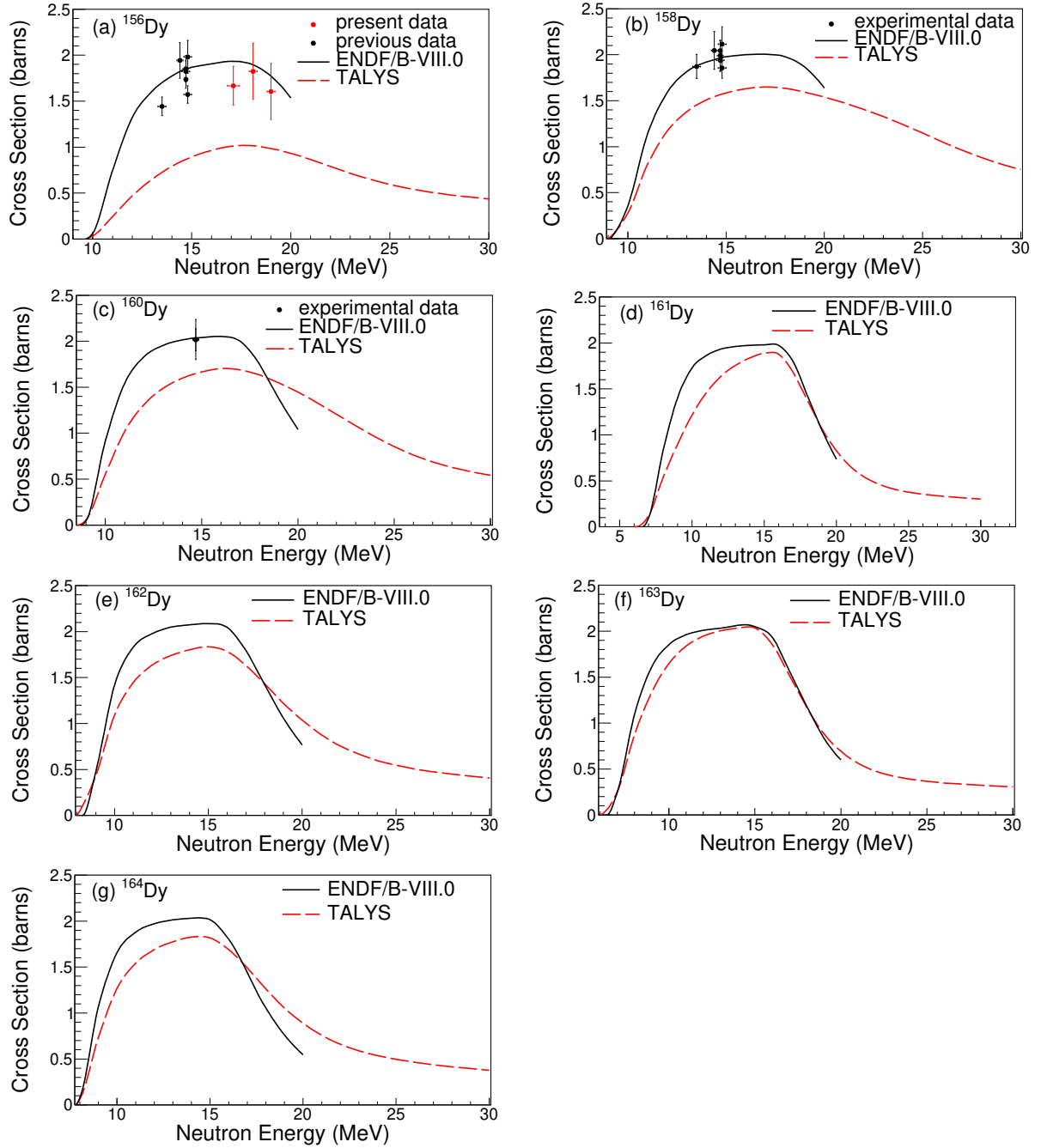


Figure 6.13: The TALYS calculations of the (n,2n) reaction based on the Generalized Superfluid level density model along with the ENDF/B-VIII.0 library [39] and the experimental data [17], when these are available, for each one of the stable isotopes of Dy: (a)  $^{156}\text{Dy}$ , (b)  $^{158}\text{Dy}$ , (c)  $^{160}\text{Dy}$ , (d)  $^{161}\text{Dy}$ , (e)  $^{162}\text{Dy}$ , (f)  $^{163}\text{Dy}$  and (g)  $^{164}\text{Dy}$ .

From Figures 6.12 and 6.13 it results that the performance of the model fails for the lightest isotopes.

## 6.5 $^{165}\text{Ho}(n,2n)^{164}\text{Ho}$ reaction: The angular momentum distribution and the ground to isomeric cross section ratio

The direct observation of the relative feeding of the ground and the isomeric state of  $^{164}\text{Ho}$ , product-nucleus of the  $^{165}\text{Ho}(n,2n)$  reaction, is a sensitive probe so as to understand the impact of the spin distribution of the excited states on the reaction rates. For this reason, the “Rspincut” keyword (**default value=1**) of TALYS was utilized. This is a multiplication factor of the spin cut-off parameter  $\sigma^2$ . This parameter represents the width of the angular momentum distribution of the level density.

In Figures 6.14 and 6.15 can be seen the theoretical trends of each phenomenological level density model for “Rspincut=1” (**default value**), “Rspincut=0.7” and “Rspincut=0.5” for the isomeric state and the ground state cross section, respectively. As can be seen even when “Rspincut” is reduced to 0.5 (half of its original value), still only the Generalized Superfluid model reproduces the present data over all energies for both reaction channels.

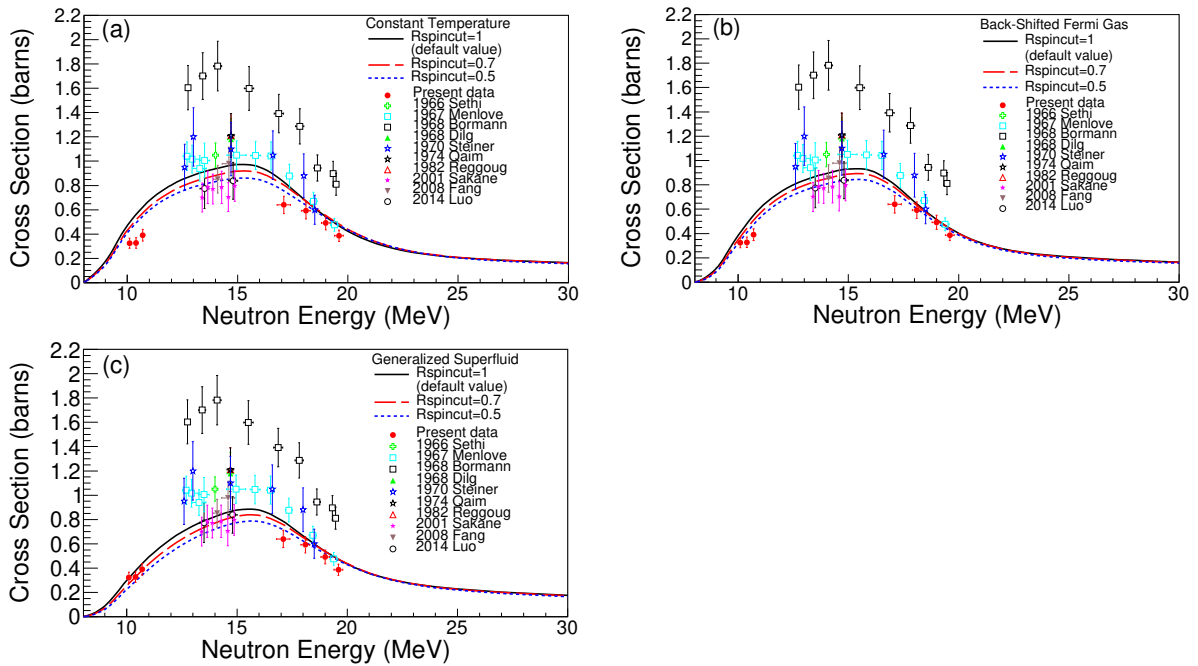


Figure 6.14: The TALYS calculations for the  $^{165}\text{Ho}(n,2n)^{164}\text{Ho}^m$  reaction corresponding to different values of the “Rspincut” parameter for (a) the Constant Temperature model, (b) the Back-Shifted Fermi Gas model and (c) the Generalized Superfluid model.

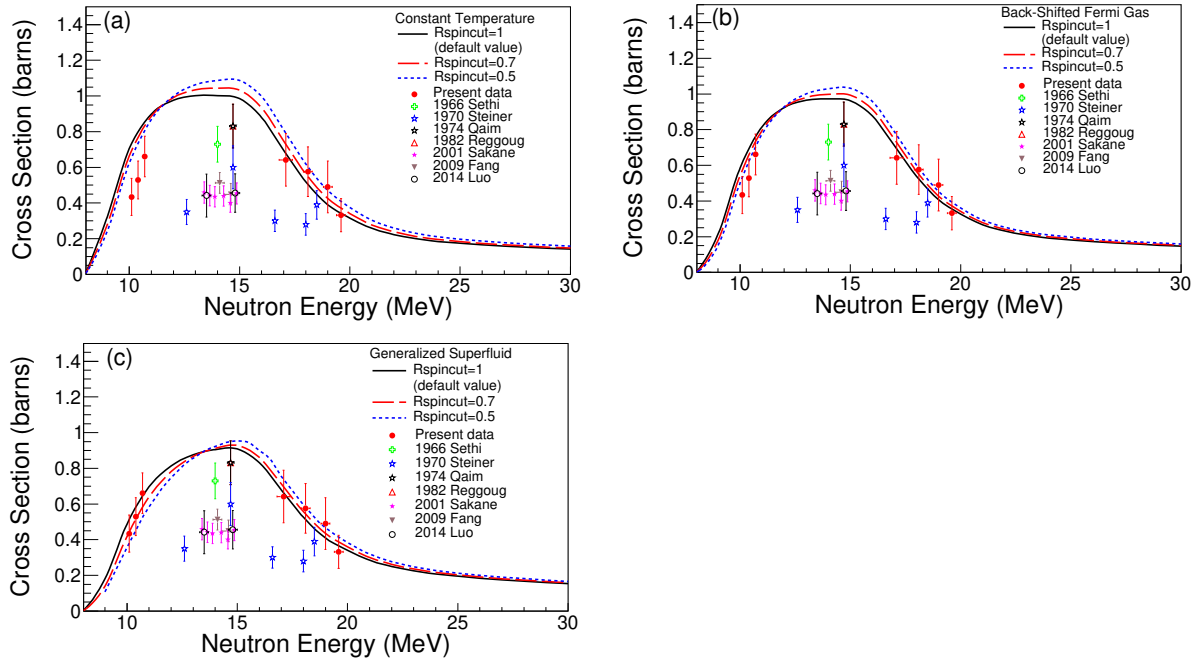


Figure 6.15: The TALYS calculations for the  $^{165}\text{Ho}(n,2n)^{164}\text{Ho}^g$  reaction corresponding to different values of the “Rspincut” parameter for (a) the Constant Temperature model, (b) the Back-Shifted Fermi Gas model and (c) the Generalized Superfluid model.

In Figure 6.16 the ratio of the ground to the isomeric state cross section is presented for all the level density models and for different values of the “Rspincut” parameter when the phenomenological level density models are concerned. As can be seen all the ratios resulting from all the theoretical trends are compatible with the measurements of the present work.

In this point it has to be clarified that TALYS determines the parametrization of level density models through an optimization procedure, as described in Ref. [110], where the mean s-wave neutron level spacing at the neutron separation energy,  $D_0$ , and the experimental discrete levels are taken into account. The change of the “Rspincut” parameter affects the spin cut-off parameter, whereas the remaining parameters of the models, such as the energy dependent level density parameter  $\alpha$  and the shell effects damping parameter  $\gamma$ , remain invariable. Therefore, when the “Rspincut” keyword is modified, the observables are not necessarily reproduced. The applied modifications in “Rspincut”, thus, aim at testing the sensitivity of the ground and isomeric state cross section to the spin distribution rather than suggesting an alternative level density models parametrization.

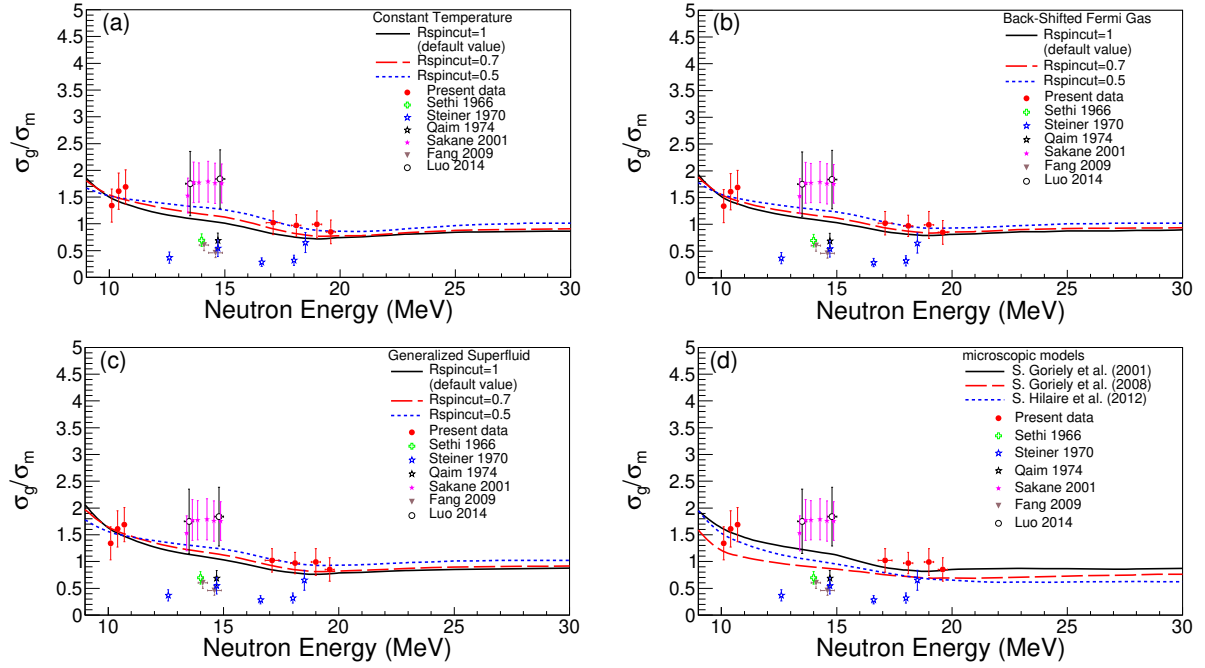


Figure 6.16: The TALYS calculations for the ratio of the ground to the isomeric state cross section of the  $^{165}\text{Ho}(n,2n)^{164}\text{Ho}$  reaction corresponding to different values of the “Rspincut” parameter for (a) the Constant Temperature model, (b) the Back-Shifted Fermi Gas model and (c) the Generalized Superfluid model. Figure (d) presents the ratio as results from the microscopic level density models.

# Chapter 7

## Summary and Discussion

Within the present work, the:

- $^{162}\text{Er}(n,2n)^{161}\text{Er}$
- $^{156}\text{Dy}(n,2n)^{155}\text{Dy}$
- $^{165}\text{Ho}(n,2n)^{164}\text{Ho}^g$
- $^{165}\text{Ho}(n,2n)^{164}\text{Ho}^m$

reactions were measured at the neutron beam energies mentioned in Table 2.1 via the activation technique relative to the  $^{197}\text{Au}(n,2n)^{196}\text{Au}$ ,  $^{27}\text{Al}(n,\alpha)^{24}\text{Na}$  and  $^{93}\text{Nb}(n,2n)^{92}\text{Nb}^m$  reference reactions. The results are summarized in Table 5.1.

The irradiations were performed at the 5.5 MV Tandem Van de Graaff accelerator of the Institute of Nuclear and Particle Physics at N.C.S.R. “Demokritos”. The low energy neutron beams (10.1-11.3 MeV) were produced via the DD reaction, whereas the neutron beams at higher energies (17.1-19.6 MeV) were produced via the DT reaction. Following the irradiations the induced activity of the samples was measured via  $\gamma$ -spectroscopy using HPGe detectors.

In the present work the full advantage of the power and accuracy of the GEANT4 toolkit was taken for the characterization of the HPGe detectors and the determination of their efficiency. In addition, a peak analysis and unfolding method for low energy  $\gamma$ -ray spectroscopy based on the GEANT4 simulation of the  $\gamma$ -ray spectrum is presented. This method was utilized for the determination of the actual counting integral of the  $\gamma$ -transition of  $^{164}\text{Ho}^m$  at 37.3 keV. This photopeak was contaminated by Ge X-ray escape peaks. Furthermore, the neutron beams produced at “Demokritos” were simulated through the GEANT4 toolkit by taking into account the full geometry of the primary targets ( $\text{D}_2$  gas cell and TiT target), as well as the deuteron beam line.

The present thesis concerns a systematic study of the (n,2n) reaction channel for the isotopes:  $^{162}\text{Er}$ ,  $^{156}\text{Dy}$  and  $^{165}\text{Ho}$ , which belong to medium-to-heavy mass region. In an attempt to understand the theoretical calculations performance for this mass region, extensive calculations were executed using the TALYS code. Calculations were

performed in order to investigate the sensitivity of the calculations when different models are considered, as well as to identify the optimum combination of models that better reproduces the measurements. In the basis of the TALYS calculations the following remarks can be drawn:

- The highest changes in the calculated excitation functions are noticed when different models are considered for the level density.
- The performance of the level density models can be improved when they are combined with different models for the pre-equilibrium emission and the  $\gamma$ -ray strength functions of the E1 transition.
- The replacement of the optical potential of Koning-Delaroche with the semi-microscopic potential of Bauge did not reveal remarkable changes in the excitation functions of the reactions under study.
- The Generalized Superfluid model fails to describe the excitation function of isotopes that belong to the limits of the valley of stability. In particular, its performance deteriorates when the lightest stable isotopes of the Er and Dy elements,  $^{162}\text{Er}$  and  $^{156}\text{Dy}$ , are considered. On the other hand, the Generalized Superfluid model can describe very effectively the cross section of isotopes that do not belong to the category of neutron deficient isotopes. For example, calculations based on this model follow the trend of the present measurements for the (n,2n) channel on  $^{165}\text{Ho}$  for both the cases of populating the isomeric and the ground state of  $^{164}\text{Ho}$ . In addition, its optimum behavior for not neutron deficient isotopes has also been discussed in Ref. [111]- [113], where the study of the (n,2n) reaction channel for the  $^{197}\text{Au}$ ,  $^{191}\text{Ir}$  and  $^{193}\text{Ir}$  isotopes is presented.
- The optimum combinations of models that better reproduce the present measurements are given in Table 6.1.

In the future, it will be really interesting to extend the cross section measurements of the (n,2n) reaction in the medium-to-heavy mass region. Some candidates for this study are the  $^{127}\text{I}$ ,  $^{133}\text{Cs}$  and  $^{136}\text{Ce}$  isotopes for which some preliminary tests about the feasibility of the experiments at the Institute of Nuclear and Particle Physics of “Demokriros” have already been performed [114, 115]. The obtained measurements can be used in order to investigate if the optimum combination of models of TALYS presented in the present thesis, as well as the remarks made about the behavior of the models apply also to these physics cases. In this way, even more strong conclusions will be drawn. Specifically, it is challenging to investigate the performance of the Generalized Superfluid model for  $^{136}\text{Ce}$ , since this is the lightest stable isotope of Ce.

# Appendices

# Appendix A

## Energy diagram

The energy diagram of a compound-nucleus interaction is a schematic representation, where the energy levels of the input and the possible output channels are presented, considering the intermediate compound-system energy level as the level of reference. For example, for the  $A + a \rightarrow X^* \rightarrow A' + a'$  hypothetical reaction, a typical energy diagram has the form of Figure A1. The excitation energy  $E_x$  of the compound-nucleus is calculated via Eq. A.1:

$$E_x = S_a + E_{a,CMS} \quad (\text{A.1})$$

where  $S_a$  is the binding energy of particle  $a$  in the  $X^*$  compound-nucleus and  $E_{a,CMS}$  is the energy of the particle  $a$  at CMS (Center of Mass System). The binding energy  $S_a$  is equal to:

$$S_a = \Delta(A) + \Delta(a) - \Delta(X^*) \quad (\text{A.2})$$

The abbreviation  $\Delta$  stands for the mass excess of the corresponding nuclei. The energy of particle  $\alpha$  at CMS is approximated using non-relativistic kinematics as follows:

$$E_{a,CMS} = E_{a,Lab} * \frac{A_A}{A_{X^*}} \quad (\text{A.3})$$

where  $A$  stands for the mass numbers of the corresponding nuclei and  $E_{a,Lab}$  is the energy at the laboratory system.

The output channels energy levels are calculated via Eq. A.4:

$$E_{oc} = \Delta(X^*) - \Delta(a') - \Delta(A') \quad (\text{A.4})$$



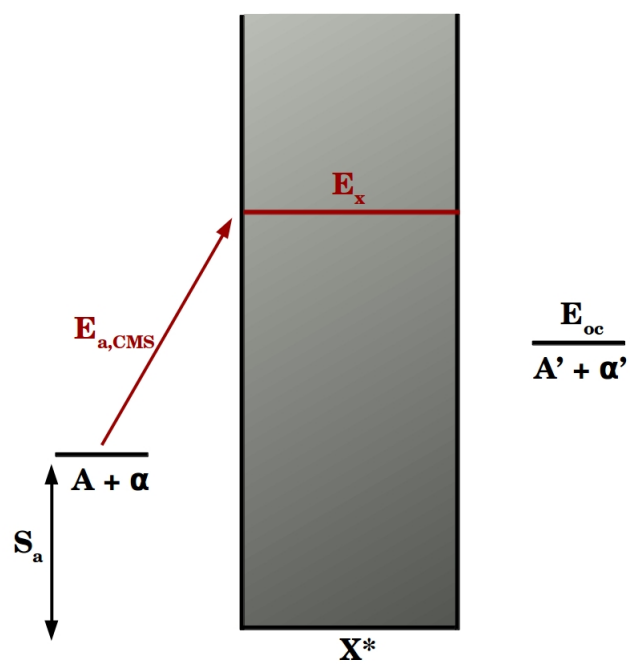


Figure A1: A typical energy diagram of an hypothetical reaction  $A+a \rightarrow X^* \rightarrow A'+a'$ .

# Appendix B

## Standard equation of activation technique

For the measurement of the cross section of a nuclear reaction at a specific energy through activation technique, the sample is irradiated with mono-energetic beam. During irradiation several nuclear reactions are induced depending on the isotopes that are present in the sample, the beam flux and the cross section of the induced reactions at the beam energy. For a particular nuclear reaction the activated nuclei production rate  $\frac{dN_{act}}{dt}$  during the irradiation time ( $t_{irr}$ ) is given by the following equation:

$$\frac{dN_{act}}{dt} = \sigma * f(t) * N_T - \lambda * N_{act} \quad (B.1)$$

where,

$\sigma$  is the reaction cross section

$f(t)$  is the beam flux at a moment  $t$

$N_T$  is the number of target-nuclei in the sample

$\lambda$  is the decay constant of the activated nuclei

By solving this equation the number of activated nuclei at the end of the irradiation can be deduced:

$$\begin{aligned} \frac{dN_{act}}{dt} * e^{\lambda t} &= \sigma * f(t) * N_T * e^{\lambda t} - \lambda * N_{act} * e^{\lambda t} \Rightarrow \\ \frac{dN_{act}}{dt} * e^{\lambda t} + \lambda * N_{act} * e^{\lambda t} &= \sigma * f(t) * N_T * e^{\lambda t} \Rightarrow \\ \frac{dN_{act}}{dt} * e^{\lambda t} + N_{act} * \frac{de^{\lambda t}}{dt} &= \sigma * f(t) * N_T * e^{\lambda t} \Rightarrow \\ \frac{d(N_{act} * e^{\lambda t})}{dt} &= \sigma * f(t) * N_T * e^{\lambda t} \end{aligned}$$

Integrating from the  $t=0$  (irradiation start) to a moment  $t$ :

$$\begin{aligned}
\int_0^t \left( \frac{d(N_{act} * e^{\lambda t})}{dt} \right) dt &= \int_0^t (\sigma * f(t) * N_T * e^{\lambda t}) dt \Rightarrow \\
N_{act} * e^{\lambda t} &= \int_0^t (\sigma * f(t) * N_T * e^{\lambda t}) dt \Rightarrow \\
N_{act} &= \sigma * N_T * \frac{\int_0^t (f(t) * e^{\lambda t}) dt}{e^{\lambda t}} \Rightarrow \\
N_{act} &= \sigma * N_T * \int_0^t (f(t) * e^{\lambda t}) dt * e^{-\lambda t} \\
\text{Multiplying with } \frac{\int_0^t f(t) dt}{\int_0^t f(t) dt} &= 1: \\
N_{act} &= \sigma * N_T * \int_0^t (f(t) * e^{\lambda t}) dt * \frac{\int_0^t f(t) dt}{\int_0^t f(t) dt} * e^{-\lambda t}
\end{aligned}$$

At the end of irradiation ( $t = t_{irr}$ ) the number of activated nuclei is given by the following equation:

$$N_0 = \sigma * \Phi * N_T * f_B \quad (\text{B.2})$$

where,  $\Phi = \int_0^{t_{irr}} f(t) dt$  is the total irradiation flux and

$$f_B = \frac{\int_0^{t_{irr}} f(t) * e^{\lambda t} dt}{\int_0^{t_{irr}} f(t) dt} * e^{-\lambda t_{irr}} \quad (\text{B.3})$$

The factor  $f_B$  corrects for the activated nuclei decay during irradiation.

After the irradiation ends, the activated samples are transferred to an appropriate detection system in order to measure the induced activity. Before the measurement starts, a time interval mediates, called “waiting time” ( $t_w$ ). This time is equal to the time needed for the dismount of the samples from the irradiation set-up and their placement in the detection set-up. In addition, some extra time is needed before entering the irradiation room for radio-protection reasons.

During  $t_w$  the activated nuclei decay according to the decay constant  $\lambda$ :

$$N = N_0 * e^{-\lambda t_w} \quad (\text{B.4})$$

During the measurement time, the cps (counts per second) recorded by the detector are given via the following equation:

$$cps = \frac{dN}{dt} * \varepsilon * I \quad (\text{B.5})$$

where,

$I$  is the intensity of the emitted radiation

$\varepsilon$  is the efficiency of the detector

Following the decay law  $\frac{dN}{dt} = \lambda * N$ :

$$cps = \lambda * N * \varepsilon * I \Rightarrow$$

$$cps = \lambda * N_0 * e^{-\lambda t} * \varepsilon * I$$

Integrating for the time interval between the measurement start ( $t_w$ ) and end ( $t_w + t_m$ ):

$$counts = \lambda * N_0 * \varepsilon * I * \int_{t_w}^{t_w+t_m} e^{-\lambda t} \Rightarrow$$

$$counts = N_0 * \varepsilon * I * (e^{-\lambda t_w} - e^{-\lambda(t_w+t_m)}) \Rightarrow$$

$$counts = N_0 * \varepsilon * I * e^{-\lambda t_w} * (1 - e^{-\lambda t_m})$$

The last equation provides the number of *counts* that have been recorded at the end of the measurement. Usually, the *counts* have to be corrected in order to obtain the actual activity of the sample. These corrections are usually related to the detection system dead-time, the self-attenuation effect, the coincidence-summing effect etc. By denoting with  $C$  the factor that corrects for all the phenomena that have been observed, the actual activity is equal to:

$$A = counts * C = N_0 * \varepsilon * I * e^{-\lambda t_w} * (1 - e^{-\lambda t_m}) * C \quad (B.6)$$

By combining Eqs. B.2 and B.6 the standard equation that provides the cross section in the activation technique is obtained:

$$\sigma = \frac{counts * C}{\Phi * N_T * \varepsilon * I * e^{-\lambda t_w} * (1 - e^{-\lambda t_m}) * f_B} \quad (B.7)$$

# Appendix C

## The $f_B$ correction factor

The  $f_B$  factor, which corrects for the activated nuclei decay during irradiation, is determined as following:

1. for constant flux  $f(t) = \Phi$ :

$$f_B = \frac{\int_0^{t_{irr}} f(t) * e^{\lambda t} dt}{\int_0^{t_{irr}} f(t) dt} * e^{-\lambda t_{irr}} \Rightarrow$$

$$f_B = \Phi * \frac{\int_0^{t_{irr}} e^{\lambda t} dt}{\Phi \int_0^{t_{irr}} dt} * e^{-\lambda t_{irr}} \Rightarrow$$

$$f_B = \frac{1}{\lambda} \frac{(e^{\lambda t_{irr}} - 1)}{t_{irr}} * e^{-\lambda t_{irr}} \Rightarrow$$

$$f_B = \frac{(1 - e^{-\lambda t_{irr}})}{\lambda * t_{irr}} \tag{C.1}$$

2. for non-constant flux the integral in Eq. B.3 has to be replaced with a sum over different time intervals:

$$f_B = \frac{\int_0^{t_{irr}} f(t) * e^{\lambda t} dt}{\int_0^{t_{irr}} f(t) dt} * e^{-\lambda t_{irr}} \Rightarrow$$

$$f_B = \frac{\sum_{lower}^{upper} f(t) * e^{\lambda t} \Delta t}{\sum_{lower}^{upper} f(t) \Delta t} * e^{-\lambda t_{irr}}$$

In this case the  $f_B$  factor is calculated by a code developed in the C++ programming language which takes into account the fluctuations in the neutron beam. The code is presented below:

```

/*this C++ code calculates the correction factor FB for the case of non-constant
flux */

# include <iostream>
# include <cmath>
# include <fstream>
using namespace std;

int main ()
{
char filename[20]; //File with neutron beam fluctuations
double half_life; //Half-life of the populated isotope
double lamda; //Decay constant of the populated isotope
double Irradiation_time; //Irradiation time
int number_of_channels; //number of channels;
double dt; //time interval corresponding to each channel
double flux[5000],ch[5000];
double sum_1=0., sum_2=0.;
cout<<"give the half-life in seconds: ";
cin>>half_life;
lamda=log(2)/half_life;
cout<<"give the name of the file: ";
cin>>filename;
cout<<"give the number of channels: ";
cin>>number_of_channels;
cout<<"give the total irradiation time in seconds: ";
cin>>Irradiation_time;
cout<<"the time interval of each channel ";
dt=Irradiation_time/number_of_channels;
double fb;

ifstream infile;
infile.open(filename);
for (int i=0;i<number_of_channels;i++){
infile>>ch[i]>>flux[i];
}
for(int j=0;j<number_of_channels;j++){
sum_2=sum_2+flux[j];
sum_1=sum_1+flux[j]*(exp((j+1)*lamda*dt)-exp((j)*lamda*dt));
}
fb=(exp(-lamda*Irradiation_time)/(lamda*dt))*(sum_1/sum_2);

cout<<"the correction factor for non constant flux is: ";
cout<<fb<<"\n";
cout<<"the correction factor for constant flux is:"<<(1-exp(-
lamda*Irradiation_time))/(lamda*Irradiation_time)<<"\n";
}

```

# Appendix D

## Equation of activation technique when the population from an isomeric state is considered

There is the case where the induced reaction populates not only the ground state, but also one or more isomeric states which decay to the ground state. These cases often demand a different handling according to the half-life of the corresponding states:

- The half-life of the isomeric state ( $T_{1/2}^m$ ) is too short in comparison with the half-life of the ground state ( $T_{1/2}^g$ ) and the irradiation time ( $T_{1/2}^m \ll T_{1/2}^g$  and  $T_{1/2}^m \ll t_{irr}$ ).

In this case the activated nuclei production rate is given by the following equation:

$$\frac{dN_{act}^g}{dt} = \sigma_g * f(t) * N_T + \lambda_m * N_{act}^m - \lambda_g * N_{act}^g \quad (D.1)$$

where,

$N_{act}^g$  is number of nuclei that are activated in the ground state

$N_{act}^m$  is number of nuclei that are activated in the isomeric state

$\sigma_g$  is the cross section for the population of the ground state

$\sigma_m$  is the cross section for the population of the isomeric state

$\lambda_g$  is the decay constant of the ground state

$\lambda_m$  is the decay constant of the isomeric state

Due to the fact that  $t_{irr} \gg T_{1/2}^m$  the saturation activity of the isomeric state is reached very soon after the beginning of the irradiation and  $\lambda_m * N_{act}^m = \sigma_m * f(t) * N_T$ :

$$\begin{aligned} \frac{dN_{act}^g}{dt} &= \sigma_g * f(t) * N_T + \sigma_m * f(t) * N_T - \lambda_g * N_{act}^g \Rightarrow \\ \frac{dN_{act}^g}{dt} &= (\sigma_g + \sigma_m) * f(t) * N_T - \lambda_g * N_{act}^g \Rightarrow \end{aligned}$$

$$\frac{dN_{act}^g}{dt} = \sigma_{tot} * f(t) * N_T - \lambda_g * N_{act}^g \quad (D.2)$$

Eq. D.2 is similar to Eq. B.1. The only difference is that the cross section of the nuclear reaction is the the sum of the cross sections for the population of the ground and the isomeric states. By following the mathematical process described in Appendix B, Eq. B.7 will be obtained.

- The ground and the isomeric state have similar half-lives ( $T_{1/2}^m \approx T_{1/2}^g$ ). Now  $\lambda_m * N_{act} \neq \sigma_m * f(t) * N_T$  because the saturation activity of the isomeric state will not be reached soon since the beginning of the irradiation:

$$\frac{dN_{act}^g}{dt} = \sigma_g * f(t) * N_T + \lambda_m * N_{act}^m - \lambda_g * N_{act}^g \Rightarrow \quad (D.3)$$

$$\begin{aligned} \frac{dN_{act}^g}{dt} &= \sigma_g * f(t) * N_T - \lambda_g * N_{act}^g + \lambda_m * \frac{\sigma_m * f(t) * N_T * (1 - e^{-\lambda_m t})}{\lambda_m} \Rightarrow \\ \frac{dN_{act}^g}{dt} + \lambda_g * N_{act}^g &= \sigma_g * f(t) * N_T + \sigma_m * f(t) * N_T * (1 - e^{-\lambda_m t}) \Rightarrow \\ \frac{dN_{act}^g}{dt} * e^{\lambda_g t} + \lambda_g * N_{act}^g * e^{\lambda_g t} &= \sigma_g * f(t) * N_T * e^{\lambda_g t} + \sigma_m * f(t) * N_T * (1 - e^{-\lambda_m t}) * e^{\lambda_g t} \Rightarrow \\ \frac{d(N_{act}^g * e^{\lambda_g t})}{dt} &= \sigma_g * f(t) * N_T * e^{\lambda_g t} + \sigma_m * f(t) * N_T * (e^{\lambda_g t} - e^{\lambda_g t - \lambda_m t}) \Rightarrow \\ \int_0^t \left( \frac{d(N_{act}^g * e^{\lambda_g t})}{dt} \right) dt &= \int_0^t (\sigma_g * f(t) * N_T * e^{\lambda_g t}) dt + \int_0^t (\sigma_m * f(t) * N_T * (e^{\lambda_g t} - e^{\lambda_g t - \lambda_m t})) dt \Rightarrow \\ N_{act}^g * e^{\lambda_g t} &= \sigma_g * N_T * \left( \int_0^t (f(t) * e^{\lambda_g t}) dt \right) + \sigma_m * N_T * \left( \int_0^t (f(t) * (e^{\lambda_g t} - e^{\lambda_g t - \lambda_m t})) dt \right) \Rightarrow \\ \sigma_g * N_T * \left( \int_0^t (f(t) * e^{\lambda_g t}) dt \right) * e^{-\lambda_g t} &+ \sigma_m * N_T * \left( \int_0^t (f(t) * (e^{\lambda_g t} - e^{\lambda_g t - \lambda_m t})) dt \right) * e^{-\lambda_g t} \Rightarrow \\ N_{act}^g &= \sigma_g * N_T * \left( \int_0^t (f(t) * e^{\lambda_g t}) dt \right) * \frac{\int_0^t f(t) dt}{\int_0^t f(t) dt} * e^{-\lambda_g t} + \sigma_m * N_T * \left( \int_0^t (f(t) * (e^{\lambda_g t} - \right. \\ &\left. e^{\lambda_g t - \lambda_m t})) dt \right) * \frac{\int_0^t f(t) dt}{\int_0^t f(t) dt} * e^{-\lambda_g t} \Rightarrow \\ N_{act}^g &= \sigma_g * N_T * \Phi * \left( \frac{\int_0^t (f(t) * e^{\lambda_g t}) dt}{\int_0^t f(t) dt} \right) * e^{-\lambda_g t} + \sigma_m * N_T * \Phi * \frac{\int_0^t (f(t) * (e^{\lambda_g t} - e^{\lambda_g t - \lambda_m t})) dt}{\int_0^t f(t) dt} * e^{-\lambda_g t} \end{aligned}$$

At the end of the irradiation time ( $t=t_{irr}$ ) the nuclei which are activated in the ground state are obtained by Eq. D.4:

$$\begin{aligned} N_{act}^g &= \\ \sigma_g * N_T * \Phi * \left( \frac{\int_0^{t_{irr}} (f(t) * e^{\lambda_g t}) dt}{\int_0^{t_{irr}} f(t) dt} \right) * e^{-\lambda_g t_{irr}} &+ \sigma_m * N_T * \Phi * \frac{\int_0^{t_{irr}} (f(t) * (e^{\lambda_g t} - e^{\lambda_g t - \lambda_m t})) dt}{\int_0^{t_{irr}} f(t) dt} * e^{-\lambda_g t_{irr}} \Rightarrow \end{aligned}$$



$$N_0^g = \sigma_g * N_T * \Phi * f'_B + \sigma_m * N_T * \Phi * f_C \quad (D.4)$$

where,

$$f'_B = \frac{\int_0^{t_{irr}} (f(t) * e^{\lambda_g t}) dt}{\int_0^{t_{irr}} f(t) dt} e^{-\lambda_g t_{irr}} \quad (D.5)$$

$$f_C = \frac{\int_0^{t_{irr}} f(t) * e^{\lambda_g t} dt}{\int_0^{t_{irr}} f(t) dt} * e^{-\lambda_g t_{irr}} - \frac{\int_0^{t_{irr}} f(t) * e^{(\lambda_g - \lambda_m)t} dt}{\int_0^{t_{irr}} f(t) dt} * e^{-\lambda_g t_{irr}} \quad (D.6)$$

The population from the isomeric state is taken into account during the “waiting time”:

$$\begin{aligned} \frac{dN^g}{dt} &= \lambda_m * N_m - \lambda_g * N_g \Rightarrow \\ \frac{dN^g}{dt} + \lambda_g * N_g &= \lambda_m * N_m \Rightarrow \\ \frac{dN^g}{dt} * e^{\lambda_g t} + \lambda_g * N_g * e^{\lambda_g t} &= \lambda_m * N_m * e^{\lambda_g t} \Rightarrow \\ \frac{d(N^g * e^{\lambda_g t})}{dt} &= \lambda_m * N_m * e^{\lambda_g t} \Rightarrow \\ \int_0^t \left( \frac{d(N^g * e^{\lambda_g t})}{dt} \right) dt &= \int_0^t (\lambda_m * N_m * e^{\lambda_g t}) dt \Rightarrow \\ N^g * e^{\lambda_g t} - N_0^g &= \lambda_m * \int_0^t (N_0^m * e^{-\lambda_m t} * e^{\lambda_g t}) dt \Rightarrow \\ N^g * e^{\lambda_g t} - N_0^g &= \lambda_m * N_0^m * \int_0^t e^{(\lambda_g - \lambda_m)t} dt \Rightarrow \\ N^g &= N_0^g * e^{-\lambda_g t} + \frac{\lambda_m}{\lambda_g - \lambda_m} * N_0^m * e^{(\lambda_g - \lambda_m)t} \end{aligned} \quad (D.7)$$

where  $N_0^m$  is the number of nuclei activated in the isomeric state at the end of the irradiation (calculated by Eq. B.2).

During the measurement time ( $t_m$ ):

$$\begin{aligned} cps &= \frac{dN^g}{dt} * \varepsilon_g * I_g \Rightarrow \\ cps &= \lambda_g * N^g * \varepsilon_g * I_g \Rightarrow \end{aligned}$$

where,

$I_g$  is the intensity of the emitted radiation

$\varepsilon_g$  in the efficiency of the detector

Eq. D.7 is substituted to the above equation:

$$\begin{aligned}
cps_g &= \lambda_g * (N_0^g * e^{-\lambda_g t} + \frac{\lambda_m}{\lambda_g - \lambda_m} * N_0^m * e^{(\lambda_g - \lambda_m)t}) * \varepsilon_g * I_g \Rightarrow \\
counts_g &= \varepsilon_g * I_g * \lambda_g * \int_{t_w}^{t_w + t_m} (N_0^g * e^{-\lambda_g t} + \frac{\lambda_m}{\lambda_g - \lambda_m} * N_0^m * e^{(\lambda_g - \lambda_m)t}) dt \Rightarrow \\
counts_g &= \varepsilon_g * I_g * \lambda_g * (N_0^g * \int_{t_w}^{t_w + t_m} e^{-\lambda_g t} dt + N_0^m * \int_{t_w}^{t_w + t_m} \frac{\lambda_m}{\lambda_g - \lambda_m} * e^{(\lambda_g - \lambda_m)t} dt) \Rightarrow \\
counts_g &= \varepsilon_g * I_g * \lambda_g * (N_0^g * \frac{1}{\lambda_g} (e^{-\lambda_g t_w} - e^{-\lambda_g(t_w + t_m)})) + N_0^m * \frac{\lambda_m}{\lambda_g - \lambda_m} * (\frac{1}{\lambda_m} * (e^{-\lambda_m t_w} - \\
&\quad e^{-\lambda_m(t_w + t_m)})) - \frac{1}{\lambda_g} * (e^{-\lambda_g t_w} - e^{-\lambda_g(t_w + t_m)})) \Rightarrow \\
counts_g &= \varepsilon_g * I_g * \lambda_g * (N_0^g * \frac{1}{\lambda_g} * e^{-\lambda_g t_w} * (1 - e^{-\lambda_g t_m}) + N_0^m * \frac{1}{\lambda_g - \lambda_m} * (e^{-\lambda_m t_w} * (1 - \\
&\quad e^{-\lambda_m t_m}) - \frac{\lambda_m}{\lambda_g} * e^{-\lambda_g t_w} * (1 - e^{-\lambda_g t_m}))) \Rightarrow \\
counts_g &= \varepsilon_g * I_g * (N_0^g * e^{-\lambda_g t_w} * (1 - e^{-\lambda_g t_m}) + N_0^m * \frac{1}{\lambda_g - \lambda_m} * (\lambda_g * e^{-\lambda_m t_w} * (1 - \\
&\quad e^{-\lambda_m t_m}) - \lambda_m * e^{-\lambda_g t_w} * (1 - e^{-\lambda_g t_m})))
\end{aligned}$$

The actual activity due to the decay of the ground state is given by Eq. D.8, where the factor C, as previously, corrects for the detector dead time, the self attenuation, the coincidence-summing effect etc.

$$\begin{aligned}
A_g &= C * counts_g = C * (\varepsilon_g * I_g * (N_0^g * e^{-\lambda_g t_w} * (1 - e^{-\lambda_g t_m}) \\
&\quad + N_0^m * \frac{1}{\lambda_g - \lambda_m} * (\lambda_g * e^{-\lambda_m t_w} * (1 - e^{-\lambda_m t_m}) - \lambda_m * e^{-\lambda_g t_w} * (1 - e^{-\lambda_g t_m}))))
\end{aligned} \tag{D.8}$$

The formula which provides the cross section of the ground state is obtained by combining Eqs. B.2, D.4 and D.8 (where Eq. B.2 refers to the isomeric state):

$$\begin{aligned}
\sigma_g &= \frac{counts_g C_g}{\Phi N_T \varepsilon_g I_g e^{-\lambda_g t_w} (1 - e^{-\lambda_g t_m}) f_B'} \tag{D.9} \\
\sigma_m &= \left( \frac{f_B}{f_B'} \frac{\frac{1}{\lambda_g - \lambda_m} (\lambda_g e^{-\lambda_m t_w} (1 - e^{-\lambda_m t_m}) - \lambda_m e^{-\lambda_g t_w} (1 - e^{-\lambda_g t_m}))}{e^{-\lambda_g t_w} (1 - e^{-\lambda_g t_m})} + \frac{f_C}{f_B'} \right)
\end{aligned}$$

# Appendix E

## The $f_C$ correction factor

The  $f_C$  correction factor is determined as following:

1. for constant flux  $f(t) = \Phi$ :

$$\begin{aligned}
 f_C &= \frac{\int_0^{t_{irr}} f(t) * (e^{\lambda_g t} - e^{(\lambda_g - \lambda_m)t}) dt}{\int_0^{t_{irr}} f(t) dt} * e^{-\lambda_g t_{irr}} \\
 f_C &= \frac{\int_0^{t_{irr}} f(t) * e^{\lambda_g t} dt}{\int_0^{t_{irr}} f(t) dt} * e^{-\lambda_g t_{irr}} - \frac{\int_0^{t_{irr}} f(t) * e^{(\lambda_g - \lambda_m)t} dt}{\int_0^{t_{irr}} f(t) dt} * e^{-\lambda_g t_{irr}} \\
 f_C &= \frac{\Phi * \int_0^{t_{irr}} e^{\lambda_g t} dt}{\int_0^{t_{irr}} f(t) dt} * e^{-\lambda_g t_{irr}} - \frac{\Phi * \int_0^{t_{irr}} e^{(\lambda_g - \lambda_m)t} dt}{\int_0^{t_{irr}} f(t) dt} * e^{-\lambda_g t_{irr}} \\
 f_C &= \frac{\Phi * \int_0^{t_{irr}} e^{\lambda_g t} dt}{\Phi * \int_0^{t_{irr}} dt} * e^{-\lambda_g t_{irr}} - \frac{\Phi * \int_0^{t_{irr}} e^{(\lambda_g - \lambda_m)t} dt}{\Phi * \int_0^{t_{irr}} dt} * e^{-\lambda_g t_{irr}} \\
 f_C &= \frac{e^{\lambda_g t_{irr}} - 1}{\lambda_g * t_{irr}} * e^{-\lambda_g t_{irr}} - \frac{e^{(\lambda_g - \lambda_m)t_{irr}} - 1}{(\lambda_g - \lambda_m) * t_{irr}} * e^{-\lambda_g t_{irr}} \\
 f_C &= \frac{1 - e^{-\lambda_g t_{irr}}}{\lambda_g * t_{irr}} - \frac{e^{-\lambda_m t_{irr}} - e^{-\lambda_g t_{irr}}}{(\lambda_g - \lambda_m) * t_{irr}} \tag{E.1}
 \end{aligned}$$

2. for non-constant flux, the integral in Eq. D.6 has to be replaced with a sum over the flux recorded in different time intervals:

$$\begin{aligned}
 f_C &= \frac{\int_0^{t_{irr}} f(t) * (e^{\lambda_g t} - e^{(\lambda_g - \lambda_m)t}) dt}{\int_0^{t_{irr}} f(t) dt} * e^{-\lambda_g t_{irr}} \Rightarrow \\
 f_C &= \frac{\int_0^{t_{irr}} f(t) * e^{\lambda_g t} dt}{\int_0^{t_{irr}} f(t) dt} * e^{-\lambda_g t_{irr}} - \frac{\int_0^{t_{irr}} f(t) * e^{(\lambda_g - \lambda_m)t} dt}{\int_0^{t_{irr}} f(t) dt} * e^{-\lambda_g t_{irr}} \Rightarrow \\
 f_C &= \frac{\sum_{lower}^{upper} f(t) * e^{\lambda_g t} dt}{\sum_{lower}^{upper} f(t) dt} * e^{-\lambda_g t_{irr}} - \frac{\sum_{lower}^{upper} f(t) * e^{(\lambda_g - \lambda_m)t} dt}{\sum_{lower}^{upper} f(t) dt} * e^{-\lambda_g t_{irr}} \Rightarrow
 \end{aligned}$$

The  $f_C$  factor is calculated according to the following code developed in C++ language, which takes into account the fluctuations in the neutron beam. The code is presented below:

```

/*this C++ code calculates the correction factor FC for the case of non-constant
flux */

# include <iostream>
# include <cmath>
# include <fstream>
using namespace std;

int main ()
{
char filename[20]; //File with the neutron beam fluctuations
double half_life_m; //Half-life of the isomeric state
double half_life_g; //Half-life of the ground state
double lamda_m; //Decay constant of the isomeric state
double lamda_g; //Decay constant of the ground state
double Irradiation_time; //Irradiation time
int number_of_channels; //number of channels
double dt; //time interval corresponding to each channel
double flux[5000],ch[5000];
double sum_1=0., sum_2=0., sum_3=0.;
cout<<"give the half-life of isomeric state in seconds: ";
cin>>half_life_m;
lamda_m=log(2)/half_life_m;
cout<<"give the half life of ground state in seconds: ";
cin>>half_life_g;
lamda_g=log(2)/half_life_g;
cout<<"give the name of the file: ";
cin>>filename;
cout<<"give the number of channels: ";
cin>>number_of_channels;
cout<<"give the total irradiation time in seconds : " ;
cin>>Irradiation_time;
cout<<"the time interval of each channel: ";
dt=Irradiation_time/number_of_channels;
double fb, fc, fd;

ifstream infile;
infile.open(filename);
for (int i=0;i<number_of_channels;i++){
infile>>ch[i]>>flux[i];
}
for(int j=0;j<number_of_channels;j++){
sum_2=sum_2+flux[j];
sum_1=sum_1+flux[j]*(exp((j+1)*lamda_g*dt)-exp((j)*lamda_g*dt));
sum_3=sum_3+flux[j]*(exp((j+1)*(lamda_g-lamda_m)*dt)-exp((j)*(lamda_g-
lamda_m)*dt));
}
fb=(exp(-lamda_g*Irradiation_time)/((lamda_g)*dt))*(sum_1/sum_2);
fd=(exp(-lamda_g*Irradiation_time)/((lamda_g-lamda_m)*dt))*(sum_3/sum_2);
fc=fb-fd;

cout<<fb<<"\n";
cout<<fd<<"\n";

cout<<"the correction factor for non constant flux is: ";
cout<<fc<<"\n";
cout<<"the correction factor for constant flux is:"<< 1/
(lamda_g*Irradiation_time)*(1+(lamda_m*exp(-lamda_g*Irradiation_time)-
lamda_g*exp(-lamda_m*Irradiation_time))/(lamda_g-lamda_m))<<"\n";
}

```

# Appendix F

## GEANT4 geometry file of the irradiation set-up in DD reaction

```
// Gas cell in Demokritos

#include "EfiDetectorConstruction.hh"
#include "G4SDManager.hh"
#include "G4Element.hh"
#include "G4Material.hh"
#include "G4Box.hh"
#include "G4Tubs.hh"
#include "G4LogicalVolume.hh"
#include "G4ThreeVector.hh"
#include "G4PVPlacement.hh"
#include "G4UnitsTable.hh"
#include "globals.hh"
#include "G4SystemOfUnits.hh"
#include "G4PhysicalConstants.hh"
#include "G4VisAttributes.hh"
#include "G4Colour.hh"

EfiDetectorConstruction::EfiDetectorConstruction()
{;}
EfiDetectorConstruction::~EfiDetectorConstruction()
{;}
G4VPhysicalVolume* EfiDetectorConstruction::Construct()
{
G4UnitDefinition::BuildUnitsTable();

//===== elements defintion =====//

G4double a;
G4double z;
G4int iz, in;
G4double density;
G4String name, symbol;
G4int ncomponents;
G4double fractionmass;
G4int natoms;

//----- defining 0
a = 15.999*g/mole;
G4Element* e10 = new G4Element(name="Oxygen", symbol=" O" , z= 8., a);
```

```

//----- defining N
a = 14.007*g/mole;
G4Element* elN = new G4Element(name="Nitrogen",symbol=" N" , z= 7., a);

//-----defining Fe
a = 55.845*g/mole;
G4Element* elFe = new G4Element(name="Iron", symbol=" Fe" , z= 26., a);

//-----defining C
a = 12.0107*g/mole;
G4Element* elC = new G4Element(name="Carbon",symbol=" C" , z= 6., a);

//-----defining P
a = 30.974*g/mole;
G4Element* elP = new G4Element(name="Phosphor",symbol=" P" , z= 15., a);

//-----defining S
a = 32.066*g/mole;
G4Element* elS = new G4Element(name="Sulfur",symbol=" S" , z= 16., a);

//-----defining Si
a = 28.0855*g/mole;
G4Element* elSi = new G4Element(name="Silicon",symbol=" Si" , z= 14., a);

//-----defining Cu
a = 63.546*g/mole;
G4Element* elCu = new G4Element(name="Copper",symbol=" Cu" , z= 29., a);

//-----defining Al
a = 26.981539*g/mole;
G4Element* elAl = new G4Element(name="Aluminium",symbol=" Al" , z= 13., a);

//-----defining Mn
a = 54.938*g/mole;
G4Element* elMn = new G4Element(name="Manganese", symbol=" Mn" , z= 25., a);

//-----defining Ni
a = 58.693*g/mole;
G4Element* elNi = new G4Element(name="Nickel",symbol=" Ni" , z= 28., a);

//-----defining Cr
a = 51.996*g/mole;
G4Element* elCr = new G4Element(name="Chromium",symbol=" Cr" , z= 24., a);

// Deuterium isotope definition
G4Isotope* isoH2 = new G4Isotope(name="deuterium", iz=1, in=2, a =
2.014*g/mole);

// Deuterium element definition
G4Element* elenrichedH = new G4Element("enrichedH", "D" ,ncomponents=1);
elenrichedH->AddIsotope(isoH2, fractionmass=100.*perCent);

//===== materials definition=====//

// ----- defining Al
a = 26.981539*g/mole;
density = 2.70*g/cm3;
G4Material* Al = new G4Material(name="Al", z=13., a, density);

// ----- defining Pt
a = 195.08*g/mole;
density = 21.45*g/cm3;
G4Material* Pt = new G4Material(name="Pt", z=78., a, density);

```

```

//-----defining Ta
a = 180.94788*g/mole;
density = 16.69*g/cm3;
G4Material* Ta = new G4Material(name="Ta", z=73., a, density);

//-----defining Mo
a = 95.940*g/mole;
density = 10.20*g/cm3;
G4Material* Mo = new G4Material(name="Mo", z=42., a, density);

//----- defining 2H material
density = 8.3729e-2*kg/m3;
G4Material* H2 = new G4Material(name="H2", density, ncomponents=1, kStateGas,
293*kelvin, 1.25*bar);
H2->AddElement(elenrichedH, fractionmass=100.0*perCent);

//-----defining Stainless Steel
density =8.02*g/cm3;
G4Material *StainlessSteel = new
G4Material(name="StainlessSteel", density, ncomponents=5);
StainlessSteel->AddElement(elFe, fractionmass=0.6996*perCent);
StainlessSteel->AddElement(elC, fractionmass=0.0004*perCent);
StainlessSteel->AddElement(elMn, fractionmass=0.01*perCent);
StainlessSteel->AddElement(elCr, fractionmass=0.19*perCent);
StainlessSteel->AddElement(elNi, fractionmass=0.10*perCent);

//----- defining Air
density = 1.29*mg/cm3;
G4Material *Air = new G4Material(name="Air ", density, ncomponents=2);
Air->AddElement(elO, fractionmass=30.0*perCent);
Air->AddElement(elN, fractionmass=70.0*perCent);

//----- defining vacuum
G4double pressure, temperature;
density = universe_mean_density;
pressure = 3.0E-18*pascal;
temperature = 2.73*kelvin;
G4Material *Vacuum = new G4Material(name="Vacuum", z=1.0, a=1.01*g/mole,
density, kStateGas, temperature,
pressure);

G4cout << "\n\n ####-----
#### \n";
G4cout << "\n\t\t#### List of isotopes used #### \n";
G4cout << "\n\n\n\n\t\t#### List of elements used #### \n";
G4cout << *(G4Element::GetElementTable());
G4cout << "\n\n\n\n\t\t#### List of materials used #### \n";
G4cout << *(G4Material::GetMaterialTable());
G4cout << "\n\n ####-----
#### \n";

//==== volumes definition ====//
// Option to switch on/off checking of volumes overlaps
// G4bool checkOverlaps = true;

//----- beam line along z axis
G4double startFi = 0.0*deg;
G4double endFi = 360.0*deg;

//----- world volume
G4double World_hx = 100./2.*cm;
G4double World_hy = 100./2.*cm;
G4double World_hz = 100./2.*cm;

```

```

G4Box *World_box
  = new G4Box("World_box",World_hx,World_hy,World_hz);

G4LogicalVolume *World_log
  = new G4LogicalVolume(World_box,Vacuum,"World_log",0,0,0);

G4VPhysicalVolume *World_phys
  = new G4PVPlacement(0,G4ThreeVector(),World_log,"World",0,false,0);

// ----- Vacuum surface a (inside the stainless steel
a)
G4double VsaOutR = 9.97/2.*cm; // 2x4.985
G4double VsaInR = 0.0*cm;
G4double VsaHalf = 90/2.*cm;

G4Tubs *Vsa_tube
  = new G4Tubs("Vsa_tube",VsaInR,VsaOutR,VsaHalf,
              startFi,endFi);

G4LogicalVolume *Vsa_log
  = new G4LogicalVolume(Vsa_tube,Vacuum,"Vsa_log",0,0,0);

G4double Pos_x = 0.0*cm;
G4double Pos_y = 0.0*cm;
G4double Pos_z = +3.68/2.*cm+0.7*cm+4.8*cm+0.0005*cm+VsaHalf;

G4VPhysicalVolume *Vsa_phys
  = new
G4PVPlacement(0,G4ThreeVector(Pos_x,Pos_y,Pos_z),Vsa_log,"VsaTube",World_log,fal
se,0);

// -----Stainless Steel surface a
G4double SSaOutR = 5.675*cm;
G4double SSaInR = 0.0*cm;
G4double SSaHalf = 90/2.*cm;

G4Tubs *SSa_tube
  = new G4Tubs("SSa_tube",SSaInR,SSaOutR,SSaHalf,
              startFi,endFi);

G4LogicalVolume *SSa_log
  = new G4LogicalVolume(SSa_tube,StainlessSteel,"SSa_log",0,0,0);

Pos_x = 0.0*cm;
Pos_y = 0.0*cm;
Pos_z = +3.68/2.*cm+0.7*cm+4.8*cm+0.0005*cm+SSaHalf;

G4VPhysicalVolume *SSa_phys
  = new
G4PVPlacement(0,G4ThreeVector(Pos_x,Pos_y,Pos_z),SSa_log,"SSaTube",World_log,fal
se,0);

// -----Stainless Steel b
G4double SSbOutR = SSaOutR;
G4double SSbInR = 0.0*cm;
G4double SSbHalf = 0.7/2.*cm;

G4Tubs *SSb_tube
  = new G4Tubs("SSb_tube",SSbInR,SSbOutR,SSbHalf,
              startFi,endFi);

G4LogicalVolume *SSb_log
  = new G4LogicalVolume(SSb_tube,StainlessSteel,"SSb_log",0,0,0);

```



```

Pos_x = 0.0*cm;
Pos_y = 0.0*cm;
Pos_z = +3.68/2.*cm+4.8*cm+0.0005*cm+SSbHalf;

G4VPhysicalVolume *SSb_phys
= new
G4PVPlacement(0,G4ThreeVector(Pos_x,Pos_y,Pos_z),SSb_log,"SSbTube",World_log,false,0);

// ----- Vacuum surface b (inside the stainless steel b)
G4double VsbOutR = 2.0/2.*cm;
G4double VsbInR = 0.0*cm;
G4double VsbHalf = 0.7/2.*cm;

G4Tubs *Vsb_tube
= new G4Tubs("Vsb_tube",VsbInR,VsbOutR,VsbHalf,
startFi,endFi);

G4LogicalVolume *Vsb_log
= new G4LogicalVolume(Vsb_tube,Vacuum,"Vsb_log",0,0,0);

Pos_x = 0.0*cm;
Pos_y = 0.0*cm;
Pos_z = +3.68/2.*cm+4.8*cm+0.0005*cm+VsbHalf;

G4VPhysicalVolume *Vsb_phys
= new
G4PVPlacement(0,G4ThreeVector(Pos_x,Pos_y,Pos_z),Vsb_log,"VsbTube",World_log,false,0);

// -----Stainless Steel surface c
G4double SScOutR = 2.04/2.*cm;
G4double SScInR = 0.0*cm;
G4double SScHalf = 4.78/2.*cm;

G4Tubs *SSc_tube
= new G4Tubs("SSc_tube",SScInR,SScOutR,SScHalf,
startFi,endFi);

G4LogicalVolume *SSc_log
= new G4LogicalVolume(SSc_tube,StainlessSteel,"SSc_log",0,0,0);

Pos_x = 0.0*cm;
Pos_y = 0.0*cm;
Pos_z = 3.68/2.*cm+0.02*cm+0.0005*cm+SScHalf;

G4VPhysicalVolume *SSc_phys
= new
G4PVPlacement(0,G4ThreeVector(Pos_x,Pos_y,Pos_z),SSc_log,"SScTube",World_log,false,0);

// ----- Vacuum surface c
G4double VscOutR = 2.0/2.*cm;
G4double VscInR = 0.0*cm;
G4double VscHalf = 4.78/2.*cm;

G4Tubs *Vsc_tube
= new G4Tubs("Vsc_tube",VscInR,VscOutR,VscHalf,
startFi,endFi);

G4LogicalVolume *Vsc_log
= new G4LogicalVolume(Vsc_tube,Vacuum,"Vsc_log",0,0,0);

Pos_x = 0.0*cm;

```

```

Pos_y = 0.0*cm;
Pos_z = 3.68/2.*cm+0.02*cm+0.0005*cm+VscHalf;

G4VPhysicalVolume *Vsc_phys
= new
G4PVPlacement(0,G4ThreeVector(Pos_x,Pos_y,Pos_z),Vsc_log,"VscTube",World_log,false,0);

//////////////////////////////////// Collimators //////////////////////////////////////
//----- 2nd collimator (before gas cell, diameter=5.0 cm)
G4double SD0=45*cm; // distance from the collimator to the centre of the gas
cell
G4double col2OutR = VsaOutR;
G4double col2InR = 0.0*cm;
G4double col2Half = 0.1/2.*cm;

G4Tubs *col2_tube
= new G4Tubs("col2_tube",col2InR,col2OutR,col2Half,
startFi,endFi);

G4LogicalVolume *col2_log
= new G4LogicalVolume(col2_tube,Ta,"col1_log",0,0,0);

Pos_x = 0.0*cm;
Pos_y = 0.0*cm;
Pos_z = -VsaHalf-0.7*cm-4.8*cm-0.0005*cm-3.68/2.*cm+SD0+col2Half;

G4VPhysicalVolume *col2_phys
= new
G4PVPlacement(0,G4ThreeVector(Pos_x,Pos_y,Pos_z),col2_log,"col2Tube",Vsa_log,false,0);

//----- 2nd collimator inside radius (before gas cell, diameter=5.0 mm)
G4double col2vOutR = 0.5/2.*cm;
G4double col2vInR = 0.0*cm;
G4double col2vHalf = 0.1/2.*cm;

G4Tubs *col2v_tube
= new G4Tubs("col2_tube",col2vInR,col2vOutR,col2vHalf,
startFi,endFi);

G4LogicalVolume *col2v_log
= new G4LogicalVolume(col2v_tube,Vacuum,"col1_log",0,0,0);

Pos_x = 0.0*cm;
Pos_y = 0.0*cm;
Pos_z = 0.0*cm;

G4VPhysicalVolume *col2v_phys
= new
G4PVPlacement(0,G4ThreeVector(Pos_x,Pos_y,Pos_z),col2v_log,"col2vTube",col2_log,
false,0);

//----- 1st collimator (diamater= 4.0 cm)
G4double SD00=43.2*cm;

G4double col1OutR = VsaOutR;
G4double col1InR = 0.0*cm;
G4double col1Half = 0.1/2.*cm;

G4Tubs *col1_tube
= new G4Tubs("col1_tube",col1InR,col1OutR,col1Half,
startFi,endFi);

```

```

G4LogicalVolume *col1_log
= new G4LogicalVolume(col1_tube, Ta, "col1_log", 0, 0, 0);

Pos_x = 0.0*cm;
Pos_y = 0.0*cm;
Pos_z = -VsaHalf-0.7*cm-4.8*cm-0.0005*cm-
3.68/2.*cm+SD0+2*col2Half+SD00+col1Half;

G4VPhysicalVolume *col1_phys
= new
G4PVPlacement(0, G4ThreeVector(Pos_x, Pos_y, Pos_z), col1_log, "col1Tube", Vsa_log, false, 0);

//----- 1st collimator inside radius (diamater= 4.0 mm)
G4double col1vOutR = 0.4/2.*cm;
G4double col1vInR = 0.0*cm;
G4double col1vHalf = 0.1/2.*cm;

G4Tubs *col1v_tube
= new G4Tubs("col1v_tube", col1vInR, col1vOutR, col1vHalf,
startFi, endFi);

G4LogicalVolume *col1v_log
= new G4LogicalVolume(col1v_tube, Vacuum, "col1_log", 0, 0, 0);

Pos_x = 0.0*cm;
Pos_y = 0.0*cm;
Pos_z = 0.0*cm;

G4VPhysicalVolume *col1v_phys
= new
G4PVPlacement(0, G4ThreeVector(Pos_x, Pos_y, Pos_z), col1v_log, "col1vTube", col1_log,
false, 0);

//////////////////////////////////////
// -----Stainless Steel bb
G4double SSbbOutR = SScOutR;
G4double SSbbInR = 0.0*cm;
G4double SSbbHalf = 0.02/2.*cm;

G4Tubs *SSbb_tube
= new G4Tubs("SSbb_tube", SSbbInR, SSbbOutR, SSbbHalf,
startFi, endFi);

G4LogicalVolume *SSbb_log
= new G4LogicalVolume(SSbb_tube, StainlessSteel, "SSbb_log", 0, 0, 0);

Pos_x = 0.0*cm;
Pos_y = 0.0*cm;
Pos_z = +3.68/2.*cm+0.0005*cm+SSbHalf;

G4VPhysicalVolume *SSbb_phys
= new
G4PVPlacement(0, G4ThreeVector(Pos_x, Pos_y, Pos_z), SSbb_log, "SSbbTube", World_log, false, 0);

// ----- Vacuum surface bb (inside the stainless steel
bb)
G4double VsbbOutR = 1.0/2.*cm;
G4double VsbbInR = 0.0*cm;
G4double VsbbHalf = 0.02/2.*cm;

G4Tubs *Vsbb_tube

```

```

= new G4Tubs("Vsbb_tube", VsbbInR, VsbbOutR, VsbbHalf,
            startFi, endFi);

G4LogicalVolume *Vsbb_log
= new G4LogicalVolume(Vsbb_tube, Vacuum, "Vsbb_log", 0, 0, 0);

Pos_x = 0.0*cm;
Pos_y = 0.0*cm;
Pos_z = +3.68/2.*cm+0.0005*cm+VsbbHalf;

G4VPhysicalVolume *Vsbb_phys
= new
G4PVPlacement(0, G4ThreeVector(Pos_x, Pos_y, Pos_z), Vsbb_log, "VsbbTube", World_log, f
alse, 0);

// -----Stainless Steel surface
G4double SSdOutR = 1.0/2.*cm;
G4double SSdInR = 0.96/2.*cm;
G4double SSdHalf = 0.0005/2.*cm;

G4Tubs *SSd_tube
= new G4Tubs("SSd_tube", SSdInR, SSdOutR, SSdHalf,
            startFi, endFi);

G4LogicalVolume *SSd_log
= new G4LogicalVolume(SSd_tube, StainlessSteel, "SSd_log", 0, 0, 0);

Pos_x = 0.0*cm;
Pos_y = 0.0*cm;
Pos_z = 3.68/2.*cm+SSdHalf;

G4VPhysicalVolume *SSd_phys
= new
G4PVPlacement(0, G4ThreeVector(Pos_x, Pos_y, Pos_z), SSd_log, "SSdTube", World_log, fal
se, 0);

// -----Mo foil
G4double Mo1OutR = 0.96/2.*cm;
G4double Mo1InR = 0.0*cm;
G4double Mo1Half = 0.0005/2.*cm;

G4Tubs *Mo1_tube
= new G4Tubs("Mo1_tube", Mo1InR, Mo1OutR, Mo1Half,
            startFi, endFi);

G4LogicalVolume *Mo1_log
= new G4LogicalVolume(Mo1_tube, Mo, "Mo1_log", 0, 0, 0);

Pos_x = 0.0*cm;
Pos_y = 0.0*cm;
Pos_z = +3.68/2.*cm+Mo1Half;

G4VPhysicalVolume *Mo1_phys
= new
G4PVPlacement(0, G4ThreeVector(Pos_x, Pos_y, Pos_z), Mo1_log, "Mo1Tube", World_log, fal
se, 0);

//----- Stainless Steel surface 0 (centred on the world volume, the D2 gas
is inside )
G4double SS0OutR = 1.0/2.*cm;
G4double SS0InR = 0.0*cm;
G4double SS0Half = 3.68/2.*cm;

G4Tubs *SS0_tube

```

```

= new G4Tubs("SS0_tube",SS0InR,SS0OutR,SS0Half,
startFi,endFi);

G4LogicalVolume *SS0_log
= new G4LogicalVolume(SS0_tube,StainlessSteel,"SS0_log",0,0,0);

Pos_x = 0.0*cm;
Pos_y = 0.0*cm;
Pos_z = 0.0*cm;

G4VPhysicalVolume *SS0_phys
= new
G4PVPlacement(0,G4ThreeVector(Pos_x,Pos_y,Pos_z),SS0_log,"SS0Tube",World_log,false,0);

//----- D2 Gas volume
G4double GasOutR = 0.96/2.*cm;
G4double GasInR = 0.0*cm;
G4double GasHalf = 3.66/2.*cm;

G4Tubs *Gas_tube
= new G4Tubs("Gas_tube", GasInR, GasOutR, GasHalf, startFi, endFi);

G4LogicalVolume *Gas_log
= new G4LogicalVolume(Gas_tube, H2, "Gas_log", 0,0,0);

Pos_x = 0.0*cm;
Pos_y = 0.0*cm;
Pos_z = +3.68/2.*cm-GasHalf;

G4VPhysicalVolume *Gas_phys
= new G4PVPlacement(0,
G4ThreeVector(Pos_x, Pos_y, Pos_z),
Gas_log, "GasTube", SS0_log, false,0);

// ----- Pt foil
G4double PtOutR = 0.96/2.*cm;
G4double PtInR = 0.0*cm;
G4double PtHalf = 0.02/2.*cm;

G4Tubs *Pt_tube
= new G4Tubs("Pt_tube",PtInR,PtOutR,PtHalf,
startFi,endFi);

G4LogicalVolume *Pt_log
= new G4LogicalVolume(Pt_tube,Pt,"Pt_log",0,0,0);

Pos_x = 0.0*cm;
Pos_y = 0.0*cm;
Pos_z = -3.68/2.*cm+PtHalf;

G4VPhysicalVolume *Pt_phys
= new
G4PVPlacement(0,G4ThreeVector(Pos_x,Pos_y,Pos_z),Pt_log,"PtTube",SS0_log,false,0);

//----- Target chamber
G4double SD=5.2*cm;

G4double TarOutR = 1.3/2.*cm;
G4double TarInR = 0.0*cm;
G4double TarHalf = 0.1/2.*cm;

G4Tubs *Tar_tube

```

```

= new G4Tubs("Tar_tube", TarInR, TarOutR, TarHalf,
            startFi, endFi);

G4LogicalVolume *Tar_log
= new G4LogicalVolume(Tar_tube, Vacuum, "Tar_log", 0, 0, 0);

Pos_x = 0.0*cm;
Pos_y = 0.0*cm;
Pos_z = -SS0Half-SD-TarHalf;
G4VPhysicalVolume *TarTube_phys
= new G4PVPlacement(0,
                    G4ThreeVector(Pos_x, Pos_y, Pos_z),
                    Tar_log, "TarTube", World_log, false, 0);

//===== Visualization attributes =====//

World_log->SetVisAttributes (G4VisAttributes::Invisible);

G4VisAttributes *SSaTubeAttr = new G4VisAttributes(G4Colour(0.5,0.5,0.5)); //
gray
SSaTubeAttr->SetVisibility(true);
SSaTubeAttr->SetForceWireframe(true);
SSa_log->SetVisAttributes(SSaTubeAttr);

G4VisAttributes *VsaTubeAttr = new G4VisAttributes(G4Colour(0.5,0.5,0.5)); //
gray
VsaTubeAttr->SetVisibility(true);
VsaTubeAttr->SetForceWireframe(true);
Vsa_log->SetVisAttributes(VsaTubeAttr);

G4VisAttributes *SSbTubeAttr = new G4VisAttributes(G4Colour(0.5,0.5,0.5)); //
gray
SSbTubeAttr->SetVisibility(true);
SSbTubeAttr->SetForceWireframe(true);
SSb_log->SetVisAttributes(SSbTubeAttr);

G4VisAttributes *VsbTubeAttr = new G4VisAttributes(G4Colour(0.5,0.5,0.5)); //
gray
VsbTubeAttr->SetVisibility(true);
VsbTubeAttr->SetForceWireframe(true);
Vsb_log->SetVisAttributes(VsbTubeAttr);

G4VisAttributes *SScTubeAttr = new G4VisAttributes(G4Colour(0.5,0.5,0.5)); //
gray
SScTubeAttr->SetVisibility(true);
SScTubeAttr->SetForceWireframe(true);
SSc_log->SetVisAttributes(SScTubeAttr);

G4VisAttributes *VscTubeAttr = new G4VisAttributes(G4Colour(0.5,0.5,0.5)); //
gray
VscTubeAttr->SetVisibility(true);
VscTubeAttr->SetForceWireframe(true);
Vsc_log->SetVisAttributes(VscTubeAttr);

G4VisAttributes *SSbbTubeAttr = new G4VisAttributes(G4Colour(0.5,0.5,0.5)); //
gray
SSbbTubeAttr->SetVisibility(true);
SSbbTubeAttr->SetForceWireframe(true);
SSbb_log->SetVisAttributes(SSbbTubeAttr);

G4VisAttributes *VsbbTubeAttr = new G4VisAttributes(G4Colour(0.5,0.5,0.5)); //
gray
VsbbTubeAttr->SetVisibility(true);
VsbbTubeAttr->SetForceWireframe(true);

```

```

Vsbb_log->SetVisAttributes(VsbbTubeAttr);

G4VisAttributes *SS0TubeAttr = new G4VisAttributes(G4Colour(0.5,0.5,0.5)); //
gray
SS0TubeAttr->SetVisibility(true);
SS0TubeAttr->SetForceWireframe(true);
SS0_log->SetVisAttributes(SS0TubeAttr);

G4VisAttributes *GasTubeAttr = new G4VisAttributes(G4Colour(1.,0.,0.)); // red
GasTubeAttr->SetVisibility(true);
GasTubeAttr->SetForceWireframe(true);
Gas_log->SetVisAttributes(GasTubeAttr);

G4VisAttributes *Mo1TubeAttr = new G4VisAttributes(G4Colour(0.,1.,0.)); //
green
Mo1TubeAttr->SetVisibility(true);
Mo1TubeAttr->SetForceWireframe(true);
Mo1_log->SetVisAttributes(Mo1TubeAttr);

G4VisAttributes *SSdTubeAttr = new G4VisAttributes(G4Colour(0.5,0.5,0.5)); //
gray
SSdTubeAttr->SetVisibility(true);
SSdTubeAttr->SetForceWireframe(true);
SSd_log->SetVisAttributes(SSdTubeAttr);

G4VisAttributes *PtTubeAttr = new G4VisAttributes(G4Colour(0.,1.,1.)); // cyan
PtTubeAttr->SetVisibility(true);
PtTubeAttr->SetForceWireframe(true);
Pt_log->SetVisAttributes(PtTubeAttr);

G4VisAttributes *col2TubeAttr = new G4VisAttributes(G4Colour(1.,1.,0.)); //
yellow
col2TubeAttr->SetVisibility(true);
col2TubeAttr->SetForceWireframe(true);
col2_log->SetVisAttributes(col2TubeAttr);

G4VisAttributes *col2vTubeAttr = new
G4VisAttributes(G4Colour(0.5,0.5,0.5)); // gray
col2vTubeAttr->SetVisibility(true);
col2vTubeAttr->SetForceWireframe(true);
col2v_log->SetVisAttributes(col2vTubeAttr);

G4VisAttributes *col1TubeAttr = new G4VisAttributes(G4Colour(1.,1.,0.)); //
yellow
col1TubeAttr->SetVisibility(true);
col1TubeAttr->SetForceWireframe(true);
col1_log->SetVisAttributes(col1TubeAttr);

G4VisAttributes *col1vTubeAttr = new
G4VisAttributes(G4Colour(0.5,0.5,0.5)); // gray
col1vTubeAttr->SetVisibility(true);
col1vTubeAttr->SetForceWireframe(true);
col1v_log->SetVisAttributes(col1vTubeAttr);

G4VisAttributes *TarTubeAttr = new G4VisAttributes(G4Colour(1.,0.,1.)); //
magenta
TarTubeAttr->SetVisibility(true);
TarTubeAttr->SetForceWireframe(true);
Tar_log->SetVisAttributes(TarTubeAttr);

return World_phys;
}

```

## Appendix G

# GEANT4 geometry file of the irradiation set-up in DT reaction

```
// TiT target in NCSR DEMOKRITOS

#include "EfiDetectorConstruction.hh"
#include "G4SDManager.hh"
#include "G4Element.hh"
#include "G4Material.hh"
#include "G4Box.hh"
#include "G4Tubs.hh"
#include "G4LogicalVolume.hh"
#include "G4ThreeVector.hh"
#include "G4PVPlacement.hh"
#include "G4UnitsTable.hh"
#include "globals.hh"
#include "G4SystemOfUnits.hh"
#include "G4PhysicalConstants.hh"
#include "G4VisAttributes.hh"
#include "G4Colour.hh"

EfiDetectorConstruction::EfiDetectorConstruction()
{;}
EfiDetectorConstruction::~EfiDetectorConstruction()
{;}
G4VPhysicalVolume* EfiDetectorConstruction::Construct()
{
G4UnitDefinition::BuildUnitsTable();

//===== elements defintion =====//

G4double a;
G4double z;
G4double iz;
G4double in;
G4double density;
G4String name, symbol;
G4int ncomponents;
G4double fractionmass;
G4int natoms;

//-----defining 0
a = 15.999*g/mole;
G4Element* e10 = new G4Element(name="Oxygen", symbol=" O" , z= 8., a);
```



```

//-----defining N
a = 14.007*g/mole;
G4Element* elN = new G4Element(name="Nitrogen",symbol=" N" , z= 7., a);

//-----defining Fe
a = 55.845*g/mole;
G4Element* elFe = new G4Element(name="Iron", symbol=" Fe" , z= 26., a);

//-----defining C
a = 12.0107*g/mole;
G4Element* elC = new G4Element(name="Carbon",symbol=" C" , z= 6., a);

//-----defining Mn
a = 54.938*g/mole;
G4Element* elMn = new G4Element(name="Manganese", symbol=" Mn" , z= 25., a);

//-----defining Cr
a = 51.996*g/mole;
G4Element* elCr = new G4Element(name="Chromium",symbol=" Cr" , z= 24., a);

//-----defining Ni
a = 58.693*g/mole;
G4Element* elNi = new G4Element(name="Nickel",symbol=" Ni" , z= 28., a);

//-----defining H3 isotope
a = 3.0160492*g/mole;
G4Isotope* isoH3 = new G4Isotope(name="tritium", iz=1, in=3, a);

//-----defining H3 element
G4Element* elenrichedH3 = new G4Element("enrichedH3", "T" ,ncomponents=1);
elenrichedH3->AddIsotope(isoH3, fractionmass=100.*perCent);

//-----defining Ti
a = 47.867*g/mole;
G4Element* Ti = new G4Element(name="Ti", symbol="Ti", z=22., a);

//===== materials definition =====//

//-----defining TiT
density = 1.8505*g/cm3;
G4Material *TiT = new G4Material(name="TiT",density,ncomponents=2);
TiT->AddElement(elenrichedH3, natoms=3);
TiT->AddElement(Ti, natoms=2);

// ----- defining Al
a = 26.981539*g/mole;
density = 2.70*g/cm3;
G4Material* Al = new G4Material(name="Al", z=13., a, density);

// ----- defining Pt
a = 195.08*g/mole;
density = 21.45*g/cm3;
G4Material* Pt = new G4Material(name="Pt", z=78., a, density);

//-----defining Cu
a = 63.546*g/mole;
density = 8.96*g/cm3;
G4Material* Cu = new G4Material(name="Cu", z=29., a, density);

//-----defining Mo
a = 95.940*g/mole;
density = 10.20*g/cm3;
G4Material* Mo = new G4Material(name="Mo", z=42., a, density);

```

```

//-----defining Ta
a = 180.94788*g/mole;
density = 16.69*g/cm3;
G4Material* Ta = new G4Material(name="Ta", z=73., a, density);

//-----defining Stainless Steel
density =8.02*g/cm3;
G4Material *StainlessSteel = new
G4Material(name="StainlessSteel", density, ncomponents=5);
StainlessSteel->AddElement(elFe, fractionmass=0.6996*perCent);
StainlessSteel->AddElement(elC, fractionmass=0.0004*perCent);
StainlessSteel->AddElement(elMn, fractionmass=0.01*perCent);
StainlessSteel->AddElement(elCr, fractionmass=0.19*perCent);
StainlessSteel->AddElement(elNi, fractionmass=0.10*perCent);

//-----Defining Air
density = 1.29*mg/cm3;
G4Material *Air = new G4Material(name="Air ", density, ncomponents=2);
Air->AddElement(elO, fractionmass=30.0*perCent);
Air->AddElement(elN, fractionmass=70.0*perCent);

// ----- defining vacuum
G4double pressure, temperature;
density = universe_mean_density;
pressure = 3.0E-18*pascal;
temperature = 2.73*kelvin;
G4Material *Vacuum = new G4Material(name="Vacuum", z=1.0, a=1.01*g/mole,
density, kStateGas, temperature,
pressure);

G4cout << "\n\n ####-----
#### \n";
G4cout << "\n\t\t#### List of isotopes used #### \n";
G4cout << "\n\n\n\n\t\t#### List of elements used #### \n";
G4cout << *(G4Element::GetElementTable());
G4cout << "\n\n\n\n\t\t#### List of materials used #### \n";
G4cout << *(G4Material::GetMaterialTable());
G4cout << "\n\n ####-----
#### \n";

//===== volumes =====//

// Option to switch on/off checking of volumes overlaps
// G4bool checkOverlaps = true;

//----- beam line along z axis
G4double startFi = 0.0*deg;
G4double endFi = 360.0*deg;

//----- world volume
G4double World_hx = 200./2.*cm;
G4double World_hy = 200./2.*cm;
G4double World_hz = 200./2.*cm;

G4Box *World_box
= new G4Box("World_box", World_hx, World_hy, World_hz);

G4LogicalVolume *World_log
= new G4LogicalVolume(World_box, Vacuum, "World_log", 0, 0, 0);

G4VPhysicalVolume *World_phys
= new G4PVPlacement(0, G4ThreeVector(), World_log, "World", 0, false, 0);

// -----Al surface 1 (centred on the world volume)

```

```

G4double Als1OutR = 11.35/2.*cm; // 5.675x2
G4double Als1InR = 0.0*cm;
G4double Als1Half = 3.88/2.*cm;

G4Tubs *Als1_tube
= new G4Tubs("Als1_tube",Als1InR,Als1OutR,Als1Half,
startFi,endFi);

G4LogicalVolume *Als1_log
= new G4LogicalVolume(Als1_tube,Al,"Als1_log",0,0,0);

G4double Pos_x = 0.0*cm;
G4double Pos_y = 0.0*cm;
G4double Pos_z = 0.0*cm;

G4VPhysicalVolume *Als1_phys
= new
G4PVPlacement(0,G4ThreeVector(Pos_x,Pos_y,Pos_z),Als1_log,"Als1Tube",World_log,f
alse,0);

// ----- Vacuum surface 0 (inside the stainless steel)
G4double Vs0OutR = 9.97/2.*cm; // 2x4.985
G4double Vs0InR = 0.0*cm;
G4double Vs0Half = 90/2.*cm;

G4Tubs *Vs0_tube
= new G4Tubs("Vs0_tube",Vs0InR,Vs0OutR,Vs0Half,
startFi,endFi);

G4LogicalVolume *Vs0_log
= new G4LogicalVolume(Vs0_tube,Vacuum,"Vs0_log",0,0,0);

Pos_x = 0.0*cm;
Pos_y = 0.0*cm;
Pos_z = +Als1Half+Vs0Half;

G4VPhysicalVolume *Vs0_phys
= new
G4PVPlacement(0,G4ThreeVector(Pos_x,Pos_y,Pos_z),Vs0_log,"Vs0Tube",World_log,fal
se,0);

// -----Stainless Steel 1
G4double SSaOutR = 5.675*cm; // (5.675-4.985) cm
G4double SSaInR = 4.985*cm;
G4double SSaHalf = 90/2.*cm;

G4Tubs *SSa_tube
= new G4Tubs("SSa_tube",SSaInR,SSaOutR,SSaHalf,
startFi,endFi);

G4LogicalVolume *SSa_log
= new G4LogicalVolume(SSa_tube,StainlessSteel,"SSa_log",0,0,0);

Pos_x = 0.0*cm;
Pos_y = 0.0*cm;
Pos_z = +Als1Half+SSaHalf;

G4VPhysicalVolume *SSa_phys
= new
G4PVPlacement(0,G4ThreeVector(Pos_x,Pos_y,Pos_z),SSa_log,"SSaTube",World_log,fal
se,0);

//////////////////////////////////// Collimators //////////////////////////////////////

```

```

//----- 2nd collimator (before TiT target, diameter=5.5 cm)
G4double SD0=45*cm; // distance from the collimator to the TiT target

G4double col2OutR = Vs0OutR;
G4double col2InR = 0.0*cm;
G4double col2Half = 0.1/2.*cm;

G4Tubs *col2_tube
  = new G4Tubs("col2_tube",col2InR,col2OutR,col2Half,
              startFi,endFi);

G4LogicalVolume *col2_log
  = new G4LogicalVolume(col2_tube,Ta,"col1_log",0,0,0);

Pos_x = 0.0*cm;
Pos_y = 0.0*cm;
Pos_z = -Vs0Half-2*Als1Half+0.43*cm+0.1*cm+0.00115*cm+SD0+col2Half;

G4VPhysicalVolume *col2_phys
  = new
G4PVPlacement(0,G4ThreeVector(Pos_x,Pos_y,Pos_z),col2_log,"col2Tube",Vs0_log,false,0);

//----- 2nd collimator inside radius (before TiT target, diameter=5.5 mm)
G4double col2vOutR = 0.55/2.*cm;
G4double col2vInR = 0.0*cm;
G4double col2vHalf = 0.1/2.*cm;

G4Tubs *col2v_tube
  = new G4Tubs("col2_tube",col2vInR,col2vOutR,col2vHalf,
              startFi,endFi);

G4LogicalVolume *col2v_log
  = new G4LogicalVolume(col2v_tube,Vacuum,"col1_log",0,0,0);

Pos_x = 0.0*cm;
Pos_y = 0.0*cm;
Pos_z = 0.0*cm;

G4VPhysicalVolume *col2v_phys
  = new
G4PVPlacement(0,G4ThreeVector(Pos_x,Pos_y,Pos_z),col2v_log,"col2vTube",col2_log,
false,0);

//----- 1st collimator (diamater= 5cm)
G4double SD00=43.2*cm;

G4double col1OutR = Vs0OutR;
G4double col1InR = 0.0*cm;
G4double col1Half = 0.1/2.*cm;

G4Tubs *col1_tube
  = new G4Tubs("col1_tube",col1InR,col1OutR,col1Half,
              startFi,endFi);

G4LogicalVolume *col1_log
  = new G4LogicalVolume(col1_tube,Ta,"col1_log",0,0,0);

Pos_x = 0.0*cm;
Pos_y = 0.0*cm;
Pos_z = -Vs0Half-
2*Als1Half+0.43*cm+0.1*cm+0.00115*cm+SD0+SD00+2*col2Half+col1Half;

G4VPhysicalVolume *col1_phys

```

```

= new
G4PVPlacement(0,G4ThreeVector(Pos_x,Pos_y,Pos_z),col1_log,"col1Tube",Vs0_log,false,0);

//----- 1st collimator inside radius (diamater= 5 mm)
G4double col1vOutR = 0.5/2.*cm;
G4double col1vInR = 0.0*cm;
G4double col1vHalf = 0.1/2.*cm;

G4Tubs *col1v_tube
= new G4Tubs("col1v_tube",col1vInR,col1vOutR,col1vHalf,
startFi,endFi);

G4LogicalVolume *col1v_log
= new G4LogicalVolume(col1v_tube,Vacuum,"col1_log",0,0,0);

Pos_x = 0.0*cm;
Pos_y = 0.0*cm;
Pos_z = 0.0*cm;

G4VPhysicalVolume *col1v_phys
= new
G4PVPlacement(0,G4ThreeVector(Pos_x,Pos_y,Pos_z),col1v_log,"col1vTube",col1_log,
false,0);

////////////////////////////////////

// -----Vacuum surface 1
G4double Vs1OutR = 9./2.*cm; // 4.5x2
G4double Vs1InR = 0.0*cm;
G4double Vs1Half = 3.88/2.*cm;

G4Tubs *Vs1_tube
= new G4Tubs("Vs1_tube",Vs1InR,Vs1OutR,Vs1Half,
startFi,endFi);

G4LogicalVolume *Vs1_log
= new G4LogicalVolume(Vs1_tube,Vacuum,"Vs1_log",0,0,0);

Pos_x = 0.0*cm;
Pos_y = 0.0*cm;
Pos_z = 0.0*cm;

G4VPhysicalVolume *Vs1_phys
= new
G4PVPlacement(0,G4ThreeVector(Pos_x,Pos_y,Pos_z),Vs1_log,"Vs1Tube",Als1_log,false,0);

// -----Al surface 2
G4double Als2OutR =Vs1OutR;
G4double Als2InR = 0.0*cm;
G4double Als2Half = 2.3/2.*cm; // (1.37+0.43+0.5) cm

G4Tubs *Als2_tube
= new G4Tubs("Als2_tube",Als2InR,Als2OutR,Als2Half,
startFi,endFi);

G4LogicalVolume *Als2_log
= new G4LogicalVolume(Als2_tube,Al,"Als2_log",0,0,0);

Pos_x = 0.0*cm;
Pos_y = 0.0*cm;
Pos_z = -Vs1Half+Als2Half;

```

```

G4VPhysicalVolume *Als2_phys
= new
G4PVPlacement(0,G4ThreeVector(Pos_x,Pos_y,Pos_z),Als2_log,"Als2Tube",Vs1_log,false,0);

// -----Vacuum surface 2
G4double Vs2OutR = 5./2.*cm; // 2.5x2
G4double Vs2InR = 0.0*cm;
G4double Vs2Half = 1.37/2.*cm;

G4Tubs *Vs2_tube
= new G4Tubs("Vs2_tube",Vs2InR,Vs2OutR,Vs2Half,
startFi,endFi);

G4LogicalVolume *Vs2_log
= new G4LogicalVolume(Vs2_tube,Vacuum,"Vs2_log",0,0,0);

Pos_x = 0.0*cm;
Pos_y = 0.0*cm;
Pos_z = +Als2Half-Vs2Half;

G4VPhysicalVolume *Vs2_phys
= new
G4PVPlacement(0,G4ThreeVector(Pos_x,Pos_y,Pos_z),Vs2_log,"Vs2Tube",Als2_log,false,0);

// -----Vacuum surface 3
G4double Vs3OutR =2.85/2.*cm;
G4double Vs3InR = 0.0*cm;
G4double Vs3Half = 0.5/2.*cm;

G4Tubs *Vs3_tube
= new G4Tubs("Vs3_tube",Vs3InR,Vs3OutR,Vs3Half,
startFi,endFi);

G4LogicalVolume *Vs3_log
= new G4LogicalVolume(Vs3_tube,Vacuum,"Vs3_log",0,0,0);

Pos_x = 0.0*cm;
Pos_y = 0.0*cm;
Pos_z = +Als2Half-2*Vs2Half-Vs3Half;

G4VPhysicalVolume *Vs3_phys
= new
G4PVPlacement(0,G4ThreeVector(Pos_x,Pos_y,Pos_z),Vs3_log,"Vs3Tube",Als2_log,false,0);

// -----Mo foil 1
G4double SD1=0.2*cm;

G4double Mo1OutR = 2.54/2.*cm;
G4double Mo1InR = 0.0*cm;
G4double Mo1Half = 0.0005/2.*cm;

G4Tubs *Mo1_tube
= new G4Tubs("Mo1_tube",Mo1InR,Mo1OutR,Mo1Half,
startFi,endFi);

G4LogicalVolume *Mo1_log
= new G4LogicalVolume(Mo1_tube,Mo,"Mo1_log",0,0,0);

Pos_x = 0.0*cm;
Pos_y = 0.0*cm;
Pos_z = -Vs3Half+0.1*cm+0.00115*cm+SD1+Mo1Half;

```

```

G4VPhysicalVolume *Mo1_phys
= new
G4PVPlacement(0, G4ThreeVector(Pos_x, Pos_y, Pos_z), Mo1_log, "Mo1Tube", Vs3_log, false
, 0);

// -----Mo foil 2
G4double Mo2OutR = 2.54/2.*cm;
G4double Mo2InR = 0.0*cm;
G4double Mo2Half = 0.0005/2.*cm;

G4Tubs *Mo2_tube
= new G4Tubs("Mo2_tube", Mo2InR, Mo2OutR, Mo2Half,
startFi, endFi);

G4LogicalVolume *Mo2_log
= new G4LogicalVolume(Mo2_tube, Mo, "Mo2_log", 0, 0, 0);

Pos_x = 0.0*cm;
Pos_y = 0.0*cm;
Pos_z = -Vs3Half+0.1*cm+0.00115*cm+SD1+2*Mo1Half+Mo2Half;

G4VPhysicalVolume *Mo2_phys
= new
G4PVPlacement(0, G4ThreeVector(Pos_x, Pos_y, Pos_z), Mo2_log, "Mo2Tube", Vs3_log, false
, 0);

// -----Cu foil
G4double CuOutR = 2.85/2.*cm;
G4double CuInR = 0.0*cm;
G4double CuHalf = 0.1/2.*cm;

G4Tubs *Cu_tube
= new G4Tubs("Cu_tube", CuInR, CuOutR, CuHalf,
startFi, endFi);

G4LogicalVolume *Cu_log
= new G4LogicalVolume(Cu_tube, Cu, "Cu_log", 0, 0, 0);

Pos_x = 0.0*cm;
Pos_y = 0.0*cm;
Pos_z = -Vs3Half+CuHalf;

G4VPhysicalVolume *Cu_phys
= new
G4PVPlacement(0, G4ThreeVector(Pos_x, Pos_y, Pos_z), Cu_log, "CuTube", Vs3_log, false, 0
);

// -----TiT foil
G4double TiTOutR = 2.54/2.*cm;
G4double TiTInR = 0.0*cm;
G4double TiTHalf = 0.00115/2.*cm;

G4Tubs *TiT_tube
= new G4Tubs("TiT_tube", TiTInR, TiTOutR, TiTHalf,
startFi, endFi);

G4LogicalVolume *TiT_log
= new G4LogicalVolume(TiT_tube, TiT, "TiT_log", 0, 0, 0);

Pos_x = 0.0*cm;
Pos_y = 0.0*cm;
Pos_z = -Vs3Half+2*CuHalf+TiTHalf;

```

```

G4VPhysicalVolume *TiT_phys
= new
G4PVPlacement(0,G4ThreeVector(Pos_x,Pos_y,Pos_z),TiT_log,"TiTTube",Vs3_log,false
,0);

//----- target
G4double SD2=1.8*cm;

G4double TarOutR = 1.3/2.*cm;
G4double TarInR = 0.0*cm;
G4double TarHalf = 0.1/2.*cm;

G4Tubs *Tar_tube
= new G4Tubs("Tar_tube",TarInR,TarOutR,TarHalf,
startFi,endFi);

G4LogicalVolume *Tar_log
= new G4LogicalVolume(Tar_tube,Vacuum,"Tar_log",0,0,0);

Pos_x = 0.0*cm;
Pos_y = 0.0*cm;
Pos_z = -Als1Half-SD2-TarHalf;
G4VPhysicalVolume *TarTube_phys
= new G4PVPlacement(0,
G4ThreeVector(Pos_x,Pos_y,Pos_z),
Tar_log,"TarTube",World_log,false,0);

//===== Visualization attributes =====//

World_log->SetVisAttributes (G4VisAttributes::Invisible);

G4VisAttributes *SSaTubeAttr = new G4VisAttributes(G4Colour(0.5,0.5,0.5)); //
gray
SSaTubeAttr->SetVisibility(true);
SSaTubeAttr->SetForceWireframe(true);
SSa_log->SetVisAttributes(SSaTubeAttr);

G4VisAttributes *Vs0TubeAttr = new G4VisAttributes(G4Colour(0.5,0.5,0.5)); //
gray
Vs0TubeAttr->SetVisibility(true);
Vs0TubeAttr->SetForceWireframe(true);
Vs0_log->SetVisAttributes(Vs0TubeAttr);

G4VisAttributes *col2TubeAttr = new G4VisAttributes(G4Colour(1.,1.,0.)); //
yellow
col2TubeAttr->SetVisibility(true);
col2TubeAttr->SetForceWireframe(true);
col2_log->SetVisAttributes(col2TubeAttr);

G4VisAttributes *col2vTubeAttr = new
G4VisAttributes(G4Colour(0.5,0.5,0.5)); // gray
col2vTubeAttr->SetVisibility(true);
col2vTubeAttr->SetForceWireframe(true);
col2v_log->SetVisAttributes(col2vTubeAttr);

G4VisAttributes *col1TubeAttr = new G4VisAttributes(G4Colour(1.,1.,0.)); //
yellow
col1TubeAttr->SetVisibility(true);
col1TubeAttr->SetForceWireframe(true);
col1_log->SetVisAttributes(col1TubeAttr);

G4VisAttributes *col1vTubeAttr = new
G4VisAttributes(G4Colour(0.5,0.5,0.5)); // gray

```



```

col1vTubeAttr->SetVisibility(true);
col1vTubeAttr->SetForceWireframe(true);
col1v_log->SetVisAttributes(col1vTubeAttr);

G4VisAttributes *Als1TubeAttr = new G4VisAttributes(G4Colour(0.,0.,0.)); //
black
Als1TubeAttr->SetVisibility(true);
Als1TubeAttr->SetForceWireframe(true);
Als1_log->SetVisAttributes(Als1TubeAttr);

G4VisAttributes *Vs1TubeAttr = new G4VisAttributes(G4Colour(0.5,0.5,0.5)); //
gray
Vs1TubeAttr->SetVisibility(true);
Vs1TubeAttr->SetForceWireframe(true);
Vs1_log->SetVisAttributes(Vs1TubeAttr);

G4VisAttributes *Als2TubeAttr = new G4VisAttributes(G4Colour(0.,0.,0.)); //
black
Als2TubeAttr->SetVisibility(true);
Als2TubeAttr->SetForceWireframe(true);
Als2_log->SetVisAttributes(Als2TubeAttr);

G4VisAttributes *Vs2TubeAttr = new G4VisAttributes(G4Colour(0.5,0.5,0.5)); //
gray
Vs2TubeAttr->SetVisibility(true);
Vs2TubeAttr->SetForceWireframe(true);
Vs2_log->SetVisAttributes(Vs2TubeAttr);

G4VisAttributes *Vs3TubeAttr = new G4VisAttributes(G4Colour(0.5,0.5,0.5)); //
gray
Vs3TubeAttr->SetVisibility(true);
Vs3TubeAttr->SetForceWireframe(true);
Vs3_log->SetVisAttributes(Vs3TubeAttr);

G4VisAttributes *CuTubeAttr = new G4VisAttributes(G4Colour(0.,1.,1.)); // cyan
CuTubeAttr->SetVisibility(true);
CuTubeAttr->SetForceWireframe(true);
Cu_log->SetVisAttributes(CuTubeAttr);

G4VisAttributes *TiTubeAttr = new G4VisAttributes(G4Colour(1.,0.,0.)); // red
TiTubeAttr->SetVisibility(true);
TiTubeAttr->SetForceWireframe(true);
TiT_log->SetVisAttributes(TiTubeAttr);

G4VisAttributes *Mo1TubeAttr = new G4VisAttributes(G4Colour(0.,1.,0.)); //
green
Mo1TubeAttr->SetVisibility(true);
Mo1TubeAttr->SetForceWireframe(true);
Mo1_log->SetVisAttributes(Mo1TubeAttr);

G4VisAttributes *Mo2TubeAttr = new G4VisAttributes(G4Colour(0.,1.,0.)); //
green
Mo2TubeAttr->SetVisibility(true);
Mo2TubeAttr->SetForceWireframe(true);
Mo2_log->SetVisAttributes(Mo2TubeAttr);

G4VisAttributes *TarTubeAttr = new G4VisAttributes(G4Colour(1.,0.,1.)); //
magenta
TarTubeAttr->SetVisibility(true);
TarTubeAttr->SetForceWireframe(true);
Tar_log->SetVisAttributes(TarTubeAttr);

return World_phys;
}

```

# Appendix H

## Efficiency and counting rate calculations

The efficiency of the detector,  $\varepsilon$ , is defined as:

$$\varepsilon = \varepsilon_I \varepsilon_G \quad (\text{H.1})$$

The term  $\varepsilon_I$  is called intrinsic efficiency and it is equal to the ratio of the detected photons to the photons impinging the detector:

$$\varepsilon_I = \frac{\textit{detected photons}}{\textit{photons impinging the detector}} \quad (\text{H.2})$$

The term  $\varepsilon_G$  is called geometrical efficiency and it depends on the solid angle,  $\Omega$ , of the detector which is “seen” from the source.

In other words, it can be said that the intrinsic efficiency depends on the transmission, absorption and energy deposition of a particular photon in the detector active volume, and therefore, it depends on the photon energy. On the other hand, the geometrical efficiency depends on the detector surface and the source to detector distance. Based on this, the absolute efficiency is defined as the ratio of the detected photons to the number of photons emitted by the source, and consequently, Eq. H.2 takes the following form:

$$\varepsilon = \frac{\textit{detected photons}}{\textit{emitted photons}} = \frac{\textit{counts}}{A * I * \textit{live time}} \quad (\text{H.3})$$

where *counts* stands for the detected counts in a specific photopeak, *A* stands for the isotope activity, *I* stands for the Intensity of the emitted photons per decay and *live time* stands for the “live time” of the measurement.

It has to be clarified that here the term efficiency stands for the full-energy peak efficiency. In a similar way, the total efficiency is defined and this refers to the total energy deposition of the photons of a specific energy to the detector: in total efficiency

the term *counts* of Eq. H.3 includes also the counts of the continuum, the escape peaks, the secondary peaks produced by the initial photon etc.

The efficiency of a particular energy at a specific source to detector distance does not depend on the decay scheme of the isotope, which means that does not include the coincidence summing phenomenon. For long source to detector distances this phenomenon is negligible, but for short distances this has a non-zero probability to affect the peak integral of a photopeak. Therefore, the ratio  $\frac{\text{counts}}{A * T * \text{live\_time}}$  expresses in such cases the counting rate of the  $\gamma$ -rays for a particular decay scheme and a specific detection geometry.

# Appendix I

## Coincidence-Summing effect

Coincidence summing effect is defined as the phenomenon where two or more photons coming from the same cascade penetrate the detector within a time interval that is less than the resolving time of the detection system. In such a case, if one photon is fully absorbed by the detector and the other is fully or partially absorbed, then a pulse equal to the sum of the pulses of each absorbed photon will be recorded.

Coincidence summing effect is distinguished in “summing-out” and “summing-in”. The term “summing-out” refers to the phenomenon which results in a reduced number of recorded counts in the full energy peak. On the other hand, if the sum of the energy of the photons is equal to the energy of a photon coming from a single transition, then the counts of the latter will be higher than in the absence of coincidence summing. This phenomenon is called “summing-in”.

The possibility of coincidence summing effect depends on the solid angle of the detector window with respect to the source,  $\Omega$ . The larger the solid angle is, the larger amount of photons will penetrate the detector within the resolving time of the detection system. Therefore, the possibility of coincidence summing effect increases with the increase of the solid angle or with the decrease of the source to detector distance [116].

# Appendix J

## Photons Attenuation

The term attenuation describes the process during which the entire or a part of the photons energy is absorbed by the matter and therefore, they are entirely disappeared or emitted in a different direction with lower energy [117]. The absorption of a photon beam with intensity  $I_0$  when it penetrates a volume of thickness  $x$  follows the exponential law:

$$I = I_0 * e^{-\mu x} \quad (\text{J.1})$$

where  $\mu$  is called linear attenuation coefficient and corresponds to the probability per unit path length that a beam photon is totally absorbed or scattered. In general,  $\mu$  is given by Eq. J.2.

$$\mu = \tau(\text{photoelectric effect}) + \sigma(\text{Compton scattering}) + \kappa(\text{pair - production}) \quad (\text{J.2})$$

The photoelectric effect, the Compton scattering and the pair-production are the main physics processes to which the photons are subjected when they penetrate matter and  $\tau$ ,  $\sigma$  and  $\kappa$  are the corresponding probabilities of these phenomena.

- Photoelectric effect

Photoelectric effect is called the effect during which the photon interacts with an atomic electron. Through this interaction the photon totally transfers its energy (below denoted as  $E_{ph}$ ) to the electron, which is emitted by the atom with kinetic energy  $E_{e^-}$  :

$$E_{e^-} = E_{ph} - E_b \quad (\text{J.3})$$

where  $E_b$  is the binding energy of the electron.

The photoelectric effect depends on the photons energy  $E_{ph}$  and the atomic mass of the absorber material  $Z$  through Eq. J.4, which is an approximation of the photoelectric effect probability.

$$\tau = Constant * \frac{Z^{4(\text{or } 5)}}{E_{ph}^{3.5}} \quad (\text{J.4})$$

- Compton Scattering

In Compton scattering the photon is scattered by an electron to an angle  $\theta$ . The energy of the scattered photons is calculated via the Eq. J.5:

$$E'_{\text{photon}} = \frac{E_{\text{photon}}}{1 + \frac{E_{\text{photon}}}{m_0 c^2} (1 + \cos\theta)} \quad (\text{J.5})$$

where  $m_0$  is the rest-mass energy of the electron (0.511 MeV). In contrast with the photoelectric effect, where the electron have to be bounded in the atomic nucleus, in Compton scattering the electron can be either bounded in an atom or can be a free electron.

The differential cross section of the Compton scattering is given by the following Eq. J.6:

$$\frac{d\sigma}{d\Omega} = Zr_0^2 \left( \frac{1}{1 + \alpha(1 - \cos\theta)} \right)^2 \left( \frac{1 + \cos^2\theta}{2} \right) \left( 1 + \frac{\alpha^2(1 - \cos\theta)^2}{(1 + \cos^2\theta)[1 + \alpha(1 - \cos\theta)]} \right) \quad (\text{J.6})$$

where  $\alpha = \frac{E_{\text{photon}}}{m_0 c^2}$  and  $r_0$  is the electron radius.

- Pair production

The pair production takes place inside the nucleus Coulomb field and it describes the possibility that a photon is replaced by an electron-positron pair. Therefore, the initial energy of the photon has to be higher than 1.022 MeV, where 1.022 MeV is the sum of the rest-mass energies of the electron and positron (0.511 MeV each). The possibility of this phenomenon increases, while the photon energy also increases.

# Appendix K

## GEANT4 tracking cuts

GEANT4 includes an option which aims at decreasing the simulation time by avoiding the tracking of secondary particles with very low energy. This is achieved by using a “tracking cut”, which is actually a cut in range. The idea of the “tracking cut” is to stop the detection of secondary particles that travel a distance smaller than the “tracking cut”. GEANT4 converts the “tracking cut” into energy cut for the simulated particles and the simulated absorption material. Through its definition the code hinders the production of the secondary particles, and the energy that they would deposit into the detector is recorded as energy deposition of their parent particles. This restriction is implemented in the simulation of photons,  $e^-$ ,  $e^+$  and protons interactions.

In Figure [K1](#) it is illustrated a qualitative GEANT4 spectrum of the energy deposition of the X-rays of 45.21, 45.99, 46.7, 47.55, 48.22 and 49.13 keV at the 50% rel. efficiency HPGe detector for (a) “tracking cut=” 1 mm and (b) “tracking cut” = 1 nm. As can be seen, in order to simulate the Ge X-ray escape peaks phenomenon in the GEANT4 simulations, the “tracking cut” has to be reduced to 1 nm.

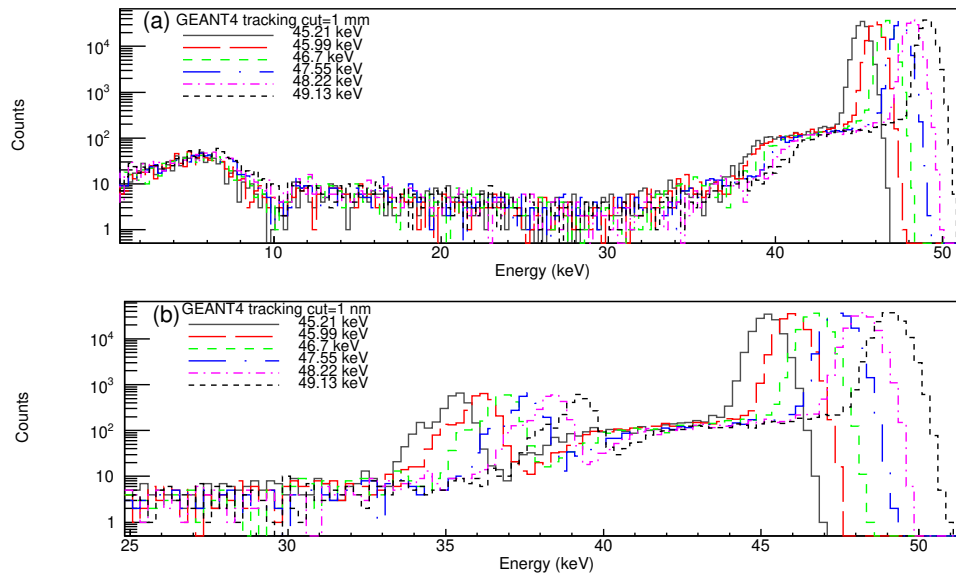


Figure K1: The Ge X-ray escape peaks production in the GEANT4 simulations for the X-rays at 45.21, 45.99, 46.7, 47.55, 48.22 and 49.13 keV, when considering (a) 1 mm and (b) 1 nm “tracking cut”.



# References

- [1] W.Ormand, Eur. Phys. J. Spec. Top. 156, 13 (2008). (DOI: <https://doi.org/10.1140/epjst/e2008-00607-1>)
- [2] A. J. Koning, S. Hilaire, and M. C. Duijvestijn, TALYS-1.0, in Proceedings of the International Conference on Nuclear Data for Science and Technology, April 22–27, 2007, Nice, France, edited by O. Bersillon, F. Gunsing, E. Bauge, R. Jacqmin, and S. Leray (EDP Sciences, Les Ulis, France, 2008), pp. 211–214. (available at [https://tendl.web.psi.ch/tendl\\_2019/tendl2019.html](https://tendl.web.psi.ch/tendl_2019/tendl2019.html))
- [3] M. Herman, R. Capote, B.V. Carlson, P. Oblozinsky, M. Sin, A. Trkov, H. Wienke, and V. Zerkin, “EMPIRE: Nuclear Reaction Model Code System for Data Evaluation”, Nucl. Data Sheets, 108 (2007) 2655-2715. (available at <https://www-nds.iaea.org/empire/index.html>)
- [4] S. Agostinelli, et al., Nucl. Instrum. Methods. Phys. Res. A 506, 250 (2003); J. Allison et al., IEEE Trans. Nucl. Sci. 53, 270 (2006); Nucl. Instrum. Methods. Phys. Res. A 835, 186 (2016). (available at <https://geant4.web.cern.ch/>)
- [5] C.J. Werner, et al., “MCNP6.2 Release Notes”, Los Alamos National Laboratory, report LA-UR-18-20808 (2018); C.J. Werner (editor), “MCNP Users Manual - Code Version 6.2”, Los Alamos National Laboratory, report LA-UR-17-29981 (2017). (available at <https://laws.lanl.gov/vhosts/mcnp.lanl.gov/index.shtml>)
- [6] “The FLUKA Code: Developments and Challenges for High Energy and Medical Applications” T. T. Böhlen, F. Cerutti, M. P. W. Chin, A. Fassò, A. Ferrari, P. G. Ortega, A. Mairani, P. R. Sala, G. Smirnov, and V. Vlachoudis, Nuclear Data Sheets 120, 211-214 (2014); “FLUKA: a multi-particle transport code” A. Ferrari, P.R. Sala, A. Fassò, and J. Ranft, CERN-2005-10 (2005), INFN/TC-05/11, SLAC-R-773. (available at <http://www.fluka.org/fluka.php?id=about&mm2=1>)
- [7] D. A. Brown, et al., “ENDF/B-VIII.0: The 8th major release of the nuclear reaction data library with CIELO-project cross sections, new standards and thermal scattering data”, Nucl. Data Sheets 148, 1 (2018). (DOI: <https://doi.org/10.1016/j.nds.2018.02.001>)

- [8] A. J. M. Plompen, et al., “The joint evaluated fission and fusion nuclear data library, JEFF-3.3”, *Eur. Phys. J. A* 56, 181 (2020). (DOI: <https://doi.org/10.1140/epja/s10050-020-00141-9>)
- [9] K. Shibata, et al., “JENDL-4.0: A new library for nuclear science and engineering”, *J. Nucl. Sci. Technol.* 48, 1 (2011). (DOI: <https://doi.org/10.1080/18811248.2011.9711675>)
- [10] V. D. Risovany, A. V. Zakharov, E. M. Muraleva, V. M. Kosenkov, and R. N. Latypov, *Journal of Nuclear Materials* 355, 163, (2006). (DOI: <https://doi.org/10.1016/j.jnucmat.2006.05.029>)
- [11] Umasankari Kannan and S. Ganesan, *Annals of Nuclear Energy* 37, 270 (2010). (DOI: <https://doi.org/10.1016/j.anucene.2009.10.012>)
- [12] Alan Baxter and Carmelo Rodriguez, *Progress in Nuclear Energy* 38, 81 (2001). (DOI: [https://doi.org/10.1016/S0149-1970\(00\)00097-4](https://doi.org/10.1016/S0149-1970(00)00097-4))
- [13] A. Stanculescu, U. Kasemeyer, and J.M. Parattea, and R. Chawla, *Journal of Nuclear Materials* 274, 146, (1999). (DOI: [https://doi.org/10.1016/S0022-3115\(99\)00082-3](https://doi.org/10.1016/S0022-3115(99)00082-3))
- [14] Vladimir Barchevtsev, Vladimir Artisyuk, and Hisathi Ninikata, *Journal of Nuclear Science and Technology* 39, 506 (2002). (DOI: <https://doi.org/10.1080/18811248.2002.9715228>)
- [15] B. Pritychenko, “Nuclear Data for Astrophysical Modeling” (2016). (available at [https://www.researchgate.net/publication/316216096\\_Nuclear\\_Data\\_for\\_Astrophysical\\_Modeling](https://www.researchgate.net/publication/316216096_Nuclear_Data_for_Astrophysical_Modeling))
- [16] B. Pritychenko, “Assessment of Stellar Nucleosynthesis Abundances Using ENDF/B-VIII.0 and TENDL-2015 Evaluated Nuclear Data Libraries”. In: Formicola A., Junker M., Gialanella L., Imbriani G. (eds) *Nuclei in the Cosmos XV*. Springer Proceedings in Physics, vol 219. Springer, Cham. (DOI: [https://doi.org/10.1007/978-3-030-13876-9\\_23](https://doi.org/10.1007/978-3-030-13876-9_23))
- [17] National Nuclear Data Center (2020, August 27), *Experimental Nuclear Reaction Data (EXFOR)*. (available at <https://www-nds.iaea.org/exfor/>)
- [18] N. Dzysiuk, A. Kadenko, I. Kadenko, and G. Primenko, *Phys. Rev. C* 86, 034609 (2012). (DOI: <https://doi.org/10.1103/PhysRevC.86.034609>)
- [19] Junhua Luo, Rong Liu, Li Jiang, and Zhenlai Liu, *J. Radioanal. Nucl. Chem.* 289, 455 (2011). (DOI: <https://doi.org/10.1103/PhysRevC.86.034609>)
- [20] Xiangzhong Kong, Yongchang Wang, and Jingkang Yang, *Appl. Radiat. Isotopes* 49, 1529 (1998). (DOI: [https://doi.org/10.1016/S0969-8043\(98\)00018-9](https://doi.org/10.1016/S0969-8043(98)00018-9))

- [21] H. Liljavirta and T. Tuurnala, Phys. Scr. 18, 75 (1978). (available at <https://iopscience.iop.org/article/10.1088/0031-8949/18/2/002>)
- [22] S.M. Qaim, Nuclear Physics A 224, 319 (1974). (DOI: [https://doi.org/10.1016/0375-9474\(74\)90690-3](https://doi.org/10.1016/0375-9474(74)90690-3))
- [23] N. Lakshmana Das, C. V. Srinivasa Rao, B. V. Thirumala Rao, and J. Rama Rao, Pramana-J. Phys. 17, 99–104 (1981). (DOI: <https://doi.org/10.1007/BF02872041Nucl>).
- [24] A. Bari, Dissertation Abstracts B 32, 5091 (1972).
- [25] E. Havlik, Acta Phys. Austr. 34, 209 (1971).
- [26] P. Rama Prasad, J. Rama Rao, and E. Kondaiah, Nucl. Phys. A 125, 57 (1969). (DOI: [https://doi.org/10.1016/0375-9474\(69\)90828-8](https://doi.org/10.1016/0375-9474(69)90828-8))
- [27] Junhua Luo, Li An, and Li Jiang, J. Radioanal. Nucl. Chem. 308, 649 (2016). (DOI: [10.1007/s10967-015-4433-6](https://doi.org/10.1007/s10967-015-4433-6))
- [28] L. A. Oms, J. M. Palms, P. Venugopala Rao, R. E. Wood, and R. W. Fink, Bull. Am. Phys. Soc.13, 1699(CA9) (1968).
- [29] Junhua Luo and Li Jiang, Phys. Rev. C 89, 014604 (2014). (DOI: <https://doi.org/10.1103/PhysRevC.89.014604>)
- [30] Kaihong Fang, Shiwei Xu, Changlin Lan, Xiaosan Xu, Xiangzhong Kong, Rong Liu, and Li Jiang, Applied Radiation and Isotopes 66, 1104-1107 (2008). (DOI: <https://doi.org/10.1016/j.apradiso.2007.10.011>)
- [31] Hitoshi Sakane, Yoshimi Kasugai, Michihiro Shibata, Toshiyuki Iida, Akito Takahashi, Tokio Fukahori, and Kiyoshi Kawade, Annals of Nuclear Energy 28, 1175-1192 (2001). (DOI: [https://doi.org/10.1016/S0306-4549\(00\)00123-7](https://doi.org/10.1016/S0306-4549(00)00123-7))
- [32] A. Reggoug, G. Paic, and M. Berrada, University of Mohammed V, Rabat, Annual Report No. 5, p. 14, 1982.
- [33] E. Steiner, P. Huber, W. Salathe, and R. Wagner, Helv. Phys. Acta 43, 17 (1970).
- [34] W. Dilg, H. Vonach, G. Winkler, and P. Hille, Nuclear Physics A 118, 9-16 (1968). (DOI: [https://doi.org/10.1016/0375-9474\(68\)90182-6](https://doi.org/10.1016/0375-9474(68)90182-6))
- [35] M. Bormann, A. Behrend, I. Riehle, and O. Vogel, Nuclear Physics A 115, 309-320 (1968). (DOI: [https://doi.org/10.1016/0375-9474\(68\)90006-7](https://doi.org/10.1016/0375-9474(68)90006-7))
- [36] H. O. Menlove, K. L. Coop, H. A. Grench, and R. Sher, Phys. Rev. 163, 1308 (1967). (DOI: <https://doi.org/10.1103/PhysRev.163.1308>)

- [37] B. Sethi and S. K. Mukherjee, Nuclear Physics 85, 227-240 (1966). (DOI: [https://doi.org/10.1016/0029-5582\(66\)90143-X](https://doi.org/10.1016/0029-5582(66)90143-X))
- [38] Kaihong Fang, Yang Xiang, Yuncheng Han, Xiangzhong Kong, Tieshan Wang, Rong Liu, and Li Jiang, Radiation Measurements 44, 68-71 (2009). (DOI: <https://doi.org/10.1016/j.radmeas.2008.11.001>)
- [39] Evaluated Nuclear Data File (ENDF) (2020, October 08), <https://www-nds.iaea.org/exfor/endl.htm>.
- [40] G. Hevesy and H. Levi, Nature 137, 185 (1936). (DOI: <https://doi.org/10.1038/137185a0>)
- [41] S.S. Belyshev, A.N. Ermakov, B.S. Ishkhanov, V.V. Khankin, A.S. Kurilik, A.A. Kuznetsov, V.I. Shvedunov, and K.A. Stopani, Nuclear Instruments and Methods in Physics Research A 745, 133 (2014). (DOI: [10.1016/j.nima.2014.01.057](https://doi.org/10.1016/j.nima.2014.01.057))
- [42] D. P. Chowdhury, J. Datta<sup>1</sup>, and A. V. R. Reddy, Radiochim. Acta 99, 1 (2011). (DOI: [10.1524/ract.2011.1889](https://doi.org/10.1524/ract.2011.1889))
- [43] Cristian Bungau, Adriana Bungau, Robert Cywinski, Roger Barlow, Thomas Robert Edgecock, Patrick Carlsson, Håkan Danared, Ferenc Mezei, Anne Ivalu Sander Holm, Søren Pape Møller, and Heine Dølrath Thomsen, Phys. Rev. ST Accel. Beams 17, 084701 (2014). (DOI: <https://doi.org/10.1103/PhysRevSTAB.17.084701>)
- [44] Nicholas Tsoufanidis, *Measurement and Detection of Radiation* (Taylor & Francis, Washington, 1995).
- [45] C. W. Reich, Nuclear Data Sheets 112, 2497 (2011) (DOI: <https://doi.org/10.1016/j.nds.2011.09.001>).
- [46] N. Nica, Nuclear Data Sheets 160, 1 (2019) (DOI: <https://doi.org/10.1016/j.nds.2019.100523>).
- [47] Balraj Singh and Jun Chen, Nuclear Data Sheets 147, 1 (2018) (DOI: <https://doi.org/10.1016/j.nds2018.01.001>).
- [48] Kenneth S. Krane, *Introductory Nuclear Physics* (Wiley, United States, 1987).
- [49] E. Georgali, N. Patronis, A. Anastasiadis, X. Aslanoglou, M. Axiotis, Z. Eleme, S. Harissopoulos, A. Kalamara, K. Karfopoulos, M. Kokkoris, A. Lagoyannis, M. Peoviti, C. Potiriadis, M. I. Savva, I. E. Stamatelatos, M. E. Stamati, A. Stamatopoulos, E. Vagena, T. Vasilopoulou, and R. Vlastou, Phys. Rev. C 102, 034610 (2020). (DOI: <https://doi.org/10.1103/PhysRevC.102.034610>).
- [50] International Reactor Dosimetry and Fusion File, IRDFF v.1.05 (2014, 09 October), <https://www-nds.iaea.org/IRDFF/>.

- [51] R.B. Firestone, Nuclear Data Sheets 108, 2319 (2007). (DOI: <https://doi.org/10.1016/j.nds.2007.10.001>)
- [52] Huang Xiaolong, Nuclear Data Sheets 108, 1093 (2007). (DOI: <https://doi.org/10.1016/j.nds.2007.05.001>)
- [53] Coral M. Baglin, Nuclear Data Sheets 113, 2187 (2012). (DOI: <https://doi.org/10.1016/j.nds.2012.10.001>)
- [54] National Center for Scientific Research “Demokritos”, Institute of Nuclear and Particle Physics, <http://www.inp.demokritos.gr/>.
- [55] G. Doukellis, T.Paradellis, and S.Kossionides, Nuclear Inst. and Methods in Physics Research A 327, 480 (1993). (DOI: [https://doi.org/10.1016/0168-9002\(93\)90714-S](https://doi.org/10.1016/0168-9002(93)90714-S))
- [56] Nuclear Wallet Cards Search, National Nuclear Data Center, <https://www.nndc.bnl.gov/wallet/wallet11.pdf>.
- [57] Horst Liskien and Arno Paulsen, NUCLEAR DATA TABLES 11, 569-619 (1973). (DOI: [https://doi.org/10.1016/S0092-640X\(73\)80081-6](https://doi.org/10.1016/S0092-640X(73)80081-6))
- [58] Wilton Catford, CatKin, The relativistic kinematics program in Excel (v. 2.02), available at <http://personal.ph.surrey.ac.uk/~phs1wc/kinematics/>.
- [59] E. Birgersson and G. Lovestam, JRC Science Hub Technical Report, Ref. No. 23794, 2009, [https://publications.jrc.ec.europa.eu/repository/bitstream/JRC51437/reqno\\_jrc51437\\_jrc51437-eur\\_number\\_23794\[1\].pdf](https://publications.jrc.ec.europa.eu/repository/bitstream/JRC51437/reqno_jrc51437_jrc51437-eur_number_23794[1].pdf).
- [60] J. Monahan, Fast Neutron Physics, Part I, p. 49, Interscience Publishers, New York 9, (1960).
- [61] H. Horstmann and H. Liskien, Relativistic calculations of kinematic parameters for nuclear reactions, CBNM EURATOM report EUR 3668 e (1968).
- [62] H. H. Andersen and J. F. Ziegler, “Hydrogen Stopping Powers and Ranges in All Elements”, vol. 3 of series ”Stopping and Ranges of Ions in Matter” Pergamon Press, New York, (1977).
- [63] J. F. Ziegler, “Helium Stopping Powers and Ranges in All Elements” vol. 4 of series ”Stopping and Ranges of Ions in Matter” Pergamon Press, New York, (1978).
- [64] J. F. Ziegler, J. P. Biersack, and M. D. Ziegler, SRIM-2008, available at <http://www.srim.org/SRIM/SRIMLEGL.htm>.
- [65] Fukui Renderer, DAWN (Drawer for Academic WritiNgs), available at [https://geant4.kek.jp/~tanaka/DAWN/About\\_DAWN.html](https://geant4.kek.jp/~tanaka/DAWN/About_DAWN.html)

- [66] GEANT4-A simulation toolkit, Reference Physics Lists, available at <https://geant4.web.cern.ch/node/155>.
- [67] Y. Dong and H. Junde, Nucl. Data Sheets 121, 1 (2014). (DOI: [10.1016/j.nds.2014.09.001](https://doi.org/10.1016/j.nds.2014.09.001))
- [68] M. J. Martin, Nucl. Data Sheets 114, 1497 (2013). (DOI: <https://doi.org/10.1016/j.nds.2013.11.001>)
- [69] E. Georgali, N. Patronis, A. Anastasiadis, X. Aslanoglou, M. Axiotis, Z. Eleme, S. Harissopoulos, A. Kalamara, K. Karfopoulos, M. Kokkoris, A. Lagoyannis, M. Peoviti, C. Potiriadis, M. I. Savva, I. E. Stamatelatos, M. E. Stamati, A. Stamatopoulos, E. Vagena, T. Vasilopoulou, and R. Vlastou Phys. Rev. C 102, 034610 (2020). (DOI: <https://doi.org/10.1103/PhysRevC.98.014622>)
- [70] E. Georgali (Feb. 2017), “Study of the  $^{162}\text{Er}(n,2n)^{161}\text{Er}$  at near threshold energies”, MSc thesis, Physics Department, University of Ioannina. (link: <http://nuclear.physics.uoi.gr/publications/efi.pdf>)
- [71] Z. Eleme (Apr. 2017), “Study of (n,x) reactions for Erbium isotopes at energies higher than 17 MeV”, MSc thesis, Physics Department, University of Ioannina. (link: <http://nuclear.physics.uoi.gr/publications/zina.pdf>)
- [72] F. Hernandez and F. El-Daoushy, Nuclear Instruments and Methods in Physics Research A 498, 340 (2003). (DOI: [10.1016/S0168-9002\(02\)02080-6](https://doi.org/10.1016/S0168-9002(02)02080-6))
- [73] S. Hurtado, M. Garcia-Leon, R. Garca-Tenorio, Nuclear Instruments and Methods in Physics Research A 518, 764 (2004). (DOI: <https://doi.org/10.1016/j.nima.2003.09.057>)
- [74] E. Browne and J. K. Tuli, Nuclear Data Sheets 114, 1849 (2013). (DOI: <https://doi.org/10.1016/j.nds.2013.11.002>)
- [75] E. Browne and J. K. Tuli, Nuclear Data Sheets 108, 2173 (2007). (DOI: [10.1016/j.nds.2007.09.002](https://doi.org/10.1016/j.nds.2007.09.002))
- [76] Yu. Khazov and A. Rodionov, and F.G. Kondev, Nuclear Data Sheets 112, 855 (2011). (DOI: <https://doi.org/10.1016/j.nds.2011.03.001>)
- [77] M. S. Basunia, Nuclear Data Sheets 107, 2323 (2006). (DOI: [10.1016/j.nds.2006.07.001](https://doi.org/10.1016/j.nds.2006.07.001))
- [78] F.G. Kondev, Nuclear Data Sheets 109, 1527 (2008). (DOI: <https://doi.org/10.1016/j.nds.2008.05.002>)
- [79] E. Georgali, N. Patronis, A. Anastasiadis, M. Axiotis, S. Harissopoulos, K. Karfopoulos, M. Kokkoris, A. Lagoyannis, C. Potiriadis, R. Vlastou, Nuclear Inst. and Methods in Physics Research, A 985, 164711 (2021). (DOI: <https://doi.org/10.1016/j.nima.2020.164711>)

- [80] B. Rosner and D. W. Mingay, X-ray spectroscopy 12, 82-86 (1983). (DOI: <https://doi.org/10.1002/xrs.1300120208>)
- [81] M. Korun and R. Marfncic, Nuclear Instruments and Methods in Physics Research A 325, 478 (1993).
- [82] U. Fano, Phys. Rev. 70 (1946) 44. (DOI: <https://doi.org/10.1103/PhysRev.70.44>)
- [83] Canberra Broad Energy Germanium Detectors (BEGe), available at <https://www.mirion.com/products/bege-broad-energy-germanium-detectors>
- [84] W. Hauser and H. Feshbach, Phys. Rev. 87, 366 (1952). (DOI: <https://doi.org/10.1103/PhysRev.87.366>)
- [85] J.J. Griffin, Phys. Rev. Lett. 17 (1966) 478. (DOI: <https://doi.org/10.1103/PhysRevLett.17.478>)
- [86] E. Gadioli, P.E. Hodgson, Pre-equilibrium Nuclear Reactions, Oxford Univ. Press, New York, 1992.
- [87] C. Kalbach, Phys. Rev. C 71, 034606 (2005). (DOI: <https://doi.org/10.1103/PhysRevC.71.034606>)
- [88] C. Kalbach, Phys. Rev. C 37, 2350 (1988). (DOI: <https://doi.org/10.1103/PhysRevC.37.2350>)
- [89] A.J. Koning and J.P. Delaroche, "Local and global nucleon optical models from 1 keV to 200 MeV", Nucl. Phys. A713, 231 (2003). (DOI: [10.1016/S0375-9474\(02\)01321-0](https://doi.org/10.1016/S0375-9474(02)01321-0))
- [90] E. Bauge, J.P. Delaroche, M. Girod, Phys. Rev. C 63, 024607 (2001). (DOI: <https://doi.org/10.1103/PhysRevC.63.024607>)
- [91] R. Capote, M. Herman, P. Oblozinsky, P.G. Young, S. Goriely, T. Belgya, A.V. Ignatyuk, A.J. Koning, S. Hilaire, V. Plujko, M. Avrigeanu, O. Bersillon, M.B. Chadwick, T. Fukahori, S. Kailas, J. Kopecky, V.M. Maslov, G. Reffo, M. Sin, E. Soukhovitskii, P. Talou, H. Yinlu, and G. Zhigang, "RIPL - Reference Input Parameter Library for calculation of nuclear reactions and nuclear data evaluation", Nucl. Data Sheets 110, 3107 (2009).
- [92] S. Watanabe, Nucl. Phys. 8, 484 (1958). (DOI: [https://doi.org/10.1016/0029-5582\(58\)90180-9](https://doi.org/10.1016/0029-5582(58)90180-9))
- [93] D.G. Madland, in Proceedings of a Specialists' Meeting on preequilibrium nuclear reactions, Semmering, Austria, February 10-12 (1988), p. 103. (available at [https://inis.iaea.org/collection/NCLCollectionStore/\\_Public/20/025/20025135.pdf?r=1&r=1](https://inis.iaea.org/collection/NCLCollectionStore/_Public/20/025/20025135.pdf?r=1&r=1))

- [94] V. Avrigeanu et al. Phys. Rev. C 90, 044612 (2014). (DOI: <https://doi.org/10.1103/PhysRevC.90.044612>)
- [95] J. Raynal, Notes on ECIS94, CEA Saclay Report No. CEA-N-2772, (1994).
- [96] D.M. Brink, Nucl. Phys. 4, 215 (1957). (DOI: [https://doi.org/10.1016/0029-5582\(87\)90021-6](https://doi.org/10.1016/0029-5582(87)90021-6))
- [97] P. Axel, Phys. Rev. 126, 671 (1962). (DOI: <https://doi.org/10.1103/PhysRev.126.671>)
- [98] J. Kopecky, M. Uhl and R.E. Chrien,, Phys. Rev. C 47, 312 (1993). (DOI: <https://doi.org/10.1103/PhysRevC.47.312>)
- [99] R. Capote, M. Herman, P. Oblozinsky, P. G. Young, S. Goriely, T. Belgya, A. V. Ignatyuk, A. J. Koning, S. Hilaire, V. Plujko, M. Avrigeanu, O. Bersillon, M. B. Chadwick, T. Fukahori, S. Kailas, J. Kopecky, V. M. Maslov, G. Reffo, M. Sin, E. Soukhovitskii, P. Talou, H. Yinlu, and G. Zhigang, “RIPL - Reference Input Parameter Library for calculation of nuclear reactions and nuclear data evaluation”, Nucl. Data Sheets 110, 3107 (2009). (available at <https://www-nds.iaea.org/RIPL-3/CRP/index.html>)
- [100] S. Goriely, Phys. Lett. B 436, 10 (1998). (DOI: [https://doi.org/10.1016/S0370-2693\(98\)00907-1](https://doi.org/10.1016/S0370-2693(98)00907-1))
- [101] A.V. Ignatyuk, G.N. Smirenkin and A.S. Tishin, Sov. J. Nucl. Phys. 21, no. 3, 255 (1975).
- [102] A. Gilbert and A.G.W. Cameron, Can. J. Phys. 43, 1446 (1965). (DOI: <https://doi.org/10.1139/p65-139>)
- [103] M.K. Grossjean and H. Feldmeier, Nucl. Phys. A444, 113 (1985). (DOI: [https://doi.org/10.1016/0375-9474\(85\)90294-5](https://doi.org/10.1016/0375-9474(85)90294-5))
- [104] P. Demetriou and S. Goriely, Nucl. Phys. A695, 95 (2001). (DOI: [https://doi.org/10.1016/S0375-9474\(01\)01095-8](https://doi.org/10.1016/S0375-9474(01)01095-8))
- [105] A. V. Ignatyuk, K. K. Istekov, and G. N. Smirenkin, Yad. Fiz. 29, 875 (1979) [Sov. J. Nucl. Phys. 29, 450 (1979)].
- [106] A. V. Ignatyuk, J. L.Weil, S. Raman, and S. Kahane, Phys. Rev. C 47, 1504 (1993). (DOI: <https://doi.org/10.1103/PhysRevC.47.1504>)
- [107] S. Goriely, F. Tondeur, and J. M. Pearson, At. Data Nucl. Data Tables 77, 311 (2001). (DOI: <https://doi.org/10.1006/adnd.2000.0857>)
- [108] S. Goriely, S. Hilaire, and A. J. Koning, Phys. Rev. C 78, 064307 (2008). (DOI: <https://doi.org/10.1103/PhysRevC.78.064307>)



- [109] S. Hilaire, M. Girod, S. Goriely, and A. J. Koning, Phys. Rev. C 86, 064317 (2012). (DOI: <https://doi.org/10.1103/PhysRevC.86.064317>)
- [110] A. J. Koning, S.Hilaire, and S.Goriely, Nuclear Physics A 810, 13-76 (2008). (DOI: <https://doi.org/10.1016/j.nuclphysa.2008.06.005>)
- [111] A. Kalamara, R. Vlastou, M. Kokkoris, N. G. Nicolis, N. Patronis, M. Serris, V. Michalopoulou, A. Stamatopoulos, A. Lagoyannis, and S. Harissopoulos, Phys. Rev. C 97, 034615 (2018). (DOI: <https://doi.org/10.1103/PhysRevC.97.034615>)
- [112] A. Kalamara, R. Vlastou, M. Kokkoris, S. Chasapoglou, A. Stamatopoulos, N. Patronis, M. Serris, A. Lagoyannis, and S. Harissopoulos, Phys. Rev. C 98, 034607 (2018). (DOI: <https://doi.org/10.1103/PhysRevC.98.034607>)
- [113] A. Kalamara, N. Patronis, R. Vlastou, M. Kokkoris, S. Chasapoglou, A. Stamatopoulos, M. Serris, V. Paneta, M. Axiotis, A. Lagoyannis, S. Harissopoulos, and I.E. Stamatelatos, Eur. Phys. J. A (2019) 55: 187. (DOI: <https://doi.org/10.1140/epja/i2019-12879-x>)
- [114] N. Patronis and E. Georgali, “Measurements of the (n,2n) channel in the mass region A=127-136”, 2<sup>nd</sup> Calibra Meeting, Athens, Greece, 8 July 2019.
- [115] M. Peoviti, “HPGe detectors characterization and feasibility study for cross section measurements of neutron induced reactions on mid-weight nuclei at INPP/NCSR “Demokritos”, MSc thesis, Physics Department, University of Ioannina.
- [116] Klaus Debertin and Ulrich Schötzig, Nuclear Instruments and Methods 158, 471 (1979).
- [117] Glenn F., Knoll. (1979). *Radiation Detection and Measurement*(New York: Wiley).